

**UNIVERSITÉ DU QUÉBEC À CHICOUTIMI**

**THÈSE PRÉSENTÉ À  
L'UNIVERSITÉ DU QUÉBEC À CHICOUTIMI  
COMME EXIGENCE PARTIELLE  
DU DOCTORAT EN INGÉNIERIE**

**PAR  
LI LIU**

**PARAMÈTRES MÉTALLURGIQUES CONTRÔLANT  
L'ÉVOLUTION MICROSTRUCTURALE DANS  
LES ALLIAGES DE FONDERIE AL-SI-MG ET AL-SI-CU**

**AVRIL 2003**



### Mise en garde/Advice

Afin de rendre accessible au plus grand nombre le résultat des travaux de recherche menés par ses étudiants gradués et dans l'esprit des règles qui régissent le dépôt et la diffusion des mémoires et thèses produits dans cette Institution, **l'Université du Québec à Chicoutimi (UQAC)** est fière de rendre accessible une version complète et gratuite de cette œuvre.

Motivated by a desire to make the results of its graduate students' research accessible to all, and in accordance with the rules governing the acceptance and diffusion of dissertations and theses in this Institution, the **Université du Québec à Chicoutimi (UQAC)** is proud to make a complete version of this work available at no cost to the reader.

L'auteur conserve néanmoins la propriété du droit d'auteur qui protège ce mémoire ou cette thèse. Ni le mémoire ou la thèse ni des extraits substantiels de ceux-ci ne peuvent être imprimés ou autrement reproduits sans son autorisation.

The author retains ownership of the copyright of this dissertation or thesis. Neither the dissertation or thesis, nor substantial extracts from it, may be printed or otherwise reproduced without the author's permission.

*Dedicated to my parents*  
谨以此献给我的父母

## RÉSUMÉ

Avec leurs caractéristiques de basse masse volumique, de bas point de fusion, d'excellente coulabilité et de bonne résistance à la corrosion, les alliages aluminium-silicium (Al-Si) sont intensivement utilisés dans les applications d'automobiles. Les pièces produites à partir de ces alliages s'étendent dans plusieurs utilisations, à savoir, des blocs de moteur, des culasses et des roues.

Deux des alliages commerciaux les plus populaires utilisés dans de telles applications sont les alliages de type A356 et 319, appartenant respectivement aux systèmes Al-Si-Mg et Al-Si-Cu. La qualité et les propriétés des pièces coulées sont déterminées par la qualité de leur microstructure, commandée par de divers paramètres tels que l'espace interdendritique (DAS, contrôlé lui même par le taux de solidification), le degré de modification de silicium eutectique et le degré d'affinage de grain, et la quantité de microporosités, d'intermétalliques et d'inclusions observées dans la microstructure. Parmi ces derniers facteurs, le taux de solidification est le plus important, car il affecte directement ou indirectement presque tous les autres paramètres microstructuraux.

La modification de la morphologie du silicium eutectique de la forme aciculaire à une forme fibreuse est habituellement effectuée par l'addition du strontium (Sr) pour améliorer la ductilité de l'alliage. Les intermétalliques qui sont présents généralement en ces alliages sont les intermétalliques du fer  $\beta$ -Al<sub>5</sub>FeSi et  $\alpha$ -Al<sub>5</sub>(Fe, Mn)<sub>3</sub>Si<sub>2</sub>, plaquettes, Mg<sub>2</sub>Si et, dans le cas des alliages 319, les intermétalliques de cuivre, CuAl<sub>2</sub>. En raison de leur fragilité, les intermétalliques de fer dont la nature est sous forme de plaquettes peuvent être tout à fait délétères aux propriétés de l'alliage, de même la présence de la porosité, en particulier en termes de qualité extérieure et solidité.

Le but du travail actuel est d'étudier les paramètres métallurgiques contrôlant l'évolution microstructurale dans les alliages de type Al-Si-Mg et Al-Si-Cu, à l'aide de la détermination des caractéristiques microstructurales des alliages de type A356 et 319 directionnellement solidifiés en fonction de la teneur du fer, de l'addition du Sr (250 ppm) et de taux de refroidissement. Les teneurs en fer choisies varient de 0.12 (% en poids) à 0.8 (% en poids), et couvrent la gamme des niveaux de Fe trouvée dans les alliages commerciaux. L'utilisation d'un moule d'extrémité froide a fourni différents taux de refroidissement le long de la taille de la même pièce coulée, les valeurs de DAS qui ont changé de ~ 23 à 85  $\mu$ m, correspondant aux niveaux de 5, 10, 30, 50 et 100 mm au-dessus de l'extrémité froide.

Les effets de ces variables sur la précipitation de la phase de  $\beta$ -Al<sub>5</sub>FeSi, les caractéristiques de la structure dendritique  $\alpha$ -Al, la modification du silicium eutectique et la formation de porosité ont été examinés en détail. Diverses techniques ont été employées

pour la caractérisation microstructurale et l'identification des phases, y compris le microscope électronique optique et de balayage, la microsonde électronique a couplés avec des rayons X d'énergie dispersive (EDX), la spectroscopie de longueur d'onde (WDS), ainsi que l'analyse thermique. Un analyseur d'image a été utilisé en même temps que le microscope optique pour la quantification.

Une analyse des résultats obtenus prouve que la quantité de fer présente dans l'alliage affecte la taille des plaquettes de  $\beta$ - $\text{Al}_5\text{FeSi}$  et de leur distribution, en particulier avec un faible taux de refroidissement. L'addition du strontium mène à la fragmentation de ces  $\beta$ -plaquettes co-eutectiques ou post-eutectiques. Cet effet diminue avec l'augmentation de la concentration en fer, et davantage d'addition de strontium mène à la précipitation des particules de type  $\text{Al}_2\text{Si}_2\text{Sr}$ , au lieu de fragmenter les plaquettes de fer.

On observe un minimum de porosité dans les alliages dont le pourcentage en poids de fer est de  $\sim 0.4$  (cas de l'alliage 319) et de  $\sim 0.4$  ou  $0.6$  (cas de l'alliage 356) dû aux améliorations de la fluidité d'alliage. Avec l'augmentation du contenu de fer au dessus de ces niveaux, la porosité est également augmentée, en raison de l'augmentation de la taille des plaquettes de fer et de l'obstacle accru dans le métal fondu. La porosité observée à n'importe quel niveau donné de fer est la résultante de la concurrence entre ces deux facteurs, c.-à-d., fluidité et taille de  $\beta$ -plaquettes, et dépend de la perméabilité des régions interdendritiques. Bien que les branches de la phase  $\beta$ - $\text{Al}_5\text{FeSi}$  mène à la formation de porosité, ces mêmes plaquettes, d'autre part, limitent également la croissance des pores. En général, le pourcentage de porosité, l'aire maximum et la longueur maximale de pore augmentent avec l'augmentation des longueurs moyennes des plaquettes du  $\beta$ - $\text{Al}_5\text{FeSi}$  dans les alliages 356 et 319.

Dans les alliages modifiés par le strontium, la formation de porosité est fréquemment associée aux oxydes de strontium (des particules ou films), aussi bien qu'aux plaquettes de  $\beta$ - $\text{Al}_5\text{FeSi}$ . Ces oxydes (avec une composition stoechiométrique proche de  $\text{Al}_2\text{SrO}_3$ ) sont formés pendant la coulée du métal liquide, et ce est dû à l'affinité élevée de l'oxygène du strontium, et sont difficiles à s'enlever par l'intermédiaire d'un dégazage. La morphologie du pore (ronde ou irrégulière) est déterminée par la forme de l'oxyde, à savoir, particules ou films épais très bien dispersés. Des pores ronds sont également observés entourés par des régions eutectiques d'Al-Si. Les films d'oxyde d'aluminium emprisonnés dans le métal fondu mènent à la formation des pores plus bruts et plus profonds que ceux formés d'oxydes de strontium. Ces pores peuvent également être liés l'un avec l'autre, et sont caractérisés par la présence du métal solidifié emprisonné dans les films d'oxyde d'aluminium, près de la périphérie. La forme de ces pores est commandée par la quantité de gaz emprisonné avec les pores pendant la solidification. Les oxydes d'aluminium et de strontium agissent également en tant que des emplacements ou sites favorables pour la précipitation d'autres microconstituants, comme par exemple, la phase de  $\beta$ - $\text{Al}_5\text{FeSi}$ .

Pour des mêmes concentrations en fer et des conditions de taux de refroidissement, les alliages de type 319 montrent des pores de plus grandes tailles que ceux dans les alliages de types 356, et ce est dû à leur plus long temps de solidification. En ce qui concerne la dimension particulière de silicium, le temps de solidification est aussi important que l'addition de strontium dans les alliages contenant un grand nombre d'éléments d'alliage

(à savoir, 319 contre alliage 356). La modification de strontium s'avère plus efficace dans l'alliage 356 que dans l'alliage 319, en raison de la différence dans tout le temps de solidification.

L'addition des éléments d'alliage tels que le magnésium et le cuivre aux alliages d'Al-7%Si, comme aussi l'addition du strontium, diminue la température de solidification silicium eutectique. Dans les alliages modifiés par le strontium, la phase dendritique primaire  $\alpha$ -Al change de forme, à savoir, des rangées parallèles à une structure equiaxe, avec des longueurs de dendrites primaires plus courtes. Les longueurs des dendrites secondaires sont commandées par le rejet des atomes de corps dissous devant les dendrites croissantes pendant la solidification. Plus la teneur en éléments d'alliage est élevée (cas de l'alliage 319), plus la taille de cellules de dendrite est petite.

Le fer Fe aide à modifier les particules eutectiques de silicium dans les alliages non-modifiés, en particulier à bas taux de refroidissement. Plus le niveau de fer est élevé, plus les particules de silicium sont fines. Dans les alliages modifiés par le strontium, la présence du fer équilibre l'augmentation de la dimension particulière de silicium avec l'augmentation de DAS, c.-à-d., diminution du taux de refroidissement, ayant pour résultat plus ou de moins de dimensions particulières uniformes de silicium, indépendamment de la composition en alliage (c.-à-d., alliage 356 ou 319). Le silicium précipite sur les plaquettes de  $\beta$ -Al<sub>5</sub>FeSi, que ce soit l'alliage modifié ou pas, ou le niveau de fer soit bas ou élevé. Cependant, l'augmentation de la superficie des plaquettes de  $\beta$ -Al<sub>5</sub>FeSi fournit plus d'emplacements de nucléation pour les particules de silicium et, par conséquent, une amélioration dans leur dimension particulière.

La surmodification des particules de silicium a lieu quand les précipités excessifs de strontium sous forme d'Al<sub>2</sub>Si<sub>2</sub>Sr prennent naissance pendant des réactions co-eutectiques ou post-eutectiques. Ces particules d'Al<sub>2</sub>Si<sub>2</sub>Sr sont de forme polygonale et sont incohérentes avec la matrice. La phase d'Al<sub>2</sub>Si<sub>2</sub>Sr peut également être précipitée directement dans la fonte quand le niveau de strontium est suffisamment élevé, dans ce cas les particules prennent la forme de short, d'aiguilles fines ou de tiges. La précipitation d'Al<sub>2</sub>Si<sub>2</sub>Sr co-eutectique a comme conséquence l'absorption de tout le strontium des régions dans lesquelles cette phase se produit. Ces régions deviennent pauvres en strontium, et toutes les particules de silicium se trouvant dans les bords ou côtés demeurent ainsi non-modifiées. La présence des particules grossières de silicium est donc un résultat de leur état non modifié, plutôt qu'en raison d'un retour de la morphologie fibreuse à la forme de plaquettes.

Le mécanisme de l'effet du fer sur la modification du silicium eutectique dans les alliages traités par le strontium peut être proposé comme suit. Dans les conditions de sous modification, les plaquettes de  $\beta$ -Al<sub>5</sub>FeSi se précipitent dans un bain de liquide Al-Si-Sr, où le strontium adhère à la surface des plaquettes. Les particules de silicium nucléés sur les plaquettes de  $\beta$ -Al<sub>5</sub>FeSi sont ainsi très fines (1-2  $\mu$ m). Cependant, ailleurs dans la matrice, les particules de silicium demeurent non modifiées (longueur moyenne  $\sim$  9-12  $\mu$ m). Dans les conditions de bonne modification, les particules d'Al<sub>2</sub>Si<sub>2</sub>Sr sont non modifiées, et ce est dû à l'épuisement du strontium dans ces secteurs, tandis que celles ailleurs dans la matrice sont bien modifiées.

En conclusion, la présente étude a essayé de présenter une compréhension détaillée des processus et des phénomènes réels impliqués dans l'évolution de la microstructure des deux alliages populaires en l'industrie de l'automobile, tenant compte de la gamme des niveaux de fer généralement obtenu dans les alliages commerciaux, et des interactions qui résultent quand de tels alliages sont soumis aux procédures normales de traitement et de solidification du métal liquide suivies dans la production des pièces coulées. On s'attend à ce qu'une telle compréhension fournisse les moyens d'améliorer la commande la microstructure et, par conséquent, la qualité de produits finis obtenus.

## ABSTRACT

With their characteristics of low specific gravity, low melting point, excellent castability and good corrosion resistance, aluminum-silicon (Al-Si) alloys are extensively employed in automotive applications. Castings produced from these alloys range from transmission cases and intake manifolds to more critical components such as engine blocks, cylinder heads and wheels.

Two of the most popular commercial alloys used in such applications are the A356 and 319 type alloys, belonging to the Al-Si-Mg and Al-Si-Cu alloy systems. The casting quality and properties are determined by the quality of their microstructure, controlled by various parameters such as the dendrite arm spacing (DAS - as determined by the solidification rate), the degree of eutectic Si modification and grain refinement, and the amount of microporosity, intermetallics and inclusions observed in the microstructure. Among these, solidification rate is the most important, as it directly or indirectly affects almost all the other microstructural parameters.

Modification of the eutectic silicon morphology from its acicular, flake-like form to a fibrous form is usually carried out through the addition of strontium (Sr) to improve the alloy ductility. Intermetallics commonly present in these alloys are the  $\beta$ -Al<sub>5</sub>FeSi and  $\alpha$ -Al<sub>5</sub>(Fe,Mn)<sub>3</sub>Si<sub>2</sub> iron intermetallics, sludge, Mg<sub>2</sub>Si and, in the case of 319 alloys, the copper intermetallic, CuAl<sub>2</sub>. Due to its brittle, platelet-like nature, the  $\beta$ -Al<sub>5</sub>FeSi iron intermetallic can be quite deleterious to the alloy properties, as can the presence of porosity, particularly in terms of surface quality and soundness.

The aim of the present work has been to investigate the metallurgical parameters controlling the microstructural evolution of Al-Si-Mg and Al-Si-Cu alloys, through a study of the microstructural characteristics of directionally solidified A356 and 319 type alloys as a function of iron content, Sr addition (~250 ppm), and cooling rate. The iron levels selected varied from 0.12 to 0.8 wt pct, and cover the range of Fe levels found in commercial casting alloys. The use of an end-chill mold provided different cooling rates along the height of the same casting, with DAS values that varied from ~23 to 85  $\mu$ m, corresponding to levels of 5, 10, 30, 50 and 100 mm above the chill end.

The effects of these variables on the precipitation of the  $\beta$ -Al<sub>5</sub>FeSi phase, the characteristics of the  $\alpha$ -Al dendrite structure, eutectic silicon modification, and porosity formation were examined in detail. Various techniques were used for microstructural characterization and phase identification, including optical and scanning electron microscopy, electron probe microanalysis coupled with energy dispersive X-ray (EDX) and wavelength dispersive spectroscopy (WDS) facilities, and thermal analysis. An image analyzer was used in conjunction with the optical microscope for quantification purposes.

An analysis of the results obtained showed that the amount of iron present in the alloy affects the size of the  $\beta$ - $\text{Al}_5\text{FeSi}$  platelets and their distribution, particularly at low cooling rates. Addition of strontium leads to fragmentation of co-eutectic or post-eutectic  $\beta$ -platelets. This effect diminishes with the increase in iron concentration, and further strontium addition leads to the precipitation of  $\text{Al}_2\text{Si}_2\text{Sr}$  phase particles, instead.

Minimum porosity levels are observed in alloys with iron levels of  $\sim 0.4$  wt pct (in 319) and  $\sim 0.4$  or  $0.6$  wt pct (in 356) due to improvements in the alloy fluidity. With increase in iron content above these levels, the porosity is also increased, due to the increase in the size of the  $\beta$ -platelets and the consequent increased hindrance to the feedability of the molten metal. The porosity observed at any given iron level is the resultant of the competition between these two factors (*i.e.*, fluidity and  $\beta$ -platelet size), and depends on the permeability of the interdendritic regions as solidification proceeds. Although branching of the  $\beta$ -platelets leads to porosity formation, the platelets, on the other hand, also limit pore growth. In general, percentage porosity, maximum pore area and maximum pore length increase with increase in the average maximum  $\beta$ - $\text{Al}_5\text{FeSi}$  platelet lengths in both 356 and 319 alloys.

In the Sr-modified alloys, porosity formation is frequently associated with strontium oxides (particles or films), as well as the  $\beta$ - $\text{Al}_5\text{FeSi}$  platelets. These oxides (with a stoichiometric composition close to  $\text{Al}_2\text{SrO}_3$ ) are formed during melting, due to the high oxygen affinity of strontium, and are difficult to remove via degassing. The pore morphology (round or irregular) is determined by the form of the oxide: *viz.*, fine dispersed particles or thick films. Round pores are also observed surrounded by Al-Si eutectic regions. Aluminum oxide films trapped in the molten metal lead to the formation of coarser and deeper pores than those formed due to the strontium oxides. These pores can also link with each other, and are characterized by the presence of solidified metal trapped within the aluminum oxide films, close to the periphery. The form of these pores is controlled by the amount of gases trapped with the pores during solidification. The aluminum and strontium oxides also act as favorable sites for the precipitation of other microconstituents, *e.g.*, the  $\beta$ - $\text{Al}_5\text{FeSi}$  phase.

Under similar Fe level and cooling rate conditions, the 319 alloys exhibit larger pore sizes than the 356 alloys, due to their longer solidification time. With respect to the silicon particle size, also, solidification time is as important as strontium addition in alloys containing a large number of alloying elements (*viz.*, 319 versus 356 alloy). Strontium modification is found to be more effective in 356 alloy than in 319 alloy, as a result of the difference in the total solidification time.

The addition of alloying elements such as Mg and Cu to Al-7%Si alloys, as also the addition of Sr, depresses the eutectic silicon solidification temperature. In Sr-modified alloys, the primary  $\alpha$ -Al dendrite solidification pattern changes from parallel rows to an equiaxed type of structure, with shorter primary dendrite lengths. The lengths of the secondary dendrite arms are controlled by the rejection of solute atoms in front of the growing dendrites during solidification. The higher the alloying content of the alloy (*i.e.*, 319), the smaller is the dendrite cell size.

Iron assists in modifying the eutectic silicon particles in the non-modified alloys, particularly at low cooling rates. The higher the iron level, the finer the silicon particles. In the Sr-modified alloys, the presence of iron balances the increase in silicon particle size with the increase in DAS, *i.e.*, decrease in cooling rate, resulting in more or less uniform silicon particle sizes, irrespective of the alloy composition (*i.e.*, 356 or 319 alloy). Silicon precipitates on the  $\beta$ -Al<sub>5</sub>FeSi platelets no matter whether the alloy is modified or not, or whether the iron level is low or high. However, the increase in the surface area of the  $\beta$ -Al<sub>5</sub>FeSi platelets provides that many more nucleation sites for the silicon particles and, hence, a refinement in their particle size.

Overmodification of the silicon particles takes place when excess strontium precipitates in the form of the Al<sub>2</sub>Si<sub>2</sub>Sr phase in co-eutectic or post-eutectic reactions. These Al<sub>2</sub>Si<sub>2</sub>Sr particles are polygonal in shape and incoherent with the matrix. The Al<sub>2</sub>Si<sub>2</sub>Sr phase can also precipitate directly from the melt when the strontium level is sufficiently high, in which case the particles take the form of short, fine needles or rods. The precipitation of co-eutectic Al<sub>2</sub>Si<sub>2</sub>Sr results in the absorption of all strontium from the regions in which this phase occurs. These regions become depleted in strontium, and thus any silicon particles in the surrounding area remain unmodified. The coarseness of the silicon particles is therefore a result of their remaining unmodified, rather than because of a reversion in morphology from fibrous to plate-like form.

The mechanism of the effect of iron on eutectic silicon modification in Sr-treated alloys can be proposed as follows. In the under-modified condition, the  $\beta$ -Al<sub>5</sub>FeSi platelets precipitate in a bath of Al-Si-Sr liquid, where the strontium adheres to the surface of the platelets. The silicon particles that nucleate on the  $\beta$ -platelets are thus very fine (1-2  $\mu$ m). Elsewhere in the matrix, however, the silicon particles remain unmodified (average length ~9-12  $\mu$ m). In the well-modified condition, Al<sub>2</sub>Si<sub>2</sub>Sr particles are unmodified owing to the depletion of strontium in these areas, whereas those elsewhere in the matrix are well modified.

In conclusion, the present study has attempted to provide an in-depth understanding of the actual processes and phenomena involved in the evolution of the microstructure of two popular automotive Al-Si-Mg and Al-Si-Cu alloys, taking into account the range of iron levels generally obtained in commercial alloys, and the interactions that result when such alloys are subjected to the normal melt treatment and solidification procedures followed in the production of castings. Such an understanding is expected to provide the means to better control the microstructure and, hence, the casting quality.

## **ACKNOWLEDGEMENTS**

I am glad to finally have the opportunity to convey my gratefulness to all those who were involved, directly or indirectly, in making this work a success. It is my great pleasure to express my sincere thanks to my supervisors, Professors F. H. Samuel and A.M. Samuel, for their invaluable guidance and help during the different stages of my work.

Financial assistance (in the form of scholarships) and in-kind support received from the Natural Sciences and Engineering Research Council of Canada (NSERC), General Motors Powertrain Group (U.S.A.), Corporativo Nematik (Mexico), the Fondation de l'Université du Québec à Chicoutimi (FUQAC), and the Centre québécois de recherche et développement de l'aluminium (CQRDA) are gratefully acknowledged.

I would like to express my appreciation to several colleagues, particularly MM Régis Boucher, Alain Bérubé and André Bouchard, for their help and for creating an enjoyable working atmosphere. Many thanks go to Dr. Huan-Zhang Lu who recommended me to join UQAC and also for his enthusiastic help during these years.

Finally, I would like to record my deep gratitude to the members of my family, especially my parents. Without their encouragement and support, I would not have been able to fulfill my goal of completing my doctorate degree successfully.

# TABLE OF CONTENTS

<b>ABSTRACT.....</b>	<b>i</b>
<b>ACKNOWLEDGEMENTS .....</b>	<b>iv</b>
<b>TABLE OF CONTENTS.....</b>	<b>v</b>
<b>LIST OF TABLES.....</b>	<b>viii</b>
<b>LIST OF TABLES.....</b>	<b>x</b>
<b>CHAPTER 1 DEFINITION OF THE PROBLEM.....</b>	<b>1</b>
1.1 INTRODUCTION .....	2
1.2 OBJECTIVES.....	6
<b>CHAPTER 2 LITERATURE REVIEW .....</b>	<b>8</b>
2.1 ALUMINUM-SILICON ALLOYS .....	9
2.2 CLASSIFICATION OF AL-SI ALLOYS .....	11
2.2.1 Al-Si-Mg Alloy System .....	13
2.2.2 Al-Si-Cu Alloy System .....	14
2.3 SOLIDIFICATION OF AL-SI ALLOYS.....	15
2.3.1 Phase Precipitation.....	15
2.3.2 Effect of Cooling Rate .....	18
2.4 MODIFICATION OF THE EUTECTIC SILICON .....	19
2.4.1 Mechanism of Eutectic Silicon Modification .....	21
2.4.2 Effect of Cooling Rate on Modification .....	23
2.4.3 Effect of Chemical Modification .....	23
2.4.3.1 Sodium (Na).....	25
2.4.3.2 Strontium (Sr) .....	26
2.4.3.3 Antimony (Sb) .....	30
2.4.3.4 Rare Earth Metals .....	31
2.4.4 Phosphorus Interaction with Modifiers.....	33
2.4.5 Effect of Modification on Mechanical Properties.....	35
2.5 IRON INTERMETALLICS .....	39
2.5.1 Formation, Fragmentation and Dissolution of Iron Intermetallics .....	42
2.5.1.1 The $\beta$ -Al <sub>5</sub> FeSi Iron intermetallic .....	43

2.5.1.2	The $\alpha$ -Al <sub>15</sub> (Mn,Fe) <sub>3</sub> Si <sub>2</sub> iron intermetallic .....	47
2.5.1.3	The $\alpha$ -Al <sub>15</sub> (Fe, Mn, Cr) <sub>3</sub> Si <sub>2</sub> iron intermetallic (Sludge) .....	47
2.5.2	Role of Alloying Elements .....	49
2.5.3	Effect of Cooling Rate .....	51
2.5.4	Sr Addition.....	52
2.6	POROSITY .....	55
2.6.1	Theory of Porosity Formation.....	57
2.6.2	Role of Hydrogen.....	60
2.6.3	Role of Alloying Elements and Inclusions .....	63
2.6.4	Role of Sr Modification .....	65
2.6.5	Role of Iron Intermetallics .....	69
<b>CHAPTER 3 EXPERIMENTAL PROCEDURE .....</b>		<b>72</b>
3.1	ALLOYS, ADDITIVES AND MELTING PROCEDURES.....	73
3.2	CASTING PROCEDURES .....	74
3.2.1	End-Chill Mold Casting – Directional Solidification .....	75
3.2.2	Graphite-Mold and Metallic-Mold Castings – Thermal Analysis .....	78
3.3	METALLOGRAPHY .....	80
3.3.1	Sample Preparation .....	80
3.3.2	Microstructural Examination – Optical Microscopy and Image Analysis ...	81
3.3.3	Phase Identification –SEM and EPMA Analysis .....	83
<b>CHAPTER 4 PRECIPITATION OF <math>\beta</math>-AL<sub>5</sub>FESI PHASE PLATELETS AND THEIR ROLE ON POROSITY FORMATION.....</b>		<b>85</b>
4.1	INTRODUCTION .....	86
4.1.1	Iron Intermetallics.....	87
4.1.2	Porosity .....	89
4.1.3	Iron-Porosity Relationship.....	90
4.2	EFFECT OF COOLING RATE AND SR MODIFICATION ON $\beta$ -AL <sub>5</sub> FESI PRECIPITATION .....	90
4.2.1	Secondary Dendrite Arm Spacing .....	91
4.2.2	Effect of Sr Modification.....	92
4.2.3	$\beta$ -Al <sub>5</sub> FeSi Platelet Characteristics .....	93
4.2.3.1	$\beta$ -Al <sub>5</sub> FeSi platelet size .....	99
4.2.3.2	$\beta$ -Al <sub>5</sub> FeSi platelet density .....	104
4.2.4	Microstructure.....	107
4.2.4.1	A319.2 alloy.....	108
4.2.4.2	B319.2 alloy.....	113
4.2.4.3	A356.2 alloy.....	115
4.2.5	Mechanism of $\beta$ -Al <sub>5</sub> FeSi Fragmentation.....	119
4.3	EFFECT OF IRON CONTENT ON POROSITY FORMATION .....	123

<b>CHAPTER 5</b>	<b>ROLE OF IRON IN RELATION TO SI MODIFICATION IN SR-TREATED ALLOYS.....</b>	<b>150</b>
5.1	INTRODUCTION .....	151
5.2	EFFECT OF IRON, COOLING RATE AND STRONTIUM ON SI PARTICLE CHARACTERISTICS .....	153
5.2.1	Si Particle Characterization from Image Analysis Data .....	153
5.2.2	Solidification Parameters from Thermal Analysis Data .....	158
5.2.3	Microstructural Analysis.....	163
5.2.4	Mechanism of Si Particle Modification .....	176
<b>CHAPTER 6</b>	<b>CHARACTERISTICS OF <math>\alpha</math>-DENDRITIC AND EUTECTIC STRUCTURES IN SR-TREATED ALLOYS .....</b>	<b>185</b>
6.1	INTRODUCTION .....	186
6.2	EXPERIMENTAL PROCEDURE .....	188
6.3	FACTORS INFLUENCING THE MAIN MICROSTRUCTURAL CHARACTERISTICS OF AL-SI ALLOYS .....	191
<b>CHAPTER 7</b>	<b>INFLUENCE OF OXIDES ON POROSITY FORMATION IN SR-TREATED ALLOYS.....</b>	<b>213</b>
7.1	INTRODUCTION .....	214
7.2	EXPERIMENTAL PROCEDURE .....	218
7.3	INFLUENCE OF OXIDES ON POROSITY FORMATION .....	221
7.3.1	Role of Strontium Oxide.....	222
7.3.2	Role of Aluminum Oxide .....	236
<b>CHAPTER 8</b>	<b>CONCLUSIONS .....</b>	<b>245</b>
<b>REFERENCES.....</b>		<b>252</b>

## LIST OF TABLES

### Chapter 2

Table 2.1	Characteristics of aluminum-silicon casting alloys <sup>1</sup> .....	11
Table 2.2	Classification of aluminum casting alloys <sup>7</sup> .....	12
Table 2.3	Sequence of phase precipitation in hypoeutectic Al-Si alloys <sup>10</sup> .....	17
Table 2.4	Some properties of possible modifiers <sup>25</sup> .....	24

### Chapter 3

Table 3.1	Chemical composition of the 319 and 356 base alloys used in the present work .....	74
Table 3.2	Chemical composition of the various alloys used in the present work and their respective codes .....	77
Table 3.3	DAS values obtained at various levels of the end-chilled castings for the alloys used .....	83

### Chapter 4

Table 4.1	Important Fe-rich phases in Al-Si alloys <sup>8</sup> .....	88
Table 4.2	(a) $\beta$ -platelet characteristics obtained for unmodified A319.2 alloy samples .....	94
Table 4.2	(b) $\beta$ -platelet characteristics obtained for Sr-modified A319.2 alloy samples .....	95
Table 4.3	$\beta$ -platelet characteristics obtained for unmodified and Sr-modified B319.2 alloy samples .....	96
Table 4.4	(a) $\beta$ -platelet characteristics obtained for unmodified A356.2 alloy samples .....	97
Table 4.4	(b) $\beta$ -platelet characteristics obtained for Sr-modified A356.2 alloy samples .....	98
Table 4.5	Samples corresponding to Figure 4.31. ....	135
Table 4.6	Reactions Observed in 319 and 356 Alloys at $\sim 0.8^\circ\text{C/s}$ .....	139
Table 4.7	Solidification Times Observed in 319 and 356 Alloys at $\sim 0.8^\circ\text{C/s}$ . ....	139

**Chapter 5**

Table 5.1	(a) Si particle characteristics obtained for unmodified A319.2 alloy samples containing various Fe levels.....	154
Table 5.1	(b) Si particle characteristics obtained for Sr-modified A319.2 alloy samples containing various Fe levels.....	155
Table 5.2	(a) Si particle characteristics obtained for unmodified A356.2 alloy samples containing various Fe levels.....	156
Table 5.2	(b) Si particle characteristics obtained for Sr-modified A356.2 alloy samples containing various Fe levels.....	157
Table 5.3	Possible reactions in an experimental 319 alloy containing 0.8 wt% Fe and 0.02 wt% Sr. ....	161

**Chapter 6**

Table 6.1	Chemical Compositions (Wt%) of Alloys Used.....	189
Table 6.2	Cooling Curve Data .....	192
Table 6.3	Temperatures and Phases Corresponding to Peaks in Figure 6.2. ....	195
Table 6.4	Percentage Porosity Observed in Al-7%Si and 319 Alloys.....	196
Table 6.5	Primary and Secondary $\alpha$ -Al Dendrite Measurements.....	210

**Chapter 7**

Table 7.1	Chemical Compositions (Wt%) of Alloys Used.....	220
Table 7.2	Percentage of Porosity Observed in Al-7%Si and 319 Alloys .....	221

## LIST OF FIGURES

### Chapter 2

Figure 2.1	Part of the Al-Si phase diagram showing composition ranges of various alloy types. <sup>6</sup> .....	10
Figure 2.2	Variation of the DAS of a 356 alloy with cooling rate. <sup>11</sup> .....	19
Figure 2.3	Rating system for a modified microstructure. <sup>15</sup> .....	21
Figure 2.4	(a) Schematic model of eutectic Si flakes with twin configuration shaded, <sup>19</sup> (b) Twinning in a crystal showing the continuity of the atom planes across the twin plane. <sup>18</sup> .....	22
Figure 2.5	Loss of sodium in an Al-13%Si alloy melt during its holding in a crucible. <sup>26</sup> .....	26
Figure 2.6	Microstructures of as-cast A356.0 alloy: (a) unmodified, and (b) 150 ppm Sr-modified. ....	27
Figure 2.7	Effect of strontium content and holding time on modification. <sup>31</sup> .....	28
Figure 2.8	Interaction between phosphorus and strontium in a sand-cast alloy. <sup>23</sup> .....	34
Figure 2.9	Variation of T6 elongation in unmodified and modified A356.2 alloys. The castings were aged at 155°C (310°F). <sup>45</sup> .....	35
Figure 2.10	Mechanical properties of A356.0 alloy modified with strontium and held for times of up to 11 hours before casting. <sup>1</sup> .....	36
Figure 2.11	Influence of solidification rate and Sr level on the tensile properties of eutectic Al-Si alloy. <sup>47</sup> .....	38
Figure 2.12	Optical micrographs showing (a) $\beta$ -Al <sub>5</sub> FeSi, (b) $\alpha$ -Al <sub>15</sub> (Fe,Mn) <sub>3</sub> Si <sub>2</sub> , and (c) sludge iron intermetallics (arrowed). <sup>6</sup> .....	42
Figure 2.13	Schematic illustration of the mechanism of $\beta$ -Al <sub>5</sub> FeSi phase fragmentation and dissolution. <sup>60</sup> .....	45
Figure 2.14	Schematic representation of $\beta$ -Al <sub>5</sub> FeSi decomposition during solution heat treatment. <sup>62</sup> .....	46
Figure 2.15	Optical micrographs showing (a) how strontium poisons the link between a parent and branching Al <sub>5</sub> FeSi needle, and (b) the poisoning and dissolution/fragmentation effect of strontium on the $\beta$ -needles. <sup>59</sup> .....	53
Figure 2.16	Variation of hydrogen solubility in aluminum melts with different temperatures. <sup>85</sup> .....	56
Figure 2.17	A shrinkage pore and a gas pore merged together to form a single pore in an Al-9 wt% Si-3 wt% Cu alloy. <sup>88</sup> .....	58
Figure 2.18	The growth process of porosity formation. <sup>90</sup> .....	59

Figure 2.19	Effect of nucleation sites on porosity development. <sup>95</sup> .....	62
Figure 2.20	As hydrogen concentrations decrease above the threshold value for grain refined Al-4.7 Mg alloy, the pore volume fractions also decrease. <sup>97</sup> .....	63
Figure 2.21	The two-stage solidification process proposed by Argo and Gruzleski, <sup>108</sup> showing microshrinkage formation in: a) an unmodified casting (short interdendritic feeding distance and irregular eutectic solidification front), and b) a modified casting (long interdendritic feeding distance and regular eutectic solidification front). .....	68

### Chapter 3

Figure 3.1	Schematic diagram of the end-chilled mold used to prepare castings. ....	76
Figure 3.2	Schematic diagram of molds used for thermal analysis and corresponding sample sections used for metallographic analysis. ....	79
Figure 3.3	End-chill casting showing specimen blank sectioning scheme (mm). ....	81
Figure 3.4	Electron probe microanalyzer used in the present work. ....	84

### Chapter 4

Figure 4.1	Dependence of DAS on the cooling rate (AF2S: Sr-modified A319-0.2%Fe alloy, CF1S: Sr-modified A356.2 alloy). ....	92
Figure 4.2	(a) Effect of cooling rate on the average maximum $\beta$ -platelet length observed in unmodified A319.2 alloys. ....	100
Figure 4.3	Effect of cooling rate on the average maximum $\beta$ -platelet length observed in unmodified and Sr-modified B319 alloy. ....	102
Figure 4.4	(a) Effect of cooling rate on the average maximum $\beta$ -platelet length observed in unmodified 356 alloys. ....	103
Figure 4.4	(b) Effect of cooling rate on the average maximum $\beta$ -platelet length observed in Sr-modified A319.2 alloys. ....	103
Figure 4.5	Effect of cooling rate on the $\beta$ -platelet density in A319.2 alloys. ....	106
Figure 4.6	Effect of cooling rate on the $\beta$ -platelet density in B319.2 alloys. ....	106
Figure 4.7	Effect of cooling rate on the $\beta$ -platelet density in A356.2 alloys. ....	107
Figure 4.8	Microstructure of as-solidified A319.2 alloy showing precipitation of: 1) $\alpha$ -Al dendrite, 2) pre-eutectic $\beta$ -Al <sub>5</sub> FeSi, 3) eutectic Si, 4) post-eutectic $\beta$ -Al <sub>5</sub> FeSi, 5a) block-like Al <sub>2</sub> Cu, 5b) eutectic Al+Al <sub>2</sub> Cu, and 6) Al <sub>5</sub> Mg <sub>8</sub> Cu <sub>2</sub> Si <sub>6</sub> phase particles. <sup>75</sup> .....	108
Figure 4.9	Microstructure of AF2-0 alloy. ....	109
Figure 4.10	Microstructure of AF2S-0 alloy. ....	109
Figure 4.11	(a) Microstructure of AF8-C alloy. ....	111
Figure 4.11	(b) Backscattered image taken from the AF8-C alloy. ....	111
Figure 4.12	Microstructure of AF8S-C alloy. ....	112
Figure 4.13	Microstructure of B4-0 alloy. ....	113

Figure 4.14	Microstructure of B4S-0 alloy.....	114
Figure 4.15	Microstructure of B8-C alloy.....	114
Figure 4.16	Microstructure of B8S-C alloy.....	115
Figure 4.17	Microstructure of CF1-0 alloy.....	116
Figure 4.18	Microstructure of CF1S-0 alloy.....	116
Figure 4.19	(a) Microstructure of CF8-C alloy.....	117
Figure 4.19	(b) Microstructure of CF8-C alloy.....	117
Figure 4.20	(a) Microstructure of CF8S-3 alloy.....	118
Figure 4.20	(b) Microstructure of CF8S-3 alloy.....	119
Figure 4.21	SEM micrograph taken from the Sr-modified A319.2-0.4%Fe alloy, showing the dissolution effect of Sr on the $\beta$ -Al <sub>5</sub> FeSi phase.....	120
Figure 4.22	Backscattered images of (a) unmodified, and (b) Sr-modified A319.2-0.8% Fe alloy showing $\beta$ -Al <sub>5</sub> FeSi platelet characteristics.....	122
Figure 4.23	Porosity parameters (percentage porosity, maximum pore area and pore density) as a function of iron content and cooling rate observed in unmodified A319.2 alloy.....	124
Figure 4.24	Porosity parameters (percentage porosity, maximum pore area and pore density) as a function of iron content and cooling rate observed in Sr-modified A319.2 alloy.....	125
Figure 4.25	Porosity parameters (percentage porosity, maximum pore area and pore density) as a function of iron content and cooling rate observed in unmodified A356.2 alloy.....	129
Figure 4.26	Porosity parameters (percentage porosity, maximum pore area and pore density) as a function of iron content and cooling rate observed in Sr-modified A356.2 alloy.....	130
Figure 4.27	Plots of percentage porosity vs. average maximum $\beta$ -platelet length in (a) unmodified, and (b) Sr-modified A319.2 alloys.....	131
Figure 4.28	Plots of maximum pore length vs. average maximum $\beta$ -platelet length in (a) unmodified, and (b) Sr-modified A319.2 alloys.....	132
Figure 4.29	Plots of percentage porosity vs. average maximum $\beta$ -platelet length in (a) unmodified and (b) Sr-modified A356.2 alloys.....	133
Figure 4.30	Plots of maximum pore length vs. average maximum $\beta$ -platelet length in (a) unmodified and (b) Sr-modified A356.2 alloy.....	134
Figure 4.31	Optical micrographs showing pores observed in different samples of A319.2 and A356.2 alloys (See Table 4.5 for alloy sample codes).....	136
Figure 4.32	Cooling curves and their first derivatives obtained for (a) 319, and (b) 356 alloys.....	138
Figure 4.33	(a) Optical micrograph showing SrO particles and films within a pore in a 319 alloy sample, and (b) SEM micrograph showing SrO particles situated inside the pore.....	141
Figure 4.34	Free energy formation vs temperature for Al-, Sr-, and Mg- oxides.....	142

Figure 4.35	SEM micrographs comparing (a) a solid $\beta$ -platelet, (b) $\beta$ -platelets that have undergone dissolution in Sr-modified 319.2 alloy samples. Note the $\alpha$ -Al dendrites appearing through parts of the $\beta$ -platelets in (b).....	143
Figure 4.36	SEM micrographs showing how the $\beta$ -Al <sub>5</sub> FeSi phase platelets nucleate gas porosity (a, b), and limit pore growth (c) in high hydrogen-containing A319.2-0.8%Fe alloy (hydrogen level: 0.25ml/100g). .....	146
Figure 4.37	SEM micrograph showing an example of how branched $\beta$ -platelets can cause shrinkage porosity. ....	146
Figure 4.38	Average maximum $\beta$ -platelet length vs. iron content for unmodified 319 and 356 alloys.....	148
Figure 4.39	Fluidity (average length of solidified tube) versus iron content for unmodified 319 and 356 alloys. ....	149

## Chapter 5

Figure 5.1	(a) Start and end of solidification temperatures, and (b) total solidification times obtained for non-modified and Sr-modified 319 and 356 alloys from thermal analysis data.....	159
Figure 5.2	Cooling curve and first derivative obtained for an experimental 319 alloy containing 0.8 wt% Fe and 0.02 wt% Sr, cooled in a hot graphite mold ( $\sim 0.8^\circ\text{C/s}$ ). ....	160
Figure 5.3	Optical microstructures obtained from the 319 alloy containing 0.2 wt% Fe: (a) non-modified AF2-C (85 $\mu\text{m}$ DAS) sample, (b) 250 ppm Sr-modified AF2S-0 (15 $\mu\text{m}$ DAS) sample. ....	164
Figure 5.4	Optical microstructures obtained from the 319 alloy containing 0.8 wt% Fe: (a) non-modified AF8-C (85 $\mu\text{m}$ DAS) sample, (b) 250 ppm Sr-modified AF8S-C (85 $\mu\text{m}$ DAS) sample.....	165
Figure 5.5	Optical microstructures obtained from the 356 alloy containing 0.2 wt% Fe: (a) non-modified CF2-C (85 $\mu\text{m}$ DAS) sample, (b) 250 ppm Sr-modified CF2S-0 (15 $\mu\text{m}$ DAS) sample.....	167
Figure 5.6	Optical microstructures obtained from the 356 alloy containing 0.6 wt% Fe: (a) non-modified CF6-C (85 $\mu\text{m}$ DAS) sample, (b) 250 ppm Sr-modified CF6S-C (85 $\mu\text{m}$ DAS) sample.....	168
Figure 5.7	Optical microstructure obtained from the 356 alloy solidified at $\sim 0.8^\circ\text{C/s}$ , showing precipitation of Si and $\beta$ -Al <sub>5</sub> FeSi phases (1: pre-eutectic $\beta$ -, and 2: co-eutectic $\beta$ -Al <sub>5</sub> FeSi).....	169
Figure 5.8	Optical micrographs obtained from the 356 alloy modified with 30 ppm Sr: (a) low-Fe alloy, and (b) high-Fe alloy samples (85 $\mu\text{m}$ DAS).....	171
Figure 5.9	Microstructures of the 250 ppm Sr-modified high-Fe 356 alloy sample: (a) optical micrograph, (b) SEM backscattered image.....	173

Figure 5.10	Plots of log (Sr) and Si contents as a function of distance from the $\beta$ -platelet in the line scans taken along (a) path #1, (b) path #2, and (c) path #3 shown in Figure 5.9(b). .....	176
Figure 5.11	(a) Mechanism of Si particle modification in under-modified (30 ppm Sr) Fe-containing Al-Si alloys. ....	178
Figure 5.11	(b) Mechanism of Si particle modification in well-modified (250 ppm Sr) Fe-containing Al-Si alloys.....	179
Figure 5.12	SEM micrograph showing an $Al_2Si_2Sr$ particle surrounded by eutectic Si region within a pore observed in the Sr-modified 356 alloy.....	182
Figure 5.13	Optical micrographs showing the modification of Si particles due to the segregation of Sr near $\alpha$ -Fe (open arrows) and $\beta$ -Fe (black arrows) intermetallics in the Al-12%Si-1.1%Fe alloy containing: (a) 0.3% Mn + 60 ppm Sr, and (b) 200 ppm Sr + 60 ppm P. ....	184

## Chapter 6

Figure 6.1	Schematic diagram of the cooling curve of an Al-Si alloy defining the various solidification parameters (temperature and time) used. ....	192
Figure 6.2	Cooling curves and first derivatives obtained for Sr-modified (a) Al-7%Si, (b) 319 alloys. ....	194
Figure 6.3	Optical micrographs showing the dendrite morphology in (a) unmodified, and (b) Sr-modified Al-12% Si alloy. ....	199
Figure 6.4	High magnification micrographs of Al-12% Si alloy showing (a) uniform dendrites in the unmodified alloy, and (b) comparatively irregular dendrites in the modified alloy.....	201
Figure 6.5	Optical micrographs showing the secondary dendrite formation in unmodified (a) Al-7% Si, (b) 356, and modified (c) Al-7% Si, (d) 356, (e) 319 alloys.....	204
Figure 6.6	Volume fractions of $\alpha$ -Al and eutectic Si in the four alloy types studied.....	207
Figure 6.7	Enlarged sections of the cooling curves obtained for (a) 319 and (b) 356 alloys, comparing the undercooling observed in the unmodified and Sr-modified cases. ....	208

## Chapter 7

Figure 7.1	Optical micrographs showing pore types observed in (a) unmodified, (b) Sr-modified Al-12% Si alloy.....	224
Figure 7.2	(a) SEM micrograph showing white particles inside a pore in Sr-modified Al-12% Si alloy; (b) high magnification SEM showing Al-Sr-O particles; (c) composite of oxygen scan and EDX spectrum (inset) corresponding to Al-Sr-O particles, (d) high magnification SEM showing microporosity associated with Al-Sr-O particles (arrowed).....	225

Figure 7.3	SEM micrographs showing irregular shrinkage-type pores in Sr-modified 319 alloy. Note the presence of Sr oxides within, and $\beta$ -Al <sub>5</sub> FeSi platelets along, the edges of the pore.....	227
Figure 7.4	SEM micrographs obtained from an RPT sample of the Sr-modified 356 alloy showing (a) a pore with fine white Al-Sr-O particles (arrowed), (b) size and distribution of Al-Sr-O particles, (c) Sr image of Al-Sr-O particles in (a).....	230
Figure 7.5	SEM micrograph of a Prefil test sample obtained from the same Sr-modified 356 alloy melt (Figure 7.4), showing microporosity (black arrows) associated with the strontium oxide cluster (white arrow). ....	231
Figure 7.6	EPMA analysis of the Prefil test sample of the Sr-modified 356 alloy showing (a) the backscattered image of Al-Sr-O films and associated microporosity, (b) the Al-, (c) the Sr-, and (d) the O images obtained from the Al-Sr-O films.....	232
Figure 7.7	Free energies of formation versus temperature for Al, Sr and Mg oxides. ....	234
Figure 7.8	Backscattered (a), and X ray images of (b) O, (c) Sr and (d) Fe obtained from an A356.2 alloy sample containing SrO particles, solidified in a cylindrical metallic mold (DAS ~25 $\mu$ m). ....	235
Figure 7.9	Optical micrograph obtained from the Sr-modified Al-12%Si (A12SS) melt, cast after stirring, showing solidified alloy material entrapped within the oxide films, and how these oxide films can link two pores. ....	236
Figure 7.10	(a) SEM micrograph taken from the A12SS sample of Figure 7.9, showing a large sized pore and the eutectic Al-Si region surrounding it, (b) high magnification micrograph of (a). Arrow in (b) points to an Al-Sr-O particle. ....	238
Figure 7.11	(a) SEM micrograph showing the bottom of an aluminum oxide-associated pore, and (b) composite of oxygen scan and EDX spectrum (inset) taken from (a).....	239
Figure 7.12	a) Backscattered image, and (b) the Al-, (c) O-, and (d) Sr images of an aluminum oxide-associated pore of the type shown in Figure 7.9.....	241
Figure 7.13	(a) Schematic diagram of end-chill mold and pouring arrangement for casting; (b,c) Radiographs of (b) H1T, and (c) H1S2 end-chill mold castings obtained from well-degassed melts of 319 alloy <sup>170</sup> (H1 : hydrogen level ~0.1 mL/100g Al; T : grain refined melt; S2 : 70 ppm Sr-modified melt).....	244

## **CHAPTER 1**

### **DEFINITION OF THE PROBLEM**

# CHAPTER 1

## DEFINITION OF THE PROBLEM

### 1.1 INTRODUCTION

Aluminum casting alloys, particularly those belonging to the aluminum-silicon (Al-Si) system, are characterized by their low specific gravity, low melting point, negligible gas solubility (with the exception of hydrogen), excellent castability and good corrosion resistance<sup>1</sup>. These characteristics make them excellent candidates for automotive and aerospace applications.

With the increasing demands of the automotive industry for smaller, lighter-weight high-performance components, Al-Si alloys, with their high strength-to-weight ratio, have today replaced iron and steel in many components, including transmission cases, intake manifolds, as well as in more critical components such as engine blocks, cylinder heads and wheels. Such applications require that the casting parts exhibit consistent strength-ductility properties throughout the casting.

The silicon (Si) content in Al-Si alloys can range from 2 to 25 wt%, where the eutectic occurs at ~12 wt% Si. Modification of the normally acicular, flake-like morphology of the eutectic Si to a fibrous form is usually carried out through the addition of strontium (Sr) to improve the alloy ductility. Copper (Cu) and magnesium (Mg) are

often added as alloying elements to increase the strength and hardenability, while iron (Fe), manganese (Mn), nickel (Ni) and chromium (Cr) are usually present as impurity elements, depending upon the source of the alloy.

Iron, probably the most detrimental, occurs as a natural impurity in most aluminum ores such as bauxite. In foundry processing, melting equipment like holding furnace pots, ladles and other melt mixing tools made of steel are the sources of iron pick-up, and remelted scrap also introduces iron into the melt. During solidification, iron, together with other alloying elements such as Cu, Mg, Zn, Mn, Ti, *etc.* partly goes into solid solution in the matrix and partly forms intermetallic compounds.<sup>2</sup> In general, the higher the Fe level present in the alloy, the greater the amount of the  $\beta$ -Al<sub>3</sub>FeSi phase platelets formed, and the greater the effect on reducing the alloy properties.

Two of the most popular commercial alloys used in the automotive and aerospace industries are the A356 (Al-7%Si-0.3%Mg) and 319 (Al-6.5%Si-3%Cu) alloys, known for their excellent castability and mechanical properties. Belonging respectively to the Al-Si-Mg and Al-Si-Cu alloy systems, the A356 alloy is hardened by magnesium through Mg<sub>2</sub>Si precipitation, whereas in the 319 alloy, copper provides high strength and improved machinability.

The casting quality and properties of these alloys are determined by the quality of their microstructure. The various microstructural parameters to consider are the dendrite arm spacing (DAS) which is controlled by the solidification rate and which provides a measure of the fineness of the microstructure, the degree of eutectic silicon modification and grain refinement, and the amount of microporosity, intermetallics and inclusions

observed in the microstructure. Intermetallics commonly present in these alloys are the  $\beta$ - $\text{Al}_5\text{FeSi}$  and  $\alpha$ - $\text{Al}_{15}(\text{Fe}, \text{Mn})_3\text{Si}_2$  iron intermetallics, sludge,  $\text{Mg}_2\text{Si}$ , and in the case of the 319 alloys, the copper intermetallic,  $\text{CuAl}_2$ .

The platelet-like  $\beta$ - $\text{Al}_5\text{FeSi}$  iron intermetallic, due to its brittle nature, can be quite deleterious to the alloy properties when, under conditions of high stress intensity, the  $\beta$ -platelets fracture or separate from the matrix, providing preferential crack paths ahead of the advancing crack, and thereby lowering the impact properties. The  $\text{CuAl}_2$  phase, particularly in its block-like form, can similarly lower the alloy properties. Segregation of the copper phase due to Sr-addition can aggravate the problem in that it becomes more difficult to dissolve the  $\text{CuAl}_2$  phase and extreme caution is required to avoid incipient melting of the phase during heat treatment.

The presence of porosity, inevitable to a certain extent in any casting, can also be detrimental, particularly in terms of surface quality and corrosion resistance. Optimization of these constituents results in the enhancement of mechanical properties. Among the various parameters influencing the microstructure of Al-Si alloys, the solidification rate is the most important, as it directly or indirectly affects almost all the other microstructural parameters mentioned above, followed by porosity, which affects the surface quality, soundness, and corrosion resistance, in addition to the mechanical properties.

Tied in to the practice of Sr modification to convert the eutectic Si particles from their coarse acicular form to a fine fibrous morphology, the consequences of the side-effects of Sr addition must also be considered: (i) the problem of copper-phase

segregation mentioned above, and (ii) the increase in porosity normally observed in Sr-modified alloys compared to the unmodified case.

Taking into consideration all of the above aspects, an extensive research program was undertaken to investigate the effect of microstructural parameters on the mechanical properties of 319 and 356 aluminum alloys popularly employed in the production of automotive castings. While investigations of the tensile and impact properties of these alloys were undertaken in another project,<sup>3</sup> the present study concentrated on the fundamental aspects of the microstructural phenomena involved.

The microstructural features focused upon were the dendrite arm spacing (DAS), the eutectic silicon, the iron intermetallics (in particular  $\beta$ -Al<sub>5</sub>FeSi), and the amount of porosity exhibited by the alloys, obtained as a consequence of the alloy, melt treatment and solidification conditions coming into play. The addition of different Fe contents, the application of Sr modification and the use of directionally solidified end-chilled castings provided the various alloy conditions studied in this work. The Fe contents ranged from 0.1 through 0.8 wt%, covering the range of Fe levels commonly observed in commercial aluminum casting alloys.

The use of a refractory end-chilled mold provided end-chilled castings that exhibited DASs ranging from  $\sim 15\mu\text{m}$  through  $\sim 85\mu\text{m}$  over distances of 5 mm through 100 mm above the chill end. Strontium modification ( $\sim 250$  ppm Sr) affected not only the eutectic silicon but also the  $\beta$ -Al<sub>5</sub>FeSi phase through its fragmentation and dissolution effect on the latter.

Apart from these normally expected microstructural changes, several other interesting phenomena were also observed in the course of these investigations, such as the role of iron on silicon modification, and that of SrO on porosity formation, which explained the microstructural features observed in the samples.

Different metallographic techniques were used to analyze the microstructural constituents and parameters. The  $\beta$ -Al<sub>5</sub>FeSi, eutectic Si and porosity characteristics were measured using a Leco 2001 image analyzer in conjunction with an Olympus optical microscope. Scanning electron microscopy (SEM), and electron probe microanalysis (EPMA) coupled with energy dispersive X-ray (EDX) and wavelength dispersion spectroscopic (WDS) facilities were also employed, for in-depth characterization and phase identification purposes.

## 1.2 OBJECTIVES

The aim of the present work was to study the metallurgical parameters controlling the microstructural evolution of Al-Si-Mg and Al-Si-Cu alloys. Microstructural characteristics, *i.e.*, dendrite arm spacing, and eutectic silicon,  $\beta$ -Al<sub>5</sub>FeSi iron intermetallic and porosity characteristics were studied in A356 and 319 as a function of cooling rate, iron content and strontium modification. This was carried out through an investigation of :

- i) The microstructural characteristics of directionally solidified 319 and A356 type alloys as a function of iron content and cooling rate;
- ii) The factors (*e.g.*, strontium addition, superheat and cooling rate) affecting the precipitation of the  $\beta$ -Al<sub>5</sub>FeSi iron intermetallic phase;

- iii) Characteristics of the  $\alpha$ -dendritic and eutectic structures in Sr-treated alloys as a function of alloy composition and solidification conditions;
- iv) The effect of iron on eutectic silicon modification, in and without the presence of strontium; and
- v) The effect of  $\beta$ - $\text{Al}_3\text{FeSi}$  phase platelets and strontium oxide on porosity formation.

**CHAPTER 2**  
**LITERATURE REVIEW**

## **CHAPTER 2**

### **LITERATURE REVIEW**

#### **2.1 ALUMINUM-SILICON ALLOYS**

Aluminum-silicon (Al-Si) base casting alloys are widely used in the automotive industry. Their main advantages consist of their low density and ability to be cast in complex shapes.<sup>4</sup> Aluminum has a density of only 2.7 g/cm<sup>3</sup>, approximately one-third as much as steel, copper or brass. As the density of silicon is 2.3g/cm<sup>3</sup>, it is one of the few elements that may be added to aluminum without the loss of a weight advantage.<sup>5</sup> Aluminum alloys containing silicon as the major alloying element constitute 85% to 90% of all aluminum casting alloys.

With the increasing demands of the automotive industry for smaller, lighter-weight high-performance components, Al-Si alloys - with their high strength-to-weight ratio - have today replaced iron and steel in many components, including transmission cases, intake manifolds, as well as in more critical components such as engine blocks, cylinder-heads and wheels. Such applications require that the casting parts exhibit consistent strength-ductility properties throughout the casting.

The casting quality and properties, in turn, are determined by the quality of the microstructure. In the case of Al-Si alloys, the various microstructural parameters to

consider are the dendrite arm spacing (DAS) which is controlled by the solidification rate, and which gives a measure of the fineness of the microstructure, the degree of eutectic silicon modification and grain refinement, and the amount of microporosity, intermetallics and inclusions observed in the microstructure. Optimization of these parameters results in the enhancement of mechanical properties.

Depending on the amount of silicon, industrial Al-Si alloys are divided into three groups: hypoeutectic alloys with a Si content between 5 and 10%, eutectic alloys with 11-13% Si, and hypereutectic alloys, commonly with a Si content between 14 and 20%, as shown in Figure 2.1.<sup>6</sup>

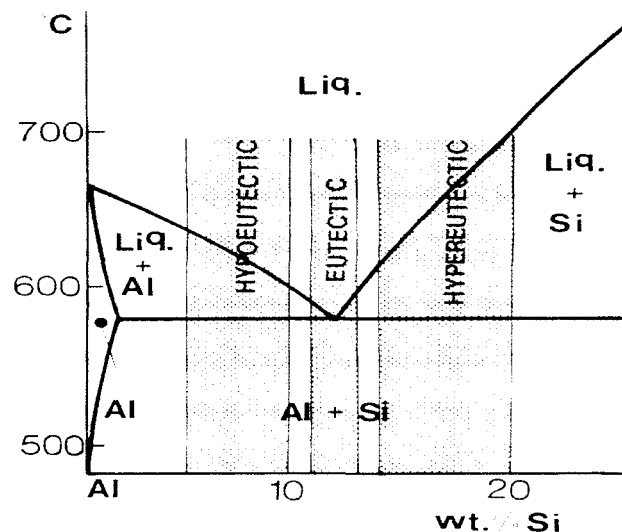


**Figure 2.1** Part of the Al-Si phase diagram showing composition ranges of various alloy types.<sup>6</sup>

Binary eutectic alloys, such as 413, 443 and 444 alloys, combine the advantages of high corrosion resistance, good weldability and low specific gravity. Hypoeutectic alloys,

such as 319 (Al-6.5%Si-3%Cu) and 356 (Al-7%Si-0.3Mg), offer good castability and corrosion resistance. The 380 (Al-8.5%Si-3.5%Cu) alloy is popularly used in die casting. In this group, the silicon provides good casting properties. The alloys can be strengthened by adding small amounts of Cu, Mg or Ni. Hypereutectic alloys, such as 390 alloy, have outstanding wear resistance, a lower thermal expansion coefficient, and very good casting characteristics. Table 2.1 shows the characteristics of some commonly used Al-Si casting alloys.<sup>1</sup>

**Table 2.1** Characteristics of aluminum-silicon casting alloys<sup>1</sup>

Alloy	Casting Method	Resistance To Tearing	Pressure Tightness	Fluidity	Shrinkage Tendency	Corrosion Resistance	Machinability	Weldability
319.0	S.P	2	2	2	2	3	3	2
332.0	P	1	2	1	2	3	4	2
355.0	S.P	1	1	1	1	3	3	2
A356.0	S.P	1	1	1	1	2	3	2
A357.0	S.P	1	1	1	1	2	3	2
380	D	2	1	2	-	5	3	4
390	D	2	2	2	-	2	4	2
413.0	D	1	2	1	-	2	4	4
443.0	P	1	1	2	1	2	5	1

S = sand, P = permanent, and D = die casting; Ratings: 1, best; 5, worst

## 2.2 CLASSIFICATION OF AL-SI ALLOYS

Aluminum alloy castings can be produced by all casting processes in a range of compositions possessing a wide variety of useful engineering properties. Specifications for casting alloys are defined by their chemical compositions. Foundry alloys are obtained either from electrolytic aluminum to which are added the constituent elements, or from recycled aluminum metal. Each country has developed its own aluminum casting alloy

nomenclature and designation. In the United States, the three-digit registration system of the Aluminum Association is most widely used.

In the Aluminum Association (AA) system, the alloys are divided into series, according as the major alloying elements present in the alloy. The nine series corresponding to various alloy systems are shown in Table 2.2.<sup>7</sup>

**Table 2.2** Classification of aluminum casting alloys<sup>7</sup>

Series	Alloy family
1XX	99.0% min Al
2XX	Al-Cu
3XX	Al-Si-Mg, Al-Si-Cu, Al-Si-Cu-Mg
4XX	Al-Si
5XX	Al-Mg
6XX	Unused
7XX	Al-Zn
8XX	Al-Sn
9XX	Unused

No commercial alloys are established currently in the 6XX and 9XX series. Alloys are registered by the Aluminum Association, with XXX.0 representing the chemical composition limit for castings, and XXX.1 and XXX.2 representing those for ingots. Several AA alloy designations also include a prefix letter. Different letters used with the same alloy number distinguish alloys of a general composition that differ in their percentage of impurities of minor alloying elements, for example 356 and A356, or 380, A380 and B380.

The present study concentrated on A356.2, A319.2 and B319.2 alloys, from the 3XX series, *viz.* those belonging to the Al-Si-Mg, Al-Si-Cu and Al-Si-Cu-Mg alloy systems, respectively.

### **2.2.1 Al-Si-Mg Alloy System**

The aluminum-silicon-magnesium group of alloys has excellent casting characteristics, weldability, pressure tightness, and corrosion resistance.<sup>7</sup> These alloys are hardened by magnesium silicide ( $Mg_2Si$ ), and are heat-treatable to provide various combinations of tensile and physical properties that prove useful in many applications, including aircraft and automotive parts. The most popular among them are the 356 alloy (containing 7% Si and 0.3% Mg) and the higher-purity version, A356. The unmodified 356.0 alloy shows a coarse eutectic phase located between the aluminum dendrites. The addition of small amounts of Sr or Na to the melt chemically modifies the eutectic Si from an acicular to a finely dispersed fibrous form which enhances the mechanical properties, in particular, the ductility. Alloy A357 is similar to alloy 356 but has a higher magnesium content (0.5wt%) and can be heat treated to a higher strength level. Alloys A356 and A357 are higher-purity versions of 356 and 357, and A357 also contains a small amount of beryllium. Both alloys are capable of much higher ductility than their lower purity counterparts. Other alloys of the Al-Si-Mg group are 359 and the die casting alloys 360, A360, and 364, that provide a combination of high strength and ductility with good casting characteristics.

### 2.2.2 Al-Si-Cu Alloy System

Aluminum-silicon-copper alloys represent the workhorse of aluminum foundry alloys. In this group, silicon provides good casting characteristics and copper gives high strength and machinability, at the expense of a somewhat reduced ductility and lower corrosion resistance. The mechanical properties of Al-Si-Cu alloys are determined primarily by the chemical composition, molten metal processing technique and heat treatment applied.

Alloy 319 (containing 6% Si and 3.5% Cu) is a preferred general-purpose alloy for sand foundries, and can also be used in permanent mold casting. It is employed extensively in a wide variety of applications on account of its excellent castability, high thermal conductivity and low thermal expansion coefficient.<sup>8</sup> In addition, it can be heat treated to obtain an optimum combination of strength and ductility. With its low Si content, the aluminum phase dominates the properties. With a successful strontium modification treatment, the silicon assumes a fine fibrous structure which improves the mechanical properties.

The Al-Si-Cu 380 alloy (8.5% Si – 3.5% Cu) is preferred for die casting. This alloy, like 319, is supplied in the as-cast temper, and usually benefits by a full T6 heat treatment. In the USA and Canada, engine castings, transmission parts and various other automotive parts are cast in 380.0 alloys, while in Europe and Japan, 380.0 engine blocks (with cast-in iron liners) are produced using high pressure die casting.

Hypereutectic alloys such as 390.0 and 393.0 containing 15 to 25% silicon exhibit excellent wear resistance and low thermal expansion. A 0.01% addition of phosphorous is recommended to obtain a refined primary silicon in order to obtain a better machinability.

## **2.3 SOLIDIFICATION OF AL-SI ALLOYS**

All commercial solidification processes involve some non-equilibrium effects. True stable equilibrium conditions seldom exist in a metal field. However, the study of equilibrium systems is extremely valuable, because it constitutes a limiting condition from which actual conditions can be estimated.<sup>9</sup> In real casting processes, the extent of deviation from equilibrium conditions has a significant effect on the actual microstructure observed.

In our work, a preheated graphite mold (600°C) was used for microstructural characterization purposes, which provided close-to-equilibrium cooling conditions and enough time for the precipitating phases to grow, to facilitate their identification using electron microscopic techniques. Thermal analysis could also be carried out simultaneously, with the graphite mold set-up, which assisted in determining the precipitation reactions taking place during solidification.

### **2.3.1 Phase Precipitation**

Solidification of hypoeutectic Al-Si foundry alloys can be characterised by a short nucleation event, the subsequent growth of equiaxed dendrites until they impinge onto each other at the dendrite coherency point, the growth and coarsening of secondary dendrite

arms, and a final eutectic precipitation in the case of a binary alloy. Thus, in the case of 319 and 356 alloys, the following main features will be observed:

- a) the formation of a dendrite network of  $\alpha$ -aluminum,
- b) the aluminum-silicon eutectic reaction,
- c) the precipitation of secondary eutectic phases such as  $\text{Al}_2\text{Cu}$  and  $\text{Mg}_2\text{Si}$ .

Compared to the case of the hypoeutectic alloys, in eutectic alloys the pre-eutectic reactions may be missing, and in hypereutectic alloys, the primary reaction involves the precipitation of silicon particles until the eutectic composition is reached.

Depending on the purity of the base material, Al-Si alloys contain varying amounts of impurity elements such as iron (Fe), manganese (Mn), copper (Cu) and zinc (Zn). Also, copper and magnesium are often added as alloying elements to increase the strength and hardening ability of the material being cast. Impurities and alloying elements partly go into solid solution in the matrix and partly form intermetallic particles during the solidification process. Therefore, in addition to the main reactions, the precipitation of iron- and manganese-containing phases will also take place.

The most common of such phases in foundry alloys are the  $\beta$ - $\text{Al}_5\text{FeSi}$  and  $\alpha$ - $\text{Al}_{15}(\text{Mn,Fe})_3\text{Si}_2$  iron intermetallics. The  $\beta$ - $\text{Al}_5\text{FeSi}$  phase tends to form thin platelets which appear as needles in a cross-section. These platelets are very hard and brittle and have a relatively low bond strength with the matrix.<sup>2</sup> The  $\beta$ -iron phase also increases porosity by blocking feeding channels between solidifying dendrites.

The  $\alpha$ -Al<sub>15</sub>(Mn,Fe)<sub>3</sub>Si<sub>2</sub> phase, with a Chinese script morphology, exhibits an irregular, curved crystal growth, conforming to the complicated shape of the interdendritic spaces (between the  $\alpha$ -Al dendrites) during solidification. This form is controlled by the temperature gradient and by the diffusion of atoms in the liquid metal. It is considered less detrimental to the mechanical properties when compared to the  $\beta$ -iron phase, because of its compact morphology.

Toward the end of the solidification process, Mg<sub>2</sub>Si, Al<sub>2</sub>Cu and other more complex phases precipitate from the remaining liquid. Under equilibrium conditions, due to the sufficient time they have to grow, the size of these phases are adequately large to facilitate phase identification using electron probe microanalysis (EPMA) and related EDX/WDS techniques. As mentioned previously, this was one of the main reasons for using metallographic samples obtained from the hot graphite mold (600°C) castings for microstructural analysis in the present work. Table 2.3 summarizes the sequence of phase precipitation in hypoeutectic Al-Si alloys.<sup>10</sup>

**Table 2.3** Sequence of phase precipitation in hypoeutectic Al-Si alloys<sup>10</sup>

Temperature (°C)	Phases precipitated	Suffix
650	Primary Al <sub>15</sub> (Mn, Fe) <sub>3</sub> Si <sub>2</sub> (sludge)	Pre-dendrite
600	Aluminum dendrites and (Al <sub>15</sub> (Mn, Fe) <sub>3</sub> Si <sub>2</sub> ) and /or Al <sub>5</sub> FeSi	Dendritic Post-dendritic Pre-eutectic
550	Eutectic Al + Si and Al <sub>5</sub> FeSi Mg <sub>2</sub> Si	Eutectic Co-eutectic
500	Al <sub>2</sub> Cu and more complex phases	Post-eutectic

### 2.3.2 Effect of Cooling Rate

The microstructures of Al-Si alloys depend strongly both on the composition and the casting process, the effect of solidification conditions (*i.e.*, cooling rate) being implicated in the latter case. It is well known that a high cooling rate produces a fine eutectic structure, small dendrite cells and arm spacing, and a reduced grain size.

Under rapid solidification conditions, the rate of heat extraction can greatly exceed the rate of heat generated by the freezing process (latent heat of solidification). As a result, the liquid undercools as its temperature falls below the liquidus temperature. If this undercooling is sufficient, the full range of heterogeneous nuclei present in the liquid can become active. This multiplied nucleation results in a fine as-cast grain size. In any event, the rapid chilling of large castings produced by any method is usually impractical due to the large amount of latent heat which must be removed.

In terms of microstructure, the dendrite arm spacing (DAS) gives a measure of the fineness of the microstructure, and can be varied considerably by the cooling rate. Figure 2.2 illustrates the DAS values obtainable in a 356 alloy over a range of cooling rates.<sup>11</sup> The DAS is by far the most important parameter in determining the mechanical properties of an Al-Si alloy. Although smaller DAS values are caused by faster solidification rates which are usually associated with finer as-cast grain sizes, it is the DAS, and not the grain size, which controls the mechanical properties.

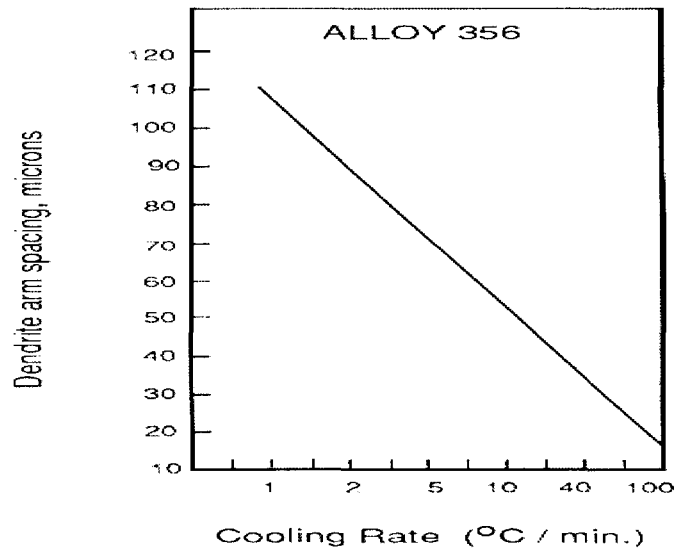


**Figure 2.2** Variation of the DAS of a 356 alloy with cooling rate.<sup>11</sup>

Rapid solidification can also result in a fibrous eutectic structure. However, the fact that these silicon fibers have smooth external surfaces and that many are twin-free simply indicates that they are an exceedingly fine form of the unmodified eutectic. On the other hand, a rapid cooling rate can minimize the detrimental effects of  $\beta$ -iron intermetallics by decreasing the average length of the  $\beta$ -phase.<sup>12,13,2</sup>

## 2.4 MODIFICATION OF THE EUTECTIC SILICON

As mentioned previously, Al-Si alloys are widely used in numerous applications where good strength and light weight are required, or where corrosion resistance or castability are desired. However, the commercial application of these alloys often depends on the successful modification of the eutectic silicon.

Modification is one of the melt treatments commonly carried out on Al-Si alloys, where, through the addition of ‘modifiers’ such as sodium and strontium, the morphology of the eutectic silicon is changed into a fibrous form in order to enhance the properties of the alloy. An unmodified alloy contains an acicular eutectic silicon structure. Such brittle, acicular Si particles act as internal stress raisers in the microstructure and provide easy paths for fracture. With modification, the eutectic structure becomes finer and the silicon becomes rounded, which contribute to higher values of ultimate tensile strength and greatly increased values of ductility.

Apart from the use of modifiers, the eutectic silicon can also be ‘modified’ through solution heat treatment or the use of high cooling rates. However, full modification is difficult to achieve by simply increasing the solidification rate of the casting alone, and thus Al-Si alloys are generally modified chemically, using modifying agents.<sup>14</sup> These are normally added to the alloy melt in the form of master alloys in desired quantities, to achieve a well-modified eutectic structure.

Apelian et al.<sup>15</sup> assessed the grain refinement and modification of Al-Si foundry alloys using thermal analysis. Figure 2.3 depicts the range of microstructures observed by the authors on the polished surfaces of a modified hypoeutectic Al-Si alloy. The structures are divided into six classes, with the unmodified structure represented by class 1, lamellar by class 2, undermodified by classes 2-4, well modified structures by class 5, and overmodified structures by class 6.

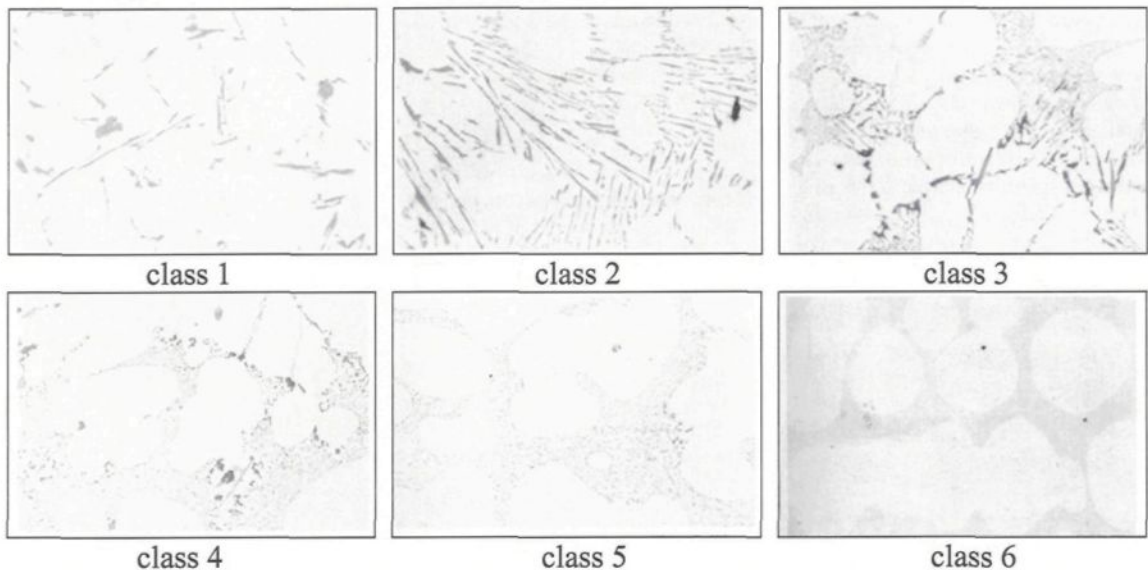


**Figure 2.3** Rating system for a modified microstructure.<sup>15</sup>

Five variables determine the exact microstructure which will form: i) type of modifier used, ii) impurities present in the melt, iii) amount of modifier used, iv) freezing rate, and v) silicon content of the alloy. These five variables interact in a highly complex manner, so that an exact quantitative prediction of the microstructure, in terms of a modification rating, for example, is rendered difficult.

#### 2.4.1 Mechanism of Eutectic Silicon Modification

Ever since Pacz<sup>16</sup> discovered the possibility of modifying Al-Si alloys, the study of the modification process has attracted many investigators. Some researchers<sup>17,18</sup> explain modification in terms of twinning during the crystallization of silicon. With respect to the Al-Si eutectic reaction, the silicon phase plays a critical role in modification. In the unmodified state, the shape of the silicon particles (or flakes) can be described in terms of

the facets on the close-packed  $\{111\}$  faces of the diamond cubic structure, generally combined with a few twins on the same planes. Transmission electron microscopic examination also shows that silicon flakes have a  $\langle 211 \rangle$  preferred growth direction. These aspects are shown in the schematic diagram of Figure 2.4(a),<sup>19</sup> while that of Figure 2.4(b)<sup>18</sup> shows how twinning occurs in a crystal.

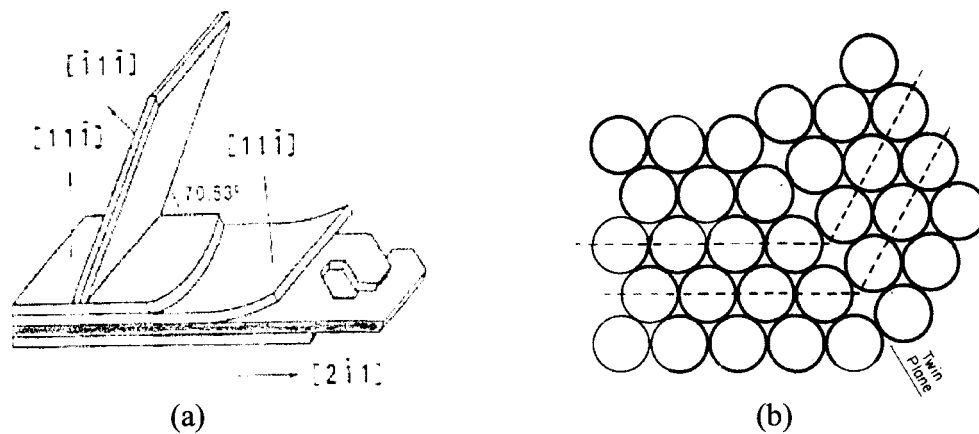


**Figure 2.4** (a) Schematic model of eutectic Si flakes with twin configuration shaded,<sup>19</sup> (b) Twinning in a crystal showing the continuity of the atom planes across the twin plane.<sup>18</sup>

Crystallization of the silicon takes place by the addition of atoms to form steps which move across the solid-liquid interface. These steps originate at twins across the  $\langle 111 \rangle$  planes. While the modified silicon is crystallographically imperfect, it is highly twinned with a rough microfaceted surface. This type of growth of the modified silicon allows free and easy branching to occur, to form the fibrous structure.

The difference between the two types appears to lie in the much larger number (orders of magnitude) of twins found in the modified silicon fibers than in the unmodified silicon platelets. It requires the addition of only a fraction of one weight-percent of

modifier to make this remarkable difference in twin density, because the incorporation of foreign atoms of a certain size into silicon enhances the formation of twins. If the modifier atom radius has the correct size compared to the silicon atomic radius ( $r_{\text{modifier}} : r_{\text{silicon}} = 1.646$ ), a growth twin will be caused at the interface.<sup>18</sup> This phenomenon has been named impurity induced twinning, and is supported by the observation that the modifier becomes concentrated in the silicon, and not the aluminum, phase.<sup>19</sup>

#### **2.4.2 Effect of Cooling Rate on Modification**

Rapid solidification in the growth rate range 400 to 1000  $\mu\text{m}$  per second can cause a fibrous eutectic structure in the absence of chemical modifiers. As mentioned earlier, this structure is similar to the unmodified silicon, and is simply an exceedingly fine form of the unmodified eutectic. It contains no, or a very low level of twinning, as observed by electron microscopy.<sup>2</sup> In practical terms it is of little consequence in commercial casting processes (with the possible exception of die casting), which do not operate at sufficiently high solidification rates to cause quench modification.

#### **2.4.3 Effect of Chemical Modification**

Several elements are known to cause silicon modification. Group IA and Group IIA elements of the Periodic Table, rare earths, (*e.g.*, La and Ce), As, Sb, Se and Cd have all been reported to exert a modification effect.<sup>20,21 22</sup> However, only Na, Sr and Sb are currently the most effective within economic constraints.<sup>23,24</sup> Of these, antimony, due to its toxic effects, is not used in North American foundries.

The amount of each modifier element required depends somewhat on the alloy composition – a higher silicon content requiring a larger amount of the modifying agent. For example, sodium is generally used in the range of 0.005-0.01 wt%. Strontium in amounts of 0.02% is sufficient to modify an Al-7% Si alloy such as 356, but up to 0.04% Sr is needed for eutectic alloys such as 413, containing ~12% Si.

The microstructural change from acicular to fibrous silicon is not a sharp one, and castings with an inadequate amount of either sodium or strontium will exhibit a mixed structure - one containing regions of fibrous silicon, lamellar silicon and acicular silicon. Modification with strontium is often less uniform than with sodium, while antimony produces only a lamellar, and never a fibrous structure.

The modification ability of elements is determined by several factors, such as the radius ratio (the ability to produce twins), the melting point, the vapour pressure and oxidation potential. Table 2.4 lists some properties of possible modifiers.<sup>25</sup>

**Table 2.4** Some properties of possible modifiers<sup>25</sup>

Element	Atomic radius (Å)	R/r <sub>Si</sub>	Melting point (K)	Vapour pressure at 1000k (atm)	-ΔG oxide (kJ mol <sup>-1</sup> )	K <sub>oxidation</sub>
Sr	2.16	1.84	1042	1 × 10 <sup>-3</sup>	480	15
La	1.87	1.59	1193	10 <sup>-6</sup>	487	-
Na	1.86	1.58	371	0.2	367	2.7 × 10 <sup>-5</sup>
Ce	1.83	1.56	1071	14970 <sup>-16</sup>	497	-

Note: Large value of K<sub>oxidation</sub> is indicative of a high tendency to oxidation.

### 2.4.3.1 Sodium (Na)

The use of sodium to modify the Al-Si eutectic has been well-known since the discovery of Pacz in 1921.<sup>16</sup> Hogan<sup>17</sup> and Hellawell<sup>18</sup> found that modification by sodium addition is a combination of two effects: neutralization of AlP so that easy nucleation of silicon is prevented, and a change in the mode of solidification of the eutectic so that the modified eutectic crystallizes with aluminum crystals in the lead instead of silicon crystals, as in the case of non-modified alloys.

Sodium is easy to use in the foundry and probably the most efficient in terms of fineness and uniformity of the eutectic structure, because it is the most effective in producing large numbers of twins in silicon. The normal amount of sodium added is some 20 to 150 ppm, but its action is only short-lived. Due to its low melting point (98°C), sodium is easily incorporated into Al-Si melts which are normally treated in the range of 775°C to 800°C. The dissolution of sodium is instantaneous at these temperatures, but its high vapor pressure (0.2 atm. at 730°C) makes it boil off almost immediately. This phenomenon is called “fading”. Consequently, sodium recoveries are very poor (20% to 30% of the addition). Figure 2.5 shows the “fading” of the Na in an Al-13%Si alloy melt with holding time.<sup>26</sup> As sodium is also sensitive to porosity and has adverse effects in terms of oxidation and aggressiveness against mold coatings, *etc.*,<sup>27</sup> it is difficult to control the Na-modification process, and its use is therefore limited.

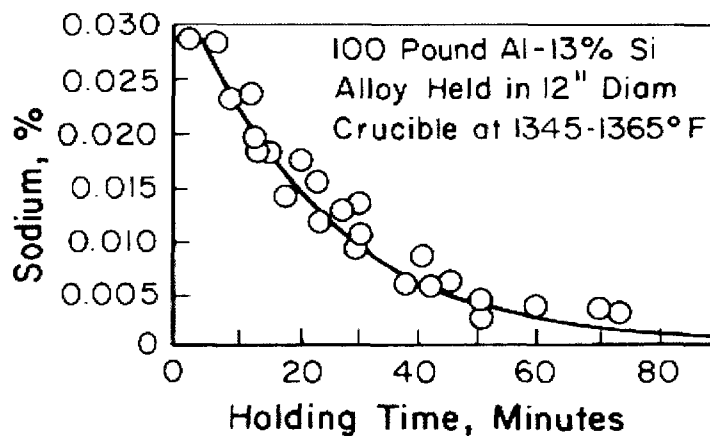


**Figure 2.5** Loss of sodium in an Al-13%Si alloy melt during its holding in a crucible.<sup>26</sup>

#### 2.4.3.2 Strontium (Sr)

Since the early seventies, strontium has been widely used because of its greater stability in the melt when compared with sodium. Modification of the Al-Si eutectic through the use of Sr is easier to control. The addition of Sr neutralizes the effect of P and promotes the formation of a fibrous silicon structure by retarding the growth rate of silicon.<sup>28,29</sup> Figure 2.6 shows the microstructures of unmodified and Sr-modified A356.0 alloy.

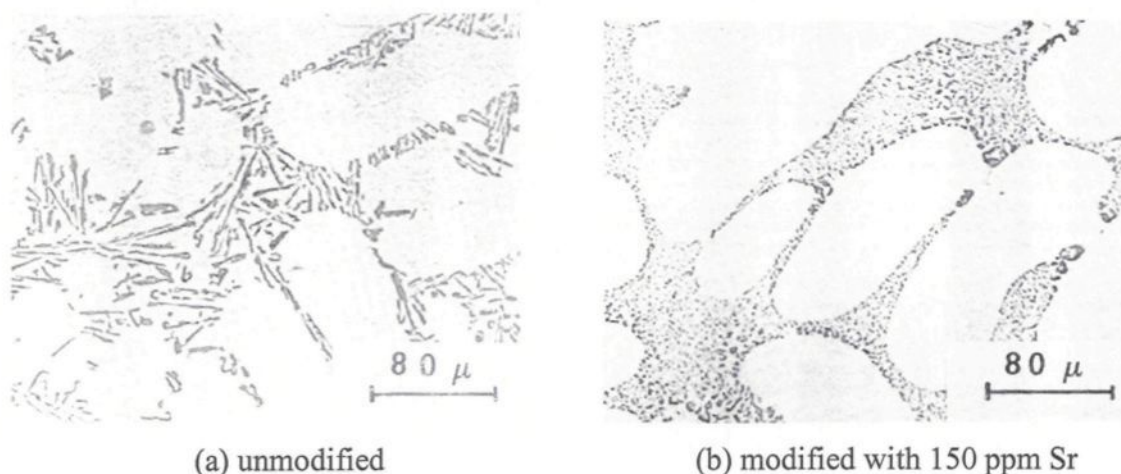


**Figure 2.6** Microstructures of as-cast A356.0 alloy: (a) unmodified, and (b) 150 ppm Sr-modified.<sup>30</sup>

Pure strontium can readily react with air and water and be covered with SrO, SrO<sub>2</sub>, Sr(OH)<sub>2</sub> and (CaSr)NO<sub>3</sub>. This layer, which can only be removed mechanically, will completely prevent dissolution. Thus, Al-Sr master alloys are always used to modify Al-Si alloys. The dissolution characteristics of a higher Sr-containing Al-Sr master alloy are quite different from a low Sr-containing one.

A high Sr-containing master alloy (Al-90%Sr) dissolves by a reactive dissolving process. This produces new intermetallic compounds such as Al<sub>2</sub>Si<sub>2</sub>Sr. Within a certain temperature range, this is an exothermic reaction, which quickly reaches the melt temperature and then surpasses it by almost 100°C. The reaction finishes in about 60 seconds, and the temperature diminishes to the bath temperature. Therefore, this master alloy dissolves the best and gets the best recoveries at a low rather than a high temperature.<sup>1</sup>

The low Sr-containing master alloy (Al-10%Sr) shows classical dissolution behavior: the dissolution improves as the temperature increases. The Al-Al<sub>4</sub>Sr eutectic,

large plates of  $\text{Al}_4\text{Sr}$  and  $\text{Al}_2\text{Sr}_2\text{Si}$  intermetallic compounds are formed in this case. Most of the Sr is locked up in these intermetallic compounds and the process of adding strontium to the melt is one of dissolving these compounds. Under this condition, strontium recoveries are high at high temperatures.<sup>1</sup>

Among the first to report on the modification effect of Sr were Hess and Blackmun,<sup>31</sup> who studied strontium as a modifying agent for hypoeutectic Al-Si alloys. From their work, they concluded that strontium is an effective modifying agent for hypoeutectic Al-Si alloys. However, an initial incubation period was required for maximum modification. Strontium retained its modifying action longer than sodium in spite of a continual loss of Sr during holding, provided a sufficient amount of Sr, approximately 0.008%, remained in the alloy. The modifying effect of Sr actually appeared to improve with holding time, again provided a sufficient amount remained.<sup>31</sup>

Figure 2.7 shows the effect of Sr and holding time on modification.

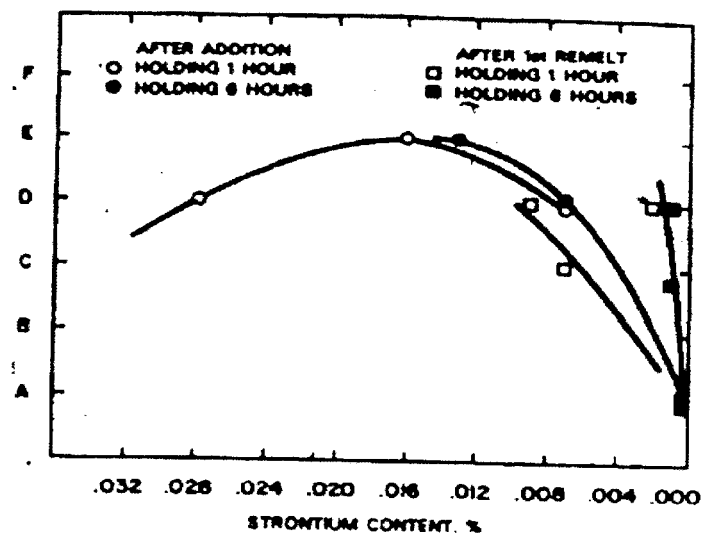


**Figure 2.7** Effect of strontium content and holding time on modification.<sup>31</sup>

This was found to be opposite to the effect with Na, where loss of Na on holding resulted in a concurrent loss of modification. The opposite effects of improved modification with increased holding time and the continual loss of Sr made it difficult to designate a minimum amount of Sr required for adequate modification. However, it appeared that an initial addition of Sr equal to or greater than the usual 0.01%-0.02% Na was required to obtain initial modification. As for the effect on mechanical properties, strontium modification caused significant increases in the mechanical properties of Al-Si alloy permanent mold castings.

Chai and Bäckerd<sup>32</sup> investigated the factors affecting the modification of Al-Si alloys by the addition of Sr-containing master alloys. They observed that in master alloys of the Al-Sr type, the size of the  $Al_4Sr$  particles affects the degree of modification: a master alloy with fine  $Al_4Sr$  particles will reduce the incubation time and can produce a well-modified structure within only a few minutes. Secondly, phosphorus has little effect on the degree of modification during the first ten minutes after the addition of Sr in the melt. The reaction between Sr and P consumes Sr, decreases the degree of modification and increases the incubation time. Also, the increase of Sr content in the melt reduces the incubation time and increases the degree of modification. Excess Sr in the melt can form  $Al_2Si_2Sr$  particles and reduce the modification efficiency.

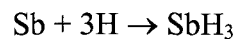
Griffiths *et al.*<sup>33</sup> studied the effect of the simultaneous additions of sodium and strontium on the modification of Al-Si alloys. They found that simultaneous additions of Na and Sr produce a modifying effect in an Al-Si eutectic alloy, similar to that found with sole additions of Na and Sr. A refinement of the primary silicon phase was also found

upon addition to a hypereutectic Al-Si alloy. The modifying effect was found to be of a long term duration with an addition of 0.1% sodium and 0.035% strontium, producing a modification which persisted for four hours. After solidification and remelting, the modified structure persisted for at least a further thirty minutes. On the basis of these results the authors have suggested that significant advantages may be gained with the use of simultaneous additions of Na and Sr and the addition of Na to Sr-modified alloys.

#### **2.4.3.3 Antimony (Sb)**

Antimony additions ranging from 0.15 to 0.3 wt% are very efficient in modifying the acicular structure to produce a lamellar eutectic. Antimony yields a lamellar eutectic structure instead of the fibrous one obtained with Na or Sr additions. The microstructural differences arise from the inability of antimony to cause extensive additional twinning in silicon. However, its stability and absolute permanent effect, associated with a tendency for less gas pick-up and less porosity formation in parts, is useful for permanent mold castings undergoing high stresses and requiring consistent properties.<sup>34</sup>

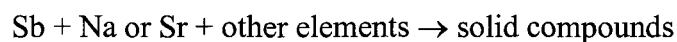
Antimony is a toxic material and can react with hydrogen dissolved in liquid aluminum to form deadly stibine gas:



As a result, antimony is not employed as a modifier in the foundry. An Sb-treated alloy is purchased as a premodified ingot from primary aluminum suppliers and is simply remelted and cast. If the industrial processes in the casthouse in the foundry are carefully carried

out, the antimony emission levels are far below the limit values established by health and environment administrations.

It was demonstrated that antimony is metallurgically incompatible with sodium or strontium and acts to destroy the modifying effect of these two elements.<sup>35</sup> This effect is due to melt phase reactions of the form:



These solid compounds can remove sodium or strontium from the solution and prevent them from acting as modifiers.

#### **2.4.3.4 Rare Earth Metals**

The rare earths are the group of fifteen elements in Group III of the Periodic Table having numbers from 57 to 71, inclusive. These elements (*e.g.* cerium (Ce), lanthanum (La), neodymium (Nd), *etc.*) are also capable of modifying the eutectic structure of cast Al-Si alloys.

Sharan<sup>36</sup> has explained rare earth metal modification using the critical growth temperature hypothesis, where the modifying element should have a tendency to form compounds with the precipitating phase (Si) at a temperature below the normal eutectic temperature and should also exhibit little compound-forming tendencies with the solvent phase ( $\alpha$ -Al). Lanthanum meets these requirements, but Ce and Nd only satisfy them partially. However, rare earth (RE) elements do satisfy the minimum criteria such as atomic radius, melting point, vapor pressure, and free energies of oxide formation, thus exhibiting the capability of modifying the eutectic Si.

Rare earth elements have been added to Al-Si alloys as mischmetal (MM - a mixture of rare earth elements) and also in the form of specific RE metals and as RE fluorides. Cerium, lanthanum, neodymium partially modify the eutectic structure, while with the use of rare earth fluorides, refinement of both the polyhedral silicon plates and the eutectic take place.<sup>20,37,38</sup> Lanthanum addition to Al-Si alloy reduces interdendritic and secondary porosity considerably. Eutectic undercooling in Al-7Si-0.3Mg alloy is increased by as much as 25K, with an increase in mischmetal addition up to 2 pct, and complete modification is obtained.<sup>22</sup>

Ye *et al.*<sup>22</sup> have investigated the role of rare earth metals in the eutectic modification of cast Al-Si alloys. They report that rare earth metals can achieve a reliable and persistent eutectic modification effect, where the silicon phase modified by rare earth metals exhibits the same changes in crystallographic structure as that achieved through modification with sodium. In both cases, the Si phase changes from growth in the  $\langle 211 \rangle$  directions to growth in the  $\langle 100 \rangle$  directions, where it develops a refined, rounded, and interconnected morphology. The eutectic modification achieved through the use of rare earths is extremely resistant to fading and may persist up to several hours of holding time at certain temperatures. However, the minimum amount of rare earth metals necessary to obtain proper modification is exceptionally large.

Chang *et al.*<sup>39</sup> reported that simultaneous refinement of both primary silicon and eutectic silicon is achieved with the addition of rare earths (added as mischmetal) to hypereutectic Al-Si alloys, where the refining effect increases with the amount of rare earth (mischmetal) addition (1, 2 and 3 wt%) and cooling rate (33°C/s through 130°C/s). The

refinement of silicon is due to the suppression of the nucleation temperature of the silicon phase, with depressions of 2-7°C in the eutectic reaction temperature being observed with the addition of the rare earths.

#### **2.4.4 Phosphorus Interaction with Modifiers**

Phosphorus can exist in aluminum casting alloys as an impurity, through contact with tools, refractories, and alloying elements and other additions which can also contain some phosphorus. In the case of hypereutectic alloys, phosphorus is also added to refine the primary silicon structure.<sup>28</sup> Silicon particles in phosphorus-free alloys solidify as a lamellar structure even if there is no modifier agent present. A high phosphorus level can cause the eutectic Si to solidify in an acicular form.

The undesirable interaction between phosphorus and modifiers (Na and Sr) is well known, and has been studied and determined in commercial alloys.<sup>40,41,42,43</sup> Generally speaking, alloys which contain higher phosphorus levels require larger amounts of modifier to achieve an acceptable, well-modified cast structure. Figure 2.8 demonstrates how, in order to get the same modification level cast structure, higher phosphorus-containing alloys need greater amounts of strontium.<sup>23</sup>

This phenomenon implies a reaction between the modifier and phosphorus. There are two possible explanations. Garat and Scallier<sup>23</sup> have found that in modified alloys, there are some measurable amounts of phosphorus in intermetallic compounds such as  $\text{NaSi}_2$ ,  $\text{Al}_2\text{Si}_2\text{Sr}$  and  $\text{Mg}_3\text{Sb}_2$ . These compounds are supposed to dissolve the phosphorus as

a solid solution and hence, remove it from the liquid. Another explanation is that the modifiers react directly with the phosphorus to form modifier-phosphorus compounds.

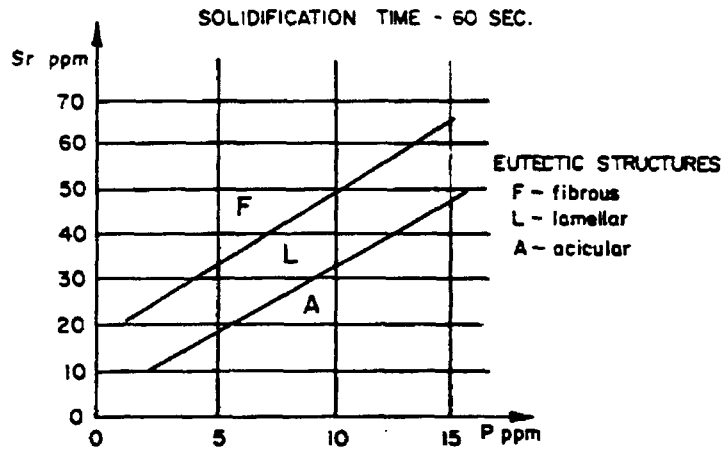


**Figure 2.8** Interaction between phosphorus and strontium in a sand-cast alloy.<sup>23</sup>

Another phenomenon that can be observed with phosphorus-containing alloys relates to the incubation period. For a phosphorus-free alloy, with Sr addition, about 30 minutes are required to achieve maximum Sr concentration in the melt. In the presence of phosphorus, during the first 1-2 hours after a strontium addition is made, the modification rating improves. This is an advantage, as it runs counter to any chemical fading. In a Na-modified alloy, there is no incubation period, due to the much more pronounced phenomenon of fading in this case.

Lee and Kang<sup>44</sup> studied the microstructural changes in 390 alloys with P and/or Sr treatment, and found that the simultaneous addition of phosphorus and strontium had a deleterious effect on the refinement of primary Si. In addition, the modification effect of

strontium was also reduced. Sigworth<sup>21</sup> has also reported that phosphorus negates the modification effect of strontium and sodium.

#### 2.4.5 Effect of Modification on Mechanical Properties

It is known that chemical modification can affect the microstructure of Al-Si alloys, and that these microstructural changes will directly influence the mechanical properties. The coarse, acicular Si platelets of the unmodified eutectic structure act as internal stress raisers in the microstructure and provide easy paths for fracture. With modification, the structure becomes finer and the silicon more rounded, both of which can result in higher values of ultimate tensile strength and ductility. An example of this is shown in Figure 2.9, where the variation in percentage elongation in unmodified and Sr-modified A356.2 alloys has been plotted as a function of ageing time.<sup>45</sup>

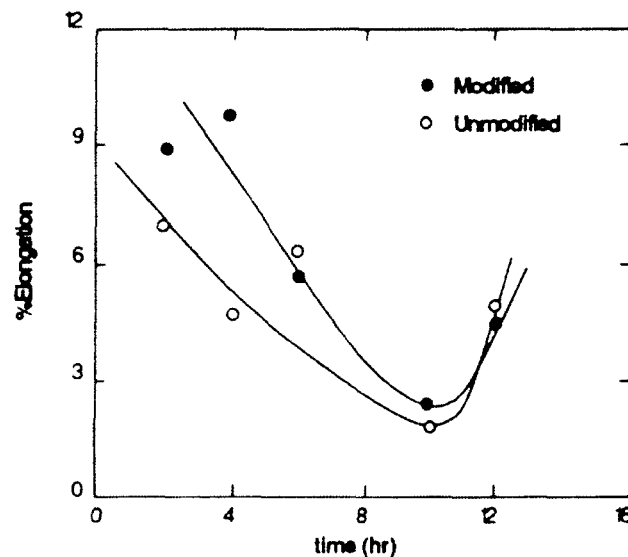


**Figure 2.9** Variation of T6 elongation in unmodified and modified A356.2 alloys. The castings were aged at 155°C (310°F).<sup>45</sup>

Modification exerts a significant improvement on the impact strength of both as-cast and heat-treated alloys. Impact strength is given to the material by the ductile aluminum matrix which separates the brittle silicon phase. Any process which reduces the size of the brittle phase particles or increases their separation, will improve impact properties. Modification does the former, and the coarsening process, which takes place during solution treatment, accomplishes the latter.<sup>1</sup> As Figure 2.10 shows, impact properties are much more sensitive to modification than tensile properties, where the impact strength of the modified alloy is seen to increase to three times its value, the elongation value is doubled, but both yield and tensile strength remain basically unaffected.

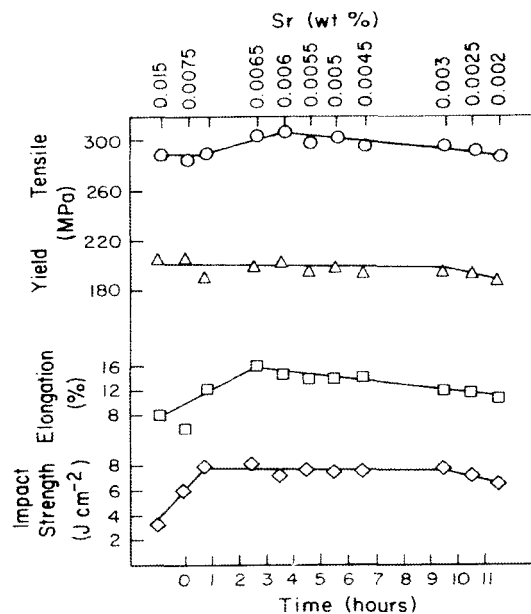


**Figure 2.10** Mechanical properties of A356.0 alloy modified with strontium and held for times of up to 11 hours before casting.<sup>1</sup>

The changes in tensile and impact properties with modification are not evident in the case of fatigue strength. Fatigue strength drops with increased amounts of silicon, but is hardly affected by modification. This is because fatigue cracks propagate along the silicon-aluminum interfaces, and the stress required to cause decohesion at these interfaces is little influenced by a modification treatment.<sup>1</sup>

Closset<sup>46</sup> investigated the modification and quality of low pressure aluminum alloy castings, and found that Sr modification substantially improves elongation and, to a lesser extent, the tensile strength of Al-Si eutectic type 413 alloy. The impact strength of the alloy was found to be very sensitive to the microstructure and was greatly improved by Sr modification of the eutectic.

Mechanical properties of modified and non-modified eutectic Al-Si alloys were also investigated by Hafiz and Kobayashi.<sup>47</sup> Their results showed that the impact toughness was highly sensitive to the Si morphology in the eutectic matrix, where a fibrous Si morphology enhanced toughness, owing to its profound effect on crack initiation and crack propagation resistance. Tensile properties, in particular elongation, were greatly improved as a consequence of the Sr modification. The higher toughness and ductility of the modified alloy were attributed to the fine fibrous morphology of the Si particles achieved by modification, and the stress/strain state in the matrix material associated with the refinement of the eutectic.

The influence of solidification rate and Sr level on the tensile properties of eutectic Al-Si alloys obtained by these authors is shown in Figure 2.11.<sup>47</sup> As can be seen, both the

ultimate tensile strength (UTS) and ductility (%El) are improved with modification and increase in cooling rate, whereas the yield strength (YS) remains unaffected.

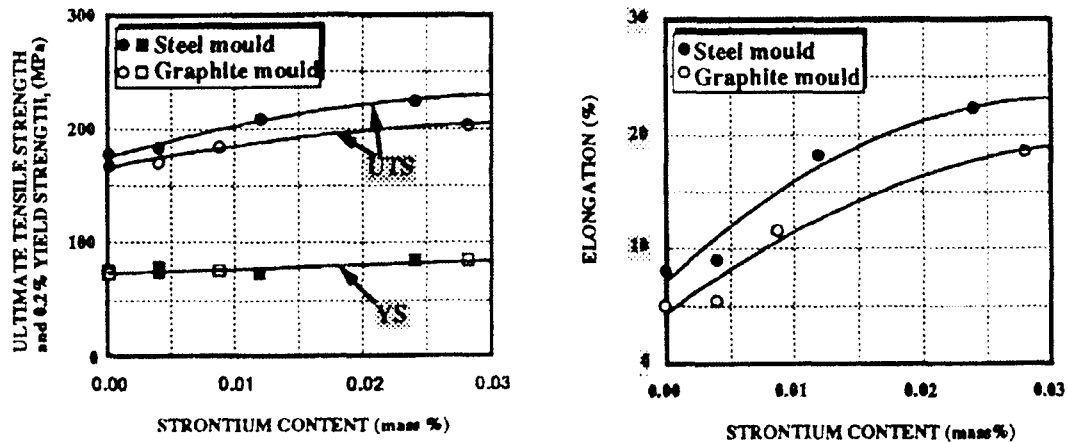


**Figure 2.11** Influence of solidification rate and Sr level on the tensile properties of eutectic Al-Si alloy.<sup>47</sup>

Closset and Fay<sup>48</sup> also studied the Sr-modification of aluminum investment casting alloys, and observed that Sr-modification improved the elongation of an A356.0 alloy poured in investment casting molds by 100%, and that even at low solidification rates, the impact strength was significantly improved by modification.

Haque *et al.*<sup>49</sup> investigated the modification of Al-Si eutectic alloys and the factors affecting them. From their experiments, they found that the tensile properties (UTS and El%) obtained for the alloys treated with sodium or strontium were more or less the same at either of the two cooling rates studied (chill mold and sand mold). The only noticeable difference was that the elongation was slightly higher for the Sr-modified alloys compared with the Na-treated alloys.

It was also observed that upon strontium treatment, the elongation showed a marked improvement compared to the unmodified alloy, and increased by more than 100%. The authors<sup>49</sup> attributed this to modification of the eutectic silicon in the aluminum matrix, where the higher strength and ductility of chill-cast specimens resulted from the combined effects of rapid cooling and modification.

The appearance of the fracture surfaces after tensile testing also showed these differences in the structure: those of the unmodified alloys had a lustrous, dark grey, well-faceted brittle appearance which resembled the appearance of silicon, whereas the modified alloys had a “lighter, silky fracture” which suggests that the fracture occurred largely through the ductile aluminum matrix.<sup>49</sup>

## **2.5 IRON INTERMETALLICS**

Iron is an impurity that is invariably present in aluminum, stemming from the bauxite ore from which aluminum is produced. In foundry processing, melting equipment such as holding furnace pots, ladles and other melt mixing tools, are also sources of iron pick-up. Remelted scrap is another means by which iron is introduced into the alloy. Dilution is the only practical way to remove the iron. Consequently, the cost of an aluminum alloy becomes inversely related to its iron content.

The amount of iron allowed by ANSI/ASTM specifications (0.8 to 1.0% maximum) in aluminum casting alloys is relatively low, particularly in the case of sand and permanent mold casting alloys,<sup>50</sup> as higher contents impair feeding ability and mechanical properties (especially ductility). Specifications normally permit considerably more iron to be present

in alloys for pressure die castings and permanent mold castings to reduce die soldering. The much higher cooling rates associated with these casting processes, lead to the precipitation of finer, and thus less harmful, microconstituents.

During solidification, iron, together with other alloying elements such as Cu, Mg, Zn, Mn, Ti, *etc.* partly goes into solid solution in the matrix and partly forms intermetallic compounds, including the plate-like  $\beta$ -Al<sub>5</sub>FeSi phase and the Chinese script-like  $\alpha$ -Al<sub>15</sub>(Mn,Fe)<sub>3</sub>Si<sub>2</sub> phase.<sup>10</sup> The formation of the  $\beta$ -Al<sub>5</sub>FeSi iron intermetallic phase is what makes iron the most deleterious impurity element in cast aluminum alloys. For example, increasing iron from 0.5 to 1.2% in an Al-13%Si casting alloy dramatically reduces its mechanical properties, particularly the elongation, due to the presence of an increased amount of  $\beta$ -Al<sub>5</sub>FeSi platelets.<sup>50</sup> These platelets act as stress raisers, which contribute to the brittleness of the material.

Nishi *et al.*<sup>51</sup> studied the effect of iron content on the mechanical properties of Al-Si-Mg-Zn alloys and found that the properties deteriorated further with further increase in iron content. According to Bonsack,<sup>52</sup> iron is probably the most undesirable impurity in binary Al-Si alloys. Grand<sup>13</sup> studied the influence of iron on Al-Si and Al-Si-Cu test bars in both sand and shell molds, and found that increasing Fe from 0.5% to 1.2% in Al-13% Si alloy dramatically reduced the elongation.

In addition to the effect on mechanical properties, large iron-rich needles which form early in the solidification process, tend to prevent the flow of liquid metal through the feeding channels and may cause unsoundness in the casting. Eklund<sup>53</sup> found that intermetallic compounds in as-cast aluminum alloys frequently appear in contact with

porosity. He showed that compounds of the AlFeSi and AlFeMnSi type favour the formation of shrinkage porosity by blocking the interdendritic feeding channels of hypoeutectic Al-Si alloys. It is therefore important to know how to avoid, or at least control, the precipitation of iron-containing intermetallic compounds during alloy solidification.

The five main types of techniques that have been employed to minimize the detrimental effect of iron are as follows:

- i) rapid solidification,<sup>54, 55</sup>
- ii) addition of neutralizers such as Mn, Co, and Cr,<sup>56</sup>
- iii) melt superheat,<sup>57</sup>
- iv) strontium modification,<sup>58, 59</sup> and
- v) non-equilibrium solution heat treatment.<sup>60</sup>

The first three techniques are used to convert, partly or fully, the crystallization of the iron intermetallic compound from the platelet or needle-like form ( $\beta$ -iron phase) to the less harmful Chinese script form ( $\alpha$ -iron phase). Techniques (iv) and (v) are considered to dissolve iron intermetallics. Each one of these methods has its own advantages and limitations. The rapid solidification technique involves solidifying the melt at a very high cooling rate and is applicable only at low levels of iron and silicon.

### 2.5.1 Formation, Fragmentation and Dissolution of Iron Intermetallics

Aluminum forms a variety of intermetallic compounds with its alloying elements. These compounds are actually solid solutions that have a substantial capacity to dissolve other elements. Their composition, although expressed as chemical formulae, vary. In addition, solute atoms in Fe-rich intermetallics often occupy Al, Fe, and Si lattice positions. The substitution of Mn and Cr for Fe is so common that these three elements are often grouped in the chemical formulae. Iron intermetallic particles can generally be divided into three different morphologies: thin platelet ( $\beta$ - $\text{Al}_5\text{FeSi}$  iron intermetallic phase), Chinese script ( $\alpha$ - $\text{Al}_{15}(\text{Mn,Fe})_3\text{Si}_2$  iron intermetallic phase) and polyhedral crystals (sludge).

Figure 2.12 shows examples of the three iron intermetallic types.<sup>6</sup> It should be mentioned that the  $\beta$ -iron platelets appear as needles in an optical micrograph. Hence the terms ' $\beta$ -needle' and ' $\beta$ -platelet' are often used interchangeably to indicate the  $\beta$ - $\text{Al}_5\text{FeSi}$  iron intermetallic phase.

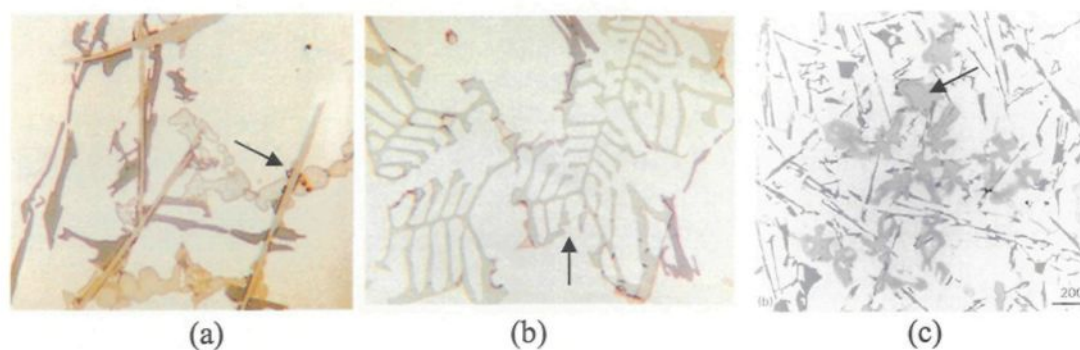


**Figure 2.12** Optical micrographs showing (a)  $\beta$ - $\text{Al}_5\text{FeSi}$ , (b)  $\alpha$ - $\text{Al}_{15}(\text{Fe,Mn})_3\text{Si}_2$ , and (c) sludge iron intermetallics (arrowed).<sup>6</sup>

### 2.5.1.1 The $\beta$ -Al<sub>5</sub>FeSi Iron intermetallic

This intermetallic is a monoclinic needle-like phase, the chemical composition of which is 27.4% iron, 13.6% silicon and 58.2% aluminum, the lattice parameters are  $a = b = 6.12\text{\AA}$ ,  $c = 41.5\text{\AA}$ ,  $\alpha = 91^\circ\text{C}$ , and the density is  $\sim 3.30 - 3.35\text{g/cm}^3$ . These crystals appear in the form of needles (actually platelets in three dimensions) that are light grey in color when observed under the optical microscope. The  $\beta$ -Al<sub>5</sub>FeSi crystal phase grows in a lateral or faceted growth mode. These crystals are bounded by slowly growing planes of low indices. As these surfaces are relatively smooth on the atomic scale, any further atoms from the liquid find few possibilities to join the interface. Thus, their growth is restricted and, hence, slow. This type of growth occurs at low driving forces or slow cooling rates, *i.e.*, at low degrees of undercooling,  $\Delta T$ .

Mondolfo<sup>61</sup> has summarized the main factors that contribute to the formation of the  $\beta$ -iron Al<sub>5</sub>FeSi phase: a) an Fe/Si ratio close to unity, b) a low cooling rate  $\sim 0.8^\circ\text{C/s}$ , and c) a low Mn and Cr concentration. The cooling rate has a direct impact on the equilibrium kinetics and quantities of iron present in the microstructure. The  $\beta$ -iron phase is brittle and possesses a relatively weak coherence with the aluminum matrix. Its presence can decrease the strength and ductility of the cast product. The precipitation of these needles/platelets occurs mostly in a pre-eutectic reaction.<sup>6</sup> Mascré<sup>12</sup> reported that while pre-eutectic  $\beta$ -needles deteriorate the mechanical properties of the alloy, those that precipitate during co-eutectic and post-eutectic reactions may, in fact, improve the properties.

Solution heat treatment is another means used to minimize the harmful effect of the  $\beta$ -iron phase. Upon solution heat treatment,  $\beta$ -iron intermetallics undergo dissolution and fragmentation, which leads to an improvement in the mechanical properties.

From their studies, Narayanan *et al.*<sup>60</sup> concluded that with increasing solution temperature, the  $\beta$ -iron phase platelets dissolve slowly through concurrent fragmentation along plate widths and dissolution at the platelet tips; that solution temperature plays a much more important role in the dissolution of iron intermetallics than does solution time; and that the thinner and shorter the  $\beta$ -iron phase platelets, the faster the fragmentation and dissolution process.

An explanation of the mechanism of  $\beta$ -Al<sub>5</sub>FeSi phase dissolution as proposed by them is shown in Figure 2.13. The solubility of Fe and Si in the matrix is larger at points such as crevice locations (A) or the tips (B), than at the flat face of the platelets. During high temperature treatment, mass transport of solute occurs from areas of high energy. The diffusion of solute atoms and matrix atoms at locations A and B will lead to dissolution of the  $\beta$ -phase platelets, causing fragmentation at these points.

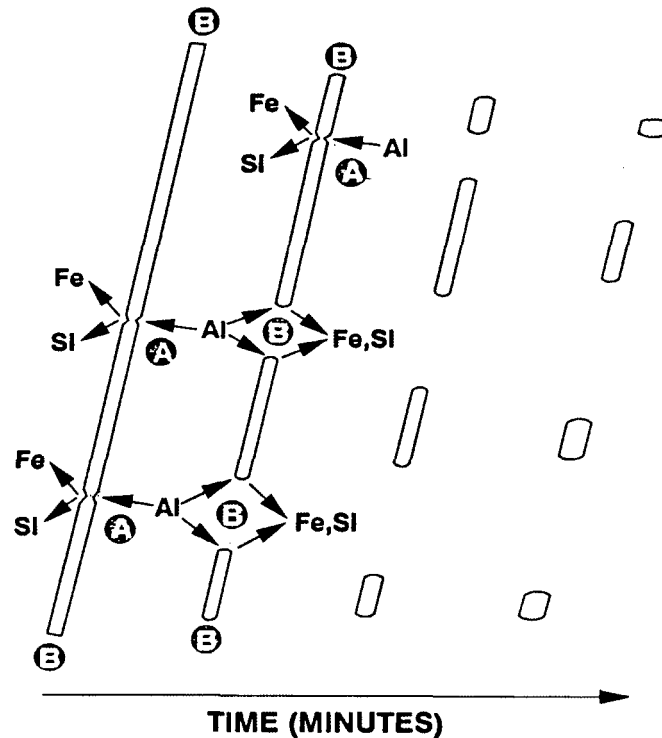
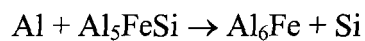


**Figure 2.13** Schematic illustration of the mechanism of  $\beta$ - $\text{Al}_5\text{FeSi}$  phase fragmentation and dissolution.<sup>60</sup>

Villeneuve and Samuel<sup>62</sup> further investigated the fragmentation and dissolution of the  $\beta$ - $\text{Al}_5\text{FeSi}$  phase during the solution heat treatment of Al-13%Si-Fe alloys. They found that the presence of a sufficiently high concentration of Sr (~350 ppm) leads to a breakdown of the  $\beta$ - $\text{Al}_5\text{FeSi}$  platelets/needles into small thin fragments via two mechanisms : a) splitting of the needles into two halves through the formation of longitudinal cracks, enhanced to a great extent by the brittle nature of the  $\beta$ -phase, and b) fragmentation of the needles, due to Si rejection, the rejection of Fe and Si from the  $\beta$ - $\text{Al}_5\text{FeSi}$  being enhanced by the presence of crevices at the needles edges.

Solution heat treatment was found to accelerate the dissolution of the  $\beta$ -iron phase, with a minimum  $\beta$ -needle length being achieved after 30 h at 540°C in the unmodified alloys, and after 10 h in the Sr-modified alloys. Dissolution of the  $\beta$ -iron phase occurred by the decomposition of  $\text{Al}_5\text{FeSi}$  into  $\text{Al}_6\text{Fe}$  and Si as follows:



A schematic representation of the decomposition mechanism is shown in Figure 2.14.

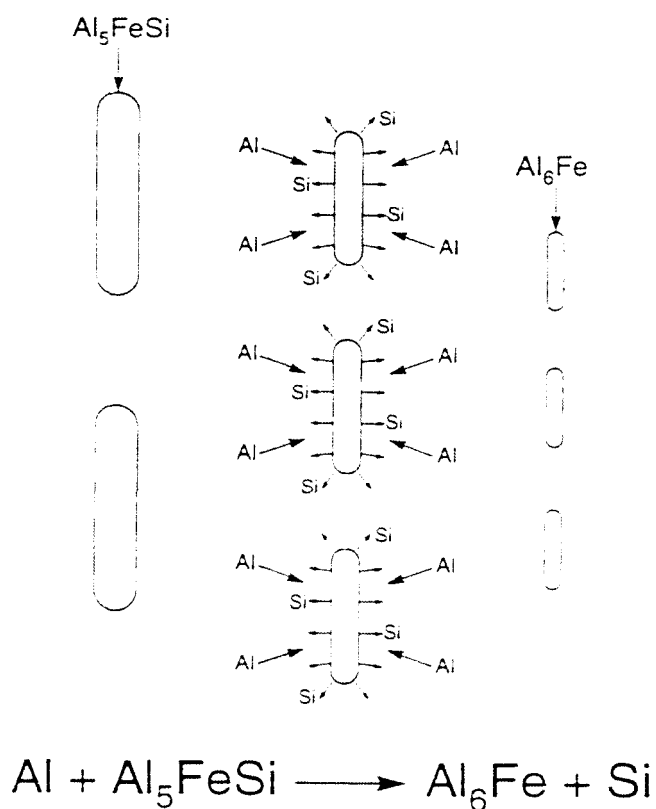


**Figure 2.14** Schematic representation of  $\beta$ - $\text{Al}_5\text{FeSi}$  decomposition during solution heat treatment.<sup>62</sup>

### 2.5.1.2 The $\alpha$ -Al<sub>15</sub>(Mn,Fe)<sub>3</sub>Si<sub>2</sub> iron intermetallic

The ternary  $\alpha$ -Al<sub>15</sub>(Mn,Fe)<sub>3</sub>Si<sub>2</sub> phase has a cubic symmetry with a chemical composition of 31.9% iron, 5.57% silicon and 62.4% aluminum. It possesses a hexagonal structure (parameters  $a = 12.3\text{\AA}$ ,  $c = 26.3\text{\AA}$ ), and has a density of  $3.58\text{ g/cm}^3$ . Under the optical microscope, this phase is light grey in color, and appears in the form of Chinese script particles.

The  $\alpha$ -AlFeSi phase shows an irregular, curved crystal growth, conforming to the complicated shape of the interdendritic spaces during solidification. The form of the  $\alpha$ -iron phase particles is controlled by the temperature gradient and by the diffusion of atoms in the liquid melt. During crystallization, atoms can add on to the solidified part of the  $\alpha$ -iron phase particles when they arrive at the solid/liquid interface. This type of growth occurs at high driving forces of solidification or rapid cooling rates, *i.e.*, at high undercooling,  $\Delta T$ . The  $\alpha$ -iron phase, due to its compact morphology, is considered less detrimental to mechanical properties compared to the  $\beta$ -iron phase.

### 2.5.1.3 The $\alpha$ -Al<sub>15</sub>(Fe, Mn, Cr)<sub>3</sub>Si<sub>2</sub> iron intermetallic (Sludge)

Iron, manganese and chromium tend to segregate at the bottom of aluminum melting and holding furnaces and form solid particles of  $\alpha$ -Al<sub>15</sub>(Fe,Mn,Cr)<sub>3</sub>Si<sub>2</sub>, or what is popularly known as “sludge” in die casting operations. The high Fe content and low holding temperature of die casting alloys make furnace sludge. This sludge is denser than molten aluminum and can be washed into castings and result in the formation of hard spots that are detrimental to machinability.<sup>63</sup>

The tendency of a molten alloy to form sludge can be predicted by the holding temperature and its “sludge factor”, an empirical formula, which serves as a guide, but not as a guarantee, to avoid sludging.<sup>64</sup> This factor is obtained by merely adding the percentages of Fe-Mn-Cr as follows:

$$\text{Sludge Factor} = (\% \text{Fe}) + 2 \times (\% \text{Mn}) + 3 \times (\% \text{Cr})$$

A sludge factor of 1.8 will normally not result in sludge formation if a casting temperature for die casting alloys of 650°C or more is maintained. However, if the holding temperature is below this range, a sludge factor of 1.4 or less may be required.<sup>65</sup>

Shabestari and Gruzleski<sup>54</sup> observed that holding an Al-12.7%Si melt at temperatures of 800-850°C for 1.5 hr was sufficient to dissolve the intermetallics completely. When the sludge dissolved at 850°C, it did not reform until a certain characteristic temperature of the alloy. The sludge was thermodynamically unstable at temperatures above this value, and the temperature of sludge formation increased when the content of iron in the alloy was increased.

The shape of the sludge formed was mostly star-like or exploded, and the intermetallics were often found within primary aluminum dendrites.<sup>54</sup> This may be explained as follows. The intermetallics which form at high temperatures consume some of the silicon present in the alloy, and shift the local chemical composition of the melt to the aluminum side of the phase diagram, with the result that primary aluminum dendrites form around the intermetallics.

### 2.5.2 Role of Alloying Elements

It has been well established that the addition of certain alloying elements such as Mn, Cr, Ni and Co can change the morphology of iron intermetallics from the deleterious plate-like morphology of the  $\beta$ -iron phase to the less harmful Chinese script morphology of the  $\alpha$ -iron phase.<sup>66</sup>

Manganese is present as an impurity in commercial Al-Si alloys and it is the most common alloying addition which is used to modify the morphology and type of the intermetallic phase. Moldolfo<sup>61</sup> has stated that manganese is the best all round addition for iron correction when compared to Cr, Ni, Co and Mo. According to ANSI/ASTM specifications, if the Fe content exceeds 0.45%, it is desirable to have Mn present in an amount equal to one half of the Fe content.<sup>56</sup> Manganese is added to the melt to promote the formation of  $\text{Al}_{15}(\text{Mn,Fe})_3\text{Si}_2$  ( $\alpha$ -iron phase). This phase has a compact morphology, which does not initiate cracks in the cast material to the same extent as does the  $\text{Al}_5\text{FeSi}$  ( $\beta$ -iron) phase.

Villeneuve<sup>67</sup> reported that in an Mn/Fe ratio of  $\sim 0.7$  in a 1.5% Fe-1.01% Mn-containing A319.2 alloy, most of the iron precipitates in the form of the  $\alpha$ - $\text{Al}_{15}(\text{Fe,Mn})_3\text{Si}_2$  Chinese script phase. Its irregular faces facilitate the motion of liquid metal, and hence, a lesser amount of porosity is observed. Colwell and Kissling<sup>68</sup> showed that Mn addition (Mn/Fe  $\sim 1:2$ ) can eliminate the formation of the  $\beta$ -iron phase to a large extent, and thus provide better alloy mechanical properties and castability.

Besides manganese additions, Cr, Mo, Co, Be and Ca have also been employed to alter the  $\beta$ -iron phase morphology. Beryllium in trace additions is found to be beneficial as it completely neutralizes the detrimental effect of iron on mechanical properties: even at iron levels in excess of the specified maximum limit of 0.5-0.6% in the alloy, hardness, tensile strength, yield strength, ductility, and fracture toughness are all seen to remain almost unchanged.<sup>69</sup> This kind of behavior has been observed even at varying solidification rates.

The improved mechanical properties of the beryllium-added Al-Si-Mg alloy with high iron impurities can be attributed to the altered shape of the Be-Fe plate-like phase in the form of polygonal or Chinese script particles, and also their location.<sup>70,71</sup> Other researchers,<sup>72,73</sup> too, have reported that in Al-Si-Mg alloys, the addition of beryllium will transform the  $\beta$ -plates into  $\alpha$ -Chinese script particles or to equiaxed crystals and/or spheroids, thus improving tensile strength and ductility even at a high Fe level.

Couture<sup>50</sup> reviewed the effect of iron impurities in aluminum cast alloys. In a detailed study of Al-13Si alloy with 0.5-1.5% Fe, the addition of 0.6% Mn produced a compact phase that was less harmful to strength and ductility than the  $\beta$ -phase. A star-shaped phase was also observed when Mo was added to Fe-contaminated Al-Si alloys.

Zednik<sup>74</sup> reported that the addition of 0.44% Co or 0.41% Mn to Al-9.1Si-0.22Mg-0.4Fe alloy produced Chinese script particles instead of the  $\beta$ -phase platelets. He also observed that the Co addition resulted in higher ductility than the Mn addition.

Magnesium is used extensively in Al-Si alloys to improve the mechanical properties through the precipitation of  $Mg_2Si$ . Samuel *et al.*<sup>75</sup> showed that the addition of Mg to

molten 319 type alloys, in amounts up to 0.5 wt pct, leads to the precipitation of  $Mg_2Si$  (or a Mg-rich) phase that appears in the form of rounded black particles dotted along the sides of the eutectic Si particles. Noticeable fragmentation of the eutectic Si (*i.e.* its modification), and transformation of a large proportion of the  $\beta$ - $Al_5FeSi$  needle-like/platelet phase into a Chinese script-like phase with a composition close to  $Al_8Mg_3FeSi_6$  is also observed.

### 2.5.3 Effect of Cooling Rate

Solidification or cooling rates directly, or indirectly, affect almost all microstructural parameters, including the amount of intermetallics observed in the microstructure. The cooling rate has a direct impact on equilibrium kinetics and the quantities of Fe present in the microstructure. A low cooling rate favours the precipitation of the  $\beta$ -iron  $Al_5FeSi$  phase. Rapid solidification favours the crystallization of the iron compound as the  $\alpha$ -iron phase rather than the  $\beta$ -iron phase.

Nnarayanan *et al.*<sup>2</sup> found that if the total undercooling, *i.e.*, the sum of the nucleation undercooling ( $\Delta T_N$ ) and the growth undercooling ( $\Delta T_G$ ), is greater than a certain critical value ( $\Delta T_C$ ), the  $\alpha$  phases will crystallize. The reverse is also true with the  $\beta$  phase forming below the critical total undercooling. With increasing cooling rate and increasing melt superheating temperature, the  $\beta$  phase start temperature decreases until it merges with the silicon eutectic temperature. At this point, the chemical composition of the remaining liquid favors the crystallization of the  $\alpha$  phase.

At low cooling rates, the  $\text{Al}_5\text{FeSi}$  needles are coarse and concentrated at grain boundaries, where they promote a brittle fracture. At higher cooling rates,  $\text{Al}_5\text{FeSi}$  particles are quite small and interspersed more uniformly. This view is also supported by Samuel *et al.*,<sup>76</sup> who found that strong linear relationships were obtained between dendrite arm spacing (DAS) and the average  $\beta$ -platelet length for alloy Fe levels ranging from 0.5 to 1.5 wt%. In an earlier study, Samuel *et al.*<sup>59</sup> also reported that the cooling rate influences both the formation and size of the  $\beta$ -platelets in the alloy, with hardly any  $\beta$ -platelets being observed in the microstructure obtained at the highest cooling rate (corresponding to a dendrite arm spacing value of  $15\mu\text{m}$ ). As the cooling rate decreases, the  $\beta$ -platelets are observed in relative abundance.

Shabestari *et al.*<sup>54</sup> reported that the morphology and volume fraction of all types of intermetallics are dependent on the cooling rate, the volume fraction increasing significantly with decreasing cooling rate. However, while the total volume percent of intermetallics increases, the number of particles of each phase per unit area decreases, as the size of the particle type increases. A fast cooling rate and manganese addition can change the brittle  $\beta$ -iron phase platelets into very small star-like compounds.

#### **2.5.4 Sr Addition**

Although strontium is mainly added to Al-Si casting alloys to modify the eutectic silicon, it also has a “modifying” effect on the iron intermetallics present in the alloy. Samuel *et al.*<sup>59</sup> found that the beneficial effect of Sr modification was manifested through its influence on the fragmentation and dissolution of the  $\beta$ - $\text{Al}_5\text{FeSi}$  needles. The strontium

was observed to "poison" the sites where "sympathetic nucleation" of the  $\beta$ -iron needles occurred. Sympathetic nucleation of the  $\beta$ -needles, as reported by the authors, was observed in the unmodified alloy at low cooling rates, which resulted in large  $\beta$ -iron entities (comprising several branched segments). The addition of strontium vastly reduced the phenomenon of sympathetic nucleation, through its poisoning action on the  $\beta$ -needle nucleation sites, reducing the number of sites available for nucleation. Consequently, the  $\beta$ -iron phase precipitated at a smaller number of sites, resulting in the precipitation of needles that were larger compared to those in the unmodified alloy.

Strontium was also found to accelerate the dissolution process, with individual  $\beta$ -needle segments breaking up into two or more fragments. The dissolution effect was seen to accelerate as the strontium level increased. The optical micrographs of Figure 2.15 show these effects.<sup>59</sup>

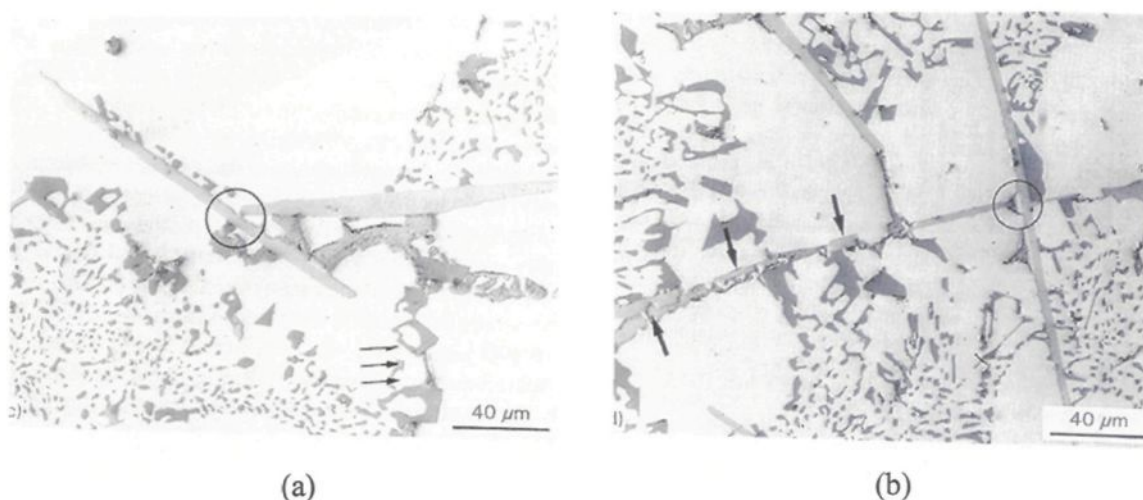


**Figure 2.15** Optical micrographs showing (a) how strontium poisons the link between a parent and branching  $\text{Al}_5\text{FeSi}$  needle, and (b) the poisoning and dissolution/fragmentation effect of strontium on the  $\beta$ -needles.<sup>59</sup>

In the another study, Samuel *et al.*<sup>75</sup> found that the addition of Sr, in the amount of 0.02 to 0.04 wt pct, apart from full modification of the eutectic Si, leads to the dissolution of more than two-thirds of the  $\beta$  needles in the alloy matrix and the modification of the  $\text{Mg}_2\text{Si}$  particles. However, the addition of Sr does not cause nucleation of the star-like  $\text{Al}_{15}(\text{Fe},\text{Mn},\text{Cr})_3\text{Si}_2$  phase through transformation of the  $\beta$ - $\text{Al}_5\text{FeSi}$  needles.

Morris *et al.*<sup>77</sup> have reported that the addition of Sr and/or Ca in a total amount of ~0.01-0.5% to a homogenized aluminum-magnesium-silicide extrusion alloy ingot containing  $\beta$ - $\text{AlFeSi}$ , transforms a major proportion of the  $\beta$ -iron phase in the ingot into the  $\alpha$ -iron phase, thereby reducing the formation of pickup upon extrusion of the ingot.

Pucella *et al.*<sup>78</sup> have pointed out that, for an Mn-free Al-11.5% Si alloy, Sr causes i) fragmentation of the  $\beta$ - $\text{Al}_5\text{FeSi}$  phase needles, ii) splitting along their lengths, and iii) the rejection of Si from the  $\beta$ -needles. This mechanism is independent of the pouring temperature or cooling rate. For the Mn-containing alloy ( $\text{Mn}/\text{Fe} \approx 0.4$ ), at a low cooling rate ( $\text{DAS} \sim 45\mu\text{m}$ ) and 720°C pouring temperature, Sr tends to transform the co-eutectic  $\alpha$ - $\text{Al}_{15}(\text{Fe},\text{Mn},\text{Cr})_3\text{Si}_2$  script phase observed in the non-modified alloy into a coarse, pre-dendrite script phase that forms with the  $\alpha$ -Al dendrites, and possesses a relatively high Fe content. Increasing the cooling rate ( $\text{DAS} \sim 15\mu\text{m}$ ) also leads to the formation of the coarse  $\alpha$ -script phase.

Modification of iron intermetallics by strontium in 413 aluminum alloys was also studied by Shabestari and Gruzleski.<sup>79</sup> They concluded that strontium is a very effective element in the modification of intermetallics in aluminum casting alloys. Strontium

additions to 413 alloy in the case of permanent-mold castings caused reductions of 45% in the size of intermetallics (sludge), 80% in the number of intermetallics per unit area, and 92% in the total volume percent of intermetallic compounds observed. In the simulated sand-cast condition, Sr caused the fragmentation of the  $\beta$ -iron phase and reductions of 54% in the length, 43% in the width, and 47% in the volume percent of the  $\beta$ -iron phase. At the same time, an increase in the  $\alpha$ -iron phase was observed.

## 2.6 POROSITY

The presence of porosity - inevitable to a certain extent in any casting - can be detrimental, particularly in terms of surface quality and corrosion resistance. Sometimes, commercial aluminum foundries have serious problems of porosity in low-pressure and gravity die castings that normally cast well and have a low reject rate.

Porosity in aluminum alloy castings occurs because of the rejection of gas from the liquid metal during solidification and/or the inability of the latter to feed through the interdendritic regions to compensate for the volume shrinkage associated with the solidification. Hydrogen is the only gas capable of dissolving to a significant extent in molten aluminum, resulting in outgassing, which leads to the formation of porosity.<sup>80,81,82,83,84</sup> The solubility of hydrogen in aluminum and its alloys is strongly dependent on the temperature, as shown in Figure 2.16.<sup>85</sup>

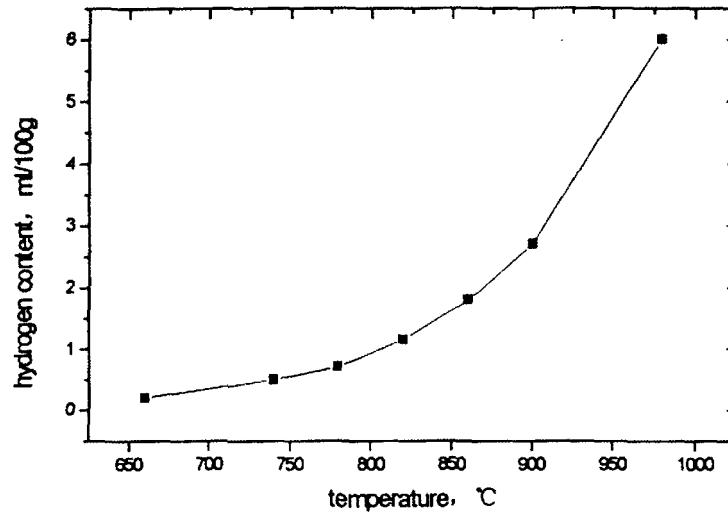


**Figure 2.16** Variation of hydrogen solubility in aluminum melts with different temperatures.<sup>85</sup>

Porosity in aluminum alloys is classified into two kinds: i) macroporosity (~1 to 10 mm), which is mainly comprised of massive shrinkage cavities, and occurs in long-freezing range alloys, caused by failure to compensate for solidification shrinkage, and ii) microporosity (~1 to 500 $\mu$ m), distributed more or less homogeneously, due to the failure to feed interdendritic regions, and the precipitation of dissolved gases (*i.e.*, gas porosity).<sup>86</sup> The latter is known to significantly influence mechanical properties and is a consequence of several interacting alloy and process parameters and/or design factors, such as local thermal conditions, feeding capacity, and applied pressure.<sup>87</sup>

Apart from the hydrogen concentration in the melt, formation of porosity is also influenced by other factors such as the Sr modification and grain refining melt treatments normally applied to Al-Si alloys, the inclusion content of the melt, as well as other minor element additions made to the melt. Grain refinement can lead to a finer dispersion of, and,

in some cases, a reduction in the amount of porosity. Inclusions, including refractory materials, furnace oxides, dross, *etc.* can be of a liquid or solid type in nature, and their presence often leads to increased porosity, poor surface quality, and a drastic reduction in the mechanical properties.

### 2.6.1 Theory of Porosity Formation

As mentioned previously, porosity formation is the result of two mechanisms:

- i) Shrinkage, resulting from the volume decrease accompanying solidification. Limited or inadequate liquid metal feeding in the dendrite solidification area gives rise to shrinkage. This type of porosity can also occur as “microshrinkage” or “microporosity”, dispersed in the interstices of dendritic solidification regions.
- ii) Gas porosity, which occurs as a consequence of the large reduction in the solubility of hydrogen in aluminum during solidification.

Figure 2.17<sup>88</sup> shows an example of a pore composed of a shrinkage pore and a gas pore.

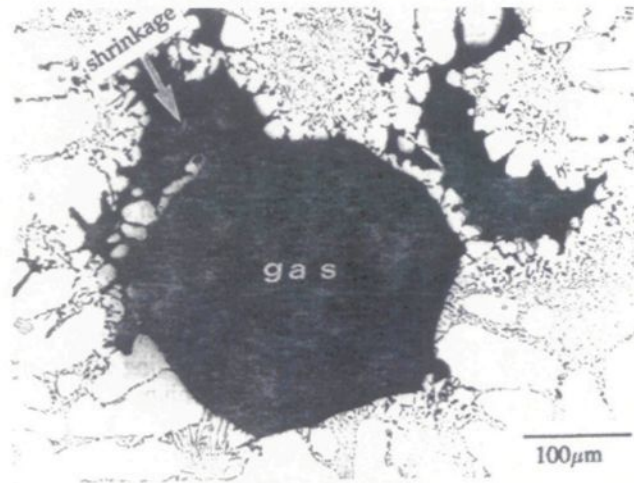


**Figure 2.17** A shrinkage pore and a gas pore merged together to form a single pore in an Al-9 wt% Si-3 wt% Cu alloy.<sup>88</sup>

According to Campbell,<sup>89</sup> the growth tendency of pores is described generically by the following equation:

$$P_g + P_s > P_{atm} + P_H + P_{s-t} \quad (2.1)$$

where  $P_g$  = equilibrium pressure of dissolved gases in the melt;

$P_s$  = pressure drop due to shrinkage;

$P_{atm}$  = pressure of the atmosphere over the system;

$P_H$  = pressure due to the metallostatic head;

$P_{s-t}$  = pressure due to surface tension at the pore/liquid interface.

The dissolved gas pressure  $P_g$  is the major driving force in forming porosity. The solubility of hydrogen, the gas most responsible for microporosity in aluminum and its alloys, decreases by a factor of thirty-five during the solidification process.  $P_s$  is also a significant driving force. In the absence of an appreciable amount of dissolved gas, trapped

eutectic liquid solidifying within an already existing dendrite network will contract. Since the liquid occupies a larger volume than the solid, this contraction will lead to microshrinkage in the interdendritic regions. These two pressures can also act synergistically to form pores within the interdendritic regions that are neither solely due to gas evolution nor due to shrinkage, as demonstrated by Figure 2.17.

For a particular casting design,  $P_{atm}$  and  $P_H$  are constant, and a decrease in  $P_{s-t}$ , as observed for modifiers like sodium or strontium, can lead to an increased probability of pore formation.

The pore growth process has been depicted schematically by Kubo and Pehlke<sup>90</sup> as shown in Figure 2.18. As can be seen, the gas porosity nucleates at the base of the dendrite arms.

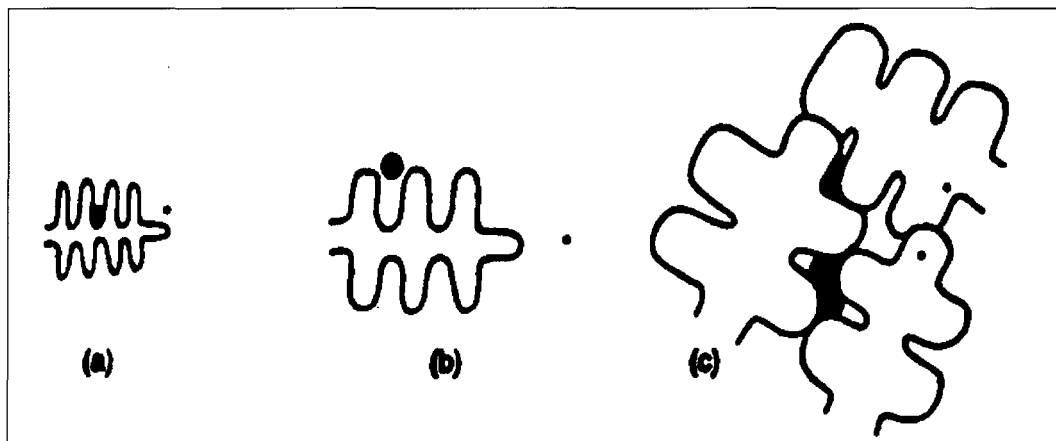


**Figure 2.18** The growth process of porosity formation.<sup>90</sup>

The synergism between the shrinkage and gas porosities overcomes the large negative free energy required to form a gas-metal surface, facilitating the nucleation shown in Figure 2.18(a). As solidification proceeds, the porosity grows due to the increased

potential for gas evolution. The radius of the porosity becomes large enough to decrease the contribution of interfacial energies, and the porosity detaches from the dendrites, as shown in Figure 2.18(b). At a still further stage of solidification, neighbouring dendrites collide, making interdendritic feeding difficult. At this stage, the porosity is thought to grow to compensate for solidification shrinkage, as shown in Figure 2.18(c).

Zou *et al.*<sup>91</sup> studied microporosity formation in A356.2 casting alloys and found that the pore density is essentially constant for various hydrogen concentrations, while the pore size and amount of porosity increase with the initial hydrogen content in the melt.

Shivkumar *et al.*<sup>92</sup> summarized the logical stages of pore formation as follows:

- i) Gradual enrichment of the liquid by hydrogen;
- ii) Nucleation of pore(s);
- iii) Instantaneous growth of the pores;
- iv) Gradual increase in pore size; and
- v) End of solidification.

### 2.6.2 Role of Hydrogen

Hydrogen is an important impurity component in aluminum and its alloys, which has to be controlled carefully in casting and working processes.<sup>93</sup> There are many potential sources of hydrogen in aluminum, including the furnace atmosphere, charge materials, fluxes, external components, and reactions between the molten metal and the mold.

Hydrogen is the only gas capable of dissolving to a significant extent in molten aluminum, while exhibiting very low solubility in the solid state.<sup>94</sup> Most of the absorbed

hydrogen is released during solidification and, if unable to escape from the solidifying metal, results in the formation of gas porosity. In general, hydrogen which finds its way into molten aluminum comes from the dissociation of water vapour at the surface of the liquid aluminum according to the reaction :



Hydrogen precipitation takes place according to the following sequence :

- i) diffusion of hydrogen atoms with the liquid pool;
- ii) formation of subcritical nuclei as a function of time and cooling;
- iii) random emergence of stable precipitates exceeding the critical size required for sustained growth; and
- iv) continued growth of the precipitated phase as long as hydrogen atoms are free to diffuse to the melt/bubble interface.<sup>95</sup>

The schematic representation of Figure 2.19 shows how the formation, growth and stabilization of hydrogen gas bubbles (nucleation sites) control porosity development during solidification.

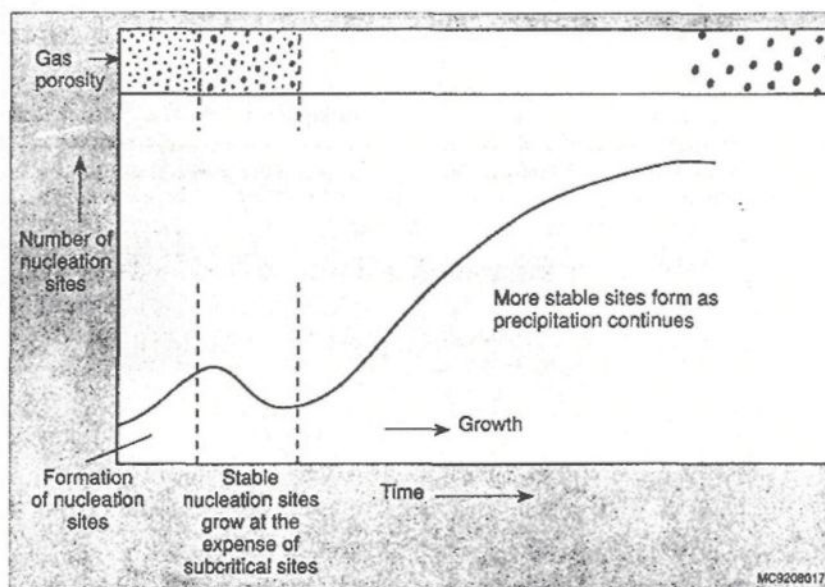


**Figure 2.19** Effect of nucleation sites on porosity development.<sup>95</sup>

Thomas and Gruzleski<sup>96</sup> established that, for any given alloy and specific solidification condition, there is a “threshold hydrogen content” below which no primary porosity is formed, and that the tendency for porosity formation is reduced with an increase in cooling rate and a decrease in the freezing range of the alloy, especially under directional solidification conditions.. Also, for hydrogen contents above the threshold value, there is approximately a linear relation between hydrogen and pore volume fraction.

Fang and Anyalebechi<sup>97</sup> also showed that, regardless of the composition or defined solidification condition, a critical or threshold dissolved hydrogen level must be exceeded for hydrogen porosity to occur. For any specific cooling rate, the pore volume fraction and pore size decline with decreased hydrogen content above the threshold value, and for a given alloy and hydrogen content, the pore volume fraction decreases with the cooling rate, as shown in Figure 2.20.<sup>97</sup>

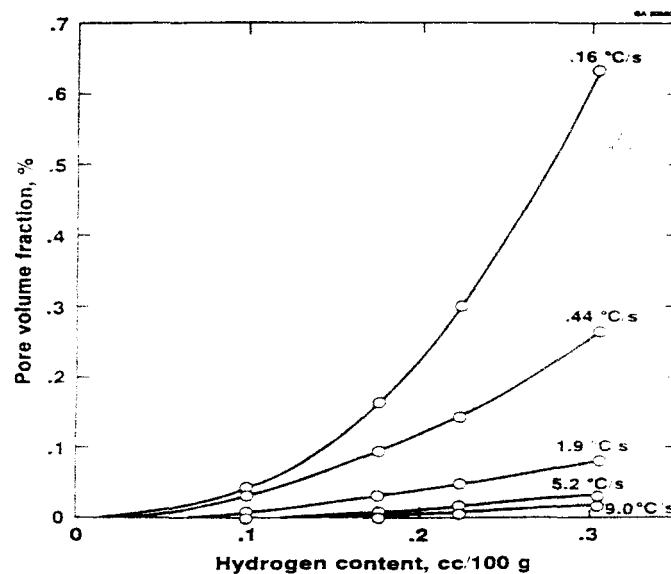


**Figure 2.20** As hydrogen concentrations decrease above the threshold value for grain refined Al-4.7 Mg alloy, the pore volume fractions also decrease.<sup>97</sup>

Kao *et al.*<sup>98</sup> studied the effect of hydrogen content on the soundness of A356 alloy plate castings, and found that the porosity content is independent of the thermal index,  $G^{0.38}/V_s^{1.62}$ , but is dependent on the hydrogen content when the index is larger than  $0.6K^{0.4}s^{1.6}/mm^2$  (where  $G$  is the thermal gradient and  $V_s$  is the solidus velocity). At a lower value, the porosity content is synergetically affected by the hydrogen content and the local pressure drop, due to fluid flow between the dendrites.

### 2.6.3 Role of Alloying Elements and Inclusions

According to Roy *et al.*,<sup>99</sup> not all alloying elements contribute to porosity formation in Al-Si-Cu base alloy systems. A number of these elements, *e.g.*, magnesium, titanium and phosphorus, result in reducing both the pore size and density. Grain refining reduces

pore density and sizes, and results in a fine dispersion of the pores throughout the alloy matrix.

Tynelius<sup>100</sup> studied the microporosity evolution in A356 alloy using a tapered wedge mold, and showed that the morphology of the solid-liquid interface and the resulting microstructure determined the pore morphology. The pores were found to be present in the grain boundaries. Grain refiner addition decreased the grain size, thus decreasing the maximum pore length, in keeping with the shorter grain facets. Area percent porosity and areal pore density increased with the grain refiner addition, while the maximum pore area remained unchanged. From these observations, it was concluded that the TiB<sub>2</sub> grain refiner particles provided nucleation sites for pores, without influencing interfacial tension, where the latter parameter controlled the pore size.

Inclusions in the melt offer heterogeneous sites for pore nucleation and thus promote porosity formation. Several types of inclusions may be present in the melt, including furnace dross, salts, oxides and refractories.

Chen and Gruzleski<sup>101</sup> studied the influence of melt cleanliness on pore formation in Al-Si alloys, and found that at the same hydrogen level, with an increased inclusion concentration, the density of reduced pressure samples decreased, while the amount of porosity and the number of pores increased. This trend was confirmed in both 356 and 319 aluminum alloys over a wide range of hydrogen levels. They also observed that with an increased dirt level, the number of pores increased and the pore shape became more rounded. Filtration, using ceramic foam filters, was seen to have a beneficial effect in

terms of reducing the porosity, particularly in dirty metals (*i.e.*, those containing a large amount of inclusions).

#### **2.6.4 Role of Sr Modification**

Modification in Al-Si alloys is a process where Na or Sr is added to the melt for the purpose of altering the shape of the eutectic Si from an acicular one to a fibrous one, in order to improve the mechanical properties. While Sr is commonly employed, a common concern is the apparent increase in porosity in modified castings, which can negate, to some extent, the benefits of modification. The influence of modification on porosity is a matter of considerable debate, arising mainly from the controversy over the behavior of Sr as a modifier.<sup>102,103,104</sup>

Several explanations have been put forward for the effect of Sr on porosity. The depression of the eutectic temperature (about 4-10°C) observed upon addition of the modifier to the melt, will lead to an extension of the freezing range of the alloy and an increase in the solidification time, and thus affect the eutectic solidification. An altering of the alloy properties, particularly in terms of the reduction of the liquid-gas interfacial energy and an increase in the volumetric shrinkage, is also proposed, as is an increase in the hydrogen concentration of the melt due to a change in either the rate at which hydrogen is absorbed into the melt or its solubility. At a constant external pressure, the higher the hydrogen concentration, the earlier the bubbles will precipitate and the faster they will grow. Thus, at high hydrogen concentrations, bubbles will be formed in the early stages of solidification.

Yet another explanation relates to the effect of strontium on the formation of oxides, increasing the oxide concentration in the melt and/or the ability of the oxides to nucleate pores, as has been found in the present study and will be discussed in detail in Chapter 6.

Bian and co-workers<sup>105</sup> also studied the effect of strontium modification on the hydrogen content and pore shape in Al-Si alloys, and found that Sr addition markedly increases the hydrogen content in the Al-Si melts and accelerates the gassing rate of the melt. They concluded that Sr-containing oxide films ( $\text{SrO}\cdot\text{Al}_2\text{O}_3$ ) are less protective than pure alumina ( $\text{Al}_2\text{O}_3$ ), and are responsible for the more rapid gas pick-up in modified alloys. They also observed that the pore shape in unmodified samples was long, fissured, irregular and rough, whereas in modified samples, the pore shape was rounded, regular and smooth.

Nouruzi<sup>94</sup> reported that there are two possible reasons that Sr may cause porosity, either solely or in combination: i) strontium forms oxide inclusions, which promote pore formation; and ii) strontium can lower the surface tension of the Al-Si alloy melt - this effect would facilitate pore nucleation and may result in increased porosity in modified alloys.

Lee and Sridhar<sup>106</sup> studied the effect of strontium on porosity formation during the solidification of Al-Si alloys using an *in-situ* X-ray temperature gradient stage (XTGS) technique to directly observe the effect. From their observations, they concluded that the addition of Sr depresses the eutectic temperature, increasing the time for pore growth. However, the addition of strontium also reduces the initial growth rate of pores, giving no significant net effect upon the final pore size. The addition of strontium leads to the

formation of large, spherical bubbles that remain stable in the casting near the oxide skin at a temperature above the liquidus.

On investigating the effect of hydrogen on the shrinkage porosity of Al-Si alloys, Shahani<sup>107</sup> found that the addition of Sr actually reduced the gas content but, however, increased the porosity of the modified casting. According to him, the amount of shrinkage porosity in castings would be determined by the gas content, the pressure drop caused by shrinkage, and the foreign particles present in the melt. Modifiers would tend to promote this type of porosity, facilitating the nucleation of pores by reducing surface tension or by acting as nucleants.

Argo and Gruzleski<sup>108</sup> have observed that micropores in modified alloys are larger, because the interdendritic feeding distance is relatively long as a result of the depression of the eutectic transformation temperature by the modification process. The longer mushy zone makes feeding more difficult and the possibility of larger isolated pockets of eutectic liquid being trapped in the interdendritic regions more likely. This results in widely dispersed isolated solidified cells which then proceed to freeze independently with a regular solid/liquid interface; thus, the pores are large and relatively isolated with each pore surrounded by sound material. In unmodified alloys, the eutectic exhibits an irregular solid/liquid interface, because of which small pockets of liquid are entrapped between advancing solidification fronts, resulting in fine concentrated microporosity, as shown in Figure 2.21(a). In modified alloys, a regular or planar interface results in a more widely dispersed and larger porosity, as shown in Figure 2.21(b).<sup>108</sup>

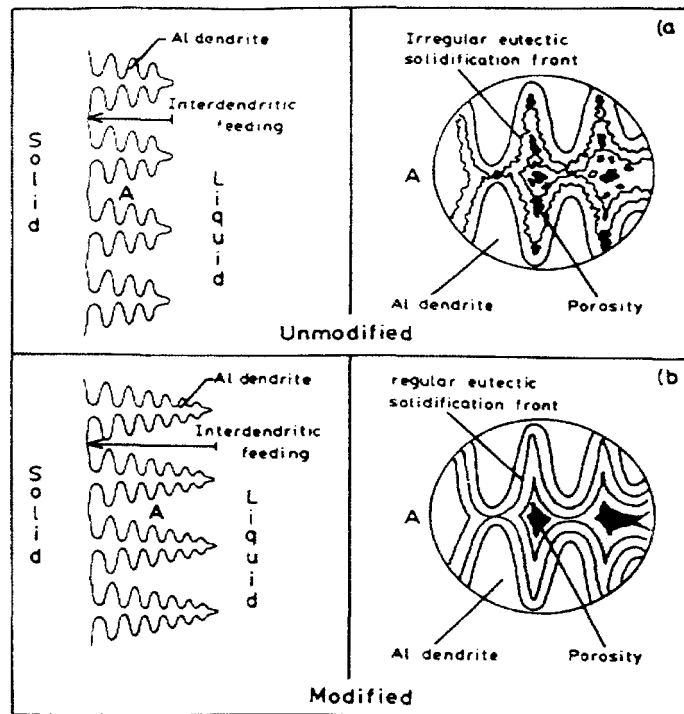


**Figure 2.21** The two-stage solidification process proposed by Argo and Gruzleski,<sup>108</sup> showing microshrinkage formation in: a) an unmodified casting (short interdendritic feeding distance and irregular eutectic solidification front), and b) a modified casting (long interdendritic feeding distance and regular eutectic solidification front).

McDonald *et al.*<sup>109</sup> studied eutectic solidification and porosity formation in Al-Si alloys in terms of the presence of Sr, and found that porosity characteristics changed in the presence of low levels of Sr, consistent with values expected from contaminated charge materials or melting equipment, that the addition of Sr changed the porosity from localized connected regions to dispersed isolated pores, and that there is a strong orientation relationship between aluminum in the eutectic and the surrounding aluminum dendrites in unmodified and overmodified (Sr) alloys, which does not exist in the case of well-modified alloys. The porosity distribution underwent a corresponding transition, from localized to

dispersed and back to localized, as Sr levels and the degree of modification changed. This was proposed as being related to changes in the permeability of the mushy zone for the different eutectic solidification modes.

### 2.6.5 Role of Iron Intermetallics

Iron is known to cause porosity and shrinkage defects in Al-Si-based casting alloys. It has been suggested that the plate-like  $\beta$ -Al<sub>5</sub>FeSi iron intermetallic phase is the primary cause of this porosity.<sup>12</sup> To date, there are only two basic mechanisms that have been suggested in the literature:

12. *The restricted feeding theory*, originally proposed by Mascré.<sup>12</sup> The  $\beta$ -iron platelets can form in the interdendritic channels during solidification, causing physical restrictions to the movement of the compensatory feed liquid. Consequently, regions undergoing shrinkage cannot be fed adequately and shrinkage porosity occurs; and
13. *The pore nucleation theory* by Roy *et al.*,<sup>88</sup> who observed that  $\beta$ -Al<sub>5</sub>FeSi platelets are very active sites for pore nucleation. Also, they limit the growth of both gas and shrinkage pores. They also found that the addition of Mn neutralizes the formation of the  $\beta$ -iron phase and hence, pore nucleation. The two Mn-containing iron compounds, *i.e.*, the  $\alpha$ -Chinese script Al<sub>15</sub>(Fe,Mn)<sub>3</sub>Si<sub>2</sub> iron phase and sludge, also limit pore growth and expansion.

Taylor and co-workers<sup>87,110,111</sup> studied the role of iron on porosity formation in Al-Si-Cu based casting alloys and found that the iron-porosity relationship is more complex than a simple incremental function based on the above two theories. In their work, they found that iron added deliberately to a commercial, unmodified, non-grain-refined Al-Si-Mg-Cu alloy causes a threefold porosity effect that is dependent on both the concentration of iron and the prevailing solidification conditions. The three aspects of the effect are as follows:

- i) The overall porosity level decreases with iron content until a minimum value occurs at 0.4 pct Fe. With further iron additions, the overall porosity level again increases.
- ii) A change in pore morphology from discrete isolated pores to spongy interdendritic pores occurs even with small, additions of iron. These spongy regions become increasingly connected as the iron content increases above 0.4 pct.
- iii) Under the poorest cooling and feeding conditions, increases in iron content above 0.4 pct lead to the development of a major, localized shrinkage defect.

Taylor *et al.*<sup>87</sup> explained the occurrence of a minimum in porosity at an intermediate iron level in terms of the solidification sequence: if solidification proceeds directly from primary dendrite formation to the ternary Al-Si- $\beta$ Al<sub>5</sub>FeSi eutectic, the porosity is minimized, and a highly localized defect can occur when solidification proceeds via the binary Al- $\beta$ Al<sub>5</sub>FeSi eutectic. They also found that the critical iron content at which the porosity was minimized was a function of the silicon content of the alloy. The iron and

silicon content of the alloy determine at which point during the solidification sequence the  $\beta$  phase appears and, therefore, when it can participate in the silicon nucleation event. At the critical iron composition, where the maximum possible amount of ternary eutectic forms, the alloy solidifies with the most open and permeable dendritic network and possibly, with the most mobile interdendritic feed liquid. As a consequence, feeding is optimized at these compositions and the lowest porosity values are obtained. At iron contents to either side of the critical iron value, there is a smaller proportion of ternary eutectic formation and, hence, porosity formation increases as the situation becomes dominated by the increasing amounts of either the Al-Si or Al- $\beta$  binary eutectic, both of which reduce permeability. The Al- $\beta$  is the more detrimental of the two eutectics, with the formation of major shrinkage porosity defects occurring more frequently and more severely as the proportion of the Al- $\beta$  eutectic increases.

**CHAPTER 3**  
**EXPERIMENTAL PROCEDURE**

## **CHAPTER 3**

### **EXPERIMENTAL PROCEDURE**

Details of the alloys and melt additives used, the general melting and casting procedures employed, and the various techniques used for microstructural characterization and phase identification, namely optical- and scanning electron microscopy, image analysis, thermal analysis and electron probe microanalysis (with EDX and WDS facilities) have been provided in this chapter. Alloy codes of samples that were examined, and which will be discussed in Chapters 4 and 5, have been collectively listed in Table 3.2 and should be referred to, to determine the specific alloy chemistry and/or condition corresponding to the microstructure under discussion. In those cases where additional alloys and/or experiments were used for certain parts of the study, the corresponding experimental details have been given in the chapter(s) concerned.

#### **3.1 ALLOYS, ADDITIVES AND MELTING PROCEDURES**

The chemical compositions of the base alloys that were used in the present study are shown in Table 3.1.

**Table 3.1** Chemical composition of the 319 and 356 base alloys used in the present work

Alloy	Element (wt%)								
	Si	Cu	Mg	Fe	Mn	Zn	Ti	Sr	Al
A319.2	6.06	2.98	0.002	0.12	0.023	0.006	0.007	0.0003	bal.
B319.2	6.22	3.21	0.40	0.15	0.026	0.0034	0.0075	--	bal.
A356.2	6.78	0.02	0.33	0.11	0.04	0.04	0.08	--	bal.

The 319 and 356.2 as-received alloys (in the form of 12.5 kg ingots) were cut into smaller pieces, cleaned, dried and melted in a 7-kg capacity SiC crucible, using an electrical resistance furnace. The melting temperature was kept at  $750 \pm 5^\circ\text{C}$ . The melts were degassed using pure dry argon injected into the melt by means of a graphite rotary degassing impeller. The degassing time/speed was kept constant at 30min/150rpm.

To the base alloys, iron additions were made using Al-25%Fe master alloy to achieve Fe levels of 0.12%, 0.2%, 0.4%, 0.6% and 0.8%, to study the amount of  $\beta\text{-Al}_5\text{FeSi}$  iron phase formed, and the effect on porosity as well as the eutectic Si particles at these different iron levels. For degassed melts (hydrogen level  $\sim 0.1$  mL/100g) and the five iron levels studied, 250 ppm Sr additions were made using Al-10%Sr master alloy, to compare modified vs unmodified structures.

### 3.2 CASTING PROCEDURES

Depending upon the objective, castings were carried out using (i) a refractory end-chilled mold, (ii) a preheated graphite mold, or else (iii) a cold metallic mold. The first provided directional solidification that allowed obtaining a range of dendrite arm spacings along the height of the casting block above the chill end. The hot graphite mold provided

close-to-equilibrium cooling conditions and allowed enough time for solidification and growth of the precipitating phases, which facilitated examination and phase identification using electron probe microanalysis. The cold metallic mold provided a much faster cooling rate ( $\sim 8^{\circ}\text{C/s}$ ). In addition, the last two mold configurations could also be used to conduct thermal analysis experiments simultaneously, to determine the various reactions taking place during solidification at the two respective cooling rates.

### **3.2.1 End-Chill Mold Casting – Directional Solidification**

A schematic diagram of the rectangular shaped end-chill mold (dimensions:  $64 \times 127 \times 254$  mm) is shown in Figure 3.1. In order to obtain directional solidification, the four walls of the mold are made of refractory material, and the bottom is a water-chilled copper base.

The molten metal was poured into the mold through ceramic foam filter discs fitted into the riser to avoid incident inclusions. The mold was preheated at  $150^{\circ}\text{C}$  to drive out moisture. The water (that circulates in the copper chill) was turned on the moment the liquid metal had half-filled the mold. Such an arrangement produced ingot blocks with solidification rates that decreased with increasing distance from the chill, resulting in microstructures that exhibited varying dendrite arm spacings, ranging from  $15\mu\text{m}$  to  $85\mu\text{m}$ , along the height of the cast block.

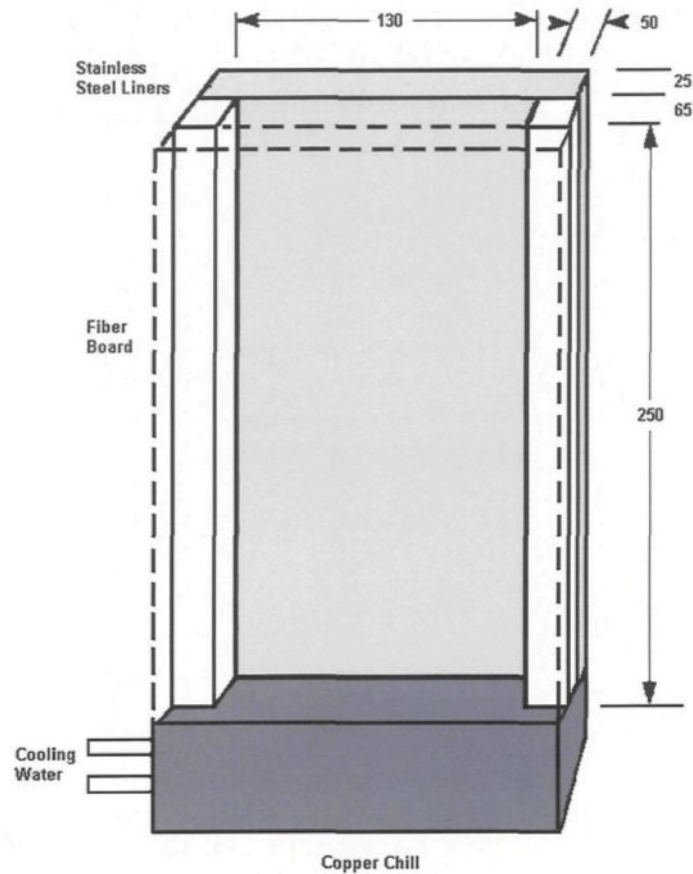


**Figure 3.1** Schematic diagram of the end-chilled mold used to prepare castings.

Table 3.2 shows the chemical compositions of the various alloys that were prepared, and their respective codes. With respect to the alloy codes, the prefix A represents the A319.2 alloy, B the 319.2 alloy (containing 0.4 wt% Mg), and C the A356.2 alloy. The letter F represents Fe, while the numbers 1, 2, 4, 6 and 8 correspond to Fe levels of 0.12%, 0.2%, 0.4%, 0.6% and 0.8%, respectively. Finally, the suffix S in any code implies that the alloy has been Sr-modified. Also, all rows in Table 3.2 corresponding to Sr-modified alloys have been given a light grey background, to distinguish them from the non-modified alloys.

**Table 3.2** Chemical composition of the various alloys used in the present work and their respective codes

Alloy Code	Element (wt%)									
	Si	Fe	Cu	Mn	Mg	Cr	B	Sr	Ti	Al
AF2	6.83	0.264	3.46	<0.00050	<0.00500	<0.00055	0.00152	<0.00013	0.003	89.4
AF2S	6.36	0.254	3.56	<0.00050	<0.00611	<0.00050	0.00161	0.0519	0.0033	89.73
AF4	6.84	0.466	3.56	<0.00050	<0.00500	0.0007	0.0025	<0.00010	0.0028	89.02
AF4S	6.19	0.42	3.43	<0.00050	<0.00500	0.0058	0.00238	0.0345	0.003	89.88
AF6	5.29	0.667	3.56	0.0013	<0.00500	<0.00061	0.00365	<0.00095	0.0027	90.42
AF6S	6.09	0.638	3.41	0.0007	<0.00500	0.001	0.00348	0.0342	0.0031	89.77
AF8	5.31	0.851	3.68	0.0021	<0.00500	0.0008	0.00449	<0.00010	0.0028	90.1
AF8S	6.14	0.847	3.43	0.0015	<0.00500	0.0015	0.00449	0.0344	0.0031	89.49
B4	6.54	0.451	3.32	0.0255	0.403	0.001	0.00259	0.0004	0.0098	89.21
B4S	6.55	0.046	3.26	0.025	0.392	0.001	0.00257	0.0226	0.0096	89.23
B8	6.5	0.877	3.62	0.105	0.407	0.0011	0.00456	<0.00010	0.1	88.24
B8S	6.59	0.879	3.63	0.102	0.401	0.0012	0.00451	0.0215	0.0981	88.13
CF1	7.29	0.112	0.014	0.0367	0.352	0.0016	0.00061	<0.00012	0.0766	92.05
CF1S	7.11	0.109	0.015	0.0361	0.348	0.0016	0.00054	0.0266	0.0793	92.2
CF2	7.25	0.213	0.052	0.0354	0.339	0.0015	0.0011	0.0002	0.0776	91.97
CF2S	7.4	0.249	0.014	0.0366	0.344	0.0015	0.0013	0.0250	0.0776	91.85
CF4	7.27	0.411	0.015	0.0364	0.336	0.0017	0.0021	<0.00010	0.0768	91.78
CF4S	7.2	0.439	0.014	0.0369	0.351	0.0017	0.00231	0.0375	0.0757	91.77
CF6	7.19	0.645	0.018	0.0375	0.333	0.0017	0.00332	<0.00010	0.0755	91.63
CF6S	7.26	0.647	0.017	0.0372	0.347	0.0017	0.00332	0.0401	0.0748	91.5
CF8	7.17	0.877	0.015	0.0375	0.338	0.0018	0.00468	<0.00012	0.0735	91.41
CF8S	7.14	0.821	0.027	0.0376	0.334	0.0019	0.00417	0.0351	0.0753	91.46

### 3.2.2 Graphite-Mold and Metallic-Mold Castings – Thermal Analysis

Thermal analysis was also carried out on the A319.2 and A356.2 alloys containing 0.2% and 0.8% iron, in both the unmodified and Sr-modified conditions. In this case, the alloy ingot pieces were melted in a 1.5 kg capacity SiC crucible, using an electrical resistance furnace. The melting temperature was kept at  $750^{\circ} \pm 5^{\circ}\text{C}$ . In those cases when the melts were modified with Sr, the required amount of Sr was added to the melt using Al-10 wt% Sr master alloy. The melt was stirred for  $\sim 10$  min to ensure homogeneous mixing.

The molten metal was then poured into (a) a cylindrical graphite mold (of 10 cm length and 6 cm diameter) preheated at  $600^{\circ}\text{C}$  to obtain close-to-equilibrium cooling conditions, and (b) a cylindrical metallic mold (of 27 cm length and 2 cm diameter) that gave a cooling rate of  $\sim 8^{\circ}\text{C/s}$  (see Figure 3.2).

In the case of the graphite mold, thermal analysis was performed by attaching a high sensitivity thermocouple (chromel-alumel, type K) to the mold system, passing through the bottom of the mold and reaching halfway up into the mold cavity. The temperature-time data was collected using a high speed data acquisition system (Strawberry Tree) linked to a computer with an acquisition rate of 5 readings/sec.

In the case of the metallic mold, the thermocouple was inserted through a hole machined along the side of the mold, such that its tip was positioned roughly at about 10 cm above the mold bottom, along the mold centreline (using an acquisition rate of 50 readings/sec). The parts of the thermocouples within the mold were protected using double-walled ceramic tubing.

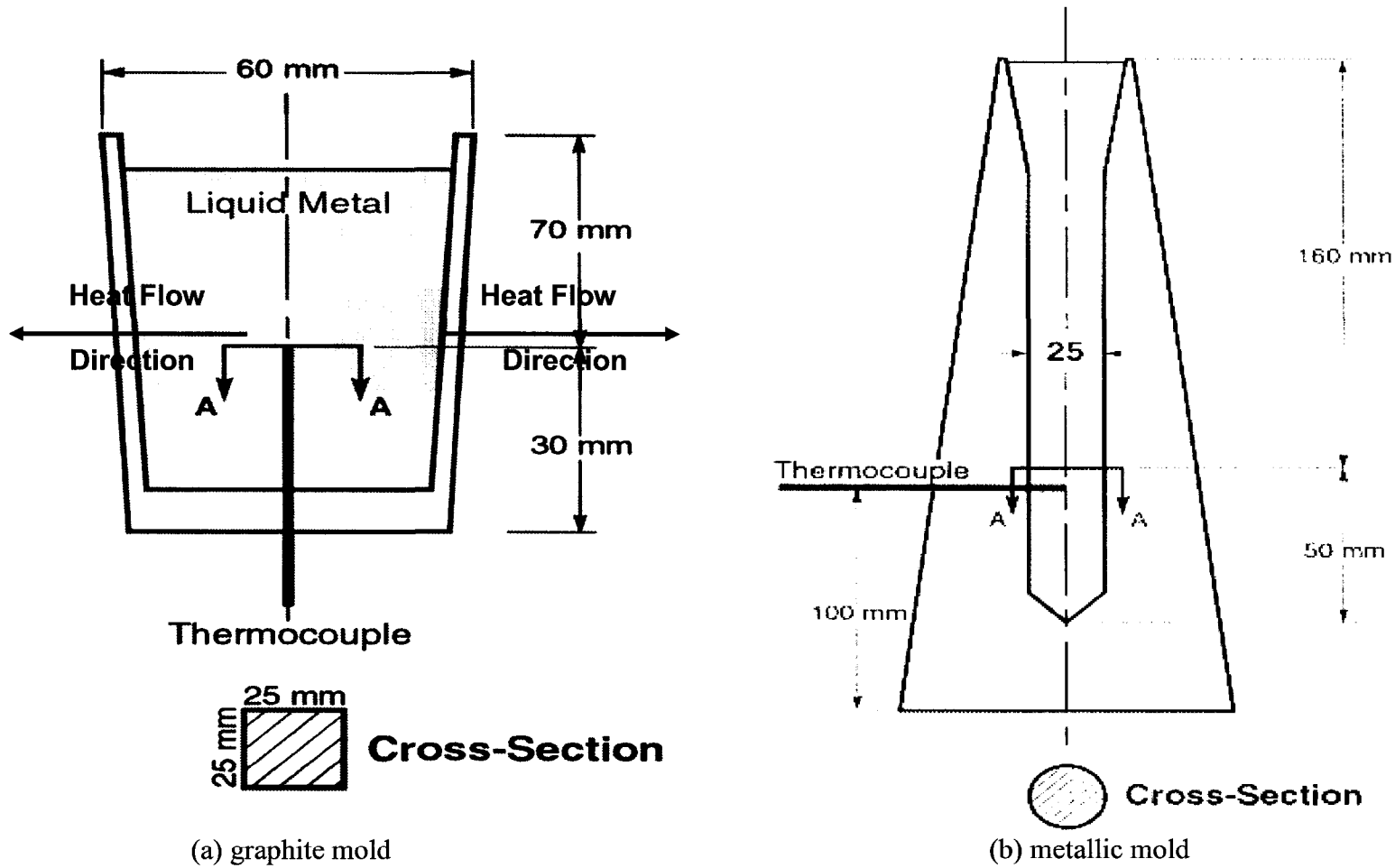


**Figure 3.2** Schematic diagram of molds used for thermal analysis and corresponding sample sections used for metallographic analysis.

From the thermal analysis data, the cooling curves and their first derivatives were plotted in each case. The Si eutectic temperature, as well as the temperature of formation of other precipitated phases (*i.e.*, the iron, copper and Mg<sub>2</sub>Si phases) were determined from the first derivative curves.

### **3.3 METALLOGRAPHY**

For microstructural examination purposes, samples were prepared from the different castings and examined using various metallographic techniques.

#### **3.3.1 Sample Preparation**

In the case of the end-chill castings, specimen blanks were sectioned from the cast blocks at the selected heights of 5, 10, 30, 50 and 100 mm above the chill end, corresponding to DAS values ranging between ~15  $\mu\text{m}$  and ~85  $\mu\text{m}$  (see Figure 3.3). Samples of dimensions of 2 cm  $\times$  3 cm were cut from the central part of each blank, mounted in bakelite and polished to a fine finish (1  $\mu\text{m}$  diamond paste).

Samples from the graphite mold and metallic mold castings were obtained as shown in Figure 3.2 (A-A sections), where the former had dimensions of 2.5 cm  $\times$  2.5 cm, and the latter had a cross-section diameter of 2.5 cm.

### 3.3.2 Microstructural Examination – Optical Microscopy and Image Analysis

Quantitative measurements of the  $\beta$ -Al<sub>5</sub>FeSi platelets (or needles as they appear in the two-dimensional sample surface under the microscope), the eutectic Si particle characteristics, percentage porosity and pore characteristics, and the dendrite arm spacings were made using a Leco 2001 image analyzer in conjunction with an Olympus BH2-UMA optical microscope. In each case, a certain number of fields were examined for each sample (“field” representing the field of view of the optical microscope and covering an area of  $2.2608 \times 10^4$  sq  $\mu\text{m}$  at 500X magnification), selected so as to cover the entire area of the sample in a regular, systematic fashion.

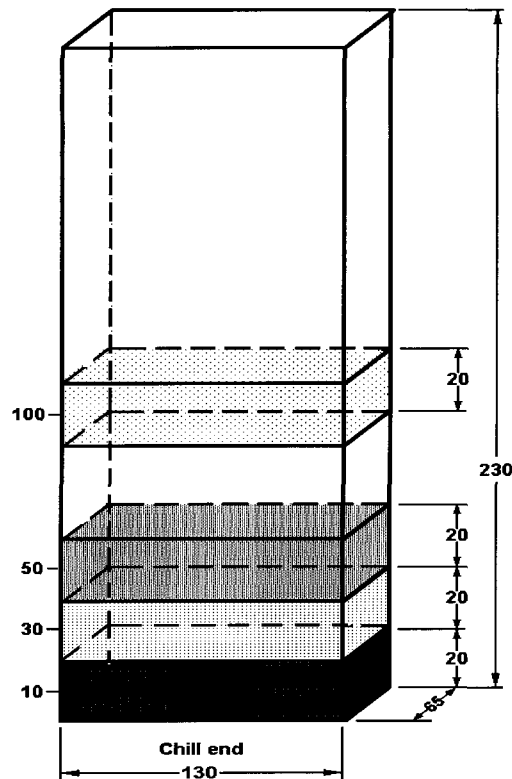


**Figure 3.3** End-chill casting showing specimen blank sectioning scheme (mm).

For the  $\beta$ -Al<sub>5</sub>FeSi platelet measurements, the three longest  $\beta$ -platelets were measured in each field and, depending upon the sample, 100-150  $\beta$ -platelet measurements were made to obtain the average maximum  $\beta$ -platelet length. By measuring the average thickness of the  $\beta$ -phase platelets, the volume fraction of  $\beta$ -phase observed in each sample was also determined. In addition, the number of platelets in each field was also counted to obtain the  $\beta$ -platelet density. The data was analyzed using statistical software programs, and histograms and plots were produced, showing the actual  $\beta$ -platelet length distributions and densities obtained.

Similarly, porosity measurements were also carried out for these samples. In this case, one hundred fields were examined at a magnification of 50X, to cover the entire sample surface, from which the percentage porosity and pore characteristics (area, length and aspect ratio) were determined. With respect to the eutectic Si phase, the Si particle characteristics (particle area, length and density) were measured over fifty fields - at magnifications of 200X for the unmodified alloys and 500X for the Sr-modified alloys, and the respective average values determined.

In the case of the graphite and metallic mold samples (thermal analysis), and end-chill casting samples corresponding to the five levels above the chill end, the  $\alpha$ -Al dendrite arm spacings were also measured. Some forty measurements were taken all over the sample surface, from which the average DAS values were determined. Table 3.3 shows the various dendrite arm spacings obtained at the five levels above the chill end that were examined.

**Table 3.3** DAS values obtained at various levels of the end-chilled castings for the alloys used

Level	Distance from chill end (mm)	Average DAS ( $\mu\text{m}$ )	
		Alloys 319 (A & B)	Alloy A356.2 (C)
1	5	16	15
2	10	23	23
3	30	47	39
4	50	60	53
5	100	83	75

In the case of the graphite mold-cast samples, the A319.2 and A356.2 alloys exhibited DAS values of  $64 \mu\text{m}$  and  $65 \mu\text{m}$ , respectively, while both alloy types showed a DAS of  $16 \mu\text{m}$  for samples obtained from the cold metallic mold.

### 3.3.3 Phase Identification –SEM and EPMA Analysis

Phase identification was carried out using the graphite mold-cast samples, employing scanning electron microscopy (SEM) and electron probe microanalysis (EPMA), coupled with energy dispersive X-ray (EDX) and wavelength dispersion spectroscopic (WDS) analyses.

Figure 3.4 shows the Jeol WD/ED combined microanalyzer (McGill Microprobe Laboratory) that was employed for this purpose (model JXA-8900R, operating at 20 kV and 30 nA, with an electron beam size of  $\sim 1 \mu\text{m}$ ).

In addition, the different end-chilled casting samples were also examined to determine - on a microscopic level - the effects of cooling rate, Sr modification and iron content on the microstructural characteristics, and thereby determine the fundamental phenomena/mechanisms underlying the observed characteristics.

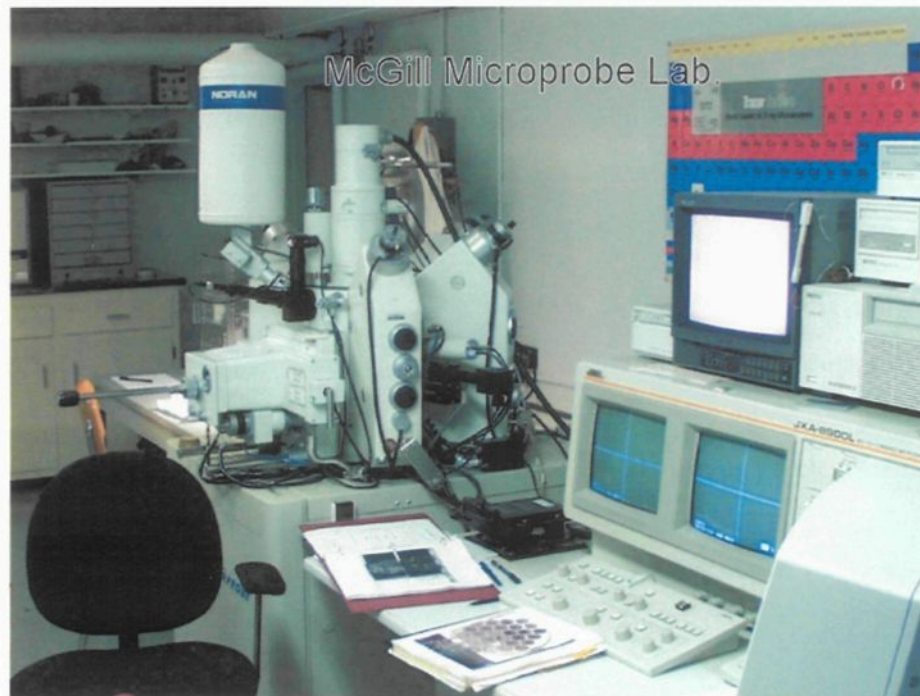


**Figure 3.4** Electron probe microanalyzer used in the present work.

## **CHAPTER 4**

# **PRECIPITATION OF $\beta$ -AL<sub>5</sub>FESI PHASE PLATELETS AND THEIR ROLE ON POROSITY FORMATION**

## CHAPTER 4

# PRECIPITATION OF $\beta$ -AL<sub>5</sub>FESI PHASE PLATELETS AND THEIR ROLE ON POROSITY FORMATION

### 4.1 INTRODUCTION

The properties of castings produced from the 356 and 319 type alloys studied are controlled by the quality of their microstructure, as determined by the dendrite arm spacing (DAS), the degree of eutectic silicon modification and grain refinement, and the amount of porosity, intermetallics and inclusions observed in the microstructure.

Two critical parameters in this respect are (a) the iron intermetallic  $\beta$ -Al<sub>5</sub>FeSi phase which, due to its brittle, platelet-like nature is detrimental to the alloy properties, and (b) porosity, which affects the soundness and surface quality of a casting. The feedability-associated problems related to the presence of the  $\beta$ -Al<sub>5</sub>FeSi platelets in the structure also lead to porosity formation. Thus, it is of interest to study the one in relation to the other.

Extensive measurements were carried out to study the formation of the  $\beta$ -Al<sub>5</sub>FeSi iron intermetallic phase in these two alloys as a function of the iron content, cooling rate and Sr-modification. Porosity measurements were also carried out on the same alloy samples. The results are presented in this chapter.

#### 4.1.1 Iron Intermetallics

Iron is the most pervasive impurity element in aluminum, stemming from impurities in bauxite ore and contamination with ferrous metals and oxides during handling and recycling.<sup>63</sup> It is known for contaminating Al-Si casting alloys, being the most deleterious element with respect to the strength, especially the alloy toughness, since it forms the needle-like  $\beta$ -Al<sub>5</sub>FeSi intermetallic phase during solidification.<sup>51,68,112,113,114</sup> Dissolution is the only practical method to reduce iron in aluminum. The solubility of iron in molten aluminum is quite high, leading to the eventual dissolution of ferrous material in contact with molten aluminum. In contrast, the solubility in solid aluminum is very low, only 0.05% at 660°C.<sup>7</sup> The solubility is even less at room temperature, or in the presence of alloying elements that form compounds with iron. Fine Fe-rich particles precipitate at intermediate temperatures and cannot be dissolved in the solid state.

Aluminum forms a variety of intermetallic compounds with its alloying elements. Intermetallic compounds are actually solid solutions that have substantial capacity to dissolve other elements. Their compositions, although expressed as chemical formulae, vary. In addition, solute atoms in Fe-rich intermetallics often occupy Al, Fe, and Si lattice positions. A number of Fe-rich intermetallic phases have been identified in Al-Si base alloys.<sup>8</sup> Some of the more common ones are listed in Table 4.1, the  $\alpha$ -Al<sub>15</sub>Fe<sub>3</sub>Si<sub>2</sub> and  $\beta$ -Al<sub>5</sub>FeSi phases being the more important. The Chinese script morphology of the  $\alpha$ -iron phase occurs during eutectic solidification. The  $\alpha$ -iron phase can also appear in the form of polyhedrons if it solidifies as a primary phase.<sup>2,115</sup> The  $\beta$ -iron phase is mostly associated

with iron levels greater than ~1% Fe, roughly the location of the eutectic trough on the Al-Si-Fe phase diagram. However, enough iron segregation occurs during solidification to cause the  $\beta$ -phase to form, even when the iron level is much less than 1%.<sup>6</sup>

**Table 4.1** Important Fe-rich phases in Al-Si alloys<sup>8</sup>

Identification	Crystal structure	Melting temperature (°C)
$\alpha$ -Al <sub>15</sub> Fe <sub>3</sub> Si <sub>2</sub>	hexagonal	860
$\beta$ -Al <sub>5</sub> FeSi	monoclinic	870
$\pi$ -Al <sub>8</sub> Mg <sub>3</sub> FeSi <sub>6</sub>	hexagonal	-
$\delta$ -Al <sub>4</sub> Fe <sub>3</sub> Si <sub>2</sub>	tetragonal	-

The  $\beta$ -Al<sub>5</sub>FeSi phase is considered the most critical among the iron intermetallics, as it significantly reduces the alloy ductility and fracture toughness. Existing in the form of thin platelets that appear as needles in the microstructure, the size of these  $\beta$  platelets or needles is controlled by the iron content and the solidification conditions of the alloy.<sup>56,116</sup> In comparison, the  $\alpha$ -iron phase, due to its compact morphology, is less harmful to the mechanical properties.

Control of the iron level is thus technically important, especially where the production of critical components is concerned. There are different measures adopted to neutralize the harmful effect of the  $\beta$ -iron phase: i) rapid solidification,<sup>54,55</sup> ii) addition of neutralizers such as Mn, Co, and Cr,<sup>56</sup> iii) melt superheat, iv) strontium modification<sup>58,59</sup> and v) non-equilibrium solution heat treatment.<sup>60</sup>

### 4.1.2 Porosity

One of the most important aspects of the quality of an alloy casting is the presence or absence of porosity in the casting. Porosity occurs in solidifying metals and alloys due to negative pressures generated during solidification contraction, and pressure developed by gases dissolved in the molten metal. Both these processes may act either together or separately to produce shrinkage or gas defects. They are generally unwanted and constitute a major problem.<sup>117</sup>

Porosity formation is essentially a nucleation and growth process involving heterogeneous nucleation in the early stages of solidification due to entrapped inclusions and contact with the mold wall or existing gas bubbles. The possibility of homogenous nucleation also exists, especially in the later stages of solidification in the interdendritic regions of the mushy zone, a zone defined by the freezing range of the alloy, where the presence of entrapped nuclei is less likely to occur.<sup>118</sup> The ability of a pore to grow in a solidifying metal, given that nucleation is relatively easy, can be best expressed by the relation,

$$P_g + P_s > P_{atm} + P_H + P_{s-t}$$

where the various terms have been explained previously in Chapter 2, Section 2.6.1.

Many process and/or design factors such as local thermal conditions,<sup>119</sup> feeding capacity,<sup>120</sup> and applied pressure<sup>121</sup> are known to affect porosity formation. Metal-related factors, including dissolved hydrogen,<sup>107</sup> inclusions,<sup>104,122</sup> modifying elements, and other minor element additions can also influence porosity formation.

### 4.1.3 Iron-Porosity Relationship

Iron has a negative influence on porosity formation. Some studies<sup>123</sup> report that the level of porosity increases monotonically with iron content. Taylor *et al.*<sup>87</sup> have reported, however, that the iron-porosity relationship is not a monotonic one. According to them, iron is not solely a detrimental element, as up to a critical iron content - of 0.4 pct, there are beneficial effects. Thereafter, there is a deleterious contribution from iron toward porosity formation, but it is only apparent under poor casting conditions. In this connection, it is interesting to note that Iwahori *et al.*<sup>124</sup> have also reported that larger riser sizes were required in order to avoid the formation of shrinkage-porosity defects in Al-Si-Cu alloy castings in cases where the iron level was increased above 0.5 pct.

Metallographic studies have shown that pores are nucleated along the long sides of the  $\beta$  platelets. However, in spite of the harmful effect of these  $\beta$  platelets as pore nucleation sites, their presence also appears to limit pore growth.<sup>123,125</sup>

Strontium is commonly added to Al-Si alloy melts to modify the silicon eutectic, but also affects the amount and distribution of porosity that results in the casting. In addition, strontium also results in the fragmentation and dissolution of the  $\beta$ -Al<sub>5</sub>FeSi phase platelets.<sup>59</sup>

## 4.2 EFFECT OF COOLING RATE AND Sr MODIFICATION ON $\beta$ -Al<sub>5</sub>FeSi PRECIPITATION

The chemical compositions and codes of the alloys that were used (for which the results are presented in this chapter) are listed in Tables 3.1 and 3.2 in Chapter 3.

Experimental procedures related to the  $\beta$ -phase and porosity measurements have also been described previously in Chapter 3. The samples used were obtained from end-chill mold castings, *viz.*, under directional solidification conditions.

#### 4.2.1 Secondary Dendrite Arm Spacing

In Al-Si cast alloys, solidification begins with the development of a dendrite network of primary ( $\alpha$ ) aluminum. The secondary dendrite arm spacing (SDAS, frequently referred to simply as DAS) is essentially determined by the alloy composition, cooling rate, local solidification time and temperature gradient. It has been shown that DAS varies with cooling rate according to the relation,<sup>126</sup>

$$\log(dT/dt) = -[\log(DAS) - 2.37]/0.4$$

where  $dT/dt$ , the cooling rate, is given in  $^{\circ}\text{C}/\text{min}$ , and the DAS in  $\mu\text{m}$ . At any particular location in the casting, the local solidification time determines the DAS and, hence, the mechanical properties.

Thus, the dendrite arm spacing is a microstructural manifestation of the cooling rate of a solidifying sample: the higher the cooling rate, the finer the DAS of the sample microstructure, and *vice versa*. In fact, DAS is often preferred to the cooling rate as an indicator of the solidification conditions of the casting, as it is easier to measure, and incorporates the influence of other solidification parameters as well.

A finer DAS refines and disperses the porosity as well as second phase constituents (*e.g.*, the  $\beta$ -iron phase) more evenly. This refinement of the microstructure leads to a substantial improvement in mechanical properties.<sup>127,128</sup> Figure 4.1 shows, for example, the

DAS values obtained from Sr-modified A319.2 and A356.2 alloy samples as a function of the distance from the chill end (*i.e.*, the cooling rate).

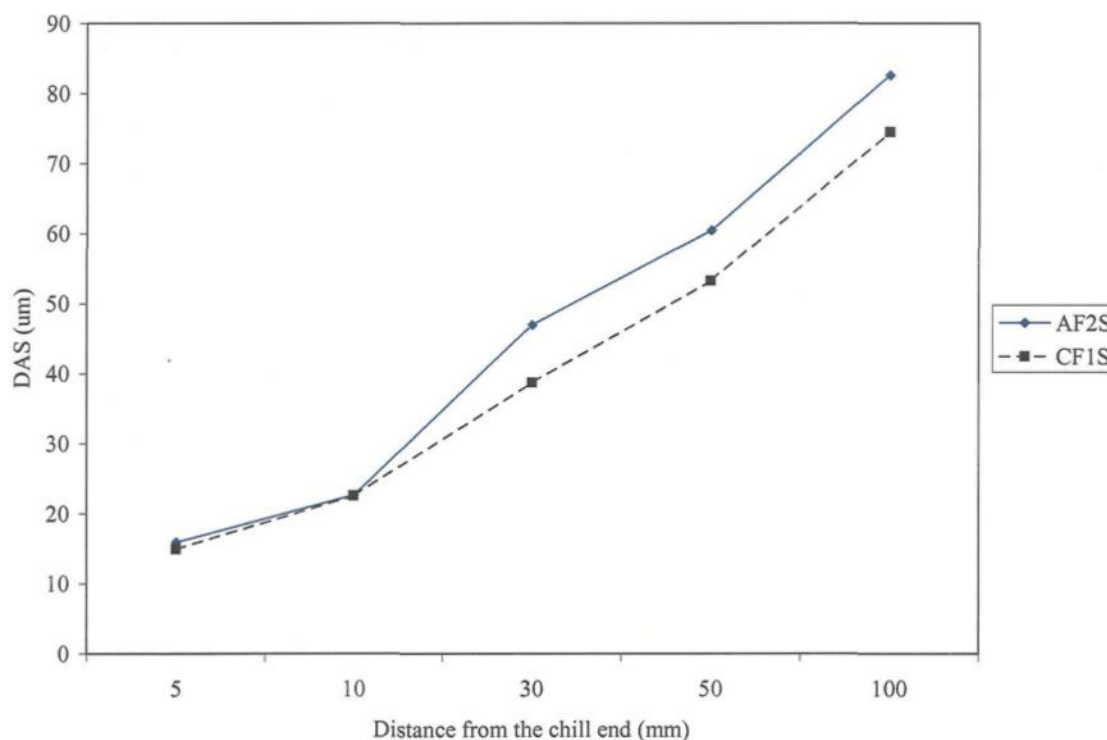


**Figure 4.1** Dependence of DAS on the cooling rate (AF2S: Sr-modified A319-0.2%Fe alloy, CF1S: Sr-modified A356.2 alloy).

#### 4.2.2 Effect of Sr Modification

Sigworth<sup>129</sup> has reported that the deleterious effects of iron may also be overcome by strontium modification, where the formation of large, brittle iron intermetallics can be suppressed in a well-modified alloy.

Morris and Miners<sup>77</sup> found that the addition of Sr to 1xxx and 6xxx series of wrought aluminum alloys can transform a major proportion of the  $\beta$ -Al<sub>5</sub>FeSi phase occurring in the ingots into the  $\alpha$ -Al<sub>3</sub>Fe<sub>2</sub>Si phase. The Sr adsorbs to the latter and prevents

the diffusion of silicon (which builds up at the  $\alpha$ -AlFeSi/Al-matrix interface) into the  $\alpha$ -Al<sub>8</sub>Fe<sub>2</sub>Si phase, resulting in an absence of  $\beta$ -Al<sub>5</sub>FeSi needles in the microstructure.<sup>130</sup> Apparently, during solidification, the Sr addition leads to local segregation of iron in certain areas, such that the Fe/Si ratio is  $> 1$ , which favors precipitation of iron intermetallics in the form of the compacted  $\alpha$ -Al<sub>8</sub>Fe<sub>2</sub>Si phase.<sup>131</sup>

Villeneuve and Samuel<sup>62</sup> reported that the addition of a sufficiently high concentration of Sr (~350 ppm) to Al-13 wt% Si-Fe alloys breaks down the  $\beta$ -needles into small, thin fragments through (i) splitting of the needles into two halves, and (ii) fragmentation due to Si rejection. Dissolution of the  $\beta$ -phase occurs by decomposition of  $\beta$ -Al<sub>5</sub>FeSi into Al<sub>6</sub>Fe and Si particles.

#### 4.2.3 $\beta$ -Al<sub>5</sub>FeSi Platelet Characteristics

Tables 4.2 through 4.4 list the data for the  $\beta$ -platelet characteristics of average maximum length and density obtained from the 319 and 356 alloys in the non-modified and Sr-modified conditions. As was explained previously in Chapter 3, the A319.2, B319.2 (higher Mg content), and A356.2 alloys are represented by the code letters A, B and C, respectively, F1 through F8 represent iron contents of 0.1%, 0.2%, 0.4%, 0.6% and 0.8% respectively, and the suffices 0, 1, 3, 5 C (or 0, 1, 2, 3, C in certain cases) denote the levels 5, 10, 30, 50, and 100 mm above the chill end (*i.e.*, cooling rates corresponding to DASs of 16, 23, 47, 61, and 83  $\mu\text{m}$  for the 319 alloys and 15, 23, 39, 53, and 75  $\mu\text{m}$  for the A356.2 alloys, respectively).

**Table 4.2(a)**  $\beta$ -platelet characteristics obtained for unmodified A319.2 alloy samples

Alloy Code	Av. Max $\beta$ -platelet length ( $\mu\text{m}$ )	SD	Density (no./ $\text{mm}^2$ )
AF2-0	31.81	18.16	351.63
AF2-1	47.79	22.25	265.30
AF2-3	64.92	39.86	63.11
AF2-5	89.63	49.23	75.51
AF2-C	117.72	63.84	91.05
AF4-0	31.02	12.59	456.03
AF4-1	33.29	19.45	364.98
AF4-3	99.98	44.69	172.36
AF4-5	146.58	76.47	129.51
AF4-C	143.14	88.17	154.31
AF6-0	32.59	13.9	1612.97
AF6-1	66.68	28.32	656.96
AF6-3	142.34	59.88	130.92
AF6-5	210.55	104.56	66.09
AF6-C	253.76	158.86	49.45
AF8-0	50.66	23.78	2311.53
AF8-1	65.88	34.91	988.19
AF8-3	190.56	95.35	145.68
AF8-5	218.3	118.44	103.92
AF8-C	204.75	146.52	75.04

SD = Standard Deviation

**Table 4.2(b)**  $\beta$ -platelet characteristics obtained for Sr-modified A319.2 alloy samples

Alloy Code	Av. Max $\beta$ -platelet length ( $\mu\text{m}$ )	SD	Density (no./ $\text{mm}^2$ )
AF2S-0	17.61	11.6	12.56
AF2S-1	36.69	21.19	120.09
AF2S-3	88.2	44.4	92.93
AF2S-5	131.65	74.27	97.48
AF2S-C	136.89	68.46	86.18
AF4S-0	27.58	13.43	387.74
AF4S-1	41.22	24.09	637.34
AF4S-3	101.23	53.54	167.97
AF4S-5	141.1	79.45	190.26
AF4S-C	137.71	81.49	132.33
AF6S-0	61.08	27.4	1116.13
AF6S-1	64.67	26.89	785.68
AF6S-3	184.02	123.61	158.55
AF6S-5	209.85	117.18	104.71
AF6S-C	238.82	167.89	77.71
AF8S-0	56.88	32.74	1099.64
AF8S-1	80.37	33.26	627.92
AF8S-2	187.65	110.3	137.83
AF8S-3	264.96	131.14	131.71
AF8S-C	318.5	255.84	84.14

SD = Standard Deviation

**Table 4.3**  $\beta$ -platelet characteristics obtained for unmodified and Sr-modified B319.2 alloy samples

Alloy Code	Av. Max $\beta$ -platelet length ( $\mu\text{m}$ )	SD	Density (no./ $\text{mm}^2$ )
B4-0	31.39	14.15	819.43
B4-1	56.26	28.84	543.93
B4-2	115.12	55.75	157.29
B4-3	160.97	76.79	111.46
B4-C	193.62	113.92	62.32
B8-0	46.89	16.85	1969.31
B8-1	72.31	28.99	1353.95
B8-2	167.52	73.31	331.54
B8-3	235.37	110.35	216.16
B8-C	293.31	179.86	109.89
B4S-0	30.83	12.13	726.82
B4S-1	40.22	18.45	543.15
B4S-2	108.61	67.63	124.96
B4S-3	145.58	61.82	92.62
B4S-C	93.88	36.32	702.33
B8S-0	34.24	11.59	1934.77
B8S-1	56.46	24.04	1350.81
B8S-2	193.82	116.98	312.39
B8S-3	286.14	232.75	204.70
B8S-C	308.62	202.94	133.90

SD = Standard Deviation

**Table 4.4(a)**  $\beta$ -platelet characteristics obtained for unmodified A356.2 alloy samples

Alloy Code	Av. Max $\beta$ -platelet length ( $\mu\text{m}$ )	SD	Density (no./ $\text{mm}^2$ )
CF1-0	10.78	5.72	51.80
CF1-1	14.36	7.1	14.13
CF1-2	34.92	15.38	13.19
CF1-3	30.72	16.41	2.83
CF1-C	45.86	39.25	8.48
CF2-0	12.53	5.49	204.86
CF2-1	12.12	5.89	94.97
CF2-2	29.25	12.87	32.02
CF2-3	38.25	20.32	37.36
CF2-C	45.52	23.91	47.72
CF4-0	17.68	8.94	167.18
CF4-1	29.65	13.28	316.31
CF4-2	77.25	31.41	118.68
CF4-3	119.93	76.3	101.25
CF4-C	130.17	42.36	89.16
CF6-0	27.89	13.41	1105.14
CF6-1	53.9	24.44	612.22
CF6-2	150.95	73.88	183.67
CF6-3	212.41	110.32	112.55
CF6-C	249.96	139.73	79.59
CF8-0	66.65	29.89	795.89
CF8-1	78.05	35.7	352.42
CF8-2	182	107	99.53
CF8-3	274.32	209.36	87.44
CF8-C	236.54	121.27	75.04

SD = Standard Deviation

**Table 4.4(b)**  $\beta$ -platelet characteristics obtained for Sr-modified A356.2 alloy samples

Alloy Code	Av. Max $\beta$ -platelet length ( $\mu\text{m}$ )	S.D	Density (no./ $\text{mm}^2$ )
CF1S-0	12.79	4.84	848.48
CF1S-1	17.5	8.46	314.74
CF1S-2	23.88	9.64	70.95
CF1S-3	28.27	14.73	87.59
CF1S-C	31.41	18.1	32.65
CF2S-0	8.8	3.33	1041.7
CF2S-1	18.32	9.38	361.05
CF2S-2	26.98	14.68	313.96
CF2S-3	44.48	20.17	100.00
CF2S-C	65.9	37.72	102.19
C4SB-0	24.49	11.11	1295.08
C4SB-1	30.62	11.94	1298.22
C4SB-2	38.02	16.54	1372.00
C4SB-3	62.92	31.29	1903.38
C4SB-C	81.49	49.6	1009.58
C6SB-0	38.47	15.74	1744.44
C6SB-1	43.81	19.71	873.20
C6SB-2	105.91	45.43	280.37
C6SB-3	151.58	95.59	192.77
C6SB-C	197.41	101.43	129.35
CF8S-0	68.81	29.31	842.98
CF8S-1	173.67	93.54	207.84
CF8S-2	199.71	115.57	133.75
CF8S-3	233.84	128.26	120.25
CF8S-C	219.87	120.19	62.48

Note: Code C4SB and C6SB correspond to castings that were repeated for CF4S and CF6S alloys. SD = Standard Deviation.

#### 4.2.3.1 $\beta$ -Al<sub>5</sub>FeSi platelet size

The data shown in Tables 4.2 - 4.4 were plotted in the form of histograms for both unmodified and Sr-modified alloys. Figures 4.2 through 4.4 depict these histograms, showing the average maximum  $\beta$  platelet lengths obtained as a function of distance from the chill end (*viz.*, cooling rate) for the three alloy types. The results may be summarized as follows.

##### *A319.2 alloy*

In regard to the cooling rate, we can see that the higher the cooling rate (*i.e.*, at 5 mm and 10 mm distance from the chill end), the shorter the  $\beta$ -platelet average maximum length in both unmodified and Sr-modified alloys (*e.g.*, 31.02  $\mu\text{m}$  for AF4-0 alloy versus 143.14  $\mu\text{m}$  for AF4-C alloy, and 27.58  $\mu\text{m}$  for AF4S-0 alloy versus 137.71  $\mu\text{m}$  for AF4S-C alloy). There are two possible explanations: i) a higher cooling rate will increase the maximum solubility of Fe in the aluminum matrix, resulting in finer  $\beta$ -particles; ii) a higher cooling rate will also result in a smaller DAS, and the overall refinement of the microstructure will result in the precipitation of finer  $\beta$ -particles.

At higher cooling rates, the effect of Sr addition on the  $\beta$ -platelet length is not very obvious, and the effect due to cooling rate is stronger than that due to Sr modification. At lower cooling rates, the  $\beta$ -platelet lengths in the higher Fe-level alloys are longer in the Sr-modified alloys than in the unmodified alloys. In this case, addition of strontium poisons

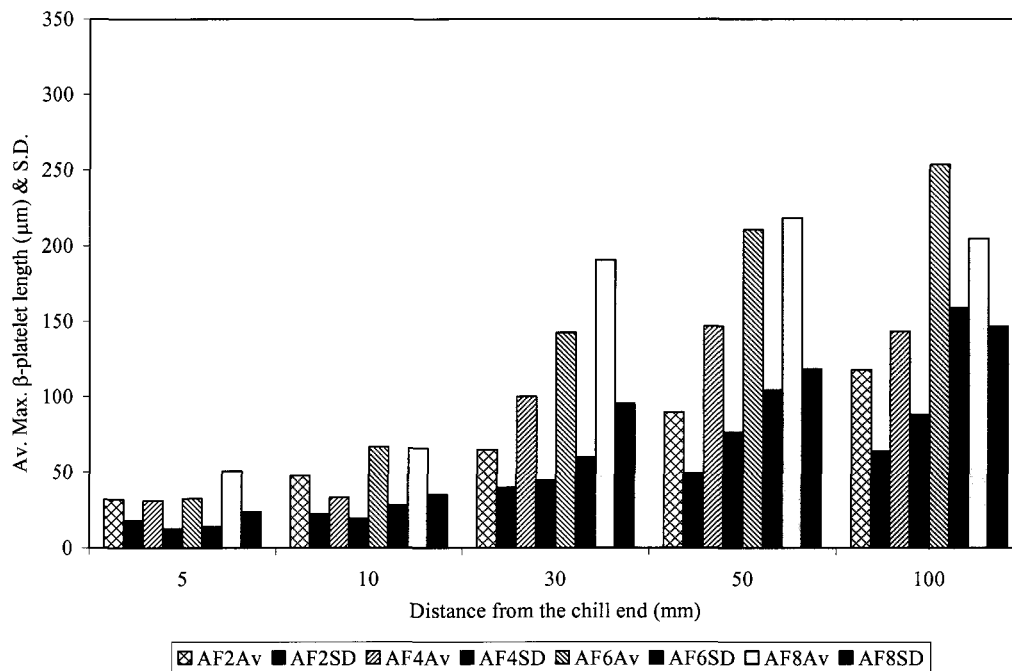


**Figure 4.2(a)** Effect of cooling rate on the average maximum  $\beta$ -platelet length observed in unmodified A319.2 alloys.

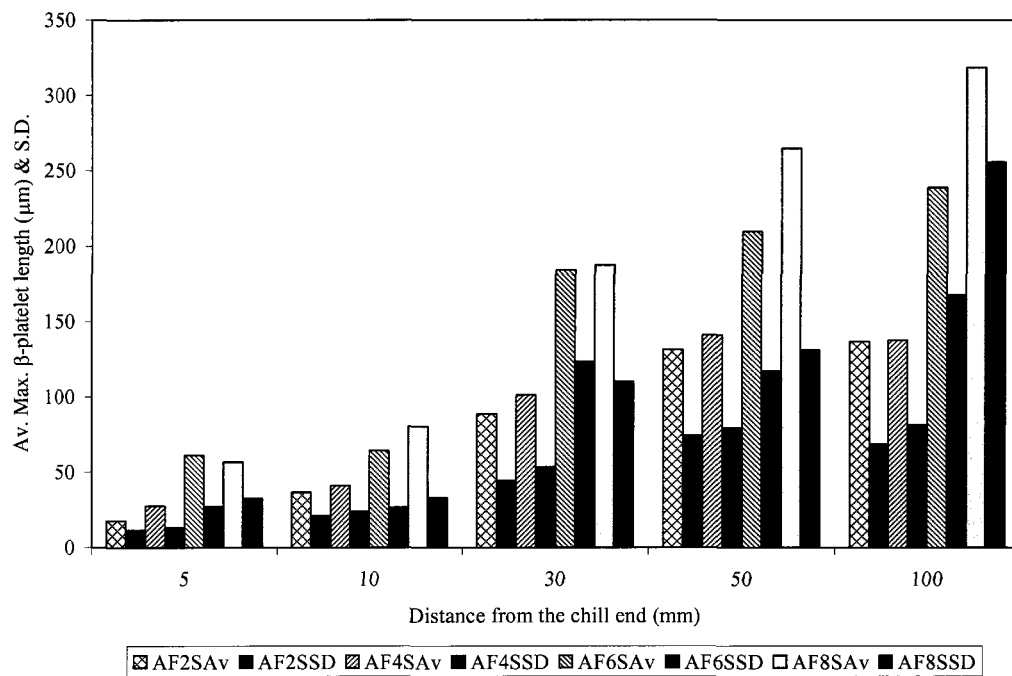


**Figure 4.2(b)** Effect of cooling rate on the average maximum  $\beta$ -platelet length observed in Sr-modified A319.2 alloys.

the  $\beta$ -needle nucleation sites. Consequently, the  $\beta$ -iron phase must precipitate at a smaller number of sites, resulting in the precipitation of needles that are larger compared to those in the unmodified alloys. This observation is in contrast to the observations of Shabestari and Gruzleski,<sup>54,55</sup> who reported that for slow cooling rates, Sr causes fragmentation of the  $\beta$ -needles and a 47% reduction in volume (that is transformed into sludge).

It can also be observed from these figures, that the higher the iron content, the longer the  $\beta$ -platelet lengths, especially at the lowest cooling rate (*cf.* 117.72  $\mu\text{m}$  for AF2-C alloy with 204.75  $\mu\text{m}$  for AF8-C alloy). This observation is in accordance with the work of Pennors *et al.*,<sup>131</sup> who observed that an increased iron content results in the precipitation of long thick needles/platelets of the  $\beta$ -Al<sub>5</sub>FeSi intermetallic phase.

#### *B319.2 alloy*

In this case also, the higher the cooling rate, the shorter the average maximum  $\beta$ -platelet length observed. In the case of the 0.4% Fe-containing alloy, the addition of 250 ppm Sr actually decreases the  $\beta$ -platelet length at the different cooling rates (see arrows in Figure 4.3). This is a very interesting observation and will be discussed in the context of the effect of iron content on porosity formation in Section 4.3.

At 0.8% Fe levels, the addition of 250 ppm Sr decreases the  $\beta$ -platelet length at higher cooling rates (up to DAS values of  $\sim 16 \mu\text{m}$ ), but increases the length at lower cooling rates (at DAS levels of  $\sim 76 \mu\text{m}$  or more). It can also be observed that the higher the iron content, the longer the  $\beta$ -platelet length, especially at the lowest cooling rate.

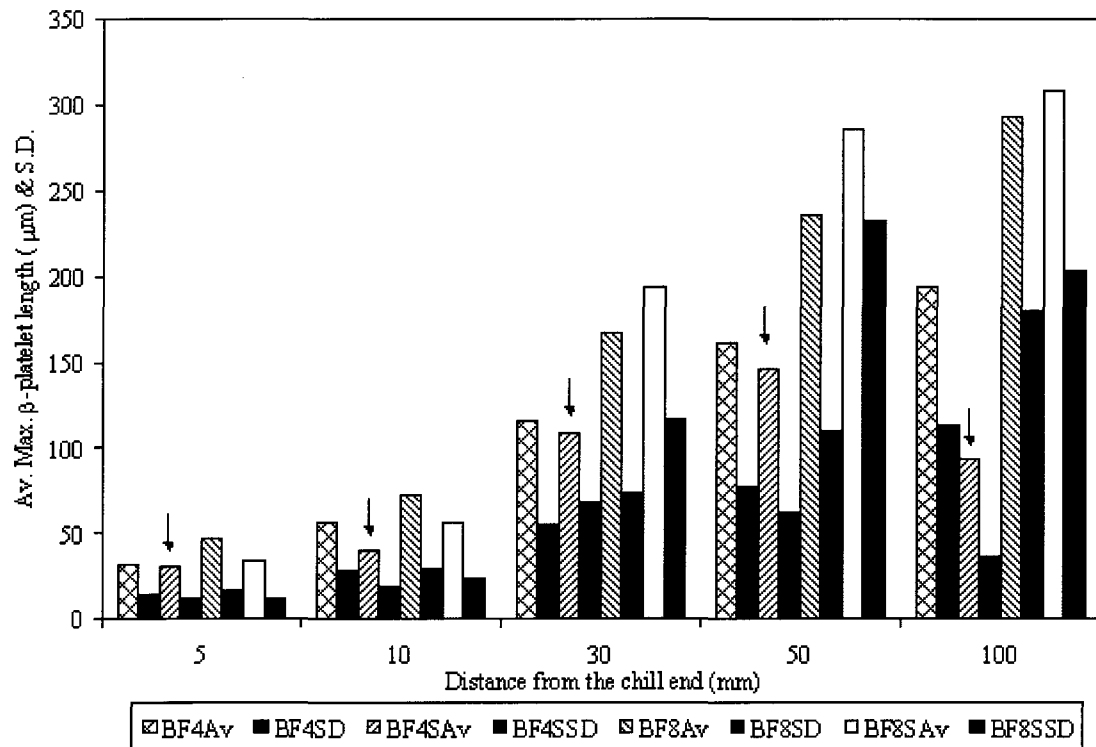


**Figure 4.3** Effect of cooling rate on the average maximum  $\beta$ -platelet length observed in unmodified and Sr-modified B319 alloy.

#### *A356.2 alloy*

In this case, too, as Figure 4.4(a) shows, the  $\beta$ -platelet lengths increase with decrease in cooling rate in the unmodified alloys. The Sr-modified alloys also show the same trend with respect to the cooling rate. However, in comparison with the unmodified alloys, the  $\beta$ -platelet lengths at the cooling rates corresponding to levels of up to 30 mm distance from the chill end are longer in the modified alloys, particularly at Fe levels of 0.6 and 0.8%, but are shorter at cooling rates corresponding to levels of 50 and 100 mm above the chill end, as observed in Figure 4.4(b). It is also seen that the  $\beta$ -platelet lengths increase

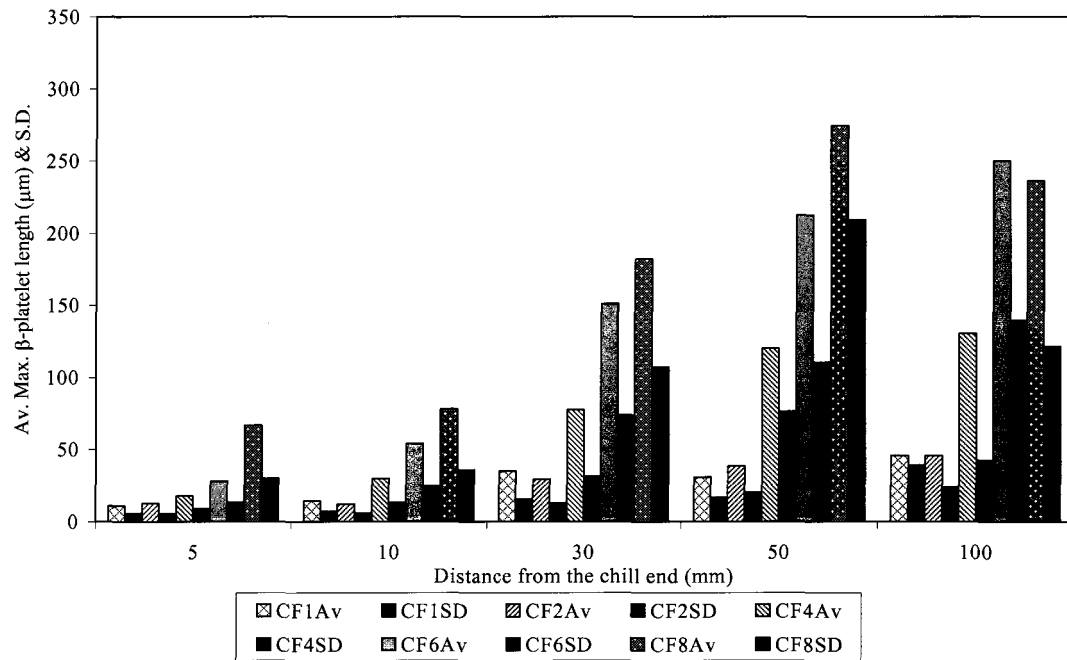


**Figure 4.4(a)** Effect of cooling rate on the average maximum  $\beta$ -platelet length observed in unmodified 356 alloys.

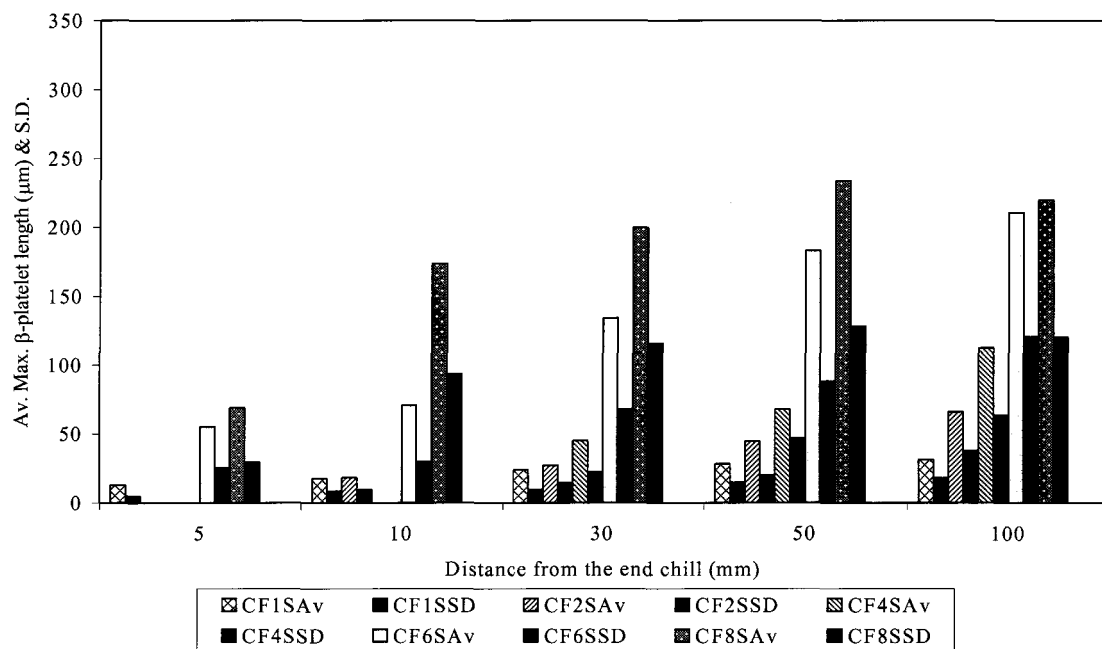


**Figure 4.4(b)** Effect of cooling rate on the average maximum  $\beta$ -platelet length observed in Sr-modified 356 alloys.

with the increase in Fe content. This is expected to be the case. The observations made in regard to the Sr-modified alloys result from a combined effect of Fe, cooling rate and the effect of Sr on the fragmentation and dissolution of the  $\beta$ -Al<sub>5</sub>FeSi phase.

#### 4.2.3.2 $\beta$ -Al<sub>5</sub>FeSi platelet density

Figures 4.5 through 4.7 show plots of the  $\beta$ -platelet density versus cooling rate for the three alloys in the unmodified and Sr-modified conditions. While the plots in all three alloy types appear to be essentially similar, certain features may be highlighted:

- i) The difference in the  $\beta$ -platelet densities between the various alloys is more evident at the higher cooling rates, and after a DAS of  $\sim 43 \pm 4 \mu\text{m}$  corresponding to the 30 mm level above the chill end, the density remains more or less the same irrespective of the Fe content of the alloy, or whether it is modified or not.
- ii) For the various Fe levels, the modified alloys exhibit highest  $\beta$ -densities at the highest Fe levels (0.8% Fe in the A319.2 and B319.2 alloys, and 0.6% Fe in the A356.2 alloy). At lower Fe levels, no clear distinction can be made.
- iii) In the B319.2 alloy (containing 0.4% Mg), except for the jump in density observed at the lowest cooling rate for the B4S alloy, both modified and unmodified alloys display identical or at least very similar  $\beta$ -platelet densities.

The presence of a sufficiently high concentration of Sr leads to a breakdown of the  $\beta$ -platelets into smaller, thinner fragments via two mechanisms:<sup>132</sup> i) splitting of the needle/platelets into two halves through the formation of longitudinal cracks, enhanced greatly by the brittle nature of the  $\beta$ -iron phase, and ii) fragmentation due to Si rejection on account of this, there is an effective increase in the density, with the addition of Sr, compared to the unmodified case. At low cooling rates, the iron intermetallics grow to large sizes, and thus particle density is reduced to a minimum.

It has been observed by Villeneuve and Samuel<sup>132</sup> that Sr addition only affects small  $\beta$ -needles. This phenomenon is more pronounced in high Fe-containing alloys. On the other hand, large  $\beta$ -needles are seen to persist, even after Sr addition or solution heat treatment. This would explain the collective features of the  $\beta$ -iron intermetallic density plots in Figures 4.5 - 4.7. In the case of the B319.2 alloys, Mg-Sr interactions due to the presence of Mg reduce the effect of Sr. Thus, both unmodified and Sr-modified alloys display very similar densities at all cooling rates. Also, as will be discussed in the next section, due to the presence of 0.026% Mn in the alloy, several  $\alpha$ -iron intermetallics were also observed in the microstructure of the B8 alloy, providing another reason for the observed similarity in  $\beta$ -iron intermetallic densities.

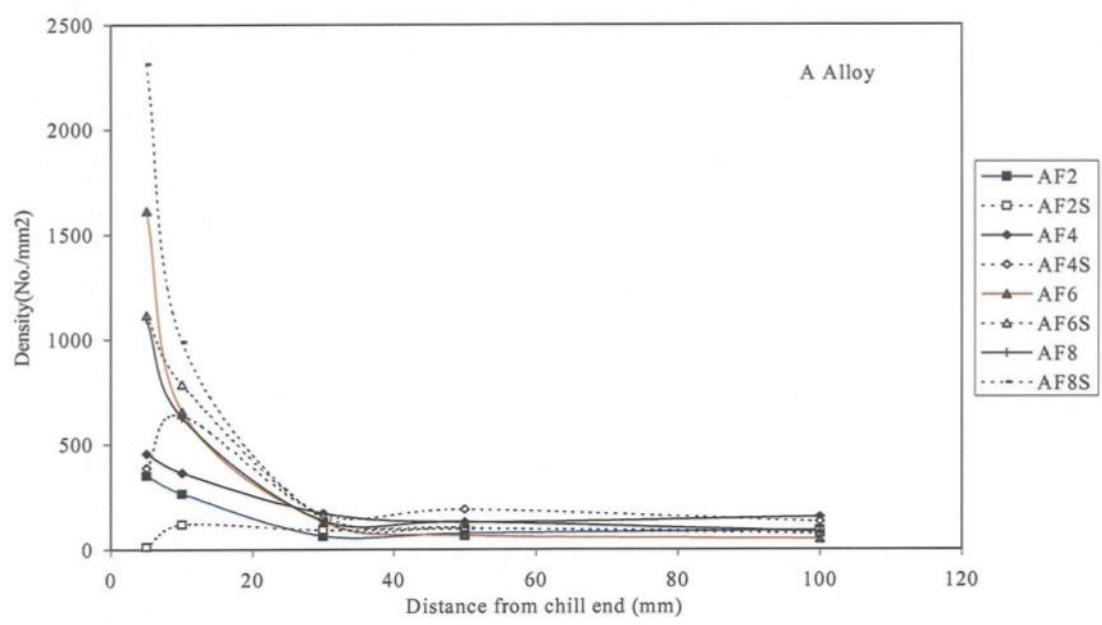


Figure 4.5 Effect of cooling rate on the  $\beta$ -platelet density in A319.2 alloys.

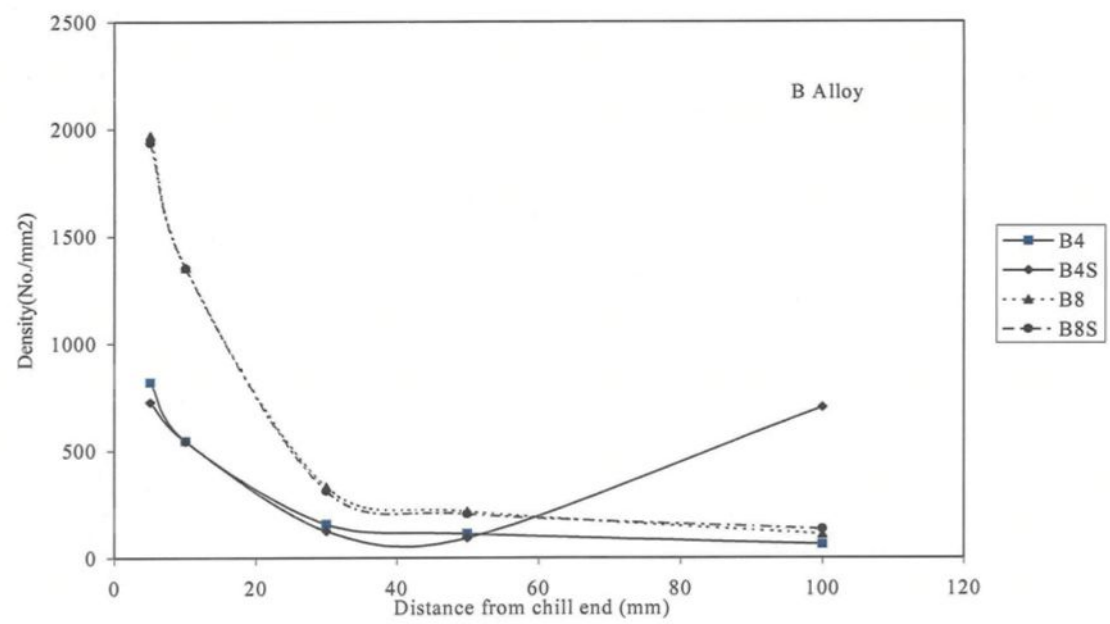
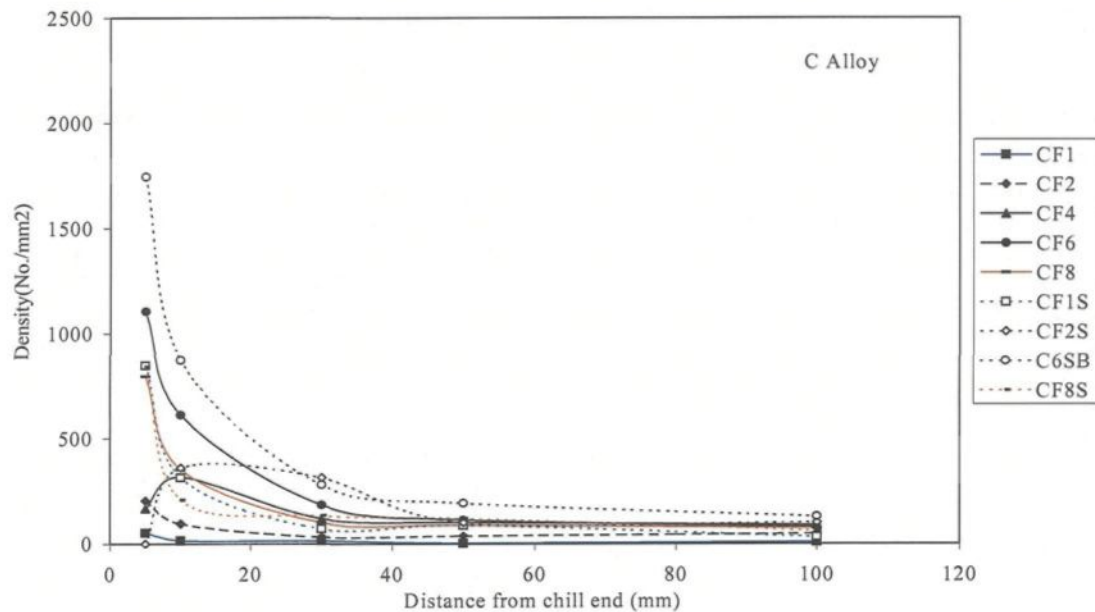


Figure 4.6 Effect of cooling rate on the  $\beta$ -platelet density in B319.2 alloys.



**Figure 4.7** Effect of cooling rate on the  $\beta$ -platelet density in A356.2 alloys.

#### 4.2.4 Microstructure

Figures 4.9 through 4.20 display the microstructures of selected samples corresponding to the three alloy types. The optical micrographs shown in these figures were taken from samples corresponding to the two extreme conditions of Fe level and cooling rate: low Fe-high cooling rate and high Fe-low cooling rate, in order to highlight/compare the microstructural differences between “optimum” and “poor” alloy conditions.

The qualitative analysis of the microstructures provided in this section were supported by quantitative image analysis result of measurements of the area fractions and average size of the  $\beta$ -iron intermetallics observed in these samples.

#### 4.2.4.1 A319.2 alloy

A typical microstructure obtained from A319.2 alloy is shown in Figure 4.8. The various phases that precipitate (marked 1 through 6) are: 1) an  $\alpha$ -Al dendrite, 2) a pre-eutectic  $\beta$ - $\text{Al}_5\text{FeSi}$  particle (big, thick needle), 3) an eutectic Si particle, 4) a post-eutectic  $\beta$ - $\text{Al}_5\text{FeSi}$  particle (thin needle), 5a) a block-like  $\text{Al}_2\text{Cu}$  particle, 5b) an eutectic ( $\text{Al}+\text{Al}_2\text{Cu}$ ) particle, and 6) an  $\text{Al}_5\text{Mg}_8\text{Cu}_2\text{Si}_6$  particle.<sup>75</sup>

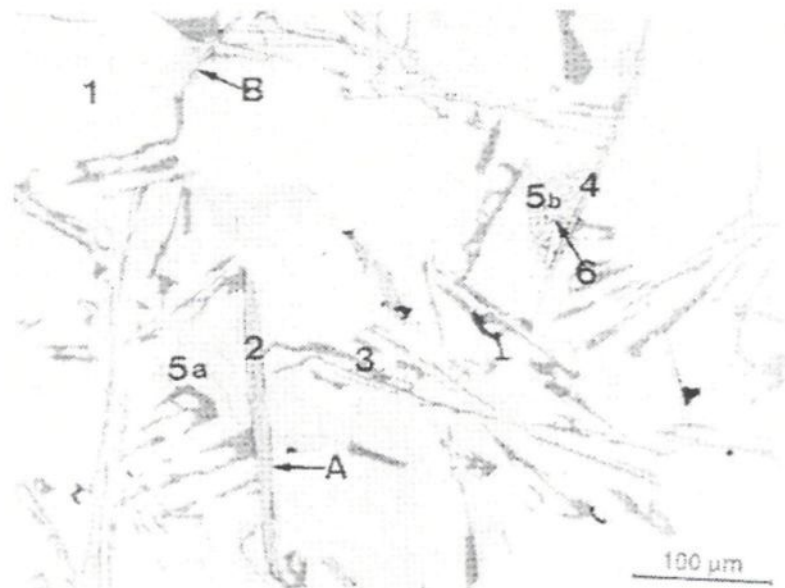


**Figure 4.8** Microstructure of as-solidified A319.2 alloy showing precipitation of: 1)  $\alpha$ -Al dendrite, 2) pre-eutectic  $\beta$ - $\text{Al}_5\text{FeSi}$ , 3) eutectic Si, 4) post-eutectic  $\beta$ - $\text{Al}_5\text{FeSi}$ , 5a) block-like  $\text{Al}_2\text{Cu}$ , 5b) eutectic  $\text{Al}+\text{Al}_2\text{Cu}$ , and 6)  $\text{Al}_5\text{Mg}_8\text{Cu}_2\text{Si}_6$  phase particles.<sup>75</sup>

In Figure 4.9, very fine  $\beta$ -needles are observed in the microstructure, often at the interface of the  $\alpha$ -Al dendrites or eutectic Si particles, indicating that they precipitated in a co-eutectic or post-eutectic reaction. The fine eutectic Si particles in Figure 4.10 show that the alloy is well modified.

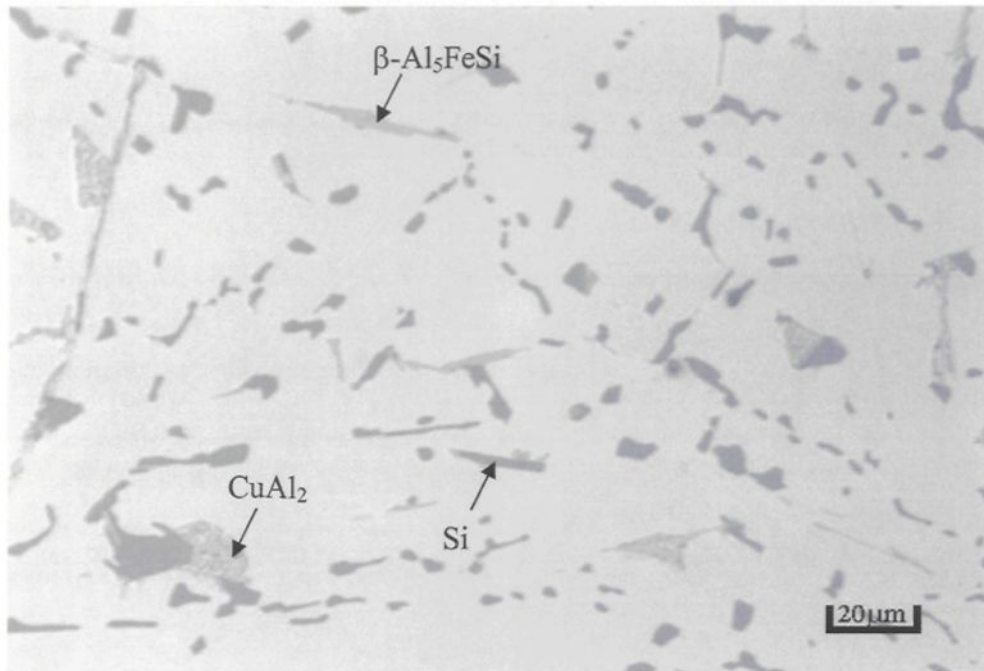


**Figure 4.9** Microstructure of AF2-0 alloy.

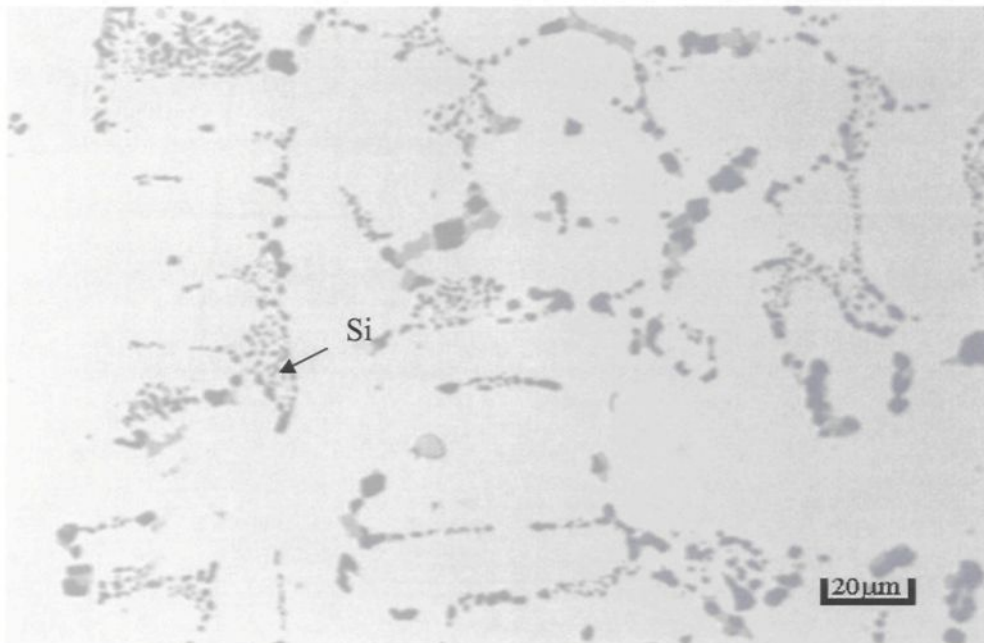


**Figure 4.10** Microstructure of AF2S-0 alloy.

Figure 4.11 shows examples of the microstructure exhibited by the AF8-C alloy sample (high Fe – low cooling rate condition). The optical micrograph of Figure 4.11(a) shows two distinct types of  $\beta$ -Al<sub>5</sub>FeSi platelets (or needles as they appear in the micrograph): large pre-eutectic  $\beta$  and smaller co-eutectic or post-eutectic  $\beta$ , corresponding to their sequence of precipitation with respect to the Al-Si eutectic reaction. The acicular eutectic Si particles indicate the unmodified nature of the alloy.

The backscattered image taken from the same sample, Figure 4.11(b), clearly reveals the platelet form of the  $\beta$ -Al<sub>5</sub>FeSi phase where the presence of the pore associated with the platelets assists in revealing the actual morphology of the  $\beta$ -phase. In comparison to the extremely large pre-eutectic  $\beta$  platelet observed at the top of the image, the  $\beta$  platelets within the pore show the much smaller size of what are most likely co- or post-eutectic  $\beta$ -Al<sub>5</sub>FeSi. Note the eutectic Si regions associated with the platelet near the bottom left of the image.

The difference in the sizes is related the rate of diffusion of the iron atoms with respect to the temperature at which the two platelet types precipitate. Mascré<sup>12</sup> confirmed that due to their size and shape, the pre-eutectic  $\beta$ -Al<sub>5</sub>FeSi are the most harmful in deteriorating the alloy mechanical properties. Due to the feedability problems related to the platelet-like nature of the  $\beta$ -phase, the occurrence of porosity is often observed in association with the  $\beta$ -platelets.

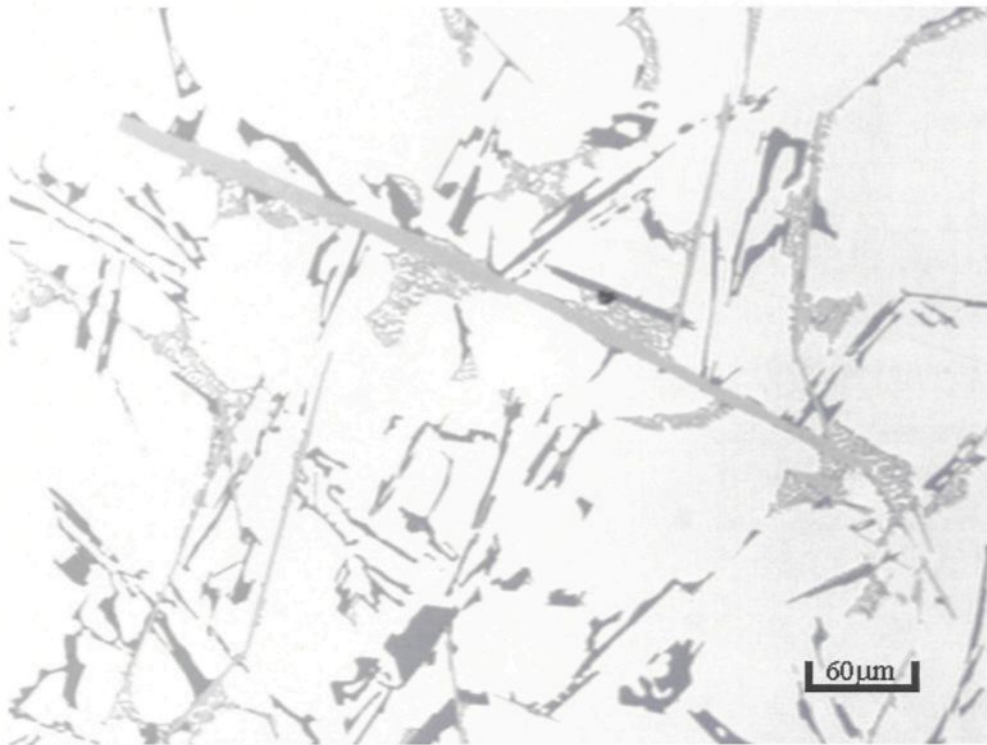


**Figure 4.11 (a)** Microstructure of AF8-C alloy.

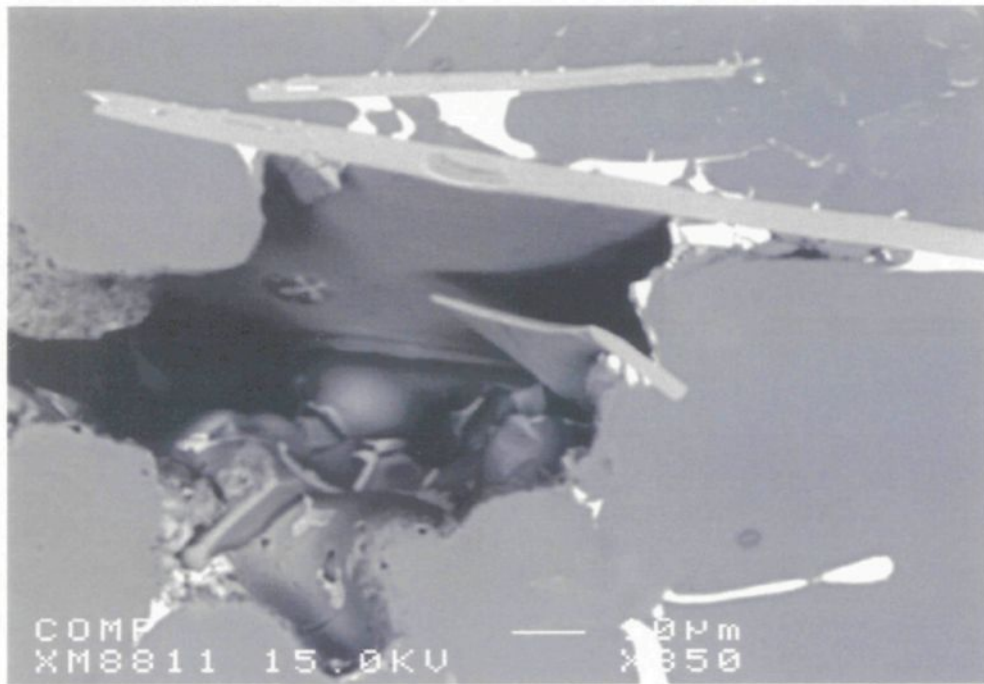


**Figure 4.11(b)** Backscattered image taken from the AF8-C alloy.

In the case of the modified alloy obtained under the same conditions (AF8S-C alloy), Figure 4.12, while the eutectic Si regions were well modified by the addition of Sr, the effect of Sr on the fragmentation and dissolution of the  $\beta$ -platelets was observed for the smaller sized (and thinner)  $\beta$  particles (see arrows), whereas the large pre-eutectic  $\beta$  remained unaffected. The persistence of such massive  $\beta$ -platelets in the microstructure provides a good indication of why the properties of alloys containing Fe levels of 0.8% or higher cannot be improved by any means, and hence why such alloys should be rejected.

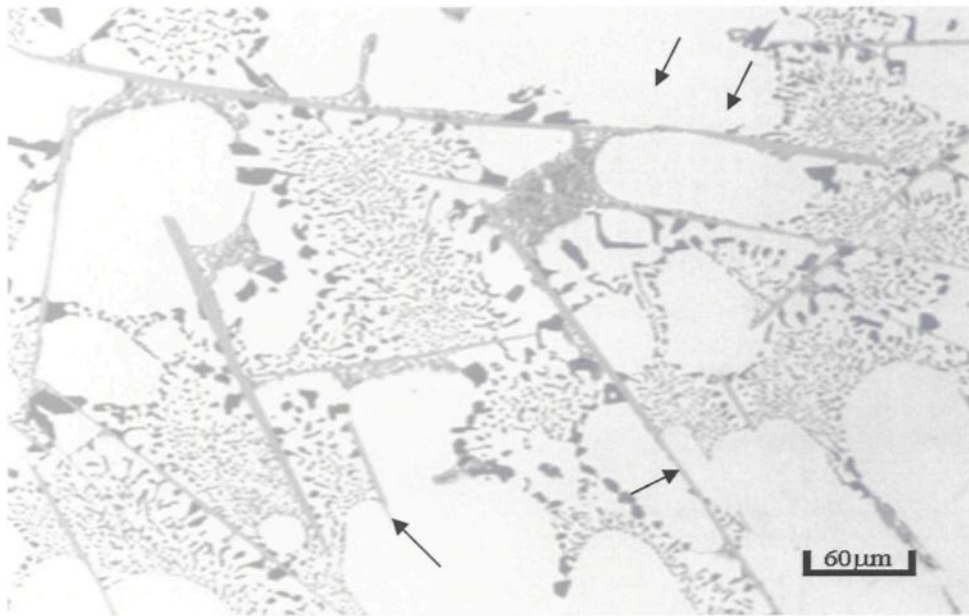


**Figure 4.12** Microstructure of AF8S-C alloy.

#### 4.2.4.2 B319.2 alloy

Figures 4.13 through 4.16 show the microstructures of the 0.4% and 0.8% Fe-containing B319.2 alloys. The B319.2 alloy is a higher Mg-containing version of A319.2 alloy employed in automotive applications. The high Mg content (0.4%) leads to the precipitation of  $Mg_2Si$  (or a Mg-rich) phase that appears in the form of rounded black particles dotted along the sides of the eutectic Si particles,<sup>75</sup> as observed clearly in Figure 4.16, and to some extent in Figure 4.15, as well (see open arrows in both figures).

It is interesting to note the difference in the appearance of the eutectic Si particles in these figures, where Mg is also known to modify the eutectic Si. Due to the presence of 0.026% Mn in the alloy, several  $\alpha$ -iron intermetallics are also observed in the microstructure of the B8-C alloy.

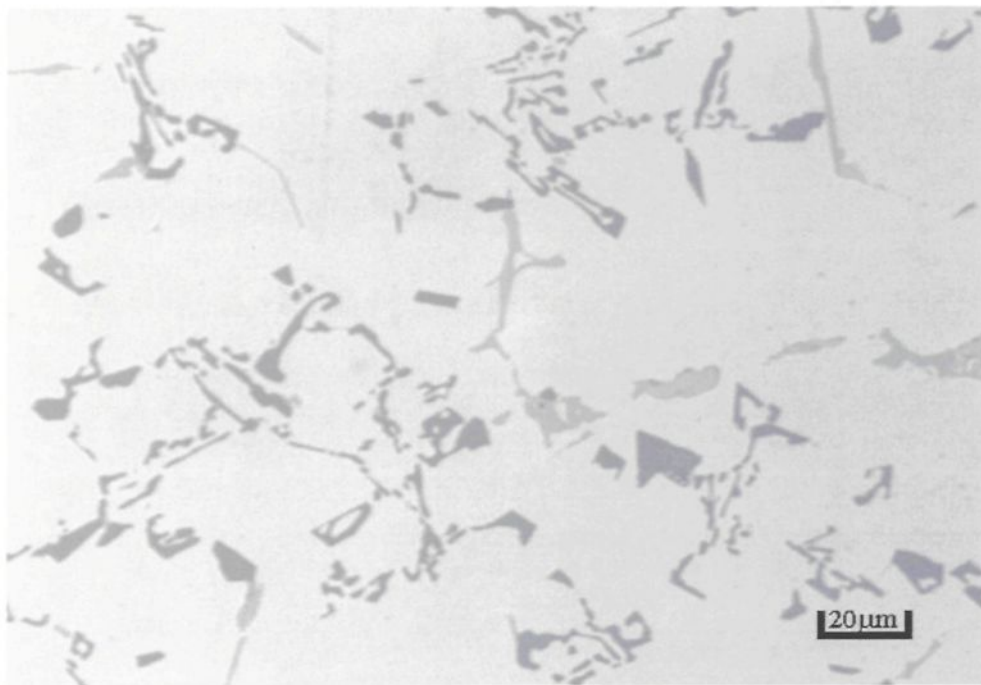


**Figure 4.13** Microstructure of B4-0 alloy.

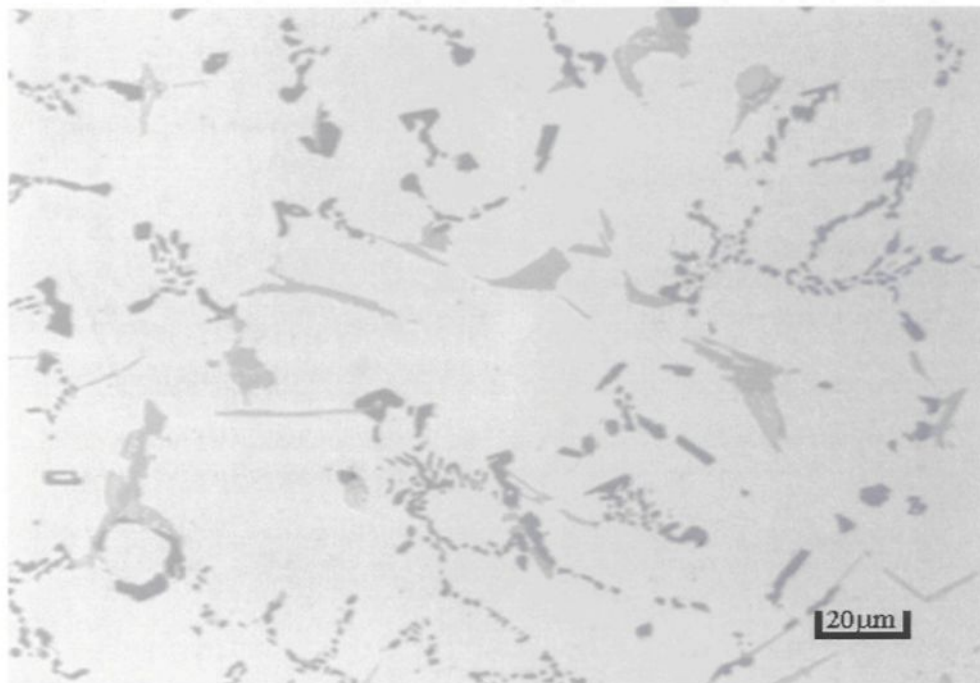


**Figure 4.14** Microstructure of B4S-0 alloy.

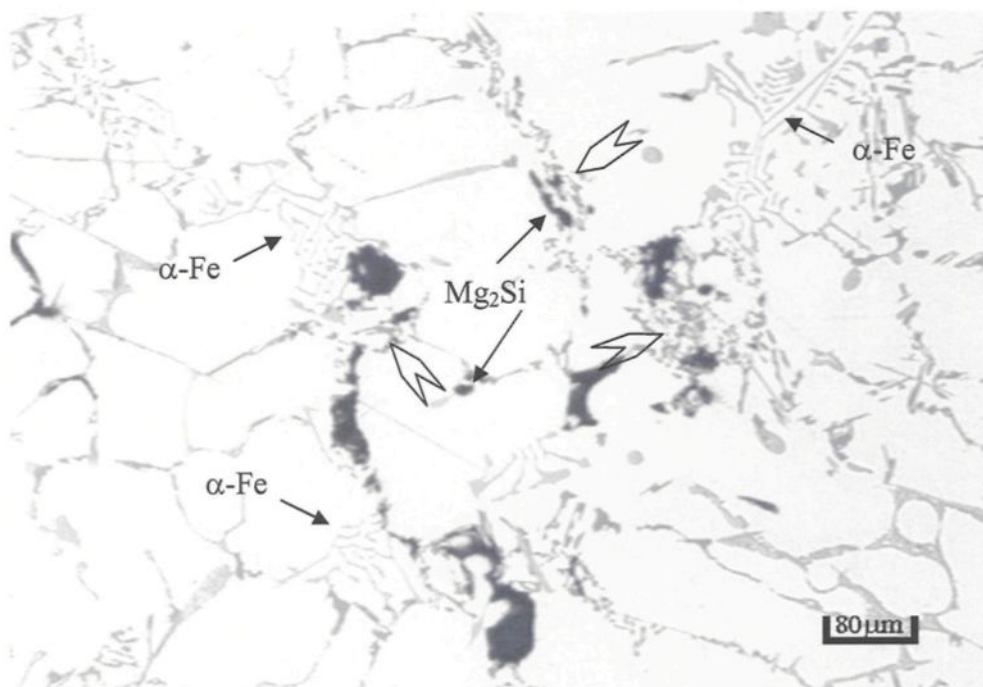


**Figure 4.15** Microstructure of B8-C alloy.

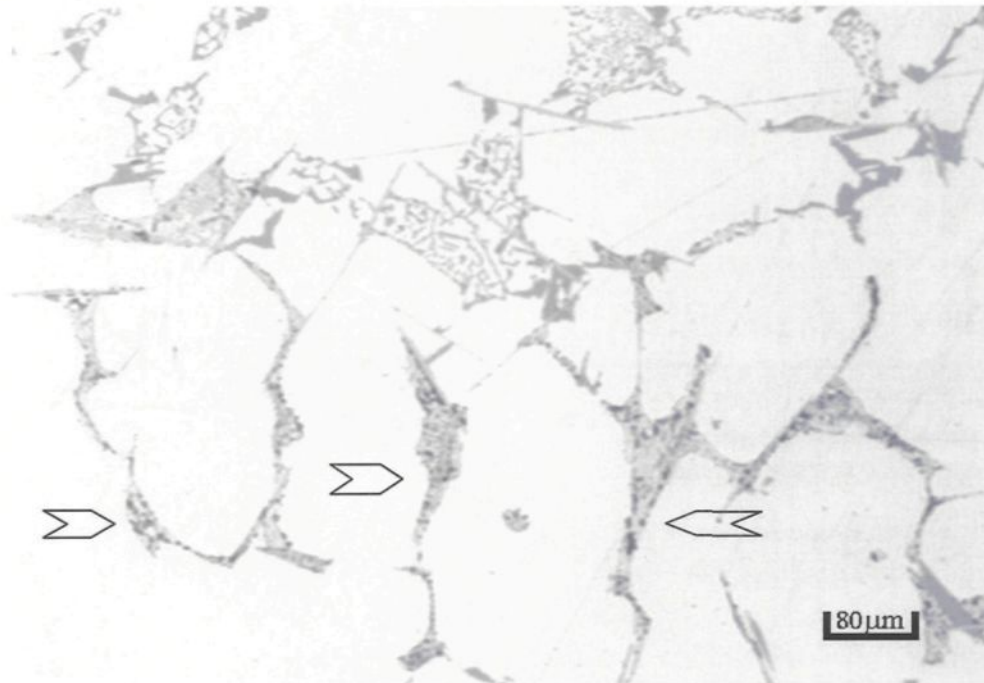


**Figure 4.16** Microstructure of B8S-C alloy.

#### 4.2.4.3 A356.2 alloy

Figures 4.17 and 4.18 show examples of the microstructures of the low-Fe alloy samples obtained at the highest cooling rate. All microconstituents are fine and, as the high magnification micrograph of Figure 4.18 shows, the eutectic Si regions are well modified in the CF1S-0 sample, as are the  $\beta$ -platelets (arrowed).

The optical micrograph of Figure 4.19(a) shows the presence of a large number of  $\beta$ - $\text{Al}_5\text{FeSi}$  platelets at the 0.8% Fe level-lowest cooling rate conditions. The high magnification micrograph of Figure 4.19(b) reveals the dimensions of the pre-eutectic  $\beta$ -platelets, and the partial transformation of the  $\beta$ -platelets into the  $\text{Al}_8\text{Mg}_3\text{FeSi}_6$  phase in two cases (arrowed), on account of the magnesium present in the alloy.

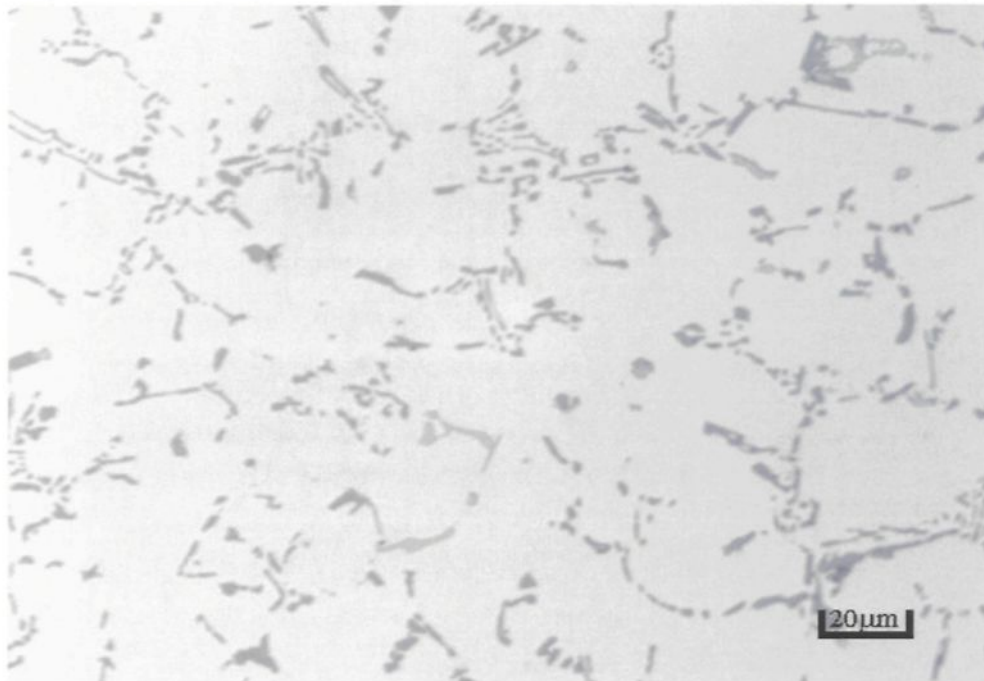


**Figure 4.17** Microstructure of CF1-0 alloy.

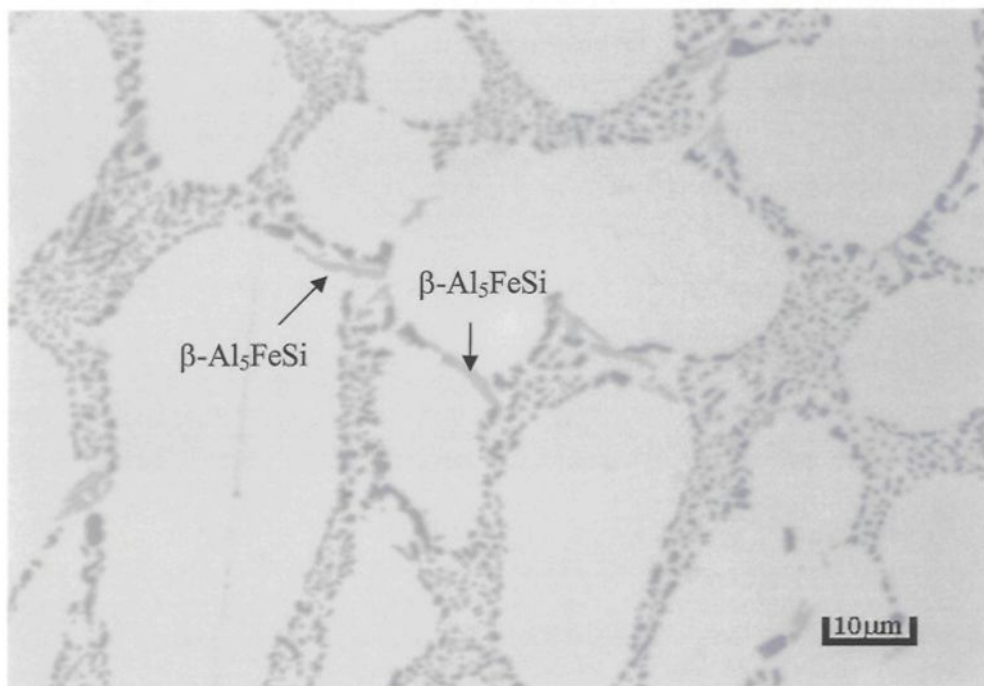


**Figure 4.18** Microstructure of CF1S-0 alloy.

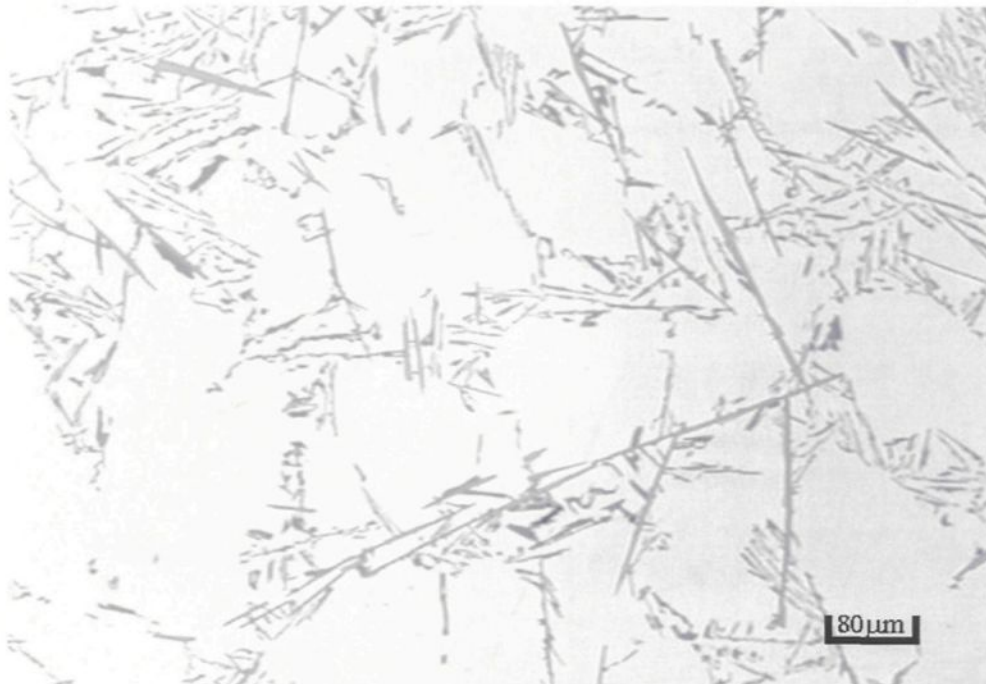


Figure 4.19 (a) Microstructure of CF8-C alloy.

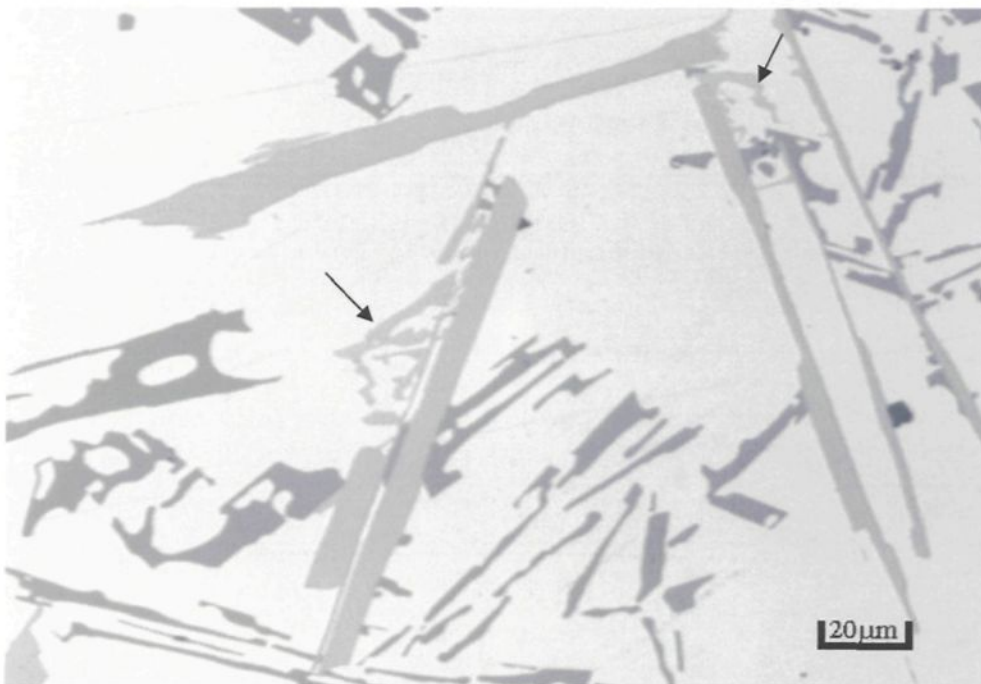
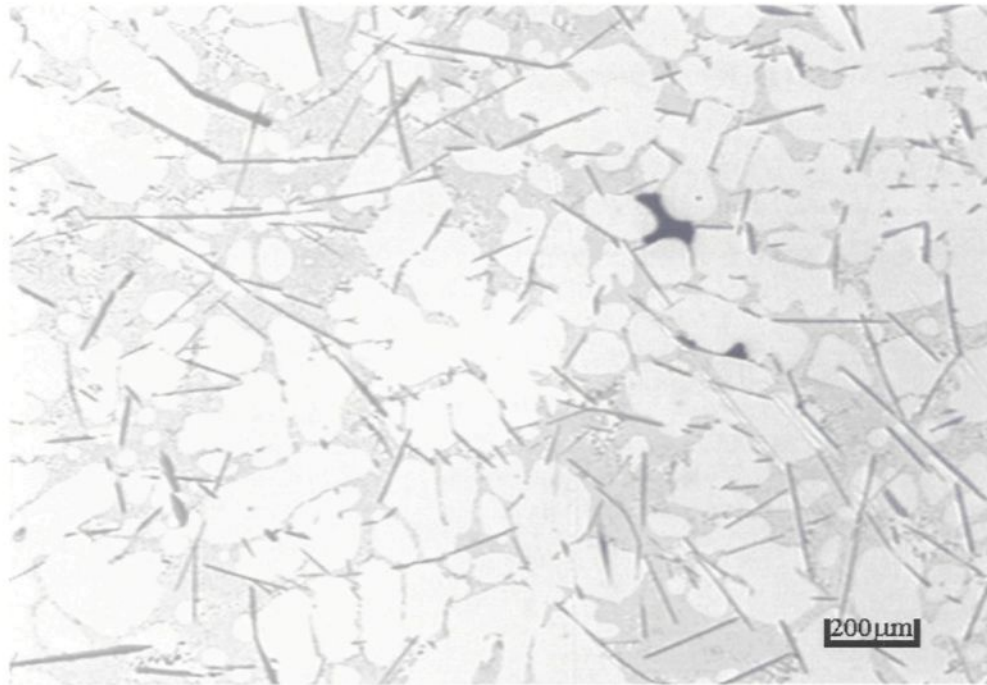
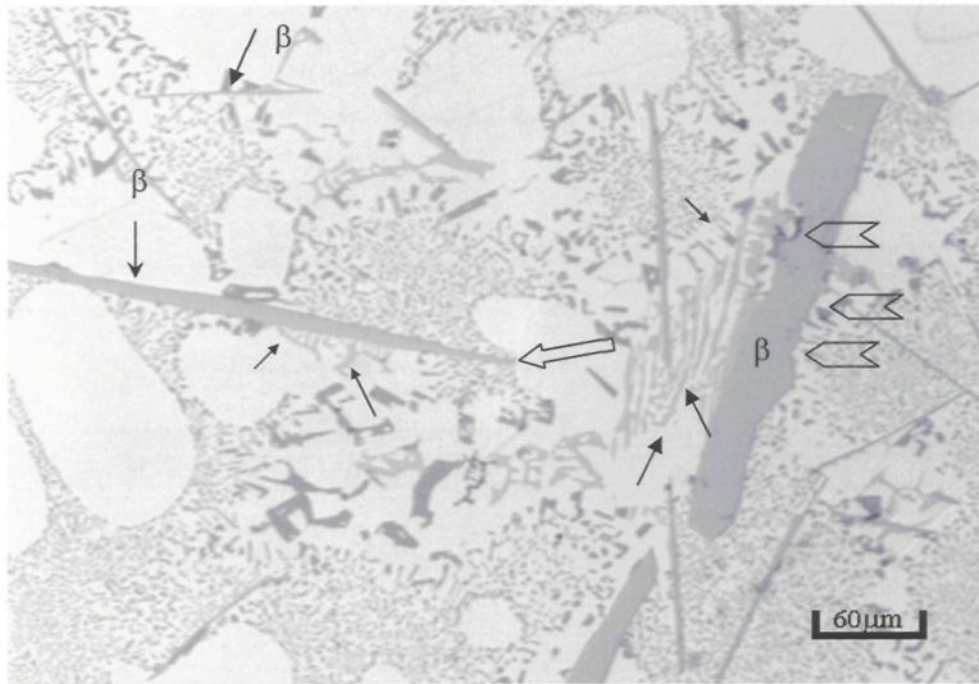


Figure 4.19(b) Microstructure of CF8-C alloy.

Figure 4.20(a) shows another example of the same alloy, in the modified condition, obtained at 50 mm level above the chill end, showing the profusion of  $\beta$ -platelets in the microstructure. The high magnification micrograph of Figure 4.20(b) shows the three types of  $\beta$ -platelets that occur, well-modified eutectic Si regions, as well as partial transformation of the large (to the right) and the long (to the left)  $\beta$ -platelets into the  $\text{Al}_8\text{Mg}_3\text{FeSi}_6$  phase (see small black arrows). Note the irregular contours of the  $\beta$ -platelets that are affected by the Sr or where the transformation takes place (see open arrow heads), and the thinning of the long  $\beta$ -platelet at its end (see open arrow).



**Figure 4.20(a)** Microstructure of CF8S-3 alloy.



**Figure 4.20(b)** Microstructure of CF8S-3 alloy.

#### 4.2.5 Mechanism of $\beta$ - $\text{Al}_5\text{FeSi}$ Fragmentation

The backscattered images of Figures 4.21 and 4.22 reveal the effect of Sr in the fragmentation and dissolution of the  $\beta$ - $\text{Al}_5\text{FeSi}$  phase. It is in this context that “Sr modification” is understood with respect to the  $\beta$ -iron phase.

As can be seen in Figure 4.21, due to the dissolution effect of Sr, the  $\alpha$ -Al dendrites appear through regions of the  $\beta$ - $\text{Al}_5\text{FeSi}$  platelet where dissolution has taken place, the  $\beta$ -platelet being observed within a shrinkage pore in the A319.2 alloy containing 0.4% Fe. Other  $\beta$ - $\text{Al}_5\text{FeSi}$  platelets (or needles as they appear in the micrograph) are fine and of small or medium size.

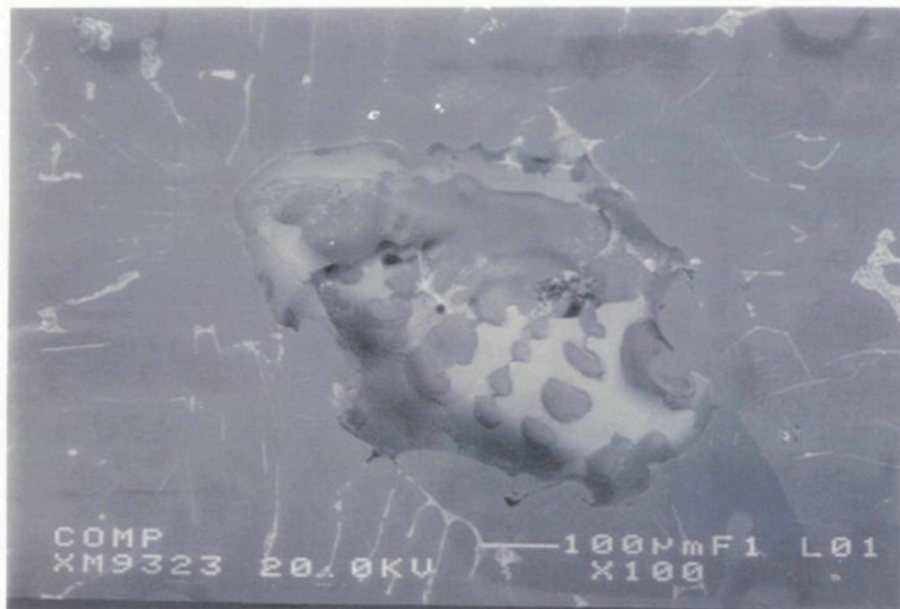


**Figure 4.21** SEM micrograph taken from the Sr-modified A319.2-0.4%Fe alloy, showing the dissolution effect of Sr on the  $\beta$ -Al<sub>5</sub>FeSi phase.

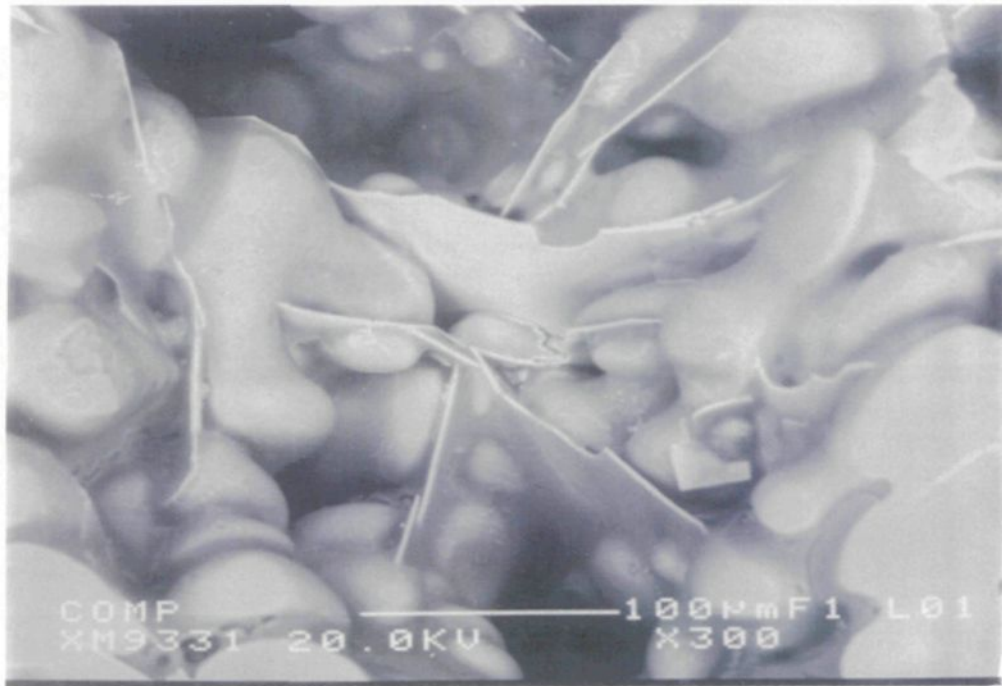
Compared to this sample, the  $\beta$ -Al<sub>5</sub>FeSi needles observed in the backscattered image taken from the 0.8% Fe – containing A319.2 alloy sample, Figure 4.22(a), shows the profusion of  $\beta$ -platelets that occur at such high Fe levels. The three-dimensional nature of the linking of these platelets is clearly viewed within the pore from which this image was taken; such  $\beta$ -platelets are what appear as branched  $\beta$ -platelets in a two-dimensional optical micrograph.

It is worth noting that the  $\beta$ -platelets appear to be solid in nature, indicating that Sr has no effect upon these platelets. Also, the fact that the  $\alpha$ -Al dendrites appear in their natural rounded form indicates that the observed pore is a shrinkage pore, and the porosity results from the blocking effect of the  $\beta$ -platelets to the liquid metal flow during the

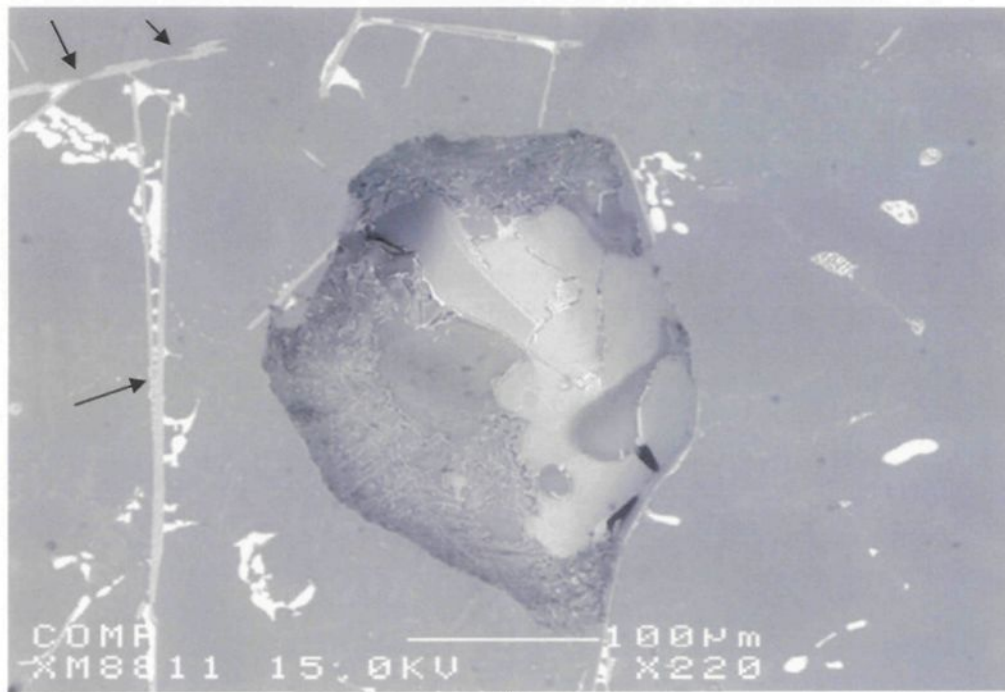
solidification process. Thus the porosity observed in conjunction with the  $\beta$ -iron platelets results from feedability-associated problems.

The backscattered image shown in Figure 4.22(b), taken from Sr modified sample (same alloy), depicts an example of a  $\beta$ -Al<sub>5</sub>FeSi platelet within a rounded pore, where the progress of fragmentation of the  $\beta$ -platelet is evident. Modified eutectic Si regions and  $\alpha$ -Al dendrites (flat, dark grey areas) are also observed around the  $\beta$ -platelet. The flattened nature of the dendrites as well as the rounded morphology of the pore indicate that this is a gas pore. Elsewhere in the matrix, other  $\beta$ -platelets (light grey needles) and CuAl<sub>2</sub> intermetallic particles (white) are also seen. The dissolution effect of Sr on the  $\beta$ -platelet at the top left corner of the figure is clearly observed (arrowed), whereas the much larger  $\beta$ -platelet perpendicular to it appears to be unaffected.

The two backscattered micrographs of Figure 4.22 demonstrate that the smaller-sized co- and post-eutectic  $\beta$ -platelets are easily fragmented due to the action of Sr, whereas large, pre-eutectic platelets resist modification, and are not affected that easily by the presence of strontium.



(a)



(b)

**Figure 4.22** Backscattered images of (a) unmodified, and (b) Sr-modified A319.2-0.8% Fe alloy showing  $\beta$ -Al<sub>5</sub>FeSi platelet characteristics.

### 4.3 EFFECT OF IRON CONTENT ON POROSITY FORMATION

Figures 4.23 through 4.26 show the plots of percentage porosity, maximum pore area and pore density that were obtained for the unmodified and Sr-modified A319.2 and A356.2 alloys, as a function of iron content and cooling rate. From these plots, the following points are observed.

For the A319.2 alloy, the lowest percentage porosity and lowest maximum pore area appear at 0.4 wt% iron content, whether the alloy is modified with Sr or not. Lower or higher iron contents increase the amount of porosity formed. At the highest cooling rate (*i.e.*, at 5 mm distance from the chill end, DAS  $\sim$  15  $\mu$ m), the effect of iron content is not that obvious.

An increase in cooling rate decreases both the total amount of porosity and the maximum pore size observed in the modified and unmodified alloys. With increasing solidification rates, less time is available for hydrogen to diffuse into the interdendritic regions of the partially solidified metal, resulting in a smaller pore size. Furthermore, the higher temperature gradients present at higher solidification rates tend to limit the length of the mushy zone, to make feeding easier and retard porosity formation.

When Sr is added, the porosity level is increased on account of two factors, one of them being the formation of strontium oxide (particles or films), due to the high affinity of strontium for oxygen. These oxides are always observed associated with microporosity. Secondly, the addition of Sr can lower the surface tension, an effect which would facilitate pore nucleation and result in increased porosity in modified alloys.

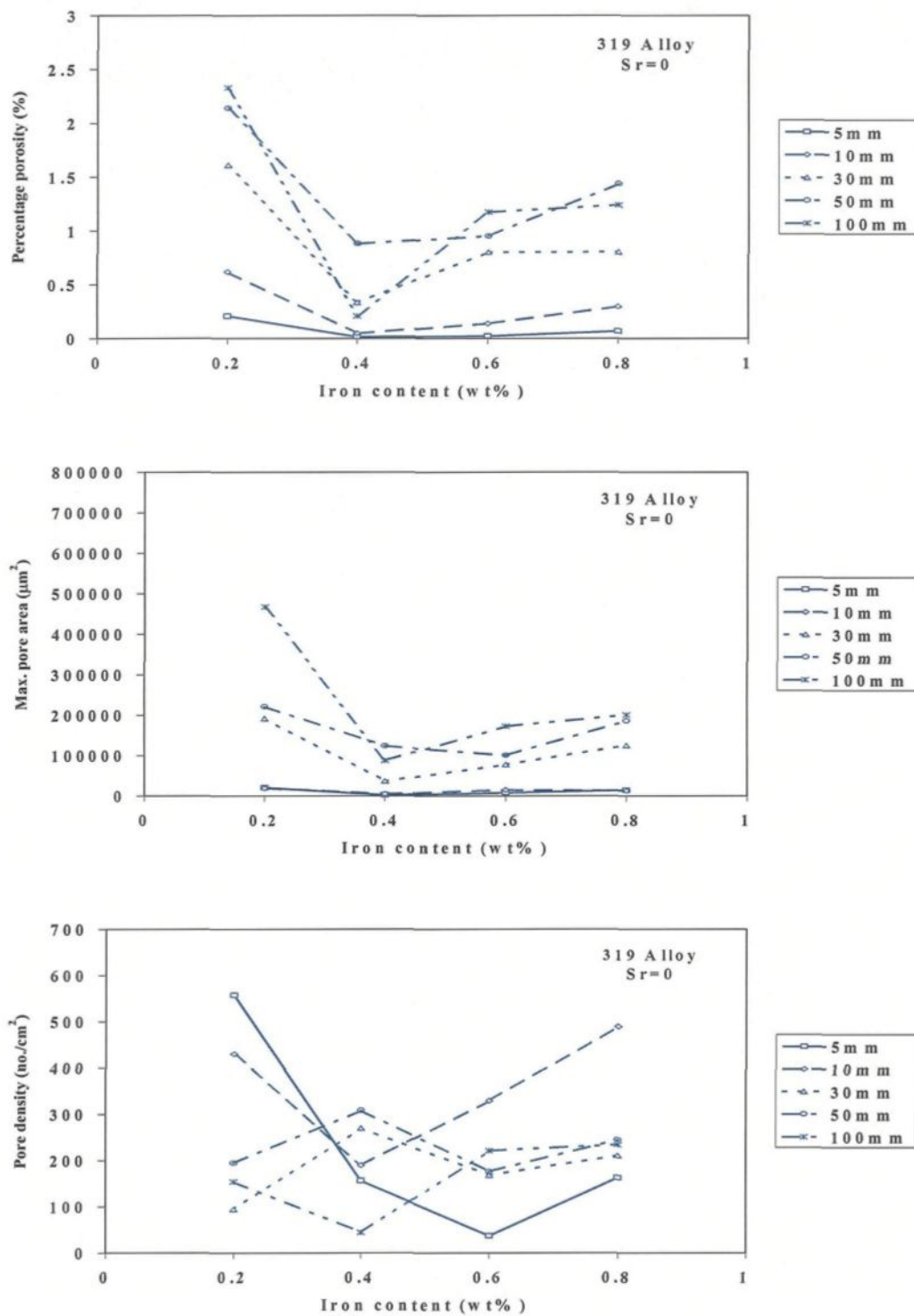


**Figure 4.23**

Porosity parameters (percentage porosity, maximum pore area and pore density) as a function of iron content and cooling rate observed in unmodified A319.2 alloy.

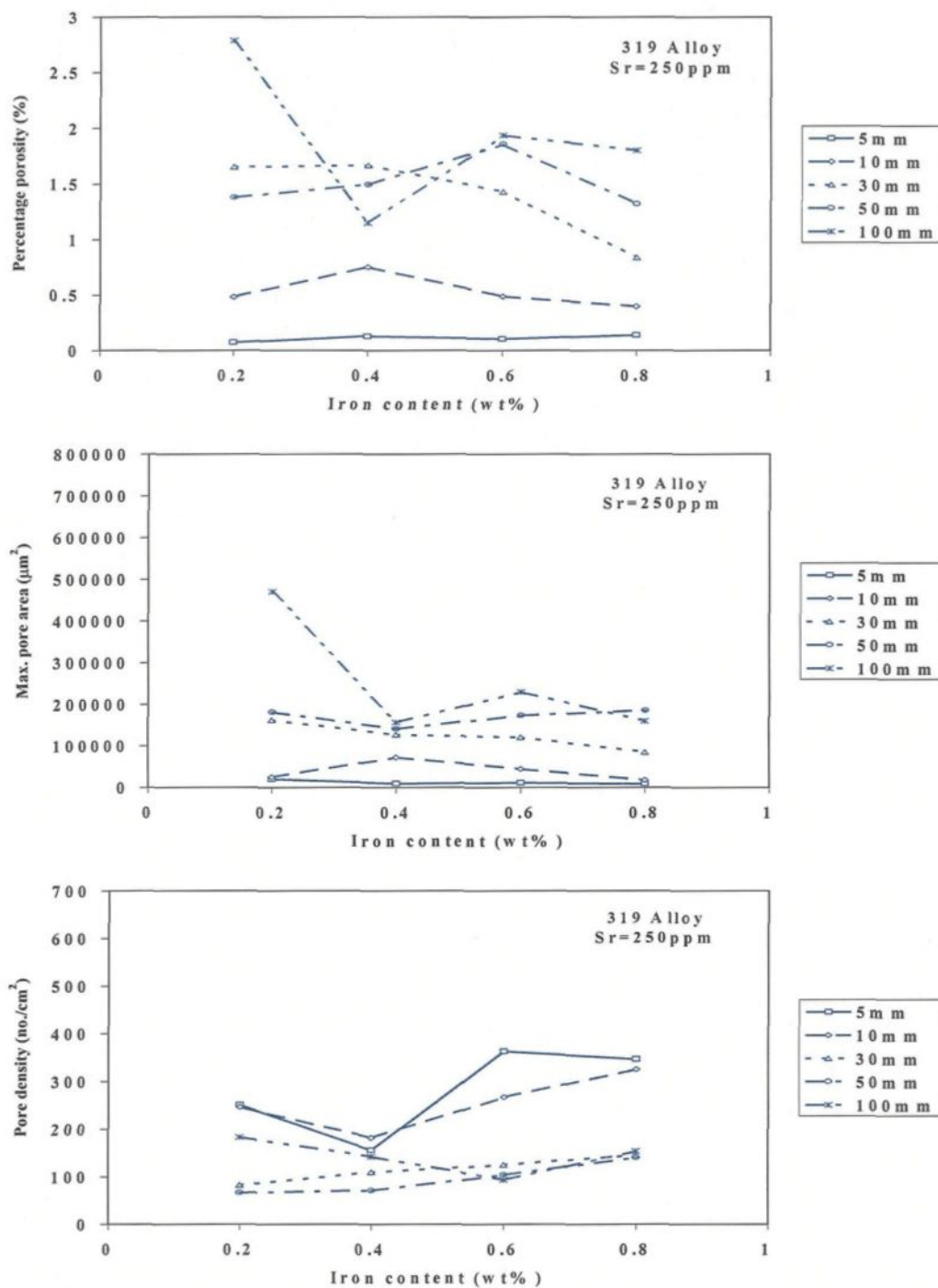


**Figure 4.24** Porosity parameters (percentage porosity, maximum pore area and pore density) as a function of iron content and cooling rate observed in Sr-modified A319.2 alloy.

In the case of A356.2 alloy, minimum porosity and pore size appear to occur at ~0.6 wt% Fe in the unmodified alloy, and at ~0.4 wt% Fe in the modified alloy. Comparing the two sets of plots, it is also noted that the A319.2 alloys exhibit much larger maximum pore areas than the A356.2 alloys and also higher overall porosity.

Taylor *et al.*<sup>87,110,111</sup> studied the role of iron (0.1 to 1 wt%) in the formation of porosity in non-grain-refined, unmodified Al-5.2%Si-1.2%Cu-0.5%Mg alloy and observed that i) the total porosity was minimized at 0.4 pct Fe; ii) a localized shrinkage-porosity defect (termed “extended defect”) developed at high iron concentrations; and iii) there was a change in porosity characteristics from a discrete pore morphology at 0.1%Fe levels to zones of sponge-like interdendritic porosity at higher Fe levels. They suggested that the mechanism by which iron causes such porosity defects may be related to the solidification sequence of the alloy.

Using a phase diagram approach and calculated segregation lines on the liquidus projection of the ternary Al-Si-Fe phase diagram, they proposed that when solidification proceeds directly from the primary ( $\alpha$ -Al) field to the ternary Al-Si- $\beta$ Al<sub>5</sub>FeSi eutectic point, the porosity is minimized at the critical iron content, whereas when solidification takes place via the binary Al- $\beta$ Al<sub>5</sub>FeSi eutectic, higher porosity levels are obtained. Large  $\beta$  needles are binary  $\beta$  which forms prior to the ternary eutectic, while small  $\beta$  needles are ternary  $\beta$ , and are the first component of the ternary eutectic to form.

They also observed that the critical iron content at which the porosity is minimized is a function of the alloy Si content (*e.g.*, for Al-10%Si alloy, the critical Fe content was found to have shifted to 0.7 pct). They further proposed that the alloy-dependent critical

iron content determines when the  $\beta$ -iron phase first solidifies and hence when it can participate in the silicon nucleation event (the  $\beta$ -platelet being observed to actively participate in the nucleation and growth of eutectic silicon).

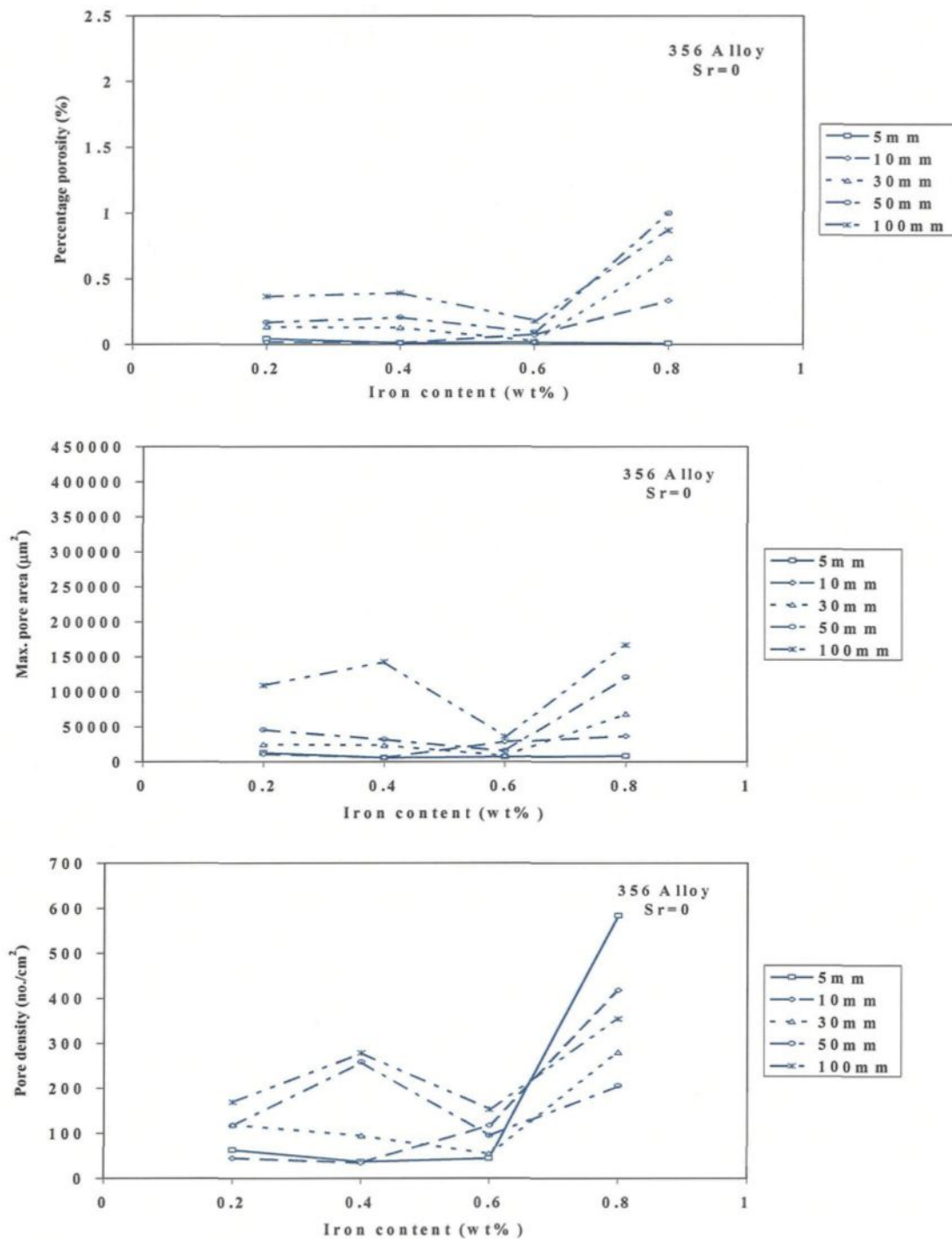
At critical Fe contents, the  $\beta$ -phase solidifies as the initial component of the ternary eutectic. At higher Fe levels, the  $\beta$ -phase is already well developed when ternary eutectic solidification commences, whereas at lower Fe levels, the  $\beta$ -phase forms as a component of the ternary eutectic only after the binary Al-Si eutectic is formed. Each of these solidification paths leads to different variations in microstructural permeability, *i.e.*, interdendritic feedability and, hence, porosity formation. At the critical Fe level, the smaller, ternary  $\beta$  do not block interdendritic liquid flow, whereas below and above the  $Fe_{crit}$  level, larger binary  $\beta$  block the interdendritic regions, causing higher porosity levels.

Comparing the present results with those of Taylor *et al.*,<sup>87,110,111</sup> minimum porosity levels are also observed at 0.4 pct Fe levels in the A319.2 alloy, and at 0.4 – 0.6 pct Fe levels in the A356.2 alloy. As the casting methods employed in the two studies are different, only a qualitative comparison can be made. As will be shown towards the end of this chapter, both alloy fluidity and average maximum  $\beta$ -platelet size were found to increase with increasing iron content in the 319 and 356 alloys. It is suggested that the competition between these two factors determines the actual porosity observed at a particular Fe level.

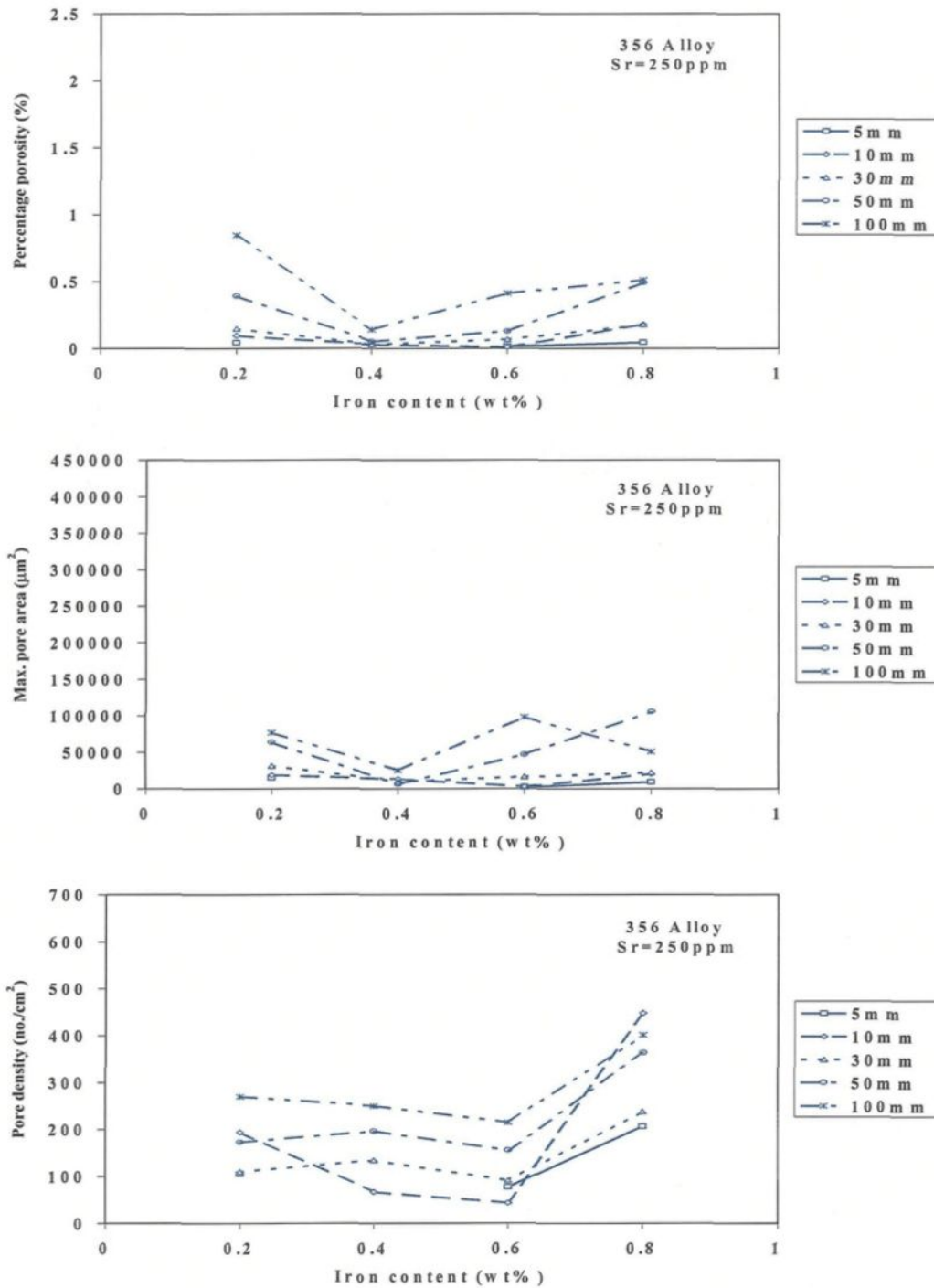
As  $\beta$ -platelet measurements in the present work were focused on the largest  $\beta$  needles observed in the microstructure (these being assumed to cause the greatest hindrance

to feedability), we cannot really comment upon the effect of small versus large  $\beta$  needles. Nevertheless, both Taylor *et al.*'s point of view and ours essentially relate the amount of porosity formed to the permeability or ease of liquid flow through the interdendritic regions during the course of solidification.

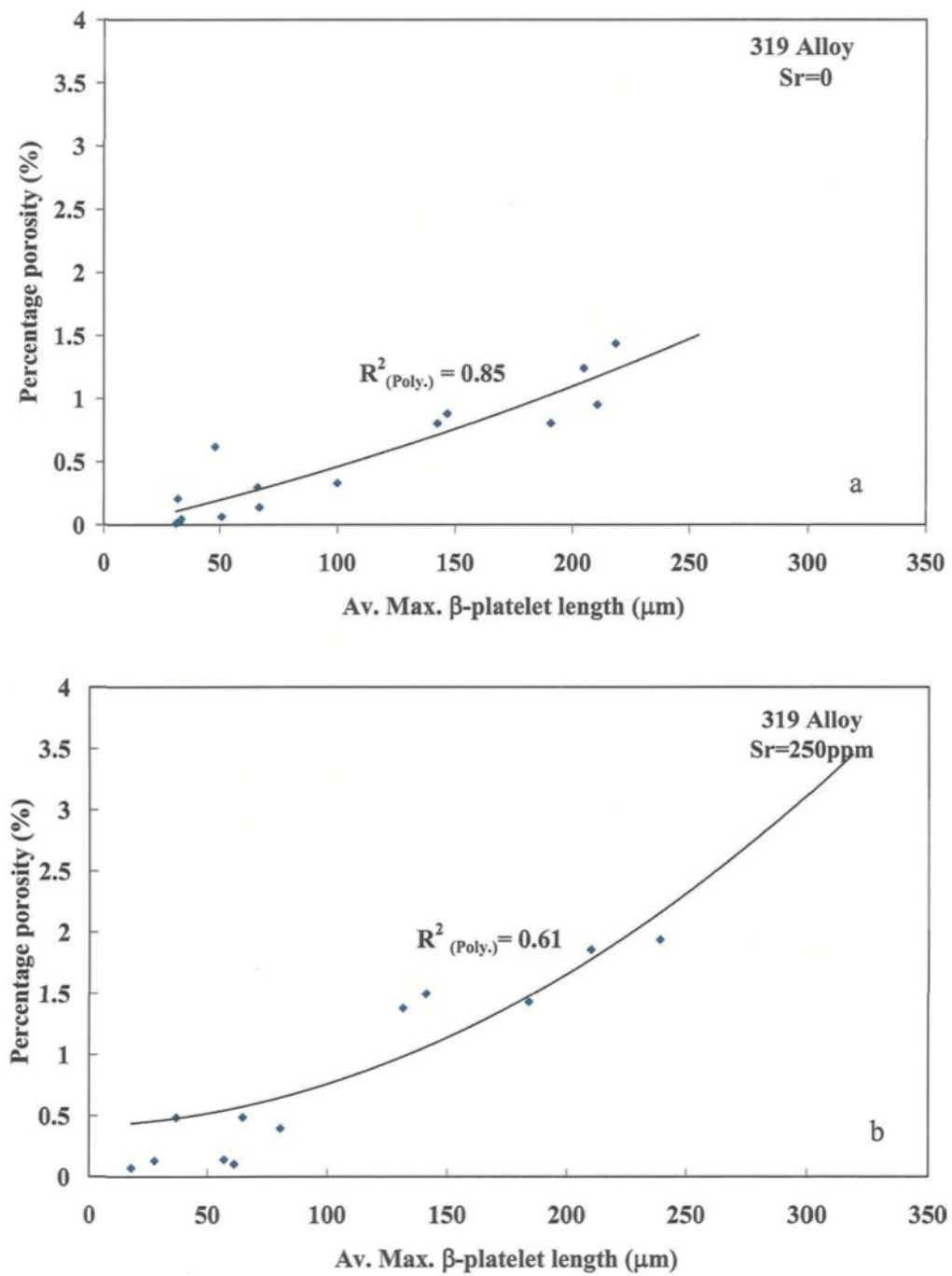
In Figures 4.27 through 4.30, the porosity parameters (percentage porosity, maximum pore area, and maximum pore length) have been plotted as a function of the average maximum  $\beta$ -Al<sub>5</sub>FeSi platelet length. It is seen that, in general, these parameters increase with the increase in average maximum  $\beta$ -platelet length for the two alloys, and that the unmodified alloys show better correlations than the Sr-modified alloys. This could be due to the fact that in the Sr-modified alloys, the SrO formed due to the presence of Sr also provides nucleation sites for porosity formation. Thus, there are two parameters influencing porosity formation, so that, in general, lower correlation factors are obtained when the porosity parameters are plotted versus the  $\beta$ -platelet size in the case of the modified alloys.



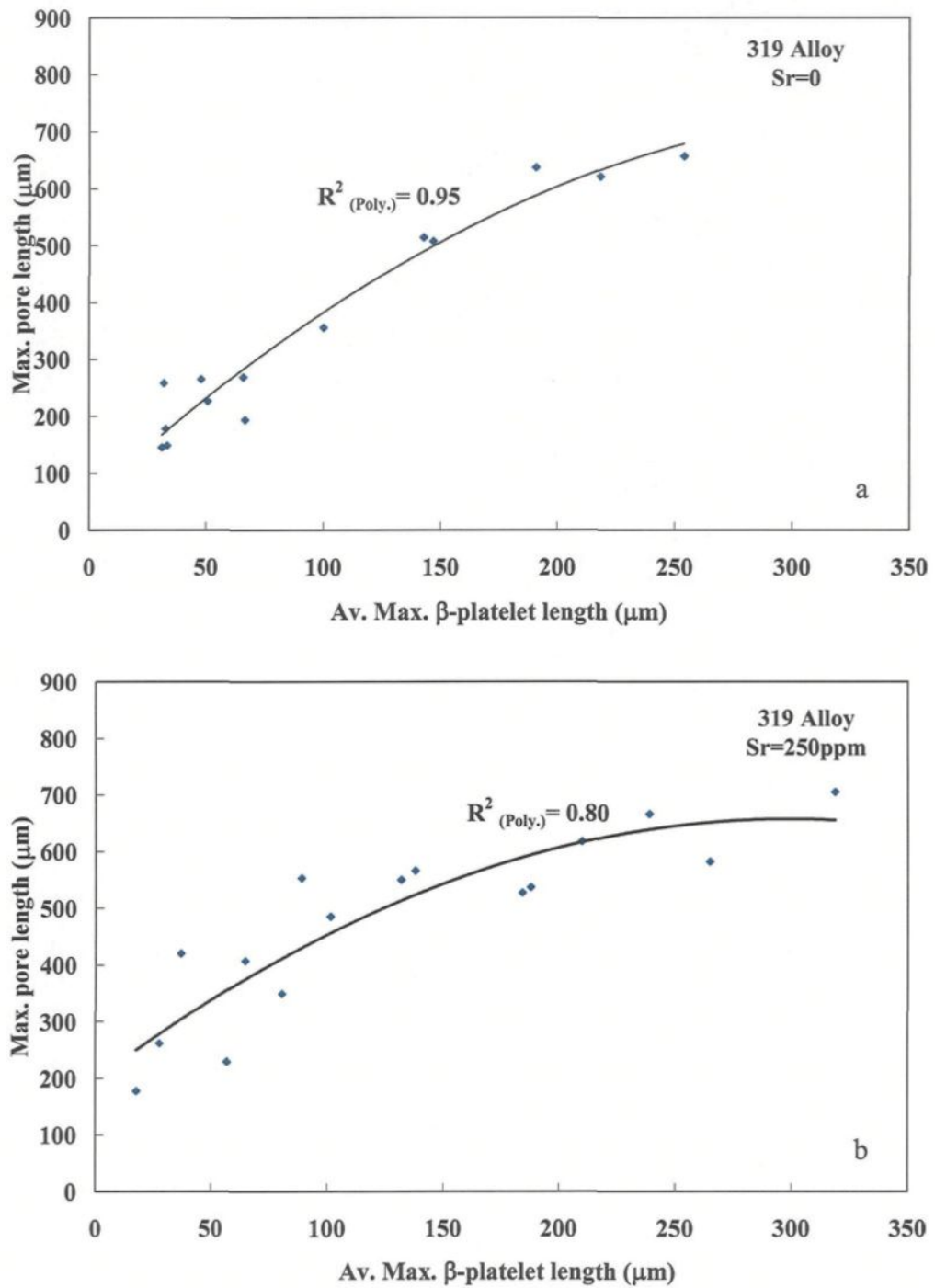
**Figure 4.25** Porosity parameters (percentage porosity, maximum pore area and pore density) as a function of iron content and cooling rate observed in unmodified A356.2 alloy.



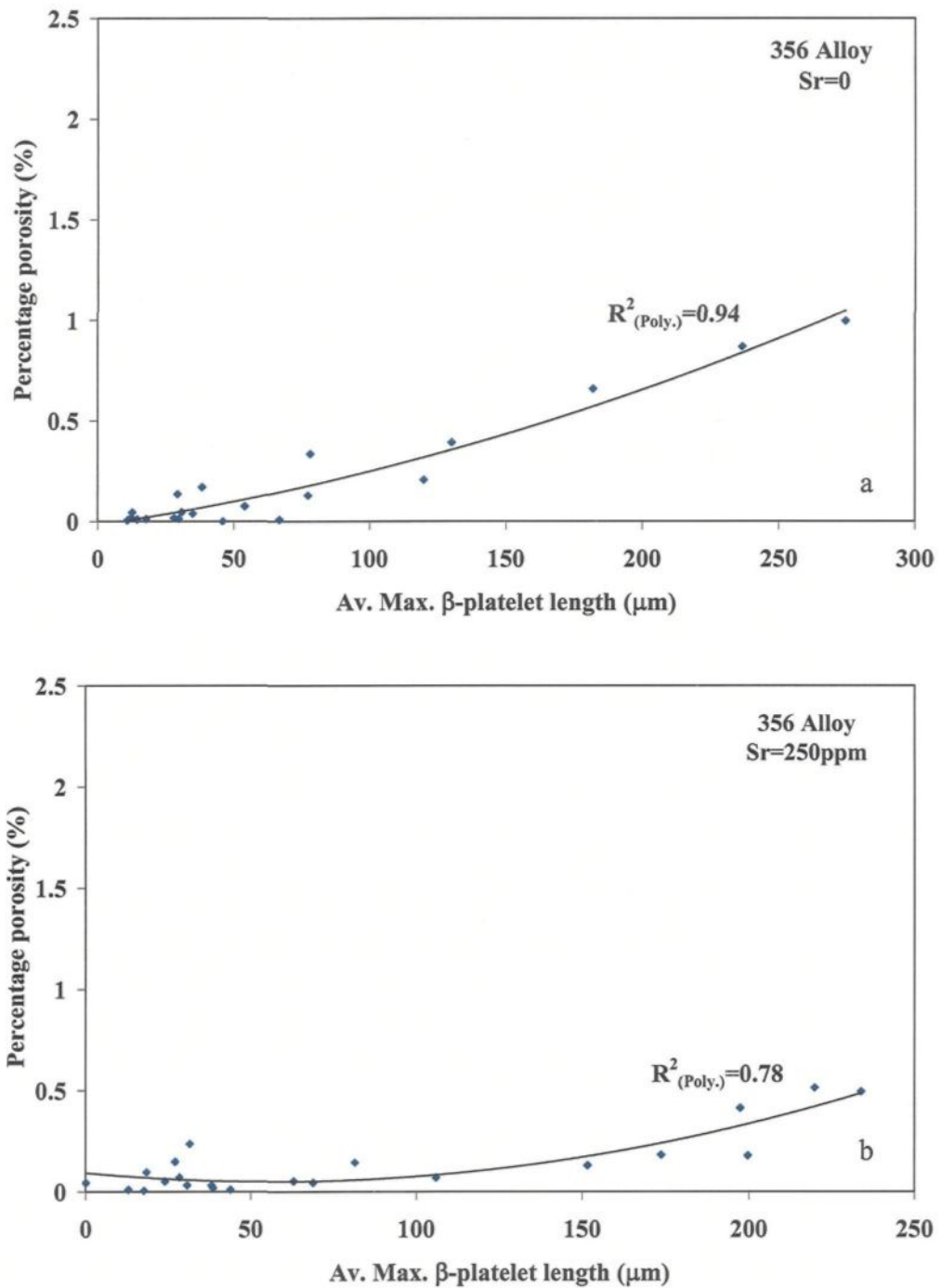
**Figure 4.26** Porosity parameters (percentage porosity, maximum pore area and pore density) as a function of iron content and cooling rate observed in Sr-modified A356.2 alloy.



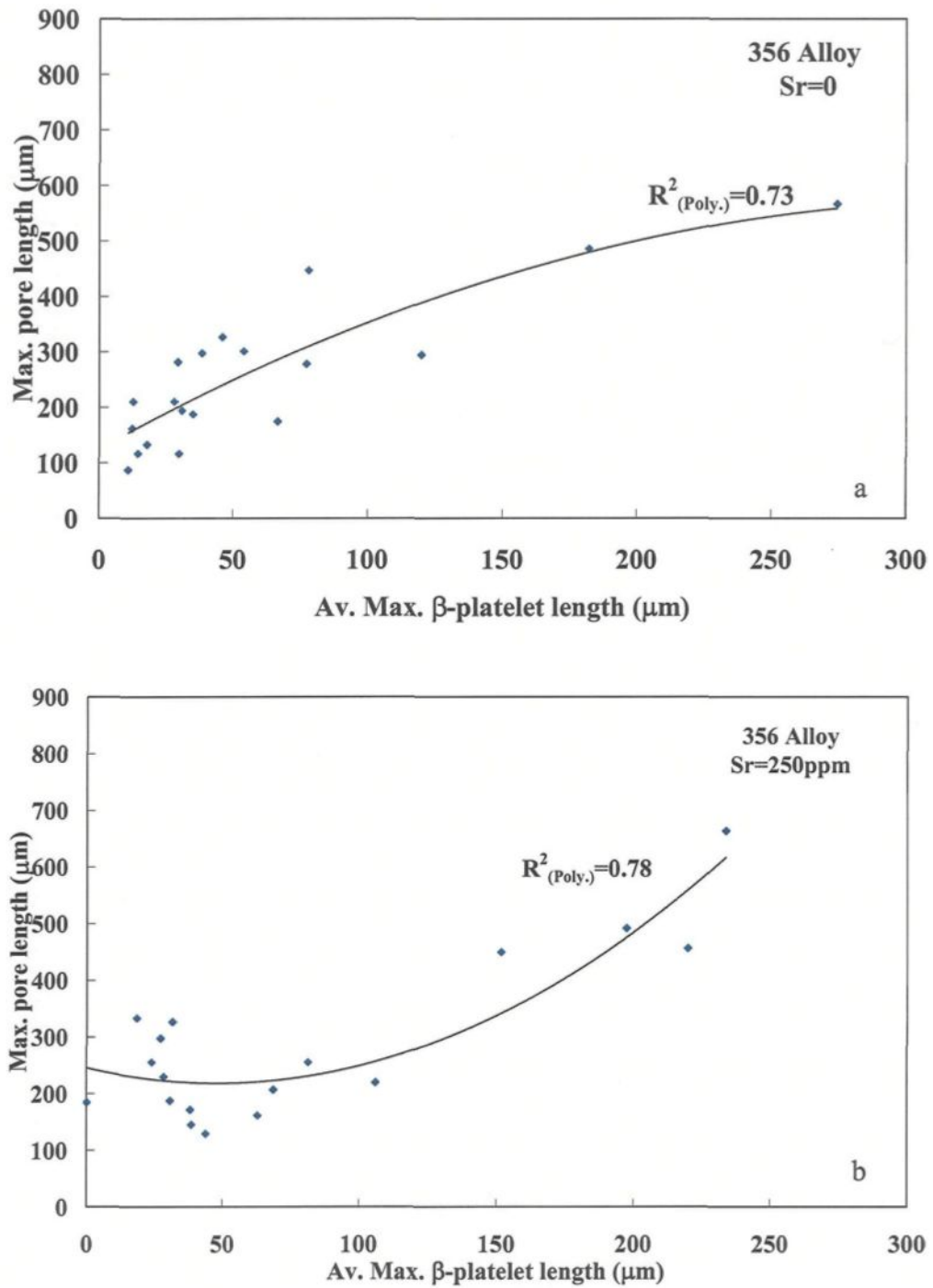
**Figure 4.27** Plots of percentage porosity vs. average maximum  $\beta$ -platelet length in (a) unmodified, and (b) Sr-modified A319.2 alloys.



**Figure 4.28** Plots of maximum pore length vs. average maximum  $\beta$ -platelet length in (a) unmodified, and (b) Sr-modified A319.2 alloys.



**Figure 4.29** Plots of percentage porosity vs. average maximum  $\beta$ -platelet length in (a) unmodified and (b) Sr-modified A356.2 alloys.



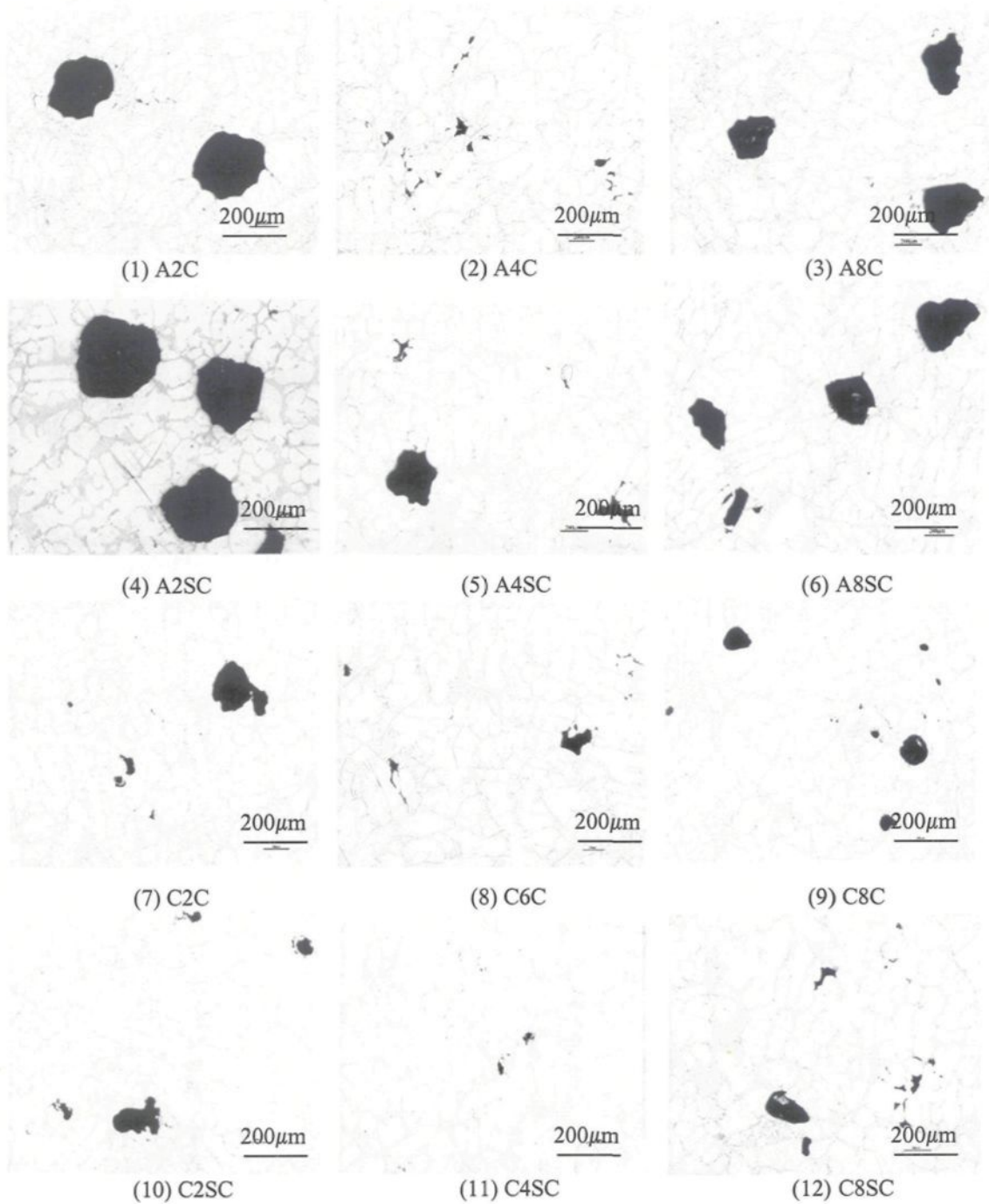
**Figure 4.30** Plots of maximum pore length vs. average maximum  $\beta$ -platelet length in (a) unmodified and (b) Sr-modified A356.2 alloy.

Figure 4.31 shows examples of the optical micrographs obtained from the samples listed in Table 4.5. These samples were obtained from unmodified and Sr-modified A319.2 and A356.2 alloy samples containing different Fe levels and obtained at the lowest cooling rate. The optical micrographs of these samples show the porosity features typically observed in each case. It can be clearly seen that the pores observed in the A319.2 alloys are much larger than those in the A356.2 alloys. Also, the Sr-modified 319 alloys exhibit larger pore sizes compared to the unmodified alloys. With respect to the four rows of micrographs in Figure 4.31, minimum porosity is displayed by the A4C, A4SC, C6C and C4SC samples, respectively.

**Table 4.5** Samples corresponding to Figure 4.31.

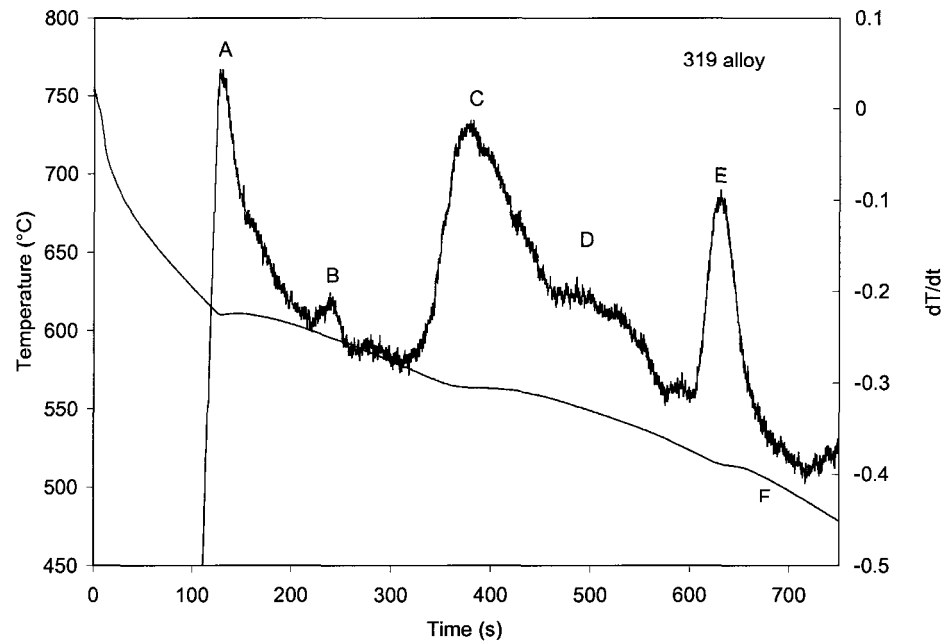
Alloy	Alloy code	Fe (wt%)	Sr (ppm)
319	A2C	0.2	0
	A4C	0.4	
	A8C	0.8	
	A2SC	0.2	250
	A4SC	0.4	
	A8SC	0.8	
356	C2C	0.2	0
	C6C	0.6	
	C8C	0.8	
	C2SC	0.2	250
	C4SC	0.4	
	C8SC	0.8	

Note: A: A319.2 alloy, C: A356.2 alloy; 2, 4, 6, 8: iron levels of 0.2, 0.4, 0.6, 0.8%;  
Suffix C: 100mm from the chill end.

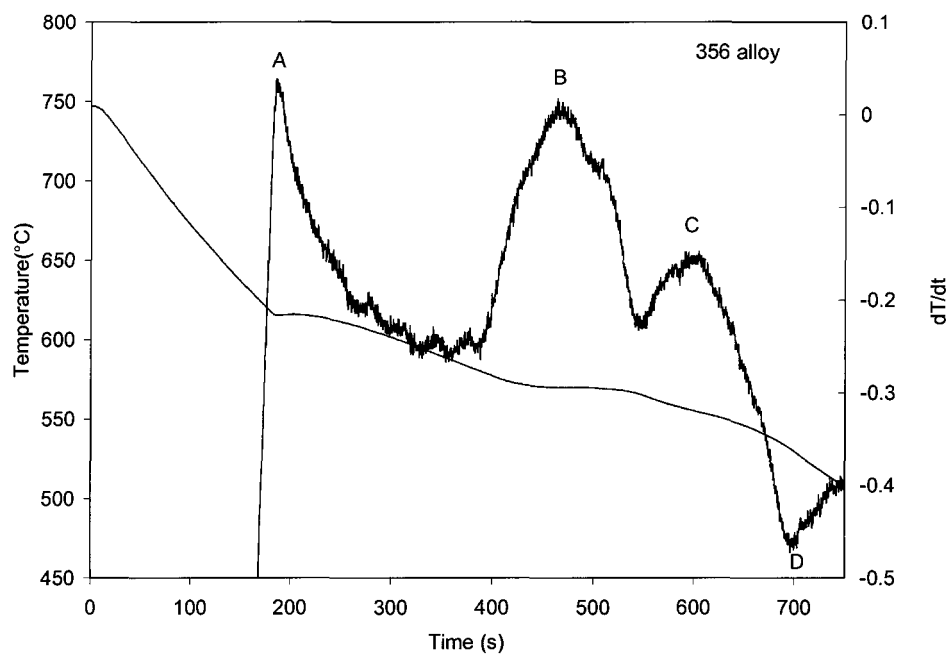


**Figure 4.31** Optical micrographs showing pores observed in different samples of A319.2 and A356.2 alloys (See Table 4.5 for alloy sample codes).

These observations may be explained on the basis of the cooling curves obtained for the two alloys. These are shown in Figure 4.32, together with their first derivative curves. The expected reactions (marked A through E) and solidification times observed (solidification rate  $\sim 0.8^{\circ}\text{C}/\text{s}$ ) are listed in Tables 4.6 and 4.7, respectively. The difference in pore characteristics between the A356.2 and A319.2 alloys may be attributed to their different solidification patterns. Table 4.7 shows that the total solidification time for the 319 alloy is much longer than that for the 356 alloy (*cf.* 586s vs 513s). This gives the pores more time to grow, resulting in larger pores being observed in the A319.2 alloy, compared to the A356.2 alloy.



(a)



(b)

**Figure 4.32** Cooling curves and their first derivatives obtained for (a) 319, and (b) 356 alloys.

**Table 4.6** Reactions Observed in 319 and 356 Alloys at  $\sim 0.8^\circ\text{C/s}$ .

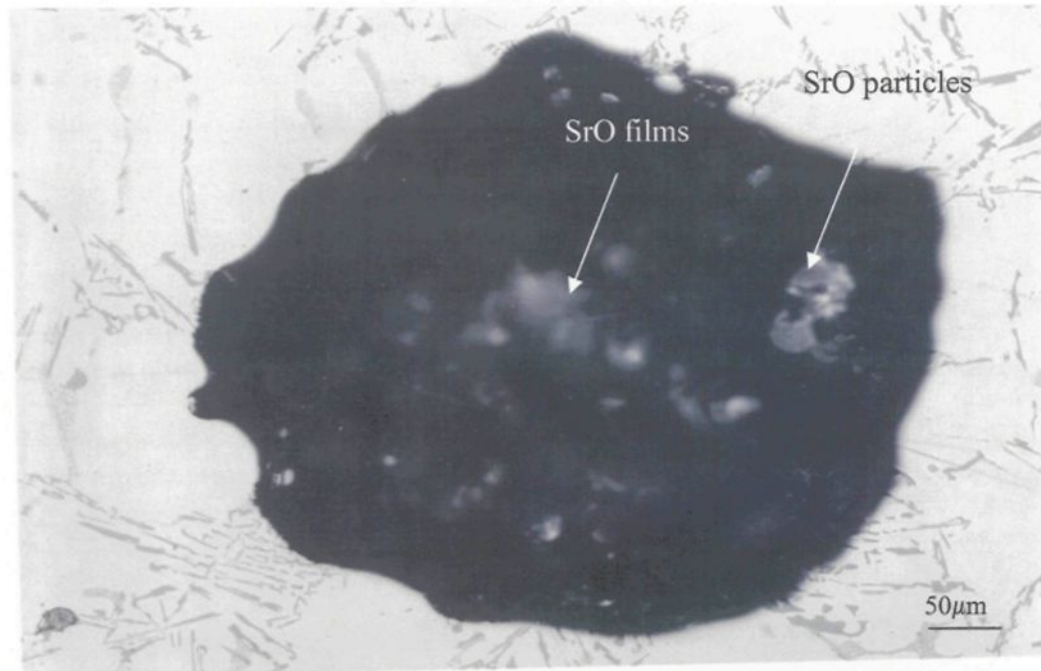
Alloy	Peak	Temperature ( $^\circ\text{C}$ )	Reaction
319	A	610.26	Precipitation of $\alpha$ -Al dendrite network
	B	595.33	Precipitation of $\beta$ - $\text{Al}_5\text{FeSi}$ phase
	C	563.54	Al-Si eutectic reaction
	D	551.23	Post-eutectic reactions
	E	514.63	Al- $\text{Al}_2\text{Cu}$ eutectic reaction
	F	491.63	End of solidification
356	A	615.23	Precipitation of $\alpha$ -Al dendrite network
	B	569.79	Al-Si eutectic reaction
	C	554.43	Precipitation of $\text{Mg}_2\text{Si}$
	D	531.16	End of solidification

**Table 4.7** Solidification Times Observed in 319 and 356 Alloys at  $\sim 0.8^\circ\text{C/s}$ .

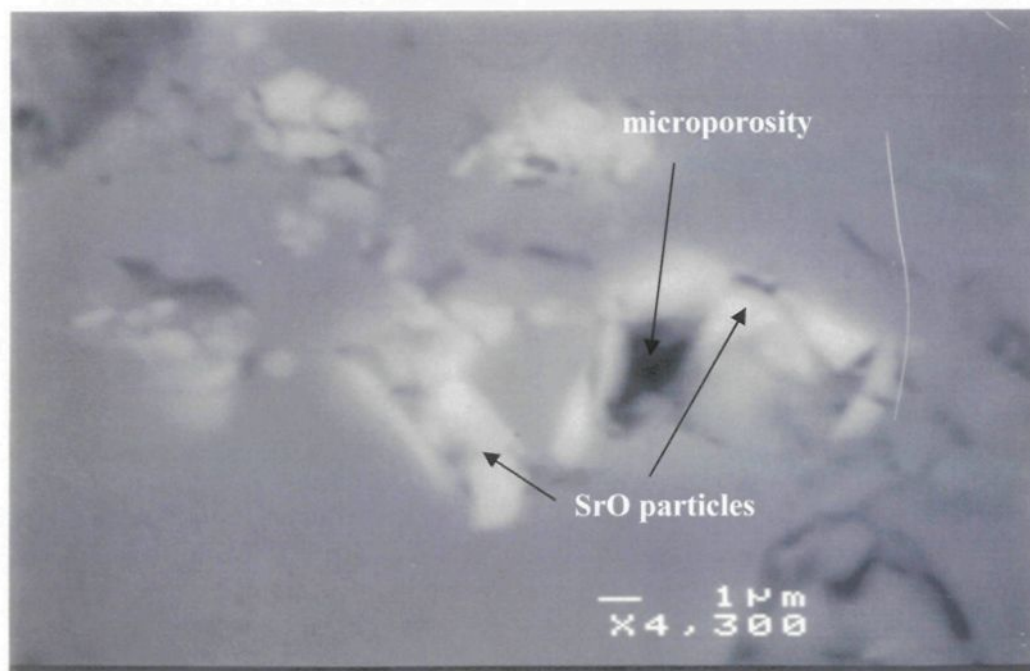
Alloy	Reaction and zone formation	Solidification Time (s)
319	1: Mushy zone	187.4
	2: Al+Si eutectic	147.4*
	3: Post-eutectic reactions	251.2
	4: Total solidification time	586
356	1: Mushy zone	201.6
	2: Al+Si eutectic	160*
	3: Post-eutectic reactions	151.4
	4: Total solidification time	513

\* Note: The duration of Al-Si eutectic reaction in 319 alloy is somewhat shorter than that of 356 alloy.

In the Sr-modified alloys, pores are often associated with the presence of strontium oxides. These SrO films or particles are formed due to the high oxygen affinity of strontium, and are extremely difficult to be removed during degassing. Figure 4.33 shows two examples of SrO seen within pores in the 319.2 alloy. As Figure 4.34 shows, the free energy needed to form SrO is lower than  $\text{Al}_2\text{O}_3$ . Thus, once formed, SrO is more stable than  $\text{Al}_2\text{O}_3$ , and has a greater role in porosity formation. Also, the depression of the eutectic temperature with Sr addition can affect the eutectic solidification, leading to an extension of the freezing range of the alloy and an increase in the solidification time. Strontium also lowers the surface tension of the melt. Thus, it is expected that Sr-modified alloys will contain more porosity than the unmodified alloys.



(a)



(b)

**Figure 4.33** (a) Optical micrograph showing SrO particles and films within a pore in a 319 alloy sample, and (b) SEM micrograph showing SrO particles situated inside the pore.

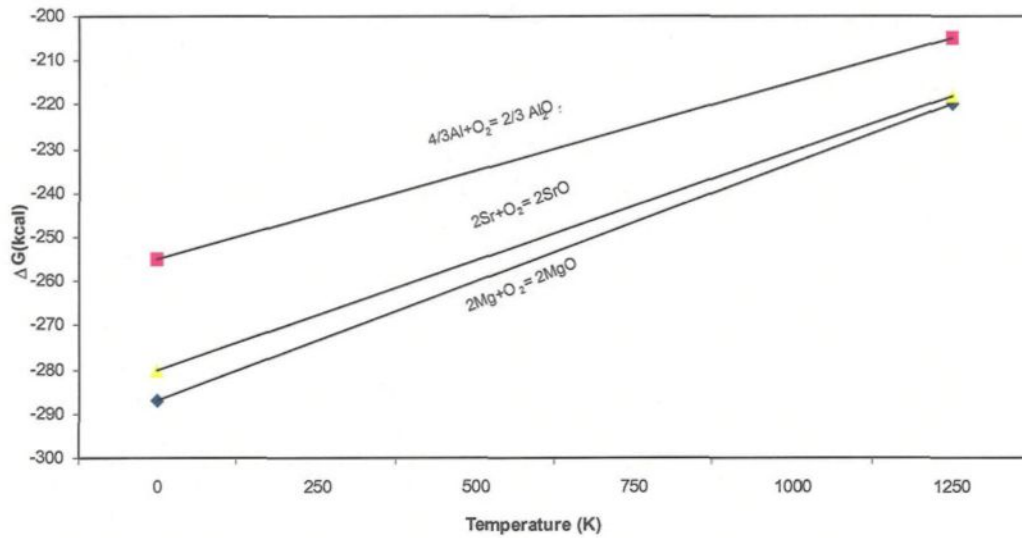
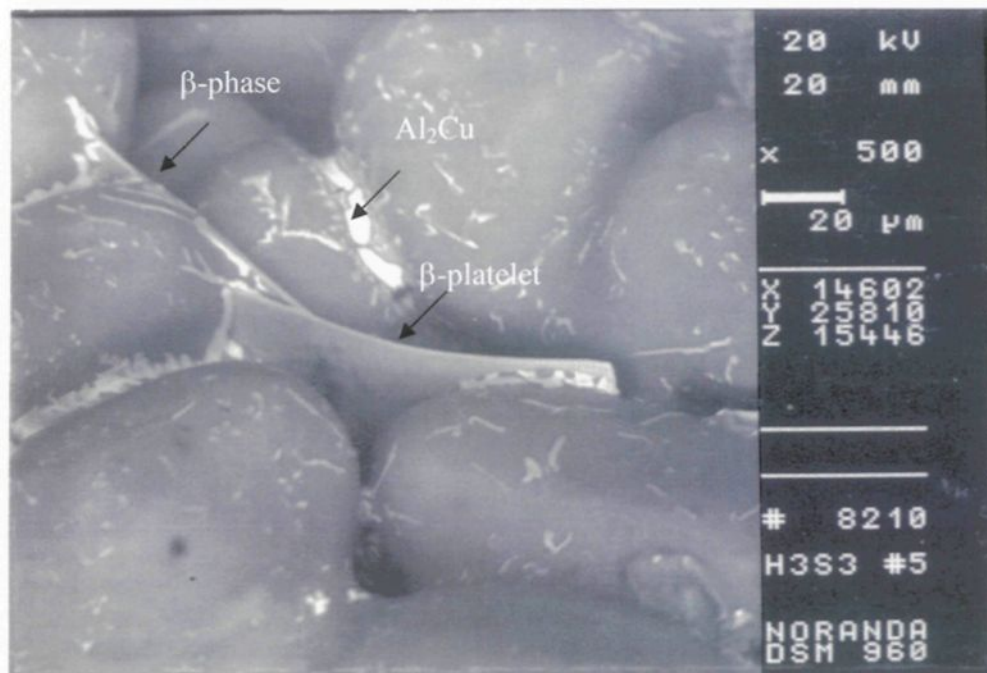
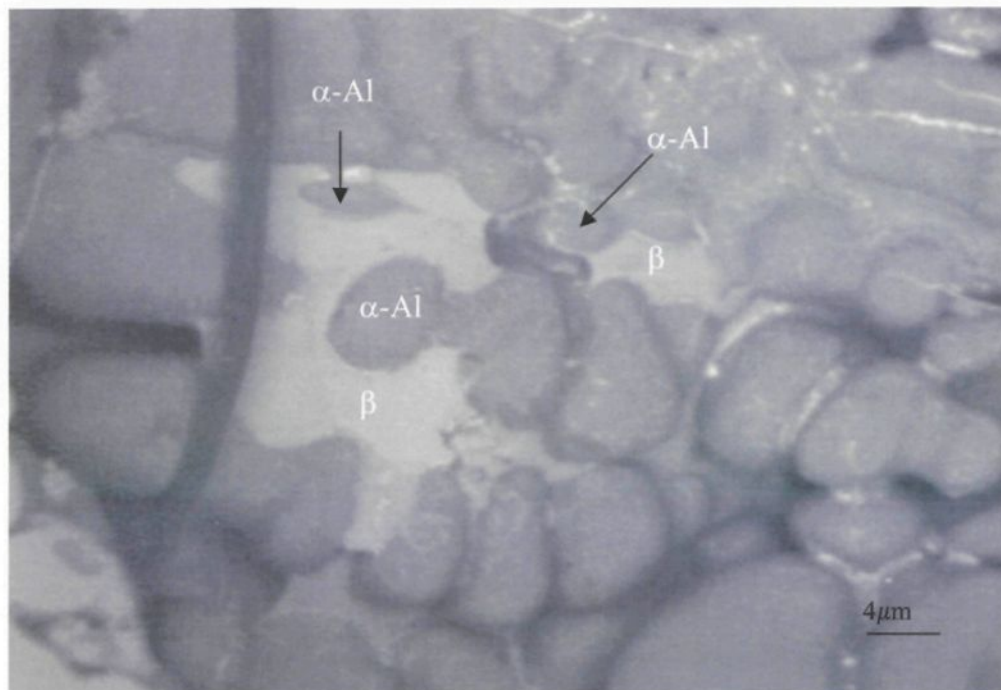


**Figure 4.34** Free energy formation vs temperature for Al-, Sr-, and Mg- oxides.

The SEM micrographs of Figure 4.35 compare the  $\beta$ -platelet morphologies in two instances. In 319.2 alloy samples, (a) the  $\beta$ -platelet appears to be solid, whereas in (b), the appearance of  $\alpha$ -Al dendrites through parts of the  $\beta$ -platelets clearly indicates that dissolution of these platelets has taken place.



(a)

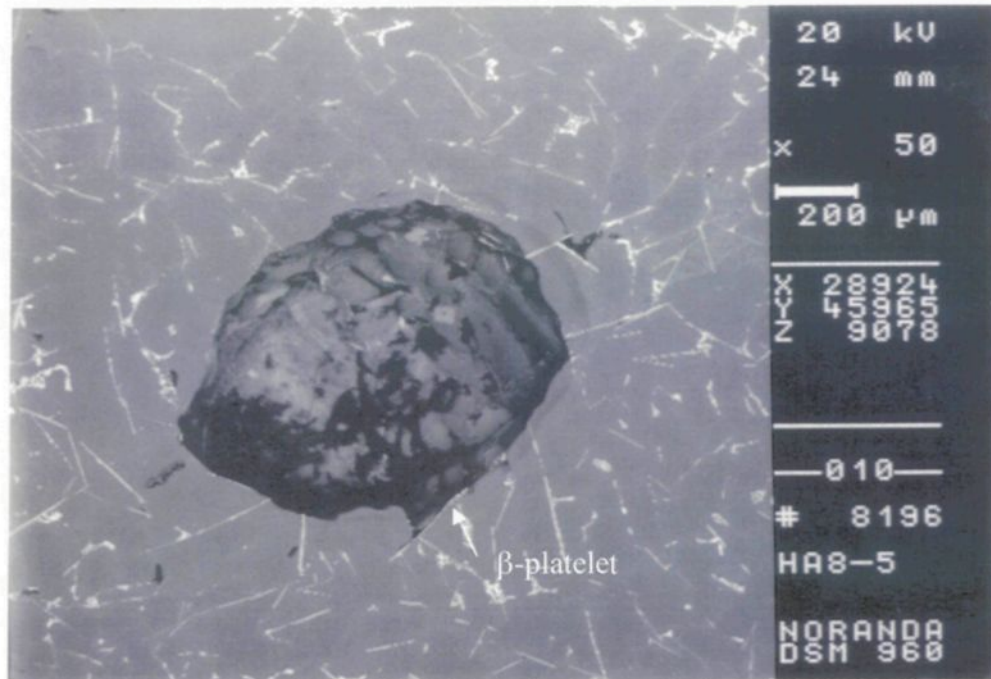


(b)

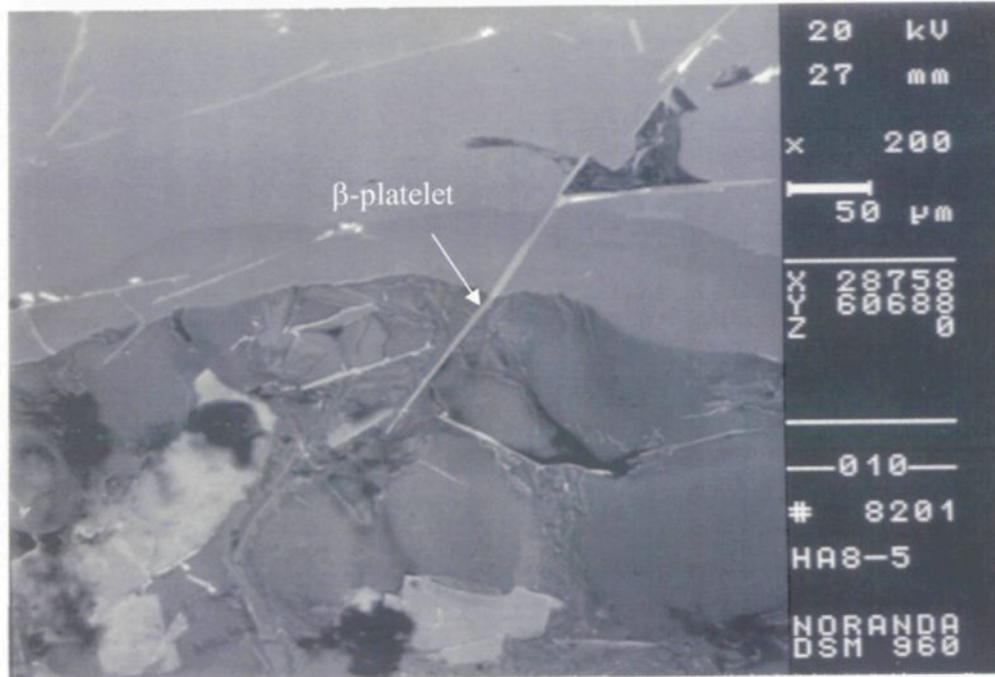
**Figure 4.35** SEM micrographs comparing (a) a solid  $\beta$ -platelet, (b)  $\beta$ -platelets that have undergone dissolution in Sr-modified 319.2 alloy samples. Note the  $\alpha$ -Al dendrites appearing through parts of the  $\beta$ -platelets in (b).

The formation of both gas and shrinkage pores on  $\beta$ -Al<sub>5</sub>FeSi platelets was also demonstrated. Figure 4.36(a), taken from high hydrogen-containing A319.2-0.8%Fe alloy, shows a gas pore nucleated on a  $\beta$ -Al<sub>5</sub>FeSi platelet, having a round shape typical of gas pores. The hydrogen content of the alloy melt was 0.25ml/100g Al. The higher magnification micrograph of Figure 4.36(b) shows this more clearly. The flattened dendrites observed inside the pore indicate that this is a gas pore. Finally, Figure 4.36(c) shows how the growth of the gas pore is limited by the  $\beta$  platelets (needles) on either side of the pore.

Figure 4.37 shows how shrinkage porosity occurs due to the  $\beta$ -platelets, particularly when they are branched (see circled area). The platelets form in the interdendritic channels during solidification, and cause physical restrictions to the movement of compensatory feed liquid, giving rise to shrinkage porosity. Thus we see that, in spite of the fact that the  $\beta$ -platelets act as pore nucleation sites, their presence can also limit pore growth.

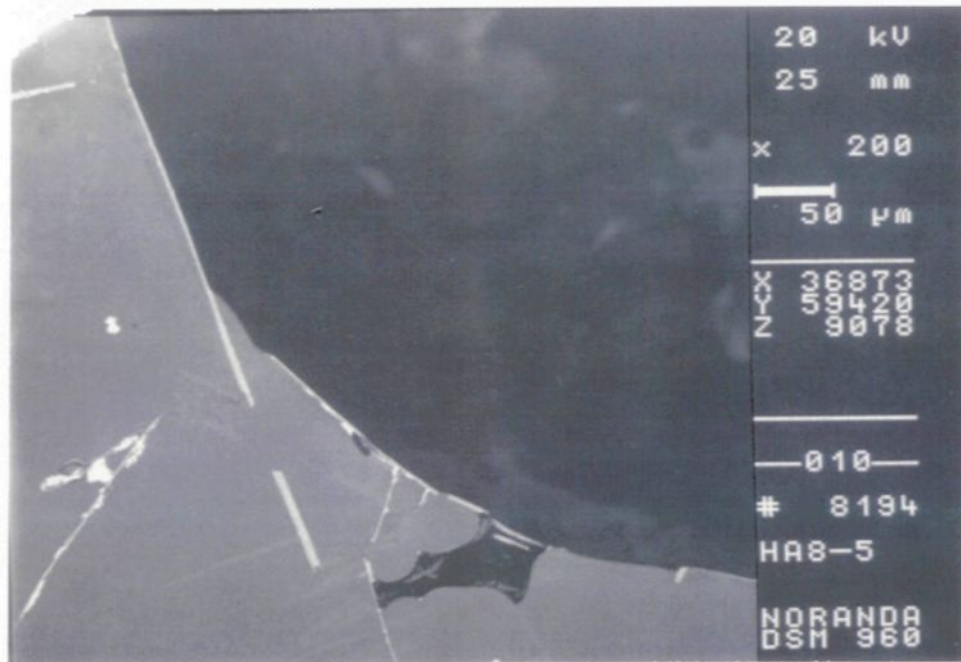


(a)



(b)

**Figure 4.36** SEM micrographs showing how the  $\beta$ - $\text{Al}_5\text{FeSi}$  phase platelets nucleate gas porosity (a, b), and limit pore growth (c) in high hydrogen-containing A319.2-0.8%Fe alloy (hydrogen level: 0.25ml/100g).



(c)

**Figure 4.36** SEM micrographs showing how the  $\beta$ -Al<sub>3</sub>FeSi phase platelets nucleate gas porosity (a, b), and limit pore growth (c) in high hydrogen-containing A319.2-0.8%Fe alloy (hydrogen level: 0.25ml/100g).

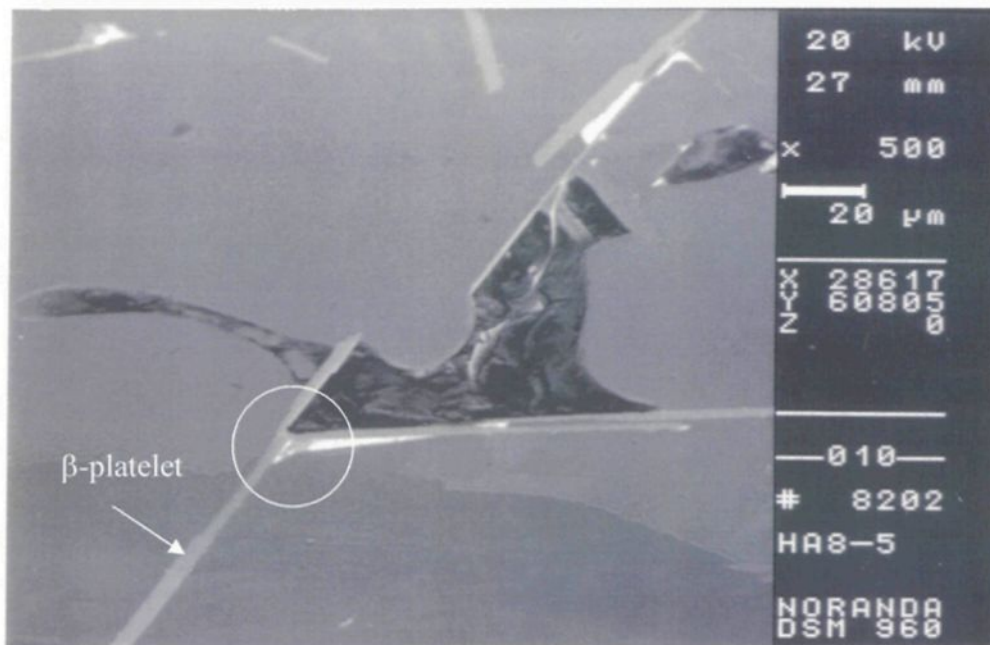


**Figure 4.37** SEM micrograph showing an example of how branched  $\beta$ -platelets can cause shrinkage porosity.

Figure 4.38 shows the average maximum  $\beta$ -Al<sub>3</sub>FeSi platelet length versus iron content for the unmodified 319 and 356 alloys, obtained at the highest and lowest cooling rates (15 $\mu$ m and 85 $\mu$ m DAS, respectively), while Figure 4.39 shows the fluidity vs. iron content for the same alloys. Fluidity of the liquid melts was measured using a 4210 Ragone Fluidity Tester, where the length of solidified metal in the quartz tube of the tester (at 200 mm Hg metallostatic pressure) indicated the corresponding fluidity. The two figures show that as the iron content increases, both the average maximum  $\beta$ -platelet length and the alloy fluidity increase. Depending upon which of these two variables has the greater influence (as determined by the alloy and solidification conditions), the porosity level will be accordingly determined. However, as Figure 4.38 shows, the DAS has the strongest influence in determining the  $\beta$ -platelet lengths.

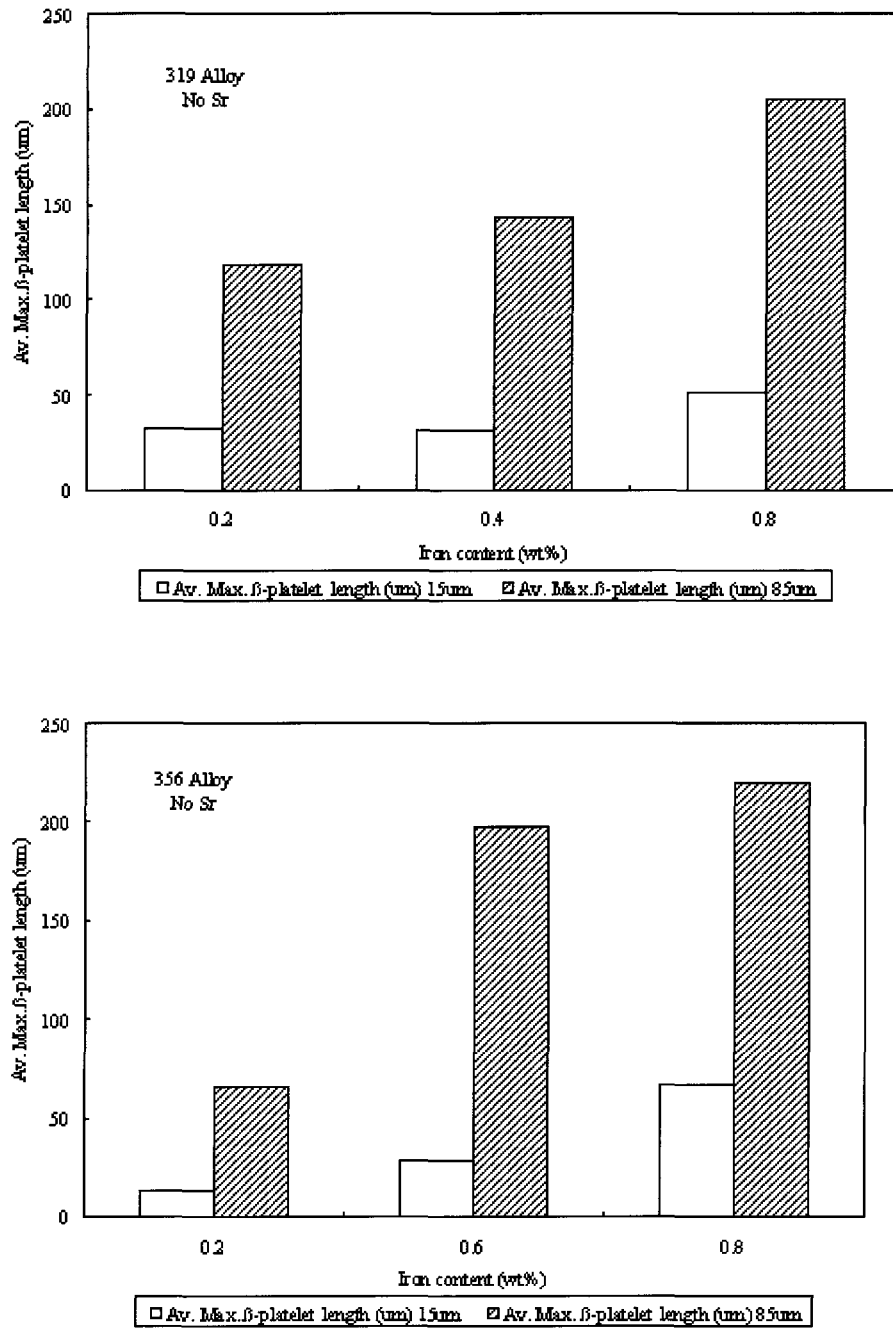


**Figure 4.38** Average maximum  $\beta$ -platelet length vs. iron content for unmodified 319 and 356 alloys.

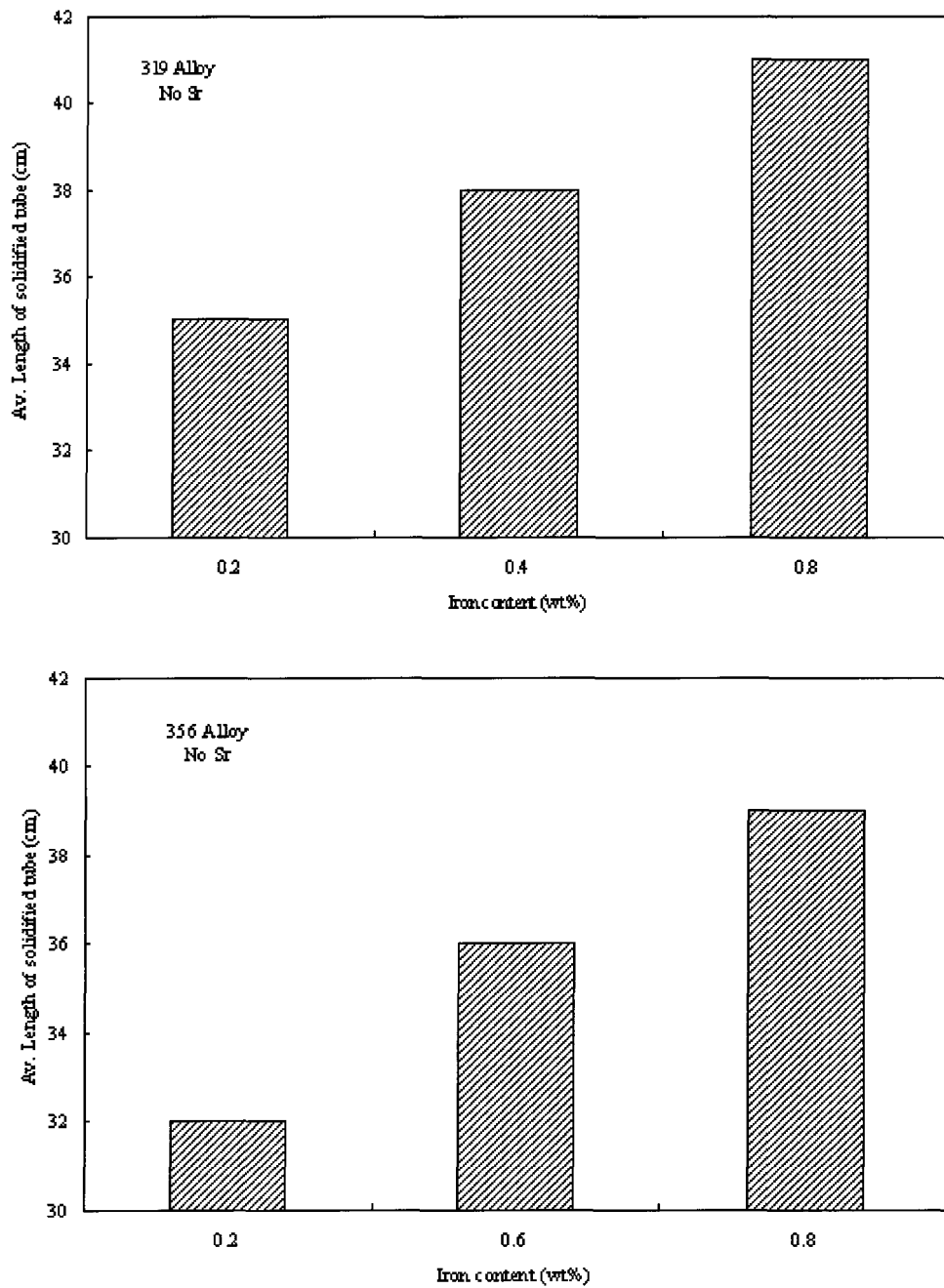


**Figure 4.39** Fluidity (average length of solidified tube) versus iron content for unmodified 319 and 356 alloys.

**CHAPTER 5**

**ROLE OF IRON IN RELATION TO SI MODIFICATION**

**IN SR-TREATED ALLOYS**

## CHAPTER 5

### ROLE OF IRON IN RELATION TO SI MODIFICATION IN SR-TREATED ALLOYS

#### 5.1 INTRODUCTION

As discussed previously in Chapter 2, “modifiers” such as sodium (Na), strontium (Sr), antimony (Sb), *etc.* are added to Al-Si alloys to enhance the mechanical properties, where, as a result of the “modification” or change in morphology of the Si phase of the Al-Si eutectic from its normally brittle, acicular form to a fibrous (or lamellar) one, large improvements in the alloy properties are observed.<sup>20,27,31,133,134</sup> Whereas the coarse acicular silicon platelets act as internal stress raisers in the microstructure and provide easy paths for fracture, the modified Si fibers are able to bend and curve easily during solidification, giving the alloy somewhat higher values of ultimate tensile strength and greatly increased values of ductility.<sup>135,136</sup> A significant improvement in the impact strength is also obtained, owing to the reduction in size of the Si particles. The details of the mechanism of eutectic silicon modification have been described in Chapter 2, Section 2.4.

The microstructural change from acicular to fibrous silicon is not a sharp one, and castings with an inadequate amount of either Na or Sr will exhibit a mixed structure - one containing regions of fibrous, lamellar, and acicular silicon. The variables that determine

the exact microstructure include the cooling rate, the type and amount of modifier used (in our case, Sr), the impurities present in the melt and, obviously, the silicon content of the alloy.<sup>1</sup>

In addition to silicon structure control, another important consideration from the microstructural point of view is controlling the iron content of the alloy. Iron is invariably present as an impurity element, or, as in the case of die casting alloys, is added to the alloy to prevent the casting from soldering to the dies. In either case, together with aluminum and other alloying elements, the iron forms several intermetallic compounds, among which the brittle, platelet-like  $\beta$ -Al<sub>5</sub>FeSi phase is particularly deleterious to the mechanical properties. The platelet nature of this phase gives rise to feeding difficulties during solidification, increasing the tendency for porosity formation. Optimization and control of iron intermetallics have been carried out using various means, such as the addition of “neutralizers” (*e.g.*, Mn, Cr, Ni, Co and Be) to the alloy to promote the formation of less deleterious script-like phases which, due to their compact morphology, are less harmful to the mechanical properties.<sup>137</sup>

The literature reveals that, although both these aspects relate to Al-Si alloys, each has been dealt with separately. In the course of the present study, while investigating the effect of Fe content on the microstructural aspects of 319 and 356 alloys (*viz.*, the silicon and  $\beta$ -Al<sub>5</sub>FeSi phase particle characteristics), some very interesting observations concerning the effect of the presence of Fe-based intermetallics on Si modification in these alloys were noted. In view of the fact that (a) Sr modification is normally carried out as a rule, and (b) Fe levels are usually minimized in Al-Si alloys, looking at the link between

these two aspects seemed very worthwhile. To the best of our knowledge, this has not been specifically reported previously in the literature.

## **5.2 EFFECT OF IRON, COOLING RATE AND STRONTIUM ON SI PARTICLE CHARACTERISTICS**

This chapter presents the results that were obtained in relation to the effect of iron and cooling rate on the Si particle characteristics in unmodified and Sr-modified 319 and 356 alloys, using both directional and conventional solidification. The role of  $Al_2Si_2Sr$  precipitation in the Sr-modified alloys is also discussed. The experimental procedures followed were the same as those described in Chapter 3.

### **5.2.1 Si Particle Characterization from Image Analysis Data**

Tables 5.1 and 5.2 summarize, respectively, the Si particle characteristics obtained from the image analysis measurements for the (a) unmodified and (b) Sr-modified A319.2 and A356.2 alloys at different Fe levels. With respect to the sample code, AF2-0 corresponds to an A319.2 alloy sample containing 0.2 wt% Fe, and obtained from the 5 mm level above the chill end. The Sr-modified sample for the same conditions is represented by the code A2FS-0. Similarly, sample codes CF6-C and CF6S-C correspond to A356.2 alloy samples containing 0.6 wt% Fe, and obtained from the 100 mm level above the chill-end, the latter code corresponding to the Sr-modified alloy sample (with Sr being denoted by the letter S).

**Table 5.1(a)** Si particle characteristics obtained for unmodified A319.2 alloy samples containing various Fe levels

Sample	Si particle characteristics						
	Av. Area ( $\mu\text{m}^2$ )	SD ( $\mu\text{m}^2$ )	Av. Length ( $\mu\text{m}$ )	SD ( $\mu\text{m}$ )	Aspect Ratio	SD	Density (No./ $\text{mm}^2$ )
AF2-0	8.94	12.21	4.90	4.36	2.21	1.06	$6.87 \times 10^3$
AF2-1	18.97	43.58	6.97	9.20	2.37	1.23	$3.21 \times 10^3$
AF2-3	26.01	58.20	9.96	13.86	2.71	1.61	$3.04 \times 10^3$
AF2-5	25.24	53.74	9.01	11.55	2.53	2.53	$1.95 \times 10^3$
AF2-C	33.57	72.71	10.74	14.77	2.54	1.55	$1.65 \times 10^3$
AF4-0	3.69	12.40	2.84	2.51	2.06	1.01	$16.51 \times 10^3$
AF4-1	13.09	23.58	6.96	7.52	2.54	1.41	$5.18 \times 10^3$
AF4-3	21.22	41.50	8.09	9.09	2.45	1.37	$1.94 \times 10^3$
AF4-5	26.25	59.97	10.25	15.45	2.95	1.88	$3.32 \times 10^3$
AF4-C	40.5	116.9	12.22	21.29	2.28	1.17	$1.97 \times 10^3$
AF6-0	5.59	12.04	3.74	3.25	2.08	0.98	$7.18 \times 10^3$
AF6-1	14.19	29.44	6.70	7.67	2.42	1.31	$3.67 \times 10^3$
AF6-3	16.86	42.17	6.56	8.38	2.22	1.20	$2.03 \times 10^3$
AF6-5	24.24	55.06	8.14	10.63	2.34	1.30	$1.36 \times 10^3$
AF6-C	34.25	81.99	10.04	14.26	2.41	1.36	$1.41 \times 10^3$
AF8-0	4.79	16.13	3.60	3.06	2.12	0.95	$8.34 \times 10^3$
AF8-1	10.12	25.74	5.28	6.15	2.35	1.22	$3.63 \times 10^3$
AF8-3	21.91	39.54	7.91	8.46	2.30	1.25	$1.09 \times 10^3$
AF8-5	26.58	52.80	9.02	10.64	2.40	1.30	$1.12 \times 10^3$
AF8-C	31.39	69.09	9.64	13.18	2.36	1.34	$1.19 \times 10^3$

Note : In Tables 5.1(a) and (b), the suffices 0, 1, 3, 5 and C in the sample codes refer to levels 5, 10, 30, 50, and 100 mm above the chill end, and F2, F4, F6 and F8 to Fe levels of 0.2, 0.4, 0.6 and 0.8 wt% in the A (A319.2) alloy. SD = Standard Deviation.

**Table 5.1 (b)** Si particle characteristics obtained for Sr-modified A319.2 alloy samples containing various Fe levels

Sample	Si particle characteristics						
	Av. Area ( $\mu\text{m}^2$ )	SD ( $\mu\text{m}^2$ )	Av. Length ( $\mu\text{m}$ )	SD ( $\mu\text{m}$ )	Aspect Ratio	SD	Density (No./ $\text{mm}^2$ )
AF2S-0	4.48	12.95	2.76	2.40	1.66	1.66	$15.55 \times 10^3$
AF2S-1	6.10	16.00	3.11	3.14	1.78	0.74	$11.49 \times 10^3$
AF2S-3	5.64	18.05	3.18	3.45	1.85	0.72	$12.28 \times 10^3$
AF2S-5	6.62	18.08	3.36	3.38	1.77	0.66	$13.61 \times 10^3$
AF2S-C	5.44	16.01	3.45	3.65	1.97	0.82	$21.28 \times 10^3$
AF4S-0	2.37	5.38	2.04	2.03	1.79	0.78	$26.39 \times 10^3$
AF4S-1	2.95	7.49	2.25	2.30	1.86	0.76	$21.85 \times 10^3$
AF4S-3	3.51	14.02	2.51	2.84	1.82	0.68	$25.38 \times 10^3$
AF4S-5	4.16	14.36	2.82	3.10	1.77	0.66	$29.86 \times 10^3$
AF4S-C	6.70	17.86	4.04	4.31	2.04	0.87	$50.0 \times 10^3$
AF6S-0	4.23	12.29	2.93	2.65	1.75	0.66	$17.26 \times 10^3$
AF6S-1	4.07	10.11	2.60	3.16	1.77	0.62	$16.75 \times 10^3$
AF6S-3	4.85	16.42	2.92	2.90	1.82	0.71	$14.0 \times 10^3$
AF6S-5	4.99	15.01	2.98	2.95	1.78	0.67	$15.1 \times 10^3$
AF6S-C	4.66	14.94	2.82	3.46	1.83	0.67	$18.58 \times 10^3$
AF8S-0	4.08	13.13	2.71	2.49	1.79	0.67	$11.69 \times 10^3$
AF8S-1	5.01	14.86	3.00	2.90	1.82	0.69	$10.94 \times 10^3$
AF8S-3	4.79	15.27	2.94	2.92	1.87	0.75	$11.16 \times 10^3$
AF8S-5	5.47	16.43	3.20	3.13	1.87	0.77	$12.65 \times 10^3$
AF8S-C	5.12	18.19	3.03	3.18	1.87	0.74	$14.91 \times 10^3$

**Table 5.2(a)** Si particle characteristics obtained for unmodified A356.2 alloy samples containing various Fe levels

Sample	Si particle characteristics						
	Av. Area ( $\mu\text{m}^2$ )	SD ( $\mu\text{m}^2$ )	Av. Length ( $\mu\text{m}$ )	SD ( $\mu\text{m}$ )	Aspect Ratio	SD	Density (No./ $\text{mm}^2$ )
CF1-0	5.29	12.53	4.02	3.76	2.34	1.23	$11.35 \times 10^3$
CF1-1	18.65	31.23	8.47	9.25	2.62	1.44	$3.35 \times 10^3$
CF1-2	18.49	31.95	8.86	10.27	2.85	1.69	$3.97 \times 10^3$
CF1-3	28.50	54.62	11.73	12.55	2.72	1.59	$2.19 \times 10^3$
CF1-C	27.24	50.49	10.90	11.50	2.75	1.53	$2.46 \times 10^3$
CF2-0	6.41	11.81	4.50	4.68	2.39	1.25	$9.65 \times 10^3$
CF2-1	11.23	18.56	6.50	6.96	2.64	1.50	$5.54 \times 10^3$
CF2-2	21.42	36.54	8.50	8.79	2.48	1.38	$2.44 \times 10^3$
CF2-3	23.01	41.72	8.89	9.82	2.50	1.38	$2.21 \times 10^3$
CF2-C	20.62	40.91	8.36	9.41	2.58	1.49	$2.39 \times 10^3$
CF4-0	6.13	12.09	4.48	4.14	2.47	1.27	$9.95 \times 10^3$
CF4-1	16.16	28.21	7.65	9.19	2.79	1.73	$3.96 \times 10^3$
CF4-2	31.78	60.50	11.78	13.56	2.80	1.77	$2.72 \times 10^3$
CF4-3	26.62	54.86	10.22	13.82	2.82	1.86	$3.23 \times 10^3$
CF4-C	34.10	65.30	12.83	15.25	3.07	2.08	$2.85 \times 10^3$
CF6-0	3.84	12.51	3.28	3.10	2.19	1.08	$11.18 \times 10^3$
CF6-1	8.83	16.67	5.42	5.90	2.40	1.24	$6.08 \times 10^3$
CF6-2	9.38	22.87	5.91	7.07	2.71	1.60	$7.23 \times 10^3$
CF6-3	19.63	48.15	8.12	11.37	2.47	1.36	$2.72 \times 10^3$
CF6-C	11.94	26.47	7.20	8.09	3.04	1.97	$5.84 \times 10^3$

Note : In Table 5.2 (a) and (b), the suffices 0, 1, 2, 3 and C in the sample codes refer to levels 5, 10, 30, 50, and 100 mm above the chill end, and F1, F2, F4 and F6 to Fe levels of 0.12, 0.2, 0.4, and 0.6 wt% in the C (A356.2) alloy. SD = Standard Deviation.

**Table 5.2 (b)** Si particle characteristics obtained for Sr-modified A356.2 alloy samples containing various Fe levels

Sample	Si particle characteristics						Density No./mm <sup>2</sup>
	Av. Area ( $\mu\text{m}^2$ )	SD ( $\mu\text{m}^2$ )	Av. Length ( $\mu\text{m}$ )	SD ( $\mu\text{m}$ )	Aspect Ratio	SD	
CF1S-0	0.60	2.56	1.10	1.21	1.75	0.62	94.37 x 10 <sup>3</sup>
CF1S-1	2.09	9.12	2.05	2.15	1.83	0.68	39.19 x 10 <sup>3</sup>
CF1S-2	1.66	4.76	1.85	1.65	1.84	0.70	41.9 x 10 <sup>3</sup>
CF1S-3	1.14	4.27	1.50	1.28	1.82	0.75	96.65 x 10 <sup>3</sup>
CF1S-C	2.42	18.33	2.30	3.16	1.87	0.76	44.83 x 10 <sup>3</sup>
CF2S-0	0.73	4.30	1.23	1.09	1.74	0.62	70.23 x 10 <sup>3</sup>
CF2S-1	1.28	4.43	1.65	1.47	1.88	0.73	60.16 x 10 <sup>3</sup>
CF2S-2	1.27	4.33	1.64	1.40	1.93	0.87	73.03 x 10 <sup>3</sup>
CF2S-3	1.92	4.18	2.03	1.63	1.73	0.66	81.07 x 10 <sup>3</sup>
CF2S-C	2.65	13.44	2.45	2.54	1.97	0.82	28.27 x 10 <sup>3</sup>
CF4S-0	1.38	4.26	1.50	1.49	1.91	0.77	52.48 x 10 <sup>3</sup>
CF4S-1	1.10	3.52	1.54	1.39	1.88	0.76	69.8 x 10 <sup>3</sup>
CF4S-2	1.05	3.49	1.50	1.40	1.87	0.78	80.7 x 10 <sup>3</sup>
CF4S-3	1.13	3.37	1.59	1.34	1.87	0.81	81.13 x 10 <sup>3</sup>
CF4S-C	1.42	3.89	1.77	1.58	1.91	0.82	61.56 x 10 <sup>3</sup>
CF6S-0	0.63	1.64	1.15	0.99	1.86	0.72	64.28 x 10 <sup>3</sup>
CF6S-1	0.75	1.84	1.24	1.11	1.82	0.71	70.34 x 10 <sup>3</sup>
CF6S-2	0.99	2.37	1.41	1.26	1.83	0.72	71.07 x 10 <sup>3</sup>
CF6S-3	1.24	2.34	1.62	1.38	1.86	0.74	67.32 x 10 <sup>3</sup>
CF6S-C	1.48	13.71	1.80	3.31	1.84	0.74	61.02 x 10 <sup>3</sup>

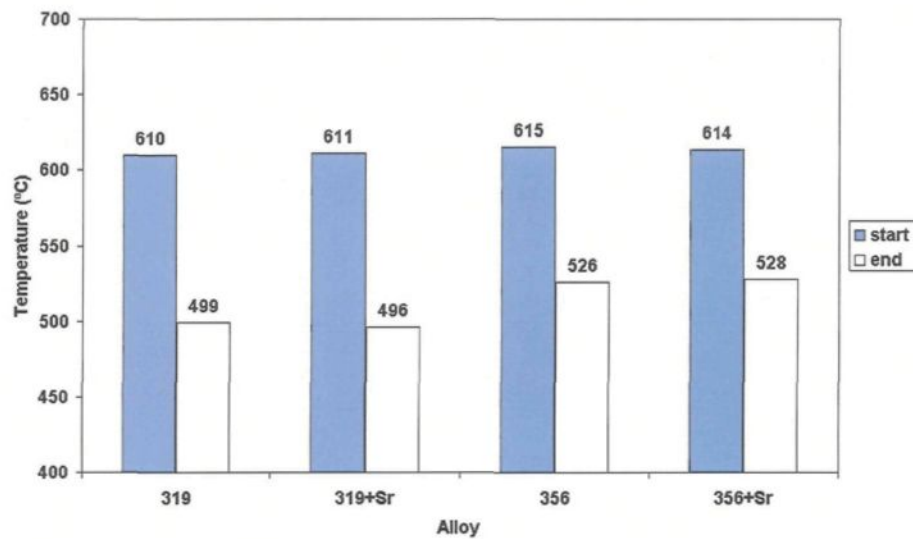
Careful scrutiny of Tables 5.1 and 5.2 revealed a number of interesting observations. For example, consider the samples obtained at the 100 mm level above the chill end, *viz.*, at DAS of  $\sim 85 \mu\text{m}$  : comparing the unmodified and Sr-modified samples of the low-Fe (AF2) and high-Fe (AF8) 319 alloys (Tables 5.1(a) and 5.1(b)), it is seen that the average Si particle sizes are significantly reduced in the Sr-modified alloys. However, increasing the Fe level is also found to reduce the Si particle size, the reduction being more noticeable in the unmodified than in the modified alloys. Similar observations are noted for the CF2 and CF6 alloy samples in the case of the 356 alloy (Tables 5.2(a) and 5.2(b)). The differences in Si particle size with increase in Fe content are considerably greater in this case, compared to the 319 alloy.

From Table 5.1(a), one also finds that the modification effect of Fe in the 319 alloys is effective in the DAS range  $\sim 15\text{-}50 \mu\text{m}$  (*i.e.*, for levels up to 30 mm above the chill end). Beyond that, the DAS is the more significant parameter in terms of controlling the Si particle size. In the Sr-modified alloys, Table 5.1(b), the values of the Si average particle areas and the standard deviation (SD) are independent of the sample level (or DAS) due to the competitive nucleation that balances the increase in DAS. Similarly, Tables 5.2(a) and 5.2(b) also show that modification of the 356 alloy is more pronounced than that of the 319 alloy under similar Fe and DAS conditions.

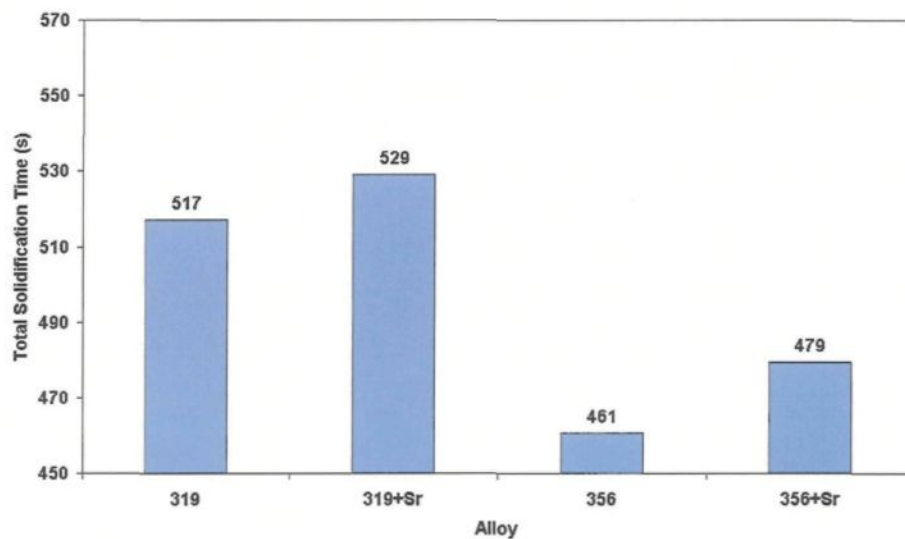
### **5.2.2 Solidification Parameters from Thermal Analysis Data**

The observations noted in Tables 5.1 and 5.2 may be explained in terms of the solidification parameters associated with the two alloys. Figure 5.1 shows the plots of (a)

the start and end of solidification temperatures, and (b) the total solidification times obtained for the two alloys, calculated from their respective cooling and first derivative curves.



(a)



(b)

**Figure 5.1** (a) Start and end of solidification temperatures, and (b) total solidification times obtained for non-modified and Sr-modified 319 and 356 alloys from thermal analysis data.

An example of the cooling curve and first derivative obtained for a 200 ppm Sr-modified experimental 319 alloy sample containing 0.8 wt% Fe (poured in the hot graphite mold, *viz.*, cooling rate  $\sim 0.8$  °C/s) is shown in Figure 5.2. The different peaks marked A through F on the first derivative curve, and the corresponding temperatures and possible reactions are listed in Table 5.3. Although presented here for purposes of defining the solidification parameters referred to in Figure 5.1, the details of the cooling curve will be referred to and discussed later, towards the end of the section.

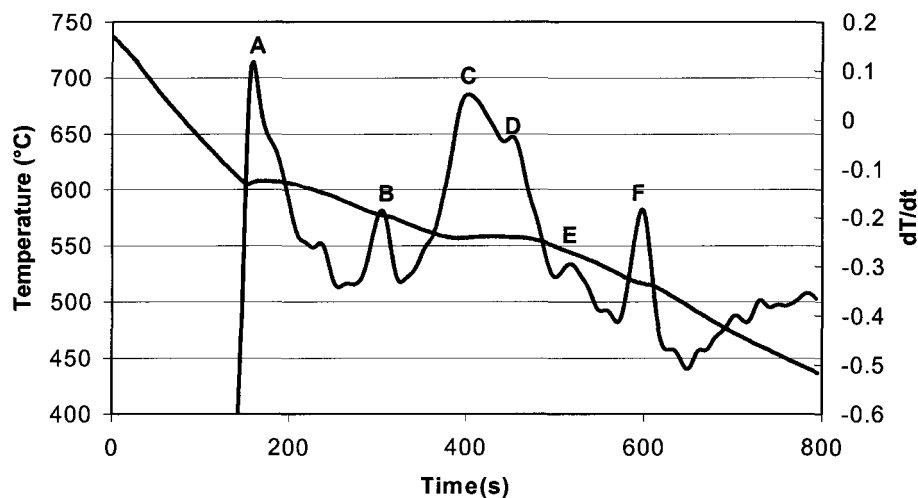


**Figure 5.2** Cooling curve and first derivative obtained for an experimental 319 alloy containing 0.8 wt% Fe and 0.02 wt% Sr, cooled in a hot graphite mold ( $\sim 0.8$  °C/s).

**Table 5.3** Possible reactions in an experimental 319 alloy containing 0.8 wt% Fe and 0.02 wt% Sr.

Alloy Composition	Reaction Peak	Temperature (°C)	Possible Reaction
319 +0.8%Fe + 200 ppm Sr	A	607.4	Start of solidification
	B	576.8	Precipitation of pre-eutectic $\beta$ - $\text{Al}_5\text{FeSi}$
	C	557.4	Precipitation of eutectic Si
	D	557.1	Precipitation of co-eutectic $\text{Al}_5\text{FeSi}$
	E	543.5	Precipitation of post-eutectic $\text{Al}_5\text{FeSi}$
	F	515.9	Precipitation of $\text{Al}_2\text{Cu}$ ; end of solidification

With reference to Figure 5.1 and the cooling curve shown in Figure 5.2, the three solidification parameters are defined as follows.

*Start of solidification temperature* = Temperature (°C) at which primary  $\alpha$ -Al dendrite network starts to form.

*End of solidification temperature* = Temperature (°C) at which the last reaction in the alloy takes place.

*Total solidification time* = Time (s) elapsed between the above two temperature points.

In the 319 alloys, the end of solidification temperatures are lower by almost 27-32 degrees, compared to the 356 alloys, Figure 5.1(a). Addition of Sr does not change these or the start of solidification temperatures much (one degree in each case). As a result, the total solidification times are relatively higher in the 319 alloys – by 56s and 50s in the

unmodified and modified cases, respectively (Figure 5.1(b)). In the case of the 356 alloys, the solidification ends with the precipitation of the  $Mg_2Si$  phase at  $\sim 526$  °C (not shown), whereas more phases precipitate in the 319 alloys, ending with the precipitation of the copper phases at  $\sim 499$  °C (see, for example, Figure 5.2). Thus, the higher total solidification time of the 319 alloys could also be considered as a contributing factor to the larger Si particle sizes observed in this alloy compared to the 356 alloys.

The salient features noted from Tables 5.1(a) and 5.1(b) can be summarized as follows.

For the 319 alloy,

- i) The higher the cooling rate (*i.e.*, the closer the distance from the chill end), the lower the Si particle size (area and length), and consequently, the higher the Si particle density for the amount of Si present in the alloy.
- ii) Addition of 250 ppm Sr considerably reduces the Si particle size, *e.g.*, from about 9 - 41  $\mu m$  in the unmodified alloy, to about 2.5 - 7  $\mu m$  in the Sr-modified alloy, *i.e.*, by about 30%.
- iii) It can also be observed that the higher the Fe content of the alloy, the lower the Si particle size, especially at the lowest cooling rate (*i.e.*, at high DASs).

For the 356 alloy,

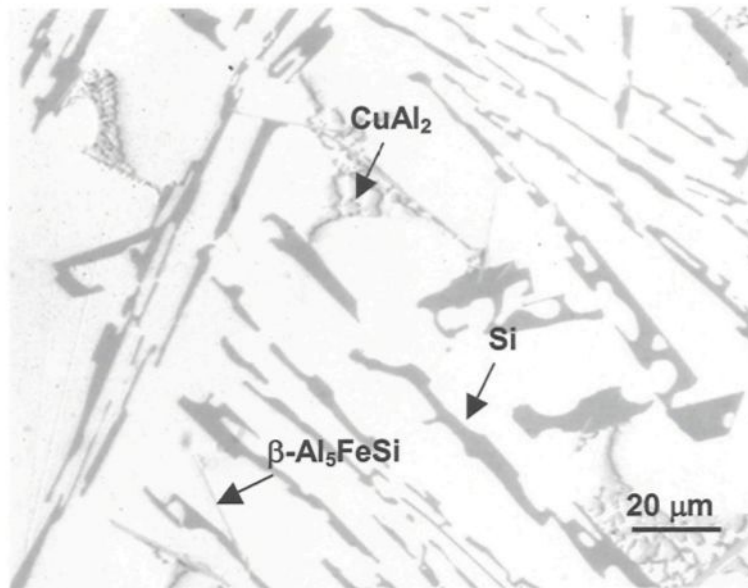
- iv) Sr and cooling rate have the same effect on the Si particle characteristics as in the 319 alloy. However, overall, the Si particle sizes are smaller, *viz.*, from about 4 - 34  $\mu m$  in the unmodified alloy, to about 1 - 5  $\mu m$  in the Sr-modified

case. This may be explained on the basis of the shorter solidification time of the 356 alloy, allowing less time for Si particle growth.

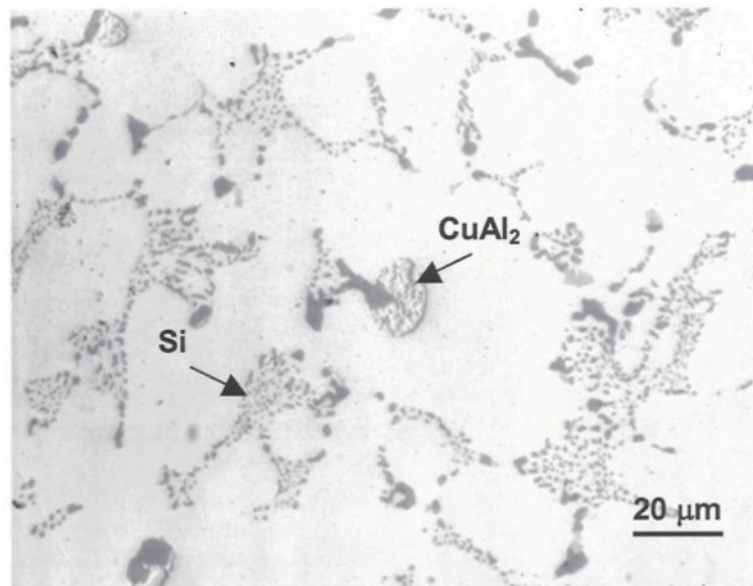
### 5.2.3 Microstructural Analysis

Typical microstructures of the low-Fe-containing 319 alloy samples obtained at the lowest (*viz.*, 85  $\mu\text{m DAS}$ ) and highest (*viz.*, 15  $\mu\text{m DAS}$ ) cooling rates (samples AF2-C and AF2S-0, respectively) are shown in Figure 5.3. These microstructures represent the two alloy-solidification condition extremes of (a) non-modified alloy - low cooling rate, and (b) modified alloy - high cooling rate. Compared to the maximum size of Si particles and other constituents in Figure 5.3(a), Figure 5.3(b) reveals how both Sr addition and a high cooling rate can optimize the solidification conditions to produce a very fine silicon structure.

The high iron content in the AF8-C alloy samples, Figure 5.4, is manifested by both the higher volume fraction of the needle/plate-like  $\beta\text{-Al}_5\text{FeSi}$  iron intermetallic phase in the microstructure, as well as the increase in the  $\beta$ -phase platelet size. The  $\text{CuAl}_2$  phase is also observed, formed along the sides of the  $\beta\text{-Al}_5\text{FeSi}$  or Si platelets, Figure 5.4(a). It is interesting to note how the finest Si particles in the AF8S-C alloy (Figure 5.4(b)) appear mainly alongside the  $\beta\text{-Al}_5\text{FeSi}$  platelets, whereas further away, they are larger in size. This was generally found to be the case wherever the Si particles near the  $\beta$ -platelets were examined.

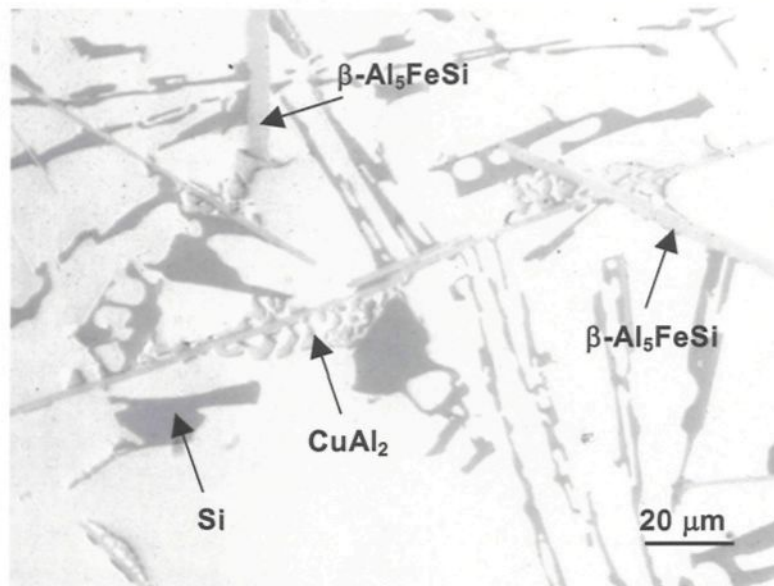


(a)

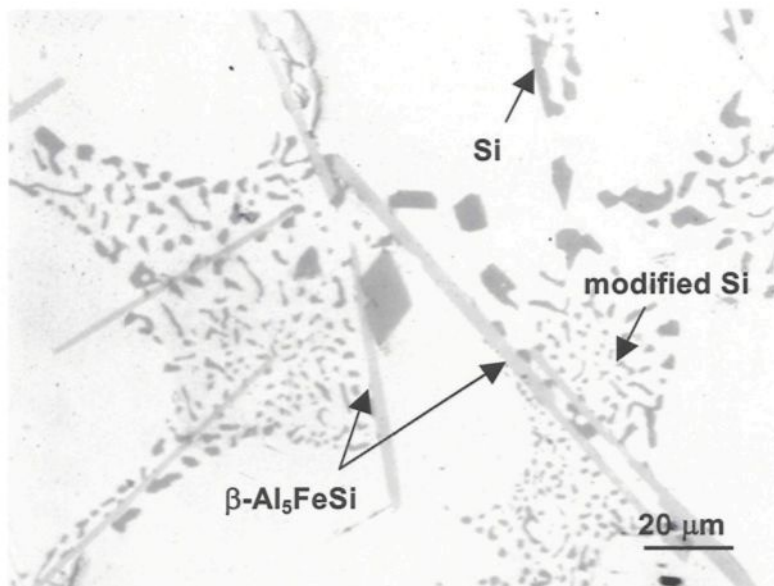


(b)

**Figure 5.3** Optical microstructures obtained from the 319 alloy containing 0.2 wt% Fe: (a) non-modified AF2-C (85  $\mu\text{m}$  DAS) sample, (b) 250 ppm Sr-modified AF2S-0 (15  $\mu\text{m}$  DAS) sample.



(a)

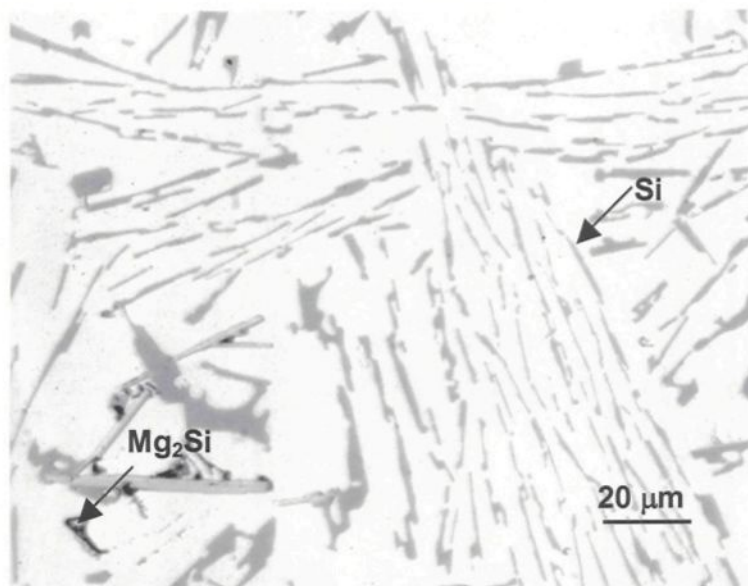


(b)

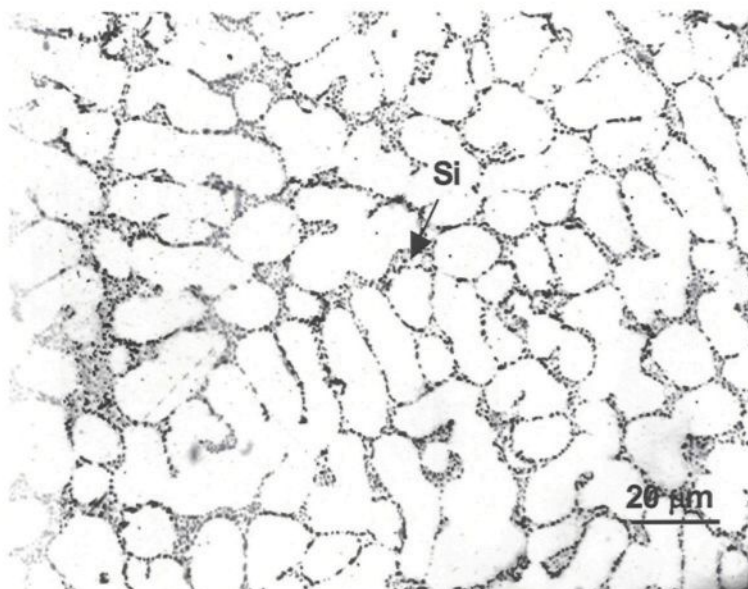
**Figure 5.4** Optical microstructures obtained from the 319 alloy containing 0.8 wt% Fe: (a) non-modified AF8-C (85  $\mu\text{m}$  DAS) sample, (b) 250 ppm Sr-modified AF8S-C (85  $\mu\text{m}$  DAS) sample.

In the case of the 356 alloy, the low-Fe (CF2-C) and high-Fe (CF6-C) samples, Figures 5.5 and 5.6, respectively, reveal the precipitation of  $Mg_2Si$ , besides the acicular Si platelets and a few platelets of the  $\beta-Al_5FeSi$  phase. At the highest cooling rate (*i.e.*,  $\sim 15 \mu m$  DAS), 250 ppm Sr addition is sufficient to produce a well-modified eutectic Si structure in the 0.2 wt% Fe-containing alloy, Figure 5.5(b), as also in the 0.6 wt% Fe containing alloy, even at  $\sim 85 \mu m$  DAS, Figure 5.6(b). In the latter case, however, precipitation of the  $Al_2Si_2Sr$  intermetallic is also observed.

Of interest to note is the fact that the Si particles in the vicinity of the large  $Al_2Si_2Sr$  particle remain unmodified. This is believed to be a consequence of the  $Al_2Si_2Sr$  phase precipitation - in a co-eutectic reaction, wherein all the Sr in the local melt region is used up, leaving none to modify neighboring Si particles.

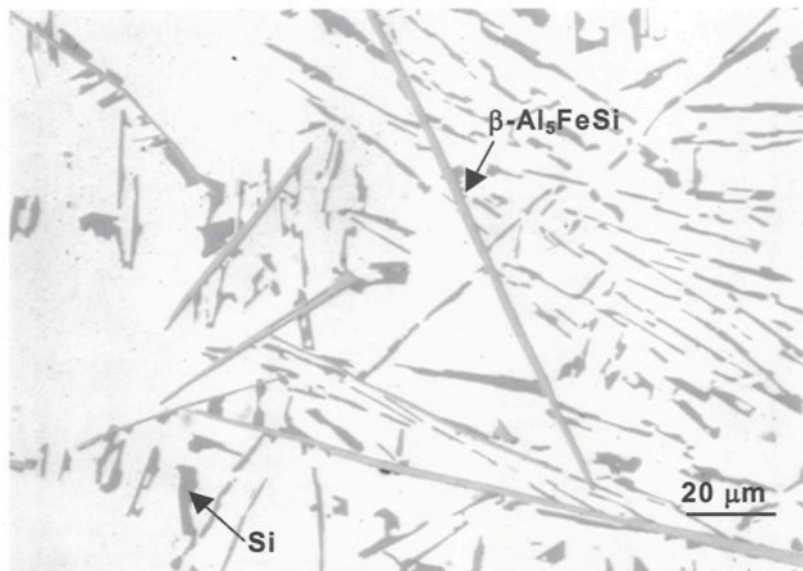


(a)

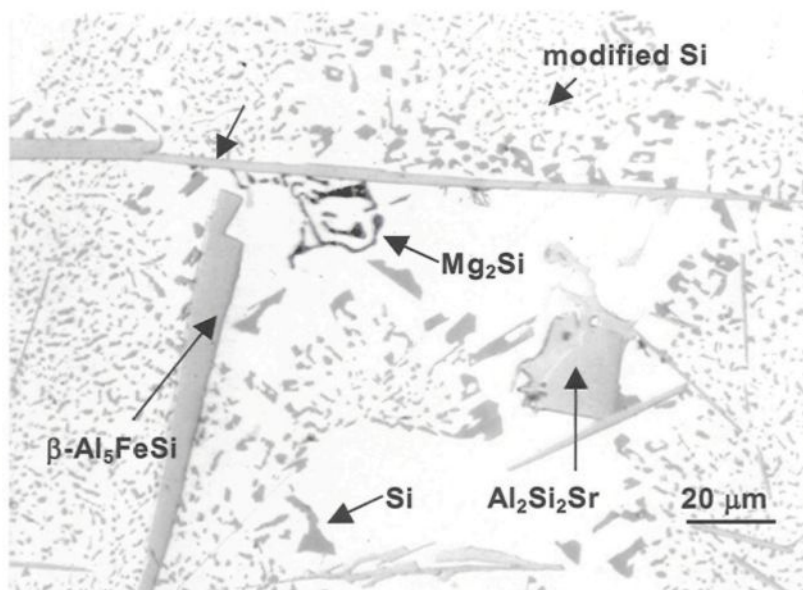


(b)

**Figure 5.5** Optical microstructures obtained from the 356 alloy containing 0.2 wt% Fe: (a) non-modified CF2-C (85  $\mu\text{m}$  DAS) sample, (b) 250 ppm Sr-modified CF2S-0 (15  $\mu\text{m}$  DAS) sample.



(a)



(b)

**Figure 5.6** Optical microstructures obtained from the 356 alloy containing 0.6 wt% Fe: (a) non-modified CF6-C (85  $\mu\text{m}$  DAS) sample, (b) 250 ppm Sr-modified CF6S-C (85  $\mu\text{m}$  DAS) sample.

Figure 5.7 shows the microstructure obtained from the 356 alloy solidified in the hot graphite mold (*viz.*, at a cooling rate of  $\sim 0.8$  °C/s), showing nucleation/precipitation of Si on pre-eutectic (arrowed 1), and co-eutectic (arrowed 2)  $\beta$ -Al<sub>5</sub>FeSi platelets.

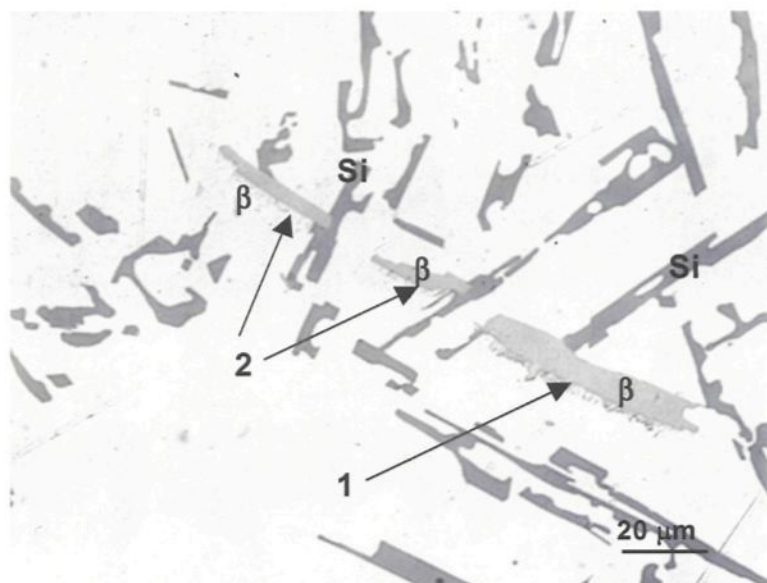


**Figure 5.7** Optical microstructure obtained from the 356 alloy solidified at  $\sim 0.8$ °C/s, showing precipitation of Si and  $\beta$ -Al<sub>5</sub>FeSi phases (1: pre-eutectic  $\beta$ -, and 2: co-eutectic  $\beta$ -Al<sub>5</sub>FeSi).

The large size of the  $\beta$ -Al<sub>5</sub>FeSi platelet (1) indicates that it must have formed at a higher temperature, *i.e.*, in a pre-eutectic reaction (giving it also a longer time to grow), whereas the much smaller size of the other two  $\beta$ -platelets (2) indicates they are very likely the products of a co-eutectic reaction.

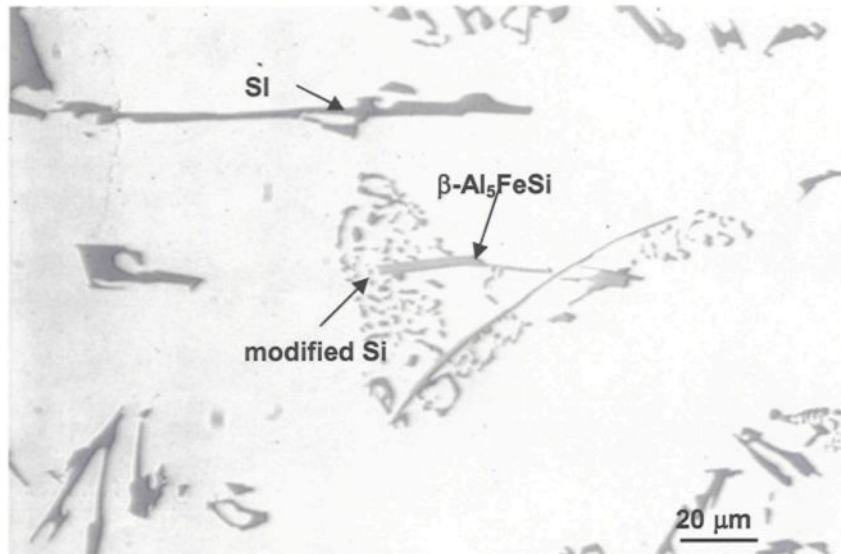
What must be noted here is that the Si precipitates on the  $\beta$ -Al<sub>5</sub>FeSi platelets, no matter whether the alloy is modified or not, or whether the iron level is low or high. The

surface area of the  $\beta$ -Al<sub>5</sub>FeSi platelets increases with increasing Fe content, thus providing many more nucleation sites for the Si particles and, therefore, a refinement of their size.

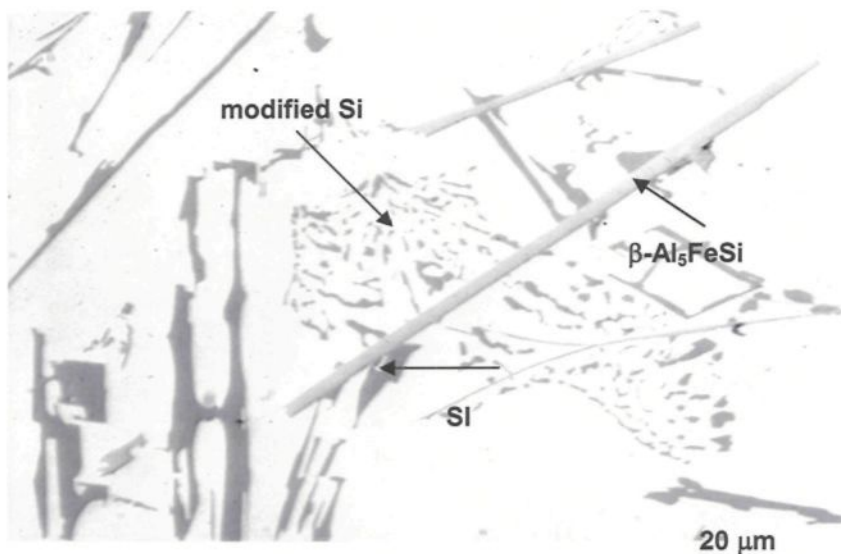
In their studies on the role of Fe on porosity formation in Al-Si-Cu alloys, Taylor *et al.*<sup>[11]</sup> have also reported that  $\beta$ -Al<sub>5</sub>FeSi platelets are the main nucleation sites for the Si phase. Nucleation of Si occurs on both large ‘primary’ or ‘binary’  $\beta$ -platelets, and possibly smaller ‘ternary’  $\beta$ -platelets, where, in the latter two cases, the  $\beta$ -Al<sub>5</sub>FeSi phase is considered as a component of the Al- $\beta$ -Al<sub>5</sub>FeSi binary eutectic and the Al-Si- $\beta$ -Al<sub>5</sub>FeSi ternary eutectic reactions. The  $\beta$ -platelets classified as ‘pre-eutectic’ and ‘co-eutectic’ in our case would correspond to the ‘primary’ and ‘binary’ terminology used by Taylor *et al.*<sup>[17]</sup> They also reported that the Si particles were often observed to grow from multiple locations along a single  $\beta$ -platelet. This is noted to some extent in Figure 5.7, where the  $\beta$ -platelets (1 and 2) show the growth of at least two, if not more, Si particles from their edges.

To separate the individual effects of Fe and Sr in the alloy, the low-Fe and high-Fe 356 alloy melts were modified using a very small amount of Sr, *i.e.*, 30 ppm, corresponding to the under-modified condition. The microstructure of the corresponding CF2-C low-Fe alloy sample (DAS  $\sim$ 85  $\mu$ m), Figure 5.8(a), clearly displays two  $\beta$ -platelets, surrounded by very fine Si particles. Elsewhere in the micrograph, large, acicular Si platelets are observed, indicating that away from regions containing the  $\beta$ -Al<sub>5</sub>FeSi platelets, the Si particles are not modified. The same effect is also observed in the high-Fe-containing CF6-C alloy sample, Figure 5.8(b). Apart from the fact that the  $\beta$ -Al<sub>5</sub>FeSi platelets are much larger in the

microstructure, modification of the Si particles is clearly noted in the regions surrounding the  $\beta$ -platelets, whereas those elsewhere appear unmodified (cf. 1-2  $\mu\text{m}$  with 9-12  $\mu\text{m}$  Si particle sizes).



(a)



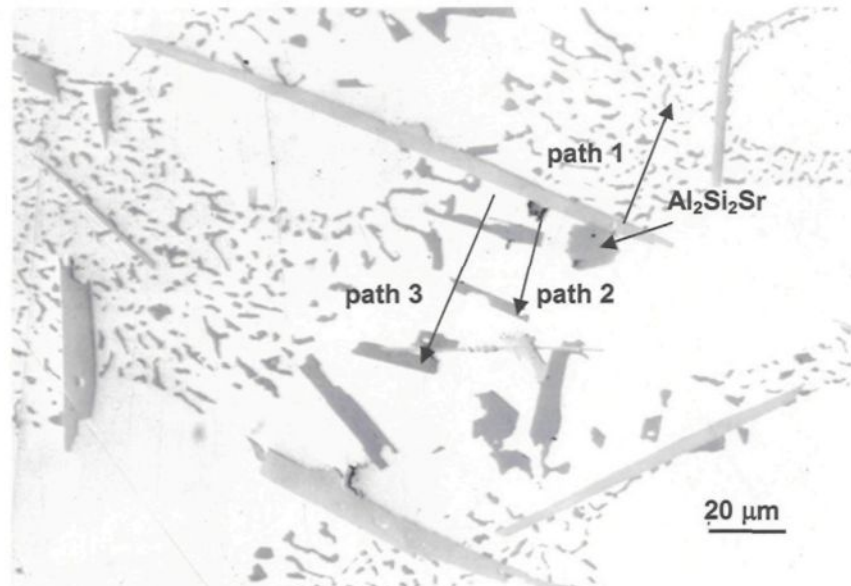
(b)

**Figure 5.8** Optical micrographs obtained from the 356 alloy modified with 30 ppm Sr: (a) low-Fe alloy, and (b) high-Fe alloy samples (85  $\mu\text{m}$  DAS).

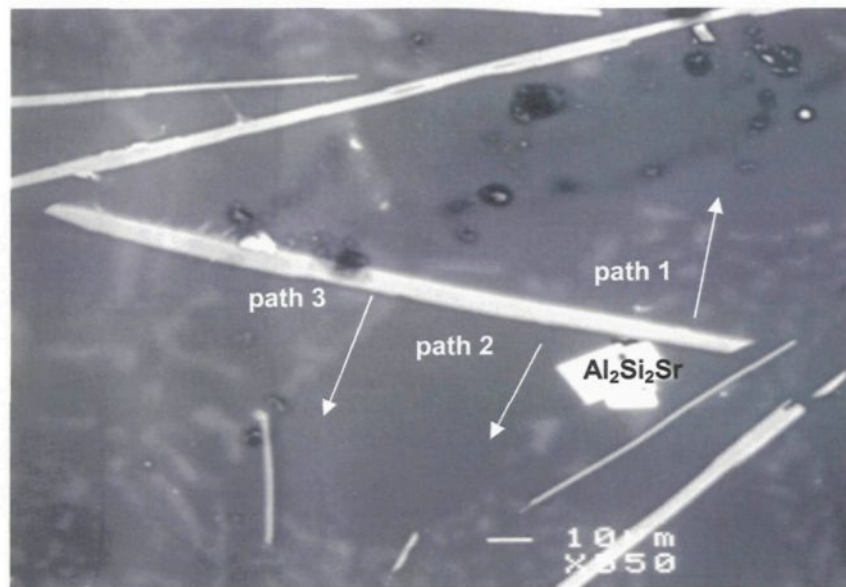
When the Sr level is increased to 250 ppm in the high-Fe-containing 356 alloy, the microstructure displays a well-modified Si structure, along with large-sized platelets of  $\beta$ - $\text{Al}_5\text{FeSi}$ , Figure 5.9(a). An  $\text{Al}_2\text{Si}_2\text{Sr}$  particle is also observed near the tip of one of the  $\beta$ -platelets (arrowed). As was observed in the case of Figure 5.6(b), the Si particles near the  $\text{Al}_2\text{Si}_2\text{Sr}$  particle are large and unmodified, as, with the formation of the Al-Si-Sr phase, the local region is depleted in strontium.

Figure 5.9(b) shows an SEM backscattered image of the microstructure of the same sample, taken from a region similar to that shown in the optical micrograph of Figure 5.9(a). The large  $\text{Al}_2\text{Si}_2\text{Sr}$  particle towards the bottom right appears very bright, due to the presence of the Sr constituent.

Line scans for Sr and Si were taken along three directions, as shown in Figure 5.9(b): path #1 – starting at the  $\beta$ -platelet edge, and moving on through a modified Si particle region, path #2 – through the matrix, adjacent to the  $\text{Al}_2\text{Si}_2\text{Sr}$  particle, and path #3 – through an unmodified Si region. It should be mentioned here that these line scans were carried out using a ‘superprobe’ with which it is possible to use a beam diameter of  $< 1\mu\text{m}$  for spot analysis purposes. The spot zone analyzed at any point, however, is  $\sim 2\mu\text{m}$  in diameter. The analysis was carried out at intervals of  $3\mu\text{m}$  to avoid overlap of the areas/zones measured along the line scan path.



(a)

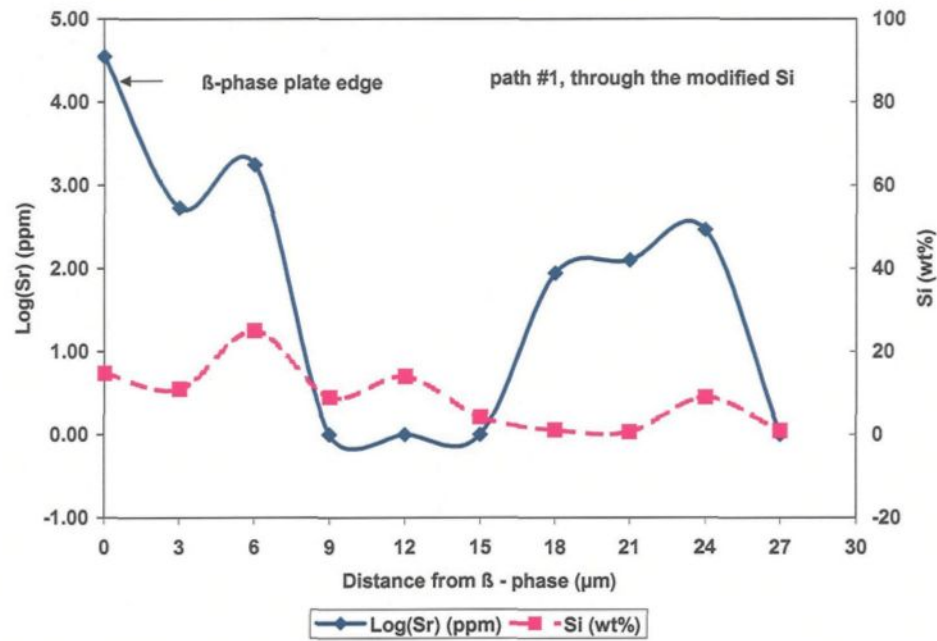


(b)

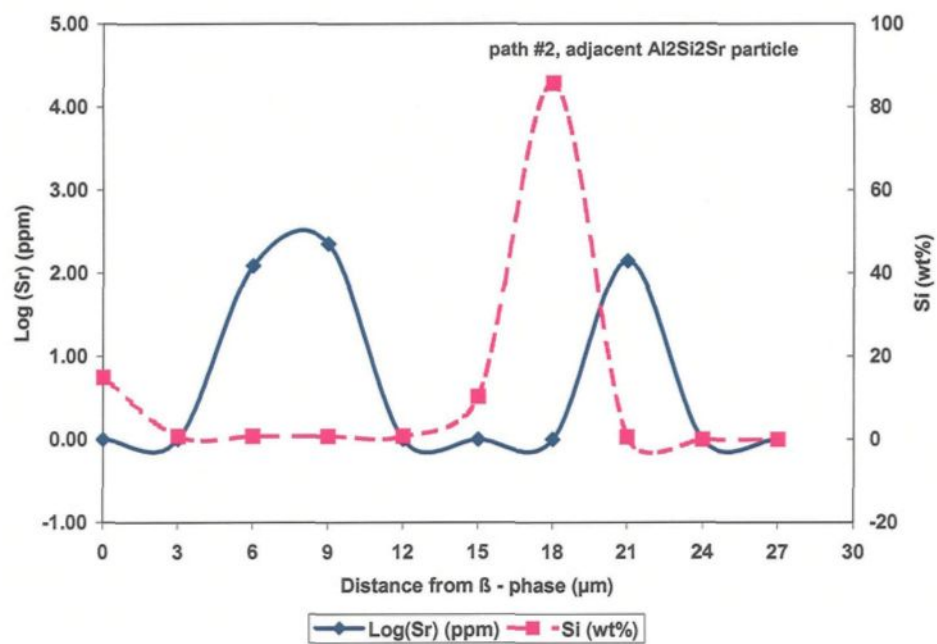
**Figure 5.9** Microstructures of the 250 ppm Sr-modified high-Fe 356 alloy sample: (a) optical micrograph, (b) SEM backscattered image.

Figure 5.10 shows the plots of log (Sr) and Si as a function of the distance from the  $\beta$ -platelet in the matrix (in multiples of 3  $\mu\text{m}$ ) taken along the three paths. The concentration profiles reflect the microstructural characteristics observed visually in Figure 5.9. In the first case, Figure 5.10(a), the Si particles have small sizes in this region. Correspondingly, the Sr concentrations are high, in general, except for the spots in the centre of the plot, where the beam passed through the aluminum region of the eutectic. Also to be noted is the high Sr value at the start of the Sr plot in the figure, near the  $\beta$ -phase plate edge, suggesting the presence of a high concentration of Sr in the vicinity of this phase.

In the second case, Figure 5.10(b), the Sr concentration shows two peaks and a valley in between, the latter corresponding to the spot where the  $\text{Al}_2\text{Si}_2\text{Sr}$  particle is closest to the path traversed. Correspondingly, a large Sr peak is observed in this area, suggesting a gradient of Sr concentration around the  $\text{Al}_2\text{Si}_2\text{Sr}$  particle. The sole peak for Si corresponds to the large Si particle crossing the path (corresponding to almost 85 wt% Si). In Figure 5.10(c), the passage of path #3 through the unmodified Si particle region shows two Si peaks in the plot, at points where the path crosses these particles, and a Sr concentration close to nil along the path (obviously, since the eutectic region is unmodified in this case).



(a)



(b)

**Figure 5.10** Plots of  $\log(\text{Sr})$  and Si contents as a function of distance from the  $\beta$ -platelet in the line scans taken along (a) path #1, (b) path #2, and (c) path #3 shown in Figure 5.9(b).

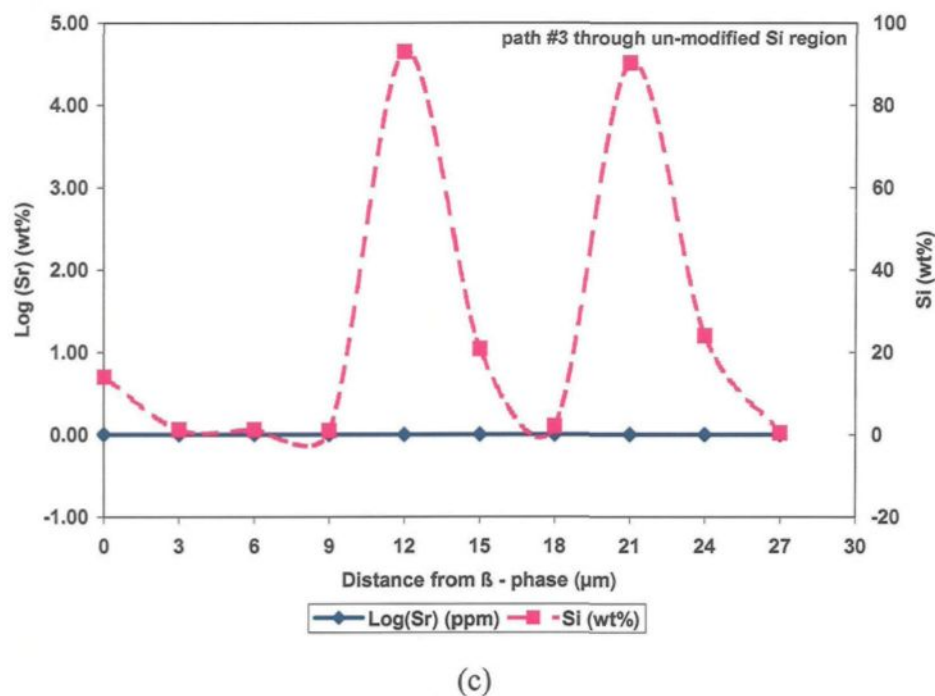


**Figure 5.10** Plots of log (Sr) and Si contents as a function of distance from the  $\beta$ -platelet in the line scans taken along (a) path #1, (b) path #2, and (c) path #3 shown in Figure 5.9(b).

#### 5.2.4 Mechanism of Si Particle Modification

The mechanism of precipitation of these phases in both the under-modified and well-modified conditions may be explained by the schematic diagrams depicted in Figure 5.11, where the temperatures at which the  $\alpha$ -Al,  $\beta$ -Al<sub>5</sub>FeSi and Al-Si eutectic precipitate are denoted by  $T_L$  (liquidus),  $T_\beta$ , and  $T_E$ , respectively. In the under-modified case (for a low Sr addition of ~30 ppm), Figure 5.11 (a), the formation of the  $\alpha$ -Al dendrite network takes place first, as shown in step 1. As solidification proceeds, the precipitation of the  $\beta$ -Al<sub>5</sub>FeSi phase occurs. From previous studies,<sup>132</sup> where Sr was found to assist in the fragmentation and dissolution of the  $\beta$ -phase, we may reasonably assume that the  $\beta$ -phase

platelets are surrounded by pools of Al-Si-Sr liquid relatively high in Sr concentration, where the Sr is absorbed on the  $\beta$ -platelet sides. Precipitation of the Al-Si eutectic thereafter will result in modified Si particles in the areas near the  $\beta$ -phase platelets, and unmodified particles elsewhere in the structure.

When the amount of Sr added is high (250 ppm), the mechanism is somewhat different, as depicted in Figure 5.11 (b). While step 1) is essentially the same, due to the much higher Sr concentration in the melt, however, the  $\beta$ -platelets are now associated with highly concentrated Al-Si-Sr patches, where the  $\text{Al}_2\text{Si}_2\text{Sr}$  particles are most likely to precipitate, in a co-eutectic reaction, as shown in step 2). The Si particles that precipitate nearby will remain unmodified due to the depletion in Sr in these local areas, but will be well-modified elsewhere, due to the sufficient amount of Sr present in the alloy (step 3).

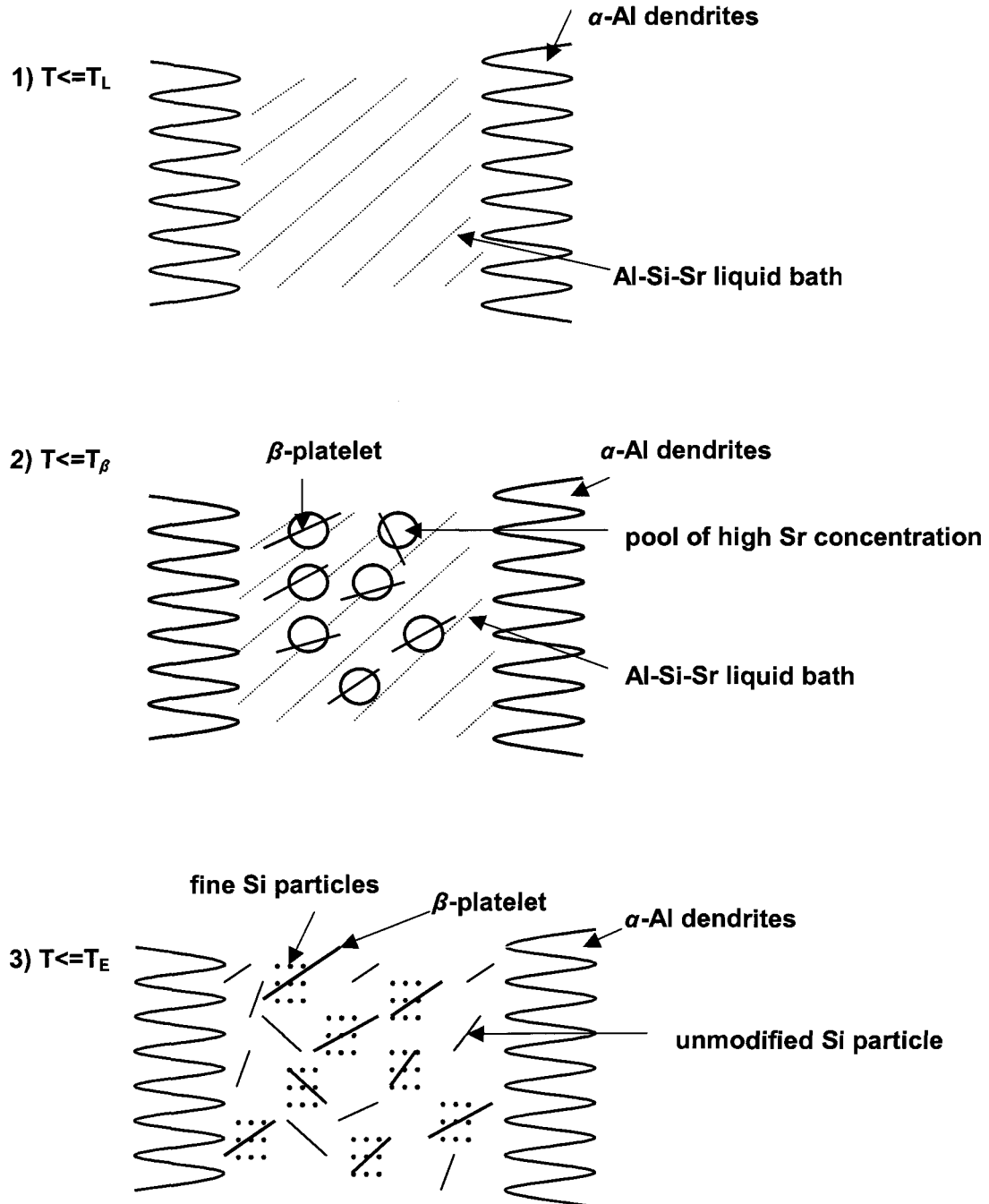


**Figure 5.11** (a) Mechanism of Si particle modification in under-modified (30 ppm Sr) Fe-containing Al-Si alloys.

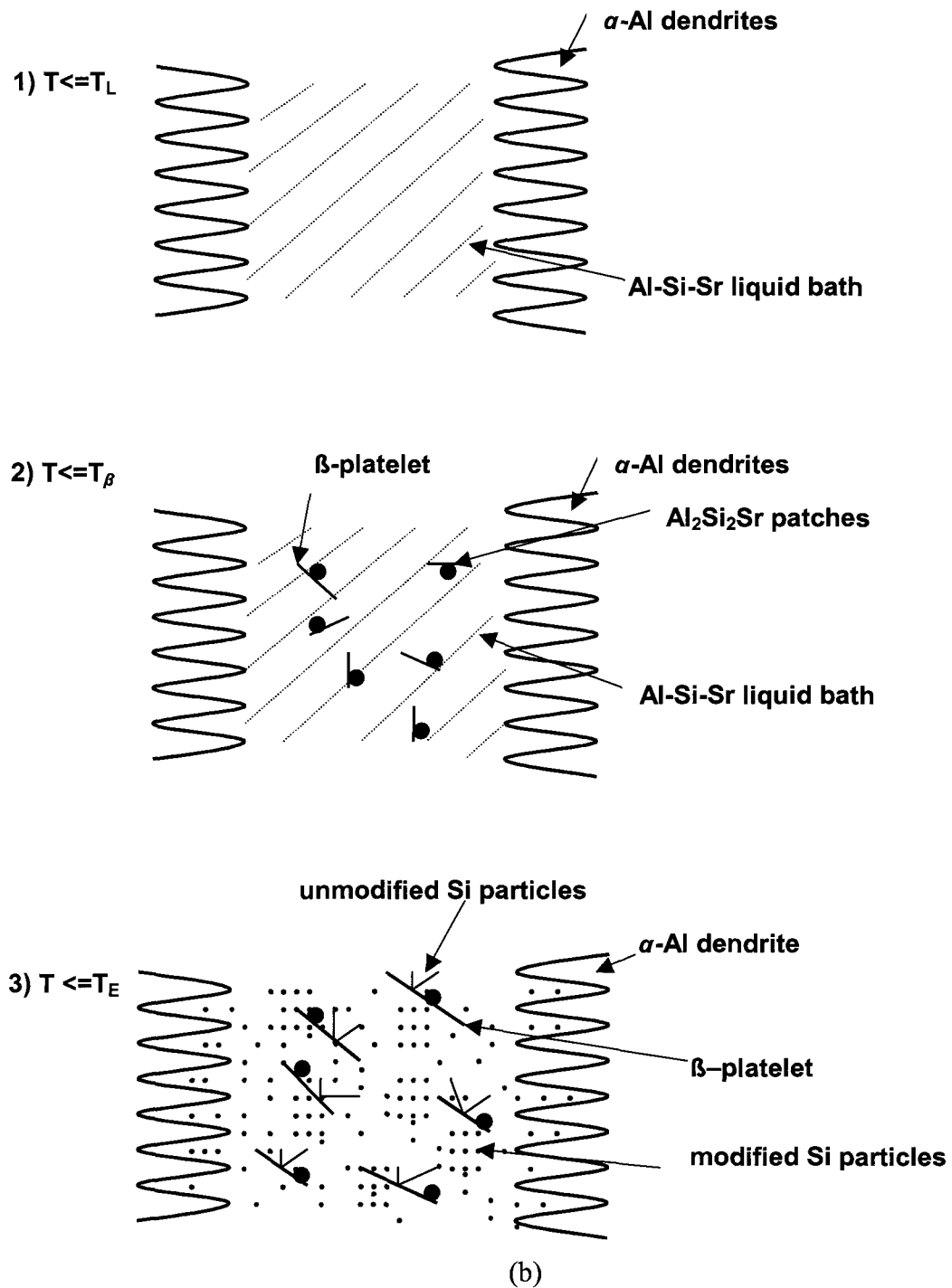


**Figure 5.11** (b) Mechanism of Si particle modification in well-modified (250 ppm Sr) Fe-containing Al-Si alloys.

Referring to the cooling curve and first derivative shown in Figure 5.2, obtained for the Sr-modified experimental 319 alloy containing 0.8 wt% Fe, it should be mentioned that an experimental alloy was used to minimize the possibility of interference from tramp elements or impurities. The different peaks marked A through F on the first derivative curve, and the corresponding temperatures and reactions are listed in Table 5.3, where the peaks D and E correspond, respectively, to the co-eutectic and post-eutectic precipitation of  $\text{Al}_2\text{Si}_2\text{Sr}$ .

According to DasGupta *et al.*,<sup>138</sup> in the 319 alloy (containing 6.5% Si), well-modified Al-Si eutectic structures are attained with Sr levels in the range 50-100 ppm. Their thermal analysis data also shows that maximum undercooling (*viz.*,  $-10\text{ }^\circ\text{C}$ ) with respect to the eutectic temperature, *i.e.*, maximum modification is observed in this range of Sr. Higher levels result in coarsening (or overmodification) of the Si particles. Thus, any amount added beyond this limit should lead to precipitation of the strontium as  $\text{Al}_2\text{Si}_2\text{Sr}$  particles. This is evidenced by the peaks D and E in Figure 5.2 in our study.

Closset and Gruzleski<sup>24</sup> also observe that, apart from the coarsening effect, a second evidence of Sr overmodification is the appearance of Sr-containing intermetallics, *e.g.*,  $\text{Al}_4\text{SrSi}_2$  in the microstructure. Furthermore, the two effects need not occur simultaneously, *i.e.*, the Sr intermetallics can precipitate without appreciable Si coarsening. The schematic diagrams of Figure 5.11 in the present study have attempted to explain how this happens.

In this connection, in a recent study on the decomposition of Fe-intermetallics in Sr-modified cast 6XXX type aluminum alloys, Samuel *et al.*<sup>139</sup> observed the formation of AlSiSr intermetallics in Al-0.521% Si-0.147% Fe-0.0186% Cu-0.005% Mg alloy modified

with various amounts of Sr (300, 500, and 800 ppm), and found that the AlSiSr particles occurred even at 300 ppm Sr additions. Due to the fact that these particles were mostly observed attached to the sides or the ends of the  $\beta$ -platelets, it was reasonably assumed that the Si rejected from the latter reacted with the Sr in the surrounding area, leading to the formation of AlSiSr intermetallics ( $Al_4Si_2Sr$  or  $Al_2Si_2Sr$ ).

For the purposes of providing more information on the nature of these AlSiSr particles, an analysis of their composition in a 600 ppm Sr-modified Al-7 pct Si alloy using wavelength dispersion spectroscopy (WDS) was carried out, and showed that the particles corresponded closely to  $Al_2Si_2Sr$  (Al : 40.214 at. pct, Sr : 18.59 at. pct, Si : 38.34 at. pct, and O : 2.8 pct). The  $Al_2Si_2Sr$  particles were mostly polyhedral in nature<sup>139</sup>. However, it was also observed that the  $Al_2Si_2Sr$  phase could precipitate directly from the melt, particularly in those cases where the Sr level was sufficiently high. In this case, it appeared in the form of short, fine needles or rods.

At this point, it is worth mentioning that the difference in the composition of the AlSiSr particles ( $Al_2Si_2Sr$  or  $Al_4Si_2Sr$ ) could result from the difference in the size of the particles analyzed. Thus, in the case of small particles, the surrounding Al matrix may influence the stoichiometry, giving the  $Al_4Si_2Sr$  formula.

It has also been mentioned that during overmodification, there is coarsening of the silicon structure, as well as the reversion of the fibrous silicon to an interconnected plate form.<sup>138,24</sup> Actually, it could be considered that this is not so much a case of reversion of the silicon morphology from fibrous to plate-like, as that of precipitation of the  $Al_2Si_2Sr$  phase during the co-eutectic reaction, causing local depletion in Sr, and thus leading to the

precipitation of *unmodified* rather than *overmodified* coarse Si particles in the neighbourhood. Figure 5.12 shows the precipitation of an  $\text{Al}_2\text{Si}_2\text{Sr}$  particle surrounded by the eutectic Si region, observed within a pore in the Sr-modified 356 low-Fe alloy sample (85  $\mu\text{m}$  DAS). Note the sharp edges of the  $\text{Al}_2\text{Si}_2\text{Sr}$  particle due to its incoherency with the matrix.

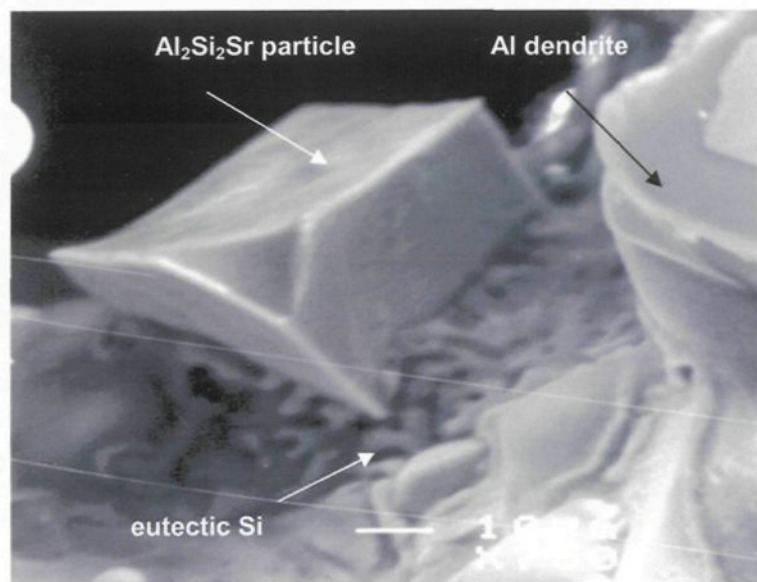


**Figure 5.12** SEM micrograph showing an  $\text{Al}_2\text{Si}_2\text{Sr}$  particle surrounded by eutectic Si region within a pore observed in the Sr-modified 356 alloy.

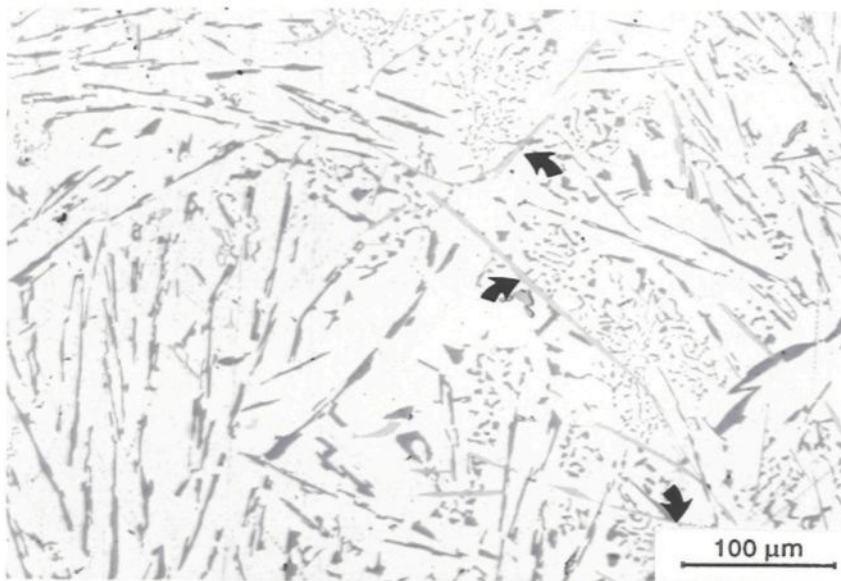
To strengthen the proposed mechanism of the role played by iron (*viz.*, Fe-intermetallics) in Si modification, two experiments were carried out using a eutectic Al-12 wt% Si alloy containing 1.1 wt% Fe. In the first case, 0.3 wt% Mn was added in order to encourage precipitation of the Fe-intermetallics in the  $\alpha$ -Fe script form. The alloy was modified with 50-60 ppm Sr. In the optical micrograph of Figure 5.13(a), modified Si particles are always observed at the edges of the  $\alpha$ -Fe script particles (open arrows),

whereas, in regions away from the script particles, the Si particles are clearly unmodified. The same effect is observed in the case of the  $\beta$ -Fe intermetallics seen in the microstructure (black arrows).

In the second experiment, the alloy was modified with 200 ppm Sr, in order to obtain a fully modified structure. Phosphorus was then added to the alloy in the amount of 60 ppm. Figure 5.13(b), corresponding to this alloy, shows that only the eutectic Si regions around the  $\beta$ -Fe intermetallics are modified (black arrows); elsewhere, the Si particles are typically acicular in nature, attributed to the interaction between P and Sr, that negates the modification effect of Sr.<sup>140</sup> This observation has been demonstrated in Figure 5.11.



(a)



(b)

**Figure 5.13** Optical micrographs showing the modification of Si particles due to the segregation of Sr near  $\alpha$ -Fe (open arrows) and  $\beta$ -Fe (black arrows) intermetallics in the Al-12%Si-1.1%Fe alloy containing: (a) 0.3% Mn + 60 ppm Sr, and (b) 200 ppm Sr + 60 ppm P.

## **CHAPTER 6**

# **CHARACTERISTICS OF $\alpha$ -DENDRITIC AND EUTECTIC STRUCTURES IN SR-TREATED ALLOYS**

## CHAPTER 6

### CHARACTERISTICS OF $\alpha$ -DENDRITE AND EUTECTIC STRUCTURES IN SR-TREATED ALLOYS

#### 6.1 INTRODUCTION

The quality of the microstructure, as well as the amount of porosity present therein determine the strength and quality of an Al-Si alloy casting. Normally, the microstructure is controlled through the processes of grain refinement and modification using small additions of Al-Ti-B and Al-Sr master alloys, respectively. Whereas grain refinement primarily reduces the grain size, modification alters the morphology of the eutectic Si from its usual acicular brittle form to a fibrous form (in the case of Na and Sr) that enhances the mechanical properties, particularly the ductility. Among the various modifiers in use, strontium has, by far, been employed most extensively. Although easier to handle than either Na or the toxic Sb, and more resistant to fade (*i.e.*, losing its modifying effect after a certain amount of time), Sr addition is also associated with porosity formation in these alloys.

From the feedability-related point of view, it has been pointed out that one should look to the Al-Si eutectic region of solidification to account for the differences in porosity observed when Sr is added to Al-Si melts.<sup>21,141,142</sup> Given that the eutectic constitutes a

sizeable fraction of the microstructure of Al-Si alloys (depending on the Si level), it would be expected that the Sr-modified eutectic structure would exert some sort of influence on porosity formation. In this connection, Dahle *et al.*,<sup>143</sup> who observed an orientation relationship between the  $\alpha$ -Al dendrites and eutectic Si in unmodified hypoeutectic Al-Si alloys, and a lack of it in the (200 ppm) Sr-modified alloys (using electron micro-diffraction techniques), have suggested that this represents a change in the mode of eutectic nucleation – from that occurring near the  $\alpha$ -Al dendrites in the Sr-free alloy, to that taking place within the eutectic liquid itself in the Sr-containing alloy. The mode in operation controls the distribution of the remaining liquid in the last stages of solidification when feeding becomes extremely difficult. This distribution, in turn, will define the connectivity of the feeding channels, and thus determine the resultant porosity profile in the solidified casting.

It is the aim of the present chapter to show the changes in both  $\alpha$ -Al dendritic and eutectic regions in Sr-containing Al-Si alloys. A series of experimental and industrial Al-Si casting alloys were selected, from simple experimental “binary” alloys such as Al-7%Si and Al-12%Si, to industrial 319 and 356 alloys, to cover a variety of alloy freezing ranges. It should be mentioned here that the term “binary alloys” in the present chapter has been used only in the sense that Al and Si are the main constituents of the corresponding alloys, as against other alloying elements that are present in addition in the 356 and 319 alloys.

## 6.2 EXPERIMENTAL PROCEDURE

Table 6.1 lists the various alloy compositions that were used and their respective alloy codes. The alloys were cut into smaller pieces, cleaned, dried and melted in a 40 kg-capacity SiC crucible. The melting temperature was kept at  $725^{\circ} \pm 5^{\circ}\text{C}$ . The melts were degassed with dry argon for  $\sim 30$  min, using a graphite rotary impeller (200 rpm; humidity of surroundings  $< 15\%$ ). A 5-cm wide, 25-cm long plate made of refractory material, placed inside the crucible at an angle of  $\sim 35$  degrees with the crucible wall, acted as a baffle during the melting and degassing process, to avoid vortex formation. In those cases when the melts were modified with Sr, the required amount of Sr was added to the melt using Al-10% Sr master alloy, before the degassing was carried out. All alloy melts (experimental as well as industrial) were grain refined using Al-5%Ti-1%B master alloy (maximum attainable B was  $\sim 40$  ppm). Samplings for chemical analysis were also taken simultaneously for each melt composition.

In the case of the experimental alloys, the alloys were first prepared by melting aluminum (purity 99.5%) at the same temperature, then adding pure silicon in the required amounts by means of a perforated graphite bell, to obtain the Al-7%Si and Al-12%Si compositions. The respective alloy melts were poured into ingot molds (made of mild steel and coated with refractory material), and the solidified ingots in each case were then remelted for treatment as described above.

**Table 6.1** Chemical Compositions (Wt%) of Alloys Used

Alloy	Code	Si	Fe	Cu	Mg	Mn	Cr	Ti	Sr	Al
<u>Experimental</u>										
Al-7%Si	A7S	6.74	0.1599	0.2825	0.0228	0.0316	0.0051	0.0246	0.0018	92.7
Al-7%Si+Sr	A7SS	6.71	0.1891	0.3656	0.0340	0.0331	0.0064	0.0274	0.0114	92.6
Al-12%Si	A12S	11.76	0.1451	0.1144	0.0119	0.0072	0.0012	0.0413	0.0010	87.9
Al-12%Si+Sr	A12SS	11.76	0.1451	0.1144	0.0119	0.0072	0.0012	0.0413	0.0245	87.8
Al-12%Si+high Sr	A12SS10	11.50	0.1811	0.0595	0.0213	0.0134	0.0065	0.0325	0.0927	88.0
<u>Industrial</u>										
319	A7SC	6.24	0.1084	3.683	0.0496	<0.0005	<0.0005	0.1332	0.0001	89.7
319+Sr	A7SCS	5.81	0.1145	3.584	0.0552	<0.0005	<0.0005	0.1466	0.0115	90.2
356	A7SM	6.50	0.1211	0.0470	0.3194	0.0008	0.0008	0.1110	0.0001	92.8
356+Sr	A7SMS	6.47	0.1332	0.0398	0.3283	0.0020	0.0020	0.1164	0.0070	92.8

For each alloy melt composition, about 1 kg of the degassed melt was transferred by means of a ladle into a 1 kg-capacity SiC crucible (length/diameter ratio: 130 cm: 85 cm) that was preheated at 750°C in a small electric resistance furnace. The transfer procedure was carried out with extreme caution to minimize turbulence, and took about 10 min. During the transfer, the SiC crucible was initially tilted at ~35 degrees, and then raised slowly while the liquid metal was poured into it, until it was in an upright position at the end of the filling.

When the melt temperature in the crucible stabilized at 725°C, the melt was poured into the preheated (600°C) cylindrical graphite crucible (see Figure 3.2 (a)). Thermal analysis was carried out at the same time, following the procedures outlined in Chapter 3, Section 3.2.2. Samplings for chemical analysis were also taken simultaneously (the spectrometric analyses were carried out at GMPT, New Hampshire facilities). From the thermal analysis data, the cooling curves and their first derivatives were plotted. From these, the different reaction temperatures and solidification times were determined.

For metallographic examination, samples (25 mm x 25 mm) were sectioned from the graphite mold castings as shown in Figure 3.2(a) (transverse section from the central part containing the thermocouple tip), mounted and polished. With respect to Figure 3.2(a), it should be noted that the direction of heat flow is parallel to the section from which the samples were cut. The microstructures were analyzed using optical microscopy and image analysis. The eutectic Si particle characteristics (length, area, aspect ratio and density), volume fractions of the  $\alpha$ -Al dendrites and eutectic Si particles, as well as the dendrite arm spacing (DAS) and lengths of primary and secondary dendrites

were measured. For measuring the  $\alpha$ -Al volume fractions, the samples were etched in Keller's reagent for the requisite amount of time, before the measurements were carried out.

### **6.3 FACTORS INFLUENCING THE MAIN MICROSTRUCTURAL CHARACTERISTICS OF AL-SI ALLOYS**

From the cooling curves obtained for each of the alloys listed in Table 6.1, the corresponding Al-Si eutectic solidification temperatures ( $T_{\text{eut}}$ ) were determined. The schematic diagram of Figure 6.1 clarifies the terminology pertaining to the various parameters used in this section. The mushy zone, eutectic, and total solidification times were also determined. These are summarized in Table 6.2. As expected, addition of Sr lowers the Al-Si eutectic solidification temperature in each alloy.

In the binary alloys, the total solidification time is roughly the sum of the mushy zone- and eutectic solidification times, where for the eutectic A12S alloy, the total solidification time equals its eutectic solidification time. In the 356 and 319 alloys, however, the total solidification times are much longer than the sums of the other two.

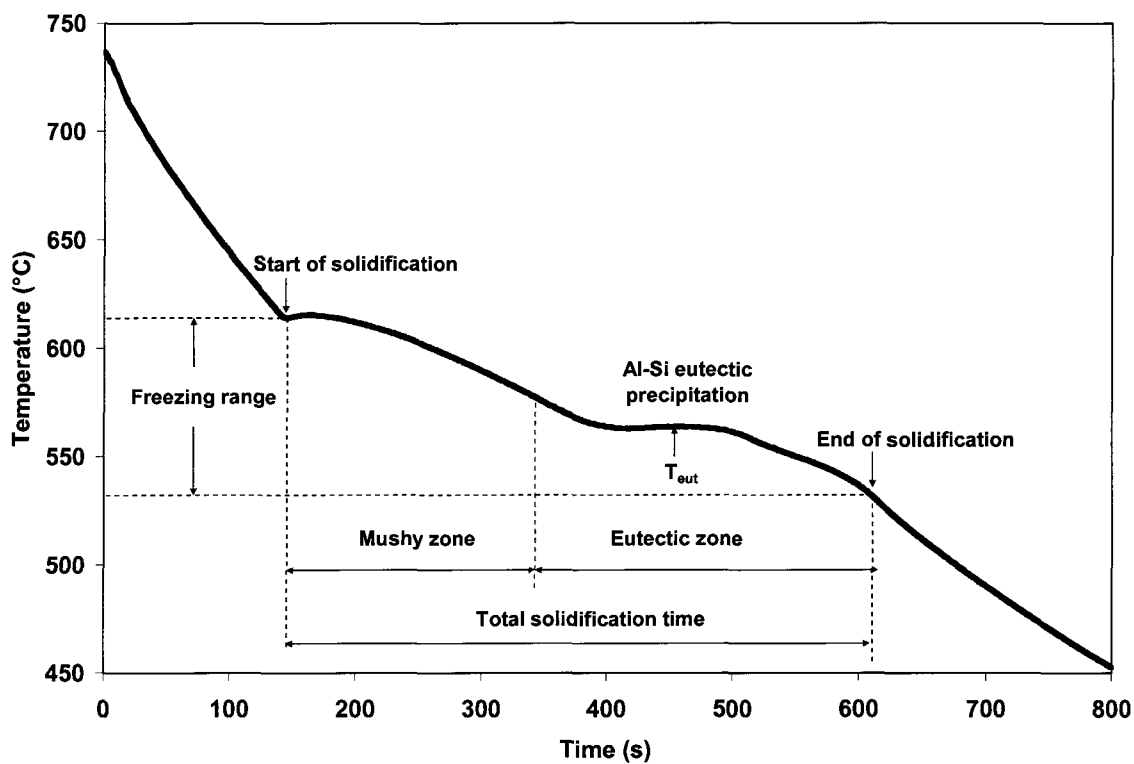


**Figure 6.1** Schematic diagram of the cooling curve of an Al-Si alloy defining the various solidification parameters (temperature and time) used.

**Table 6.2** Cooling Curve Data

Alloy	Alloy Code	$T_{eut}$ (°C)	Solidification times (s)		
			Mushy zone	Eutectic	Total
Al-7%Si	A7S	573.0	150	195	351
Al-7%Si+Sr	A7SS	565.0	189	172	360
Al-12%Si	A12S	573.6	-	411	411
Al-12%Si+Sr	A12SS	566.7	34	365	399
356	A7SM	570.1	159	156	461
356+Sr	A7SMS	563.8	194	154	479
319	A7SC	563.7	169	130	517
319+Sr	A7SCS	555.8	195	129	529

Comparing the Sr-free and Sr-modified conditions for the two commercial alloys, the mushy zone times increase in the modified alloys, whereas the eutectic solidification times are almost the same in either condition (this will be discussed in more detail later on, with reference to Table 6.5 and Figure 6.7). Also, compared to the 356 alloy, the  $T_{\text{eut}}$  is about six degrees lower in the 319 alloy due to the presence of 3.6% Cu in this alloy (see Table 6.2). This factor, together with the larger number of reactions occurring in the 319 alloy, results in its exhibiting a longer total solidification time than the 356 alloy.

Figure 6.2 displays the cooling curves and first derivatives for Sr-modified Al-7%Si and 319 alloys. The peaks marked A through E are listed in Table 6.3, and were identified with reference to the atlas of Backerud *et al.*<sup>6</sup> on the solidification of aluminum foundry alloys. In the case of the A7SS (modified Al-7%Si) alloy, the three main reactions observed correspond to the formation of the  $\alpha$ -Al dendrite network (peak A), followed by the precipitation of the Al-Si eutectic (peak B), and, due to the presence of Sr (in amounts higher than that required for obtaining a fully modified eutectic structure), the co-eutectic and post-eutectic precipitation of the  $\text{Al}_2\text{Si}_2\text{Sr}$  phase (marked C and D in Figure 6.2(a)). In the A7SCS (modified 319) alloy, Figure 6.2(b), several additional reactions occur, corresponding to the precipitation of the  $\alpha$ - and  $\beta$ -Fe intermetallics (peak C, over a range of temperature), and the precipitation of the copper intermetallics (peaks D and E). Noticeable differences in the end-of-solidification times and temperatures between the two alloys are also observed (see Table 6.2 for actual values).

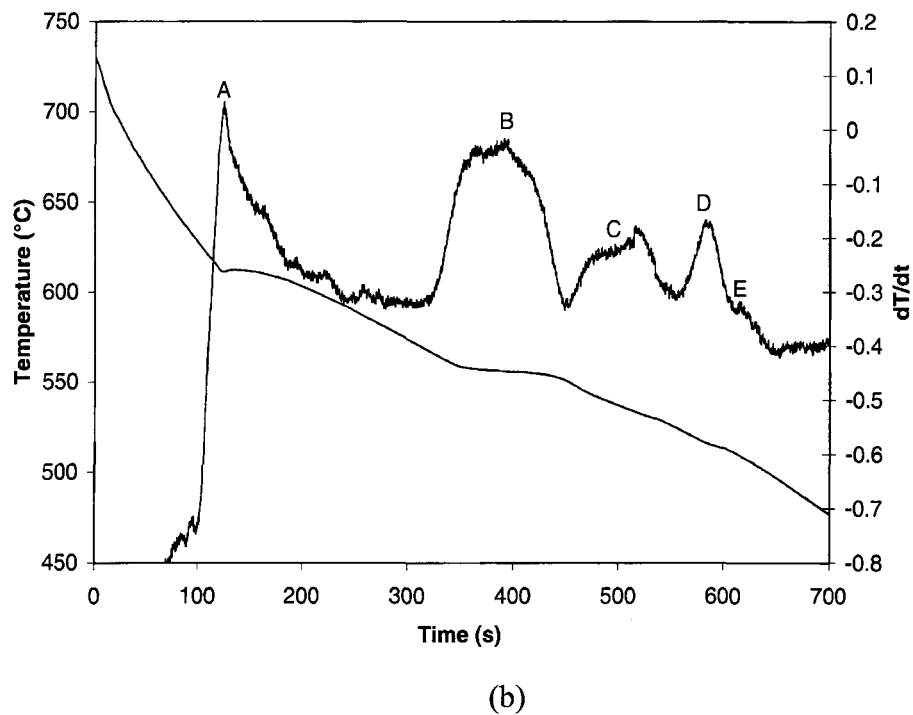
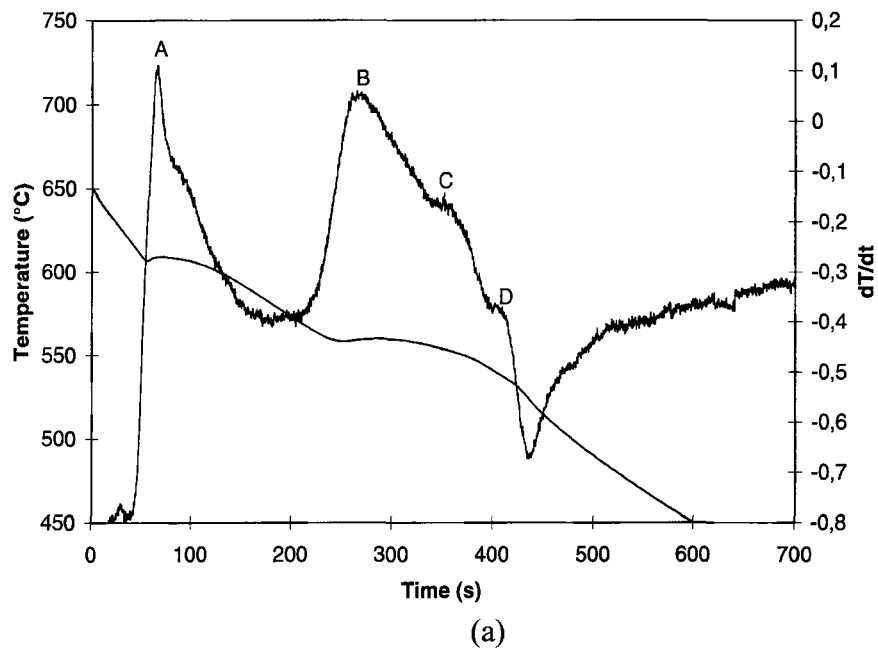


**Figure 6.2** Cooling curves and first derivatives obtained for Sr-modified (a) Al-7%Si, (b) 319 alloys.

**Table 6.3** Temperatures and Phases Corresponding to Peaks in Figure 6.2.

Figure	Peak	Temperature (°C)	Phases/Reactions
2(a) A7S alloy	A	608.8	Formation of $\alpha$ -Al dendritic network
	B	559.5-561	Eutectic Si
	C	553.6	Co-eutectic $\text{Al}_2\text{Si}_2\text{Sr}$
	D	537.9	Post-eutectic $\text{Al}_2\text{Si}_2\text{Sr}$
2(b) A7SCS alloy	A	611	Formation of $\alpha$ -Al dendritic network
	B	555.8	Eutectic Si
	C	540.6-533.2	$\alpha$ - & $\beta$ -Fe phases, $\text{Al}_2\text{Si}_2\text{Sr}$
	D	516.1	$\text{CuAl}_2$
	E	508.5	$\text{Al}_5\text{Mg}_8\text{Si}_6\text{Cu}_2$

The significance of the longer total solidification time exhibited by the 319 alloy (*cf.* A7S alloy, Table 6.2) may be judged from a comparison of the percentage porosity levels observed in the corresponding metallographic samples of these two alloys, obtained from the graphite mold/thermal analysis castings (DAS  $\sim 85 \mu\text{m}$ ). As Table 6.4 shows, the percentage porosity jumps from 0.36% in the Al-7%Si alloy to 2.2% in the 319 alloy, whereas a 250 ppm Sr addition to 319 hardly alters its porosity level. On the other hand, modifying the ‘binary’ alloy doubles its porosity content, *i.e.*, alters it significantly. In other words, while the addition of Sr increases the porosity in binary Al-Si alloys, the longer solidification time in the 319 alloy also appears to have a considerable influence on the amount of porosity formed in the alloy, (*viz.*, in alloys containing a higher number of alloying elements), in addition to that of Sr.

**Table 6.4** Percentage Porosity Observed in Al-7%Si and 319 Alloys

Alloy	Hydrogen Level (mL/100g)	Percentage Porosity (%)			
		Alloy Code <sup>a</sup>	No Sr	Alloy Code <sup>a</sup>	250 ppm Sr
Al-7%Si	0.1	A7S (351s)	0.36	A7SS (360s)	0.86
319	0.1	A7SC (517s)	2.2	A7SCS (529s)	2.3
	0.25 <sup>b</sup>		2.86 <sup>b</sup>		3.4 <sup>b</sup>

<sup>a</sup> total solidification times (s) given in parentheses below the alloy codes

<sup>b</sup> gassed melt

It could be argued that this does not establish the importance of solidification time *per se* in that other factors such as heat transfer rates have not been considered. However, given the fact that the graphite mold castings from which these samples were prepared were obtained under very similar experimental (*i.e.*, melt- and mold-temperature) conditions, it would not be unreasonable to consider it as an influential parameter.

As will be discussed later on in another context, Table 6.4 also shows that, compared to the porosity values obtained from well-degassed 319 alloy melt samples (hydrogen level ~0.1 mL/100g), the porosity levels displayed by samples taken from 319 alloy melts that were deliberately gassed (hydrogen content ~0.25 mL/100g) were comparatively much higher.

The phenomenon of feedability has been looked at from two viewpoints: (a) the freezing range of the alloy, and (b) the effect of eutectic solidification, *viz.*, the nature of the Al-Si eutectic solidification front. The difference between the liquidus and solidus temperatures of an alloy defines its equilibrium freezing range, and a short freezing range

is considered best for interdendritic feeding. The permeability of the region between these two temperature points controls the feeding and, hence, the microporosity that is expected to result upon solidification.

Quenching experiments on samples of unmodified and modified Al-Si eutectic alloys<sup>144,145</sup> appear to indicate that the solid/liquid interface is more or less smooth and regular (or planar) in modified Al-Si alloys, whereas it is highly irregular in the unmodified alloys. Consequently, it has been suggested that liquid entrapment and porosity formation would be more likely to occur during eutectic solidification in unmodified alloys than in the modified alloys.

Argo and Gruzleski<sup>108</sup> proposed a two-stage solidification process to account for microshrinkage formation in unmodified vs. modified alloy castings. According to them, a short interdendritic feeding distance in the unmodified alloy (represented by a smaller number of secondary dendrite arms per primary Al-dendrite) allows for easier feeding, so that microshrinkage formation takes place in the last region to solidify. The irregular solid/liquid interface then facilitates the distribution of microporosity in this region. A longer mushy zone (which reduces the feedability) in the case of the modified alloy results in a wider dispersion of isolated pockets of eutectic liquid, which then solidify with a regular solid/liquid interface, producing larger pores than those observed in the unmodified case.

In the context of the investigations pertaining to the results presented in this chapter, the microstructures of the four sets of unmodified-modified alloys (*i.e.*, A12S-A12SS, A7S-A7SS, A7SM-A7SMS (356), and A7SC-A7SCS (319)) were examined to

discern any differences in the development and growth of the  $\alpha$ -Al dendrites and that of the Al-Si eutectic between the unmodified and modified alloys and to compare them with the observations reported in the literature.

Figure 6.3 shows the microstructures obtained for the A12S and A12SS alloys. In both cases, the majority of the microstructure consists of the Al-Si eutectic, with a small amount of primary  $\alpha$ -Al dendrites observed therein. The Si particles are acicular in the unmodified alloy, Figure 6.3(a), and very fine in the modified alloy, Figure 6.3(b). The pattern of the dendrites gives an indication of the growth of the dendrites along the direction of heat flow.

In comparison to the lack of exaggerated growth in any particular lateral direction in Figure 6.3(a), in the modified alloy, Figure 6.3(b), due to the undercooling that occurs with the addition of Sr, the increased temperature difference between the liquidus and solidus (and thus a steeper thermal gradient) permits the growth of larger, branching dendrites whose lengths appear to be more prominent compared to their other dimensions. As the temperature falls monotonically from the hot interior liquid to the freezing interface and further on to the mold wall, the freezing front persists as a simple plane normal to the temperature gradient. The parallel rows of dendrites, observed in Figure 6.3(b), confirm this.



(a)

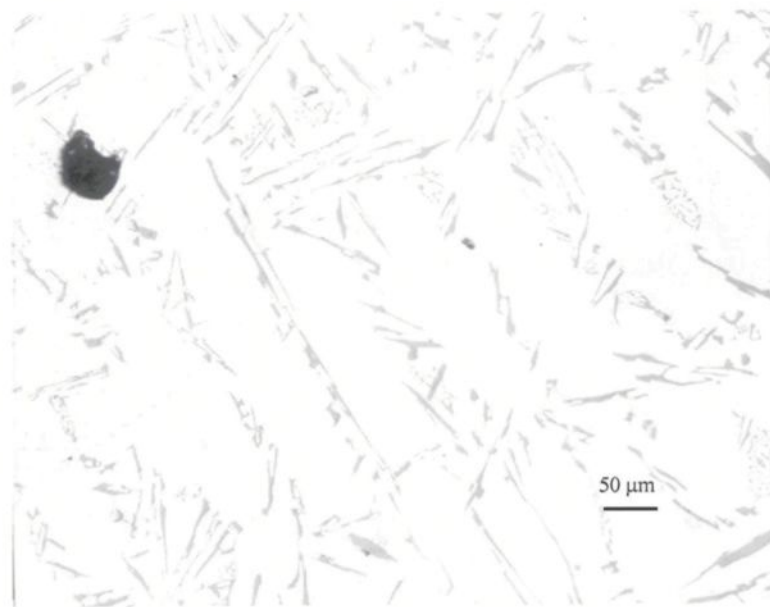


(b)

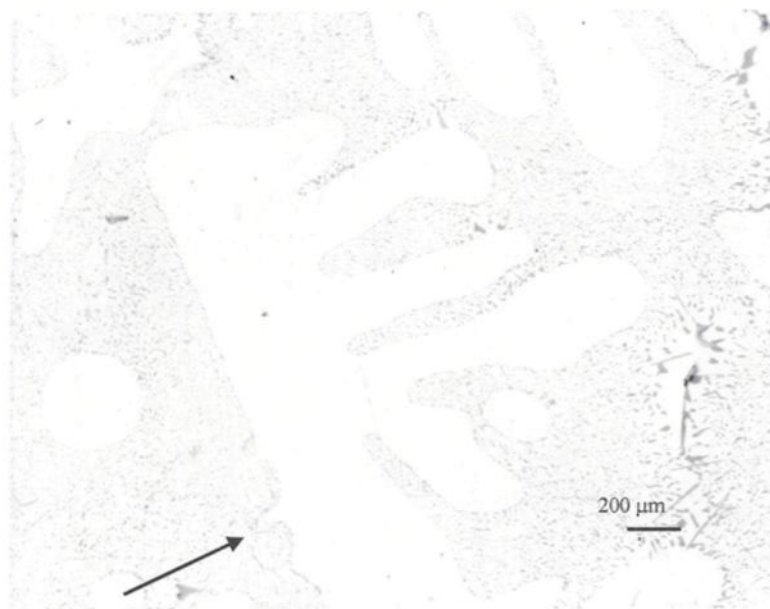
**Figure 6.3** Optical micrographs showing the dendrite morphology in (a) unmodified, and (b) Sr-modified Al-12% Si alloy.

In the high magnification micrographs of the two alloys shown in Figure 6.4, if one looks closely, it can be seen that the contours of the dendrites in the unmodified alloy, Figure 6.4(a), are, in fact, also regular. It is only the acicular nature of the eutectic Si in the one case (A12S), and their fineness in the other (A12SS), that accentuates the smoothness of the dendrite contours in the latter case, Figure 6.4(b).

Under quiescent or rapid cooling conditions, the melt just ahead of the freezing interface is always undercooled, so that it is actually at a higher temperature than the adjacent solid. This is because of the release of latent heat of fusion (into both the liquid and solid). If some point in the freezing front advances ahead of the rest, it finds itself in liquid that can absorb heat and encourage further freezing. These random points grow into spikes and the freezing front loses its planar character. Due to the undercooling that occurs in the Sr-modified alloy, the regularity of the dendrites in Figure 6.4(b) is marred by such spikes (see arrow, for example), resulting in the irregularly shaped dendrites observed in the figure.



(a)



(b)

**Figure 6.4** High magnification micrographs of Al-12% Si alloy showing (a) uniform dendrites in the unmodified alloy, and (b) comparatively irregular dendrites in the modified alloy.

Figure 6.5 shows the microstructures of the A7S, A7SM (356), A7SS, A7SMS (356) and A7SCS (319) alloys, respectively. Compared to the unmodified alloys (Figures 6.5(a)-(b)), the modified alloys (Figures 6.5(c)-(e)) show a more equiaxed dendritic structure. In the case of the modified 319 alloy, Figure 6.5(e), the interdendritic regions are filled with the copper phase ( $\text{CuAl}_2$ ), as delineated by the darkened contours of the  $\alpha$ -Al dendrites (*cf.* the fine, light grey, dotted Al-Si eutectic areas appearing in other interdendritic regions in the micrograph). Although the copper phase particles are not clearly observed in Figure 6.5(e), they were confirmed to be the  $\text{CuAl}_2$  phase occurring either as the Al- $\text{CuAl}_2$  eutectic or in its block-like form,<sup>146</sup> when observed at a high magnification (200X).

Yang *et al.*<sup>147</sup> have proposed a model for the simulation of the microstructural evolution in multicomponent Al-Si alloys (*viz.*, 356 alloy) with equiaxed dendrite and eutectic morphology, based upon the mixture-theory (continuum approach) model. In general, the growth velocity of equiaxed dendrites and eutectic can be calculated as a function of the undercooling  $\Delta T$  as

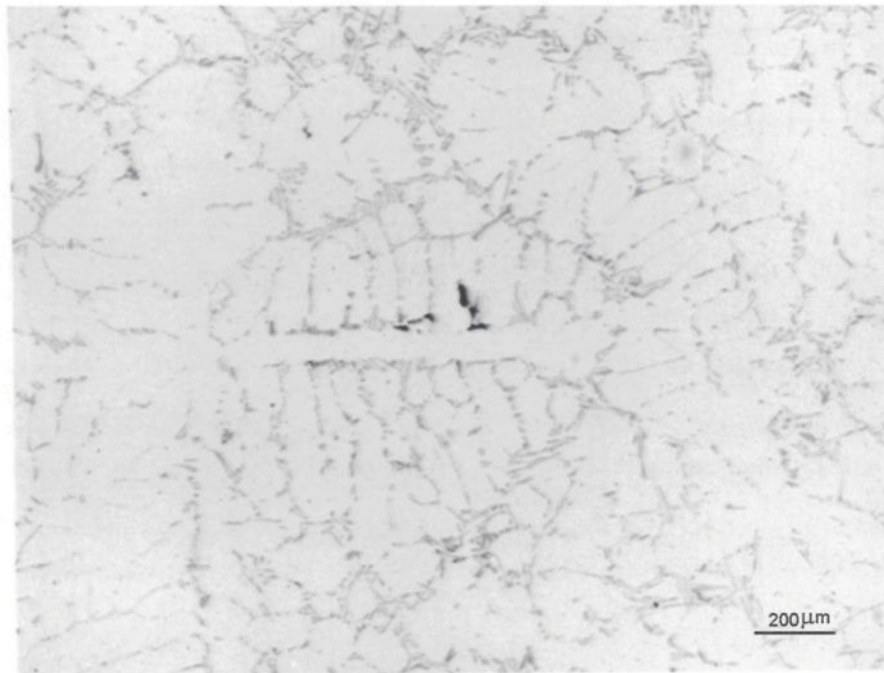
$$dr_E/dt = \mu \bullet (\Delta T)^2 \quad (6.1)$$

where  $r_E$  is the radius of the eutectic grain or of the *equivalent dendrite envelope*, and  $\mu$  is a growth coefficient which depends on the type of equiaxed grain. The growth coefficient is different for primary phase and eutectic grains. The *dendrite envelope* is defined as the surface touching the tips of all primary and secondary arms, and the *equivalent dendrite envelope* is the sphere having the same volume as the dendrite envelope. The driving force

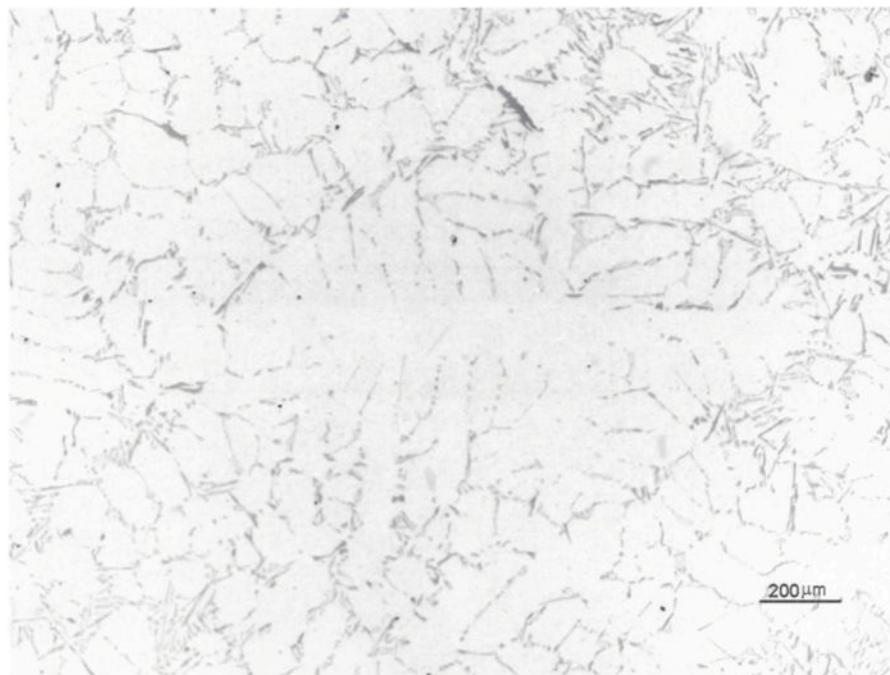
for the dendrite growth is determined by the melt undercooling at the tip of the primary dendrite (grain). In binary alloys, for dendrite growth, constitutional and thermal undercooling are the controlling factors, while in the case of eutectic growth, thermal undercooling is assumed to be the controlling parameter.

The four solidification parameters of interest are the liquidus temperature ( $T_L$ ), the eutectic temperature ( $T_E$ ), the liquidus slope ( $m_L$ ) and the partition coefficient ( $K$ ), and can be calculated easily from the phase diagrams of binary alloy systems. When considering multicomponent alloys (such as 356 or 319), however, the solute transport equations must be solved for each component element, *i.e.*, the slopes and partition coefficients must be known for each in order to determine their effect on the equilibrium temperature.

Such complicated theoretical calculations are not within the scope of the present experimental study. Nevertheless, on the basis of the temperature and time data gathered from the cooling curves, and the microstructural observations and image analysis measurements, certain fundamental conclusions can still be made. From Equation 6.1, the more the undercooling, the faster will be the growth rate of the dendrites, as is the case for the modified alloys. This would account for the more equiaxed dendritic structures observed in Figures 6.5(c) through (e).

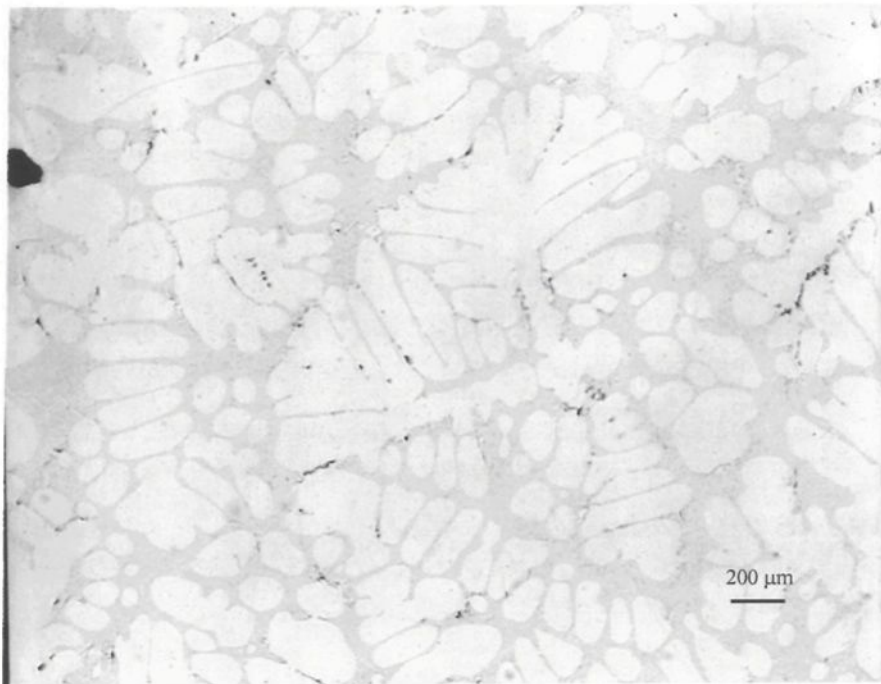


(a)

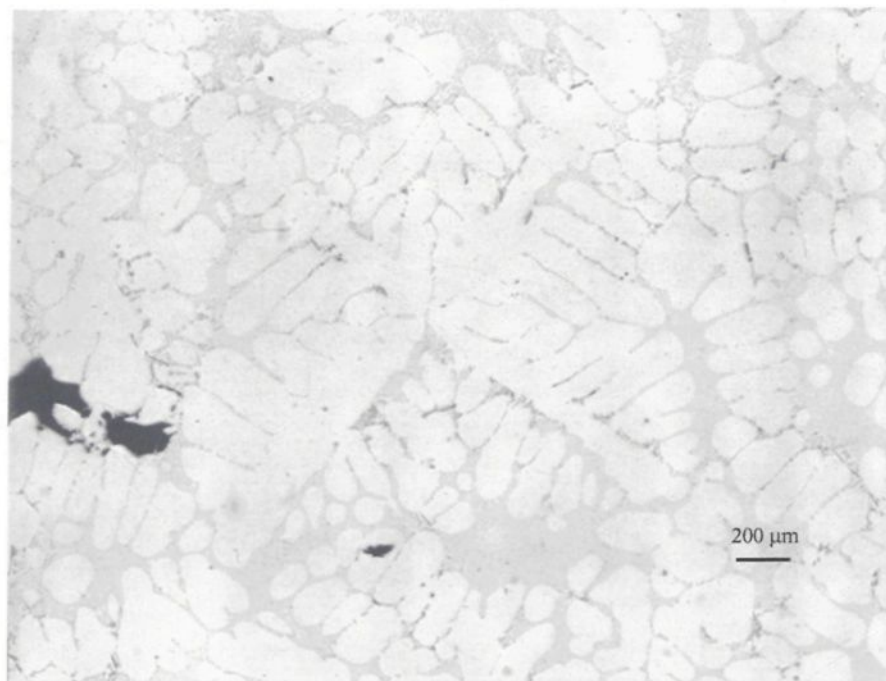


(b)

**Figure 6.5** Optical micrographs showing the secondary dendrite formation in unmodified (a) Al-7% Si, (b) 356, and modified (c) Al-7% Si, (d) 356, (e) 319 alloys.

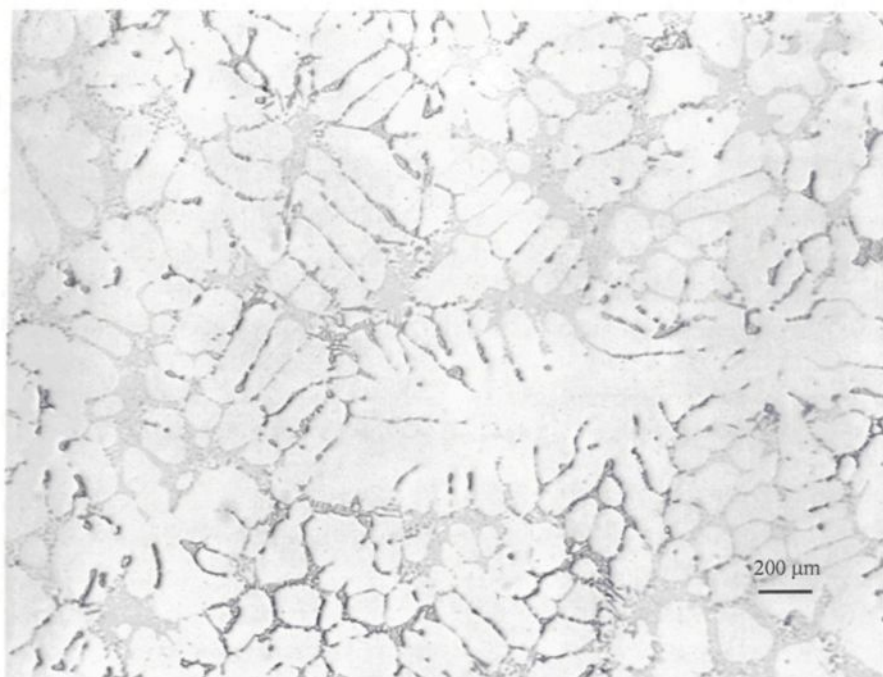


(c)



(d)

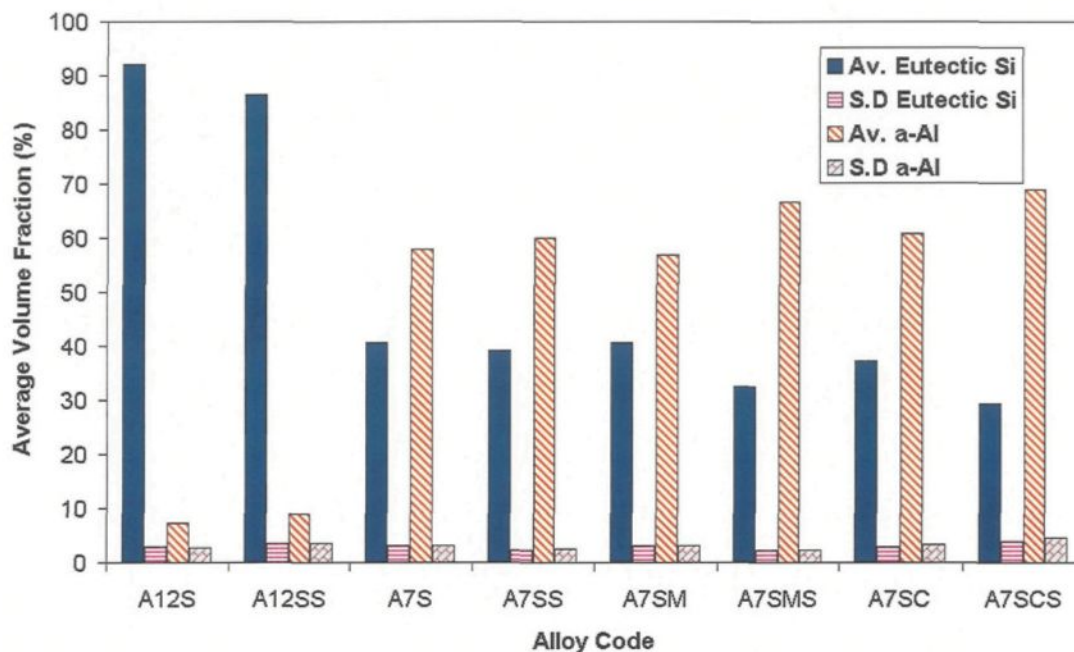
**Figure 6.5** Optical micrographs showing the secondary dendrite formation in unmodified (a) Al-7% Si, (b) 356, and modified (c) Al-7% Si, (d) 356, (e) 319 alloys.



(e)

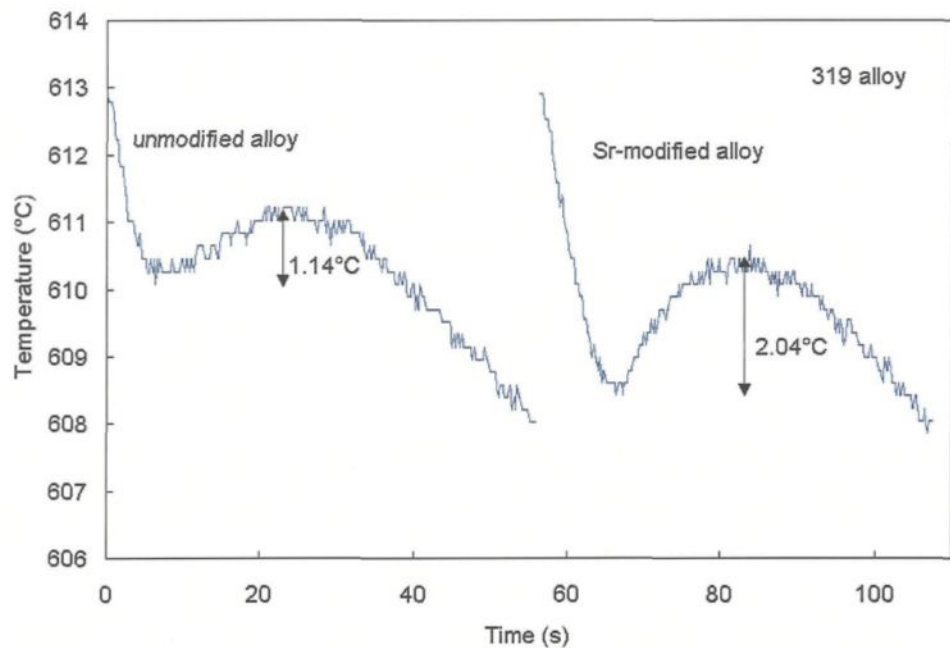
**Figure 6.5** Optical micrographs showing the secondary dendrite formation in unmodified (a) Al-7% Si, (b) 356, and modified (c) Al-7% Si, (d) 356, (e) 319 alloys.

Image analysis measurements were also carried out on these alloy samples, where the  $\alpha$ -Al dendrite and eutectic Si particle characteristics and volume fractions were measured. The measurements were carried out over a certain number of fields (“field” denoting the field of observation of the optical microscope, and covering an area of  $1.41301 \times 10^5 \mu\text{m}^2$  at 200X magnification), such that the entire sample surface was traversed in a regular, systematic fashion. From these, the average  $\alpha$ -Al and average eutectic Si volume fractions were determined. The corresponding values and their standard deviations (SD) are plotted in Figure 6.6.

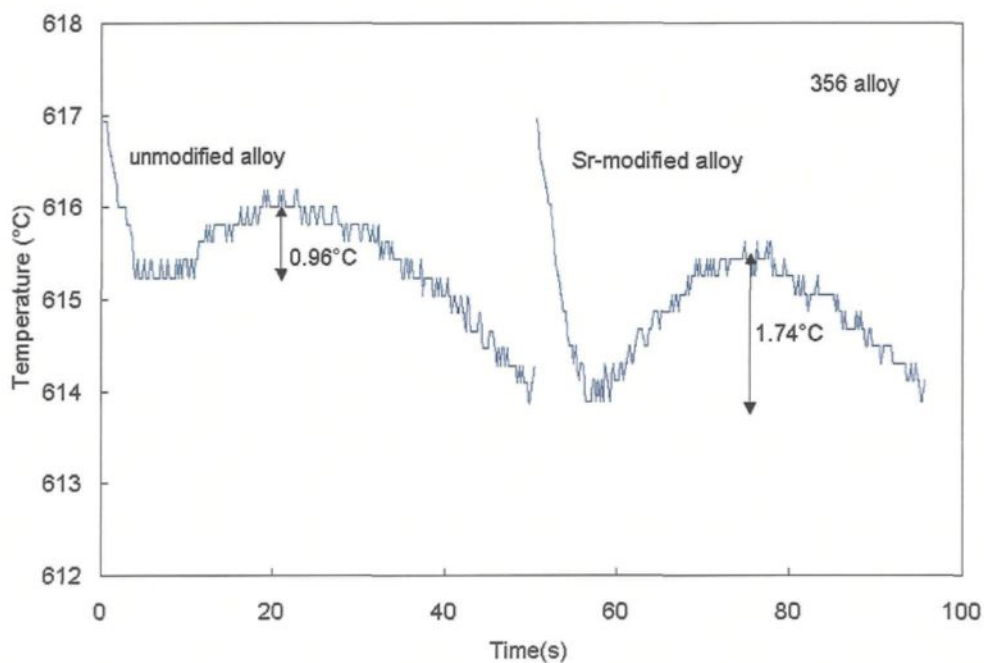


**Figure 6.6** Volume fractions of  $\alpha$ -Al and eutectic Si in the four alloy types studied.

From Figure 6.6, it is seen that, regardless of the alloy composition, the addition of Sr increases the  $\alpha$ -Al volume fraction, with a corresponding decrease in the amount of eutectic Si. Comparing the three 7% Si-containing alloys (*viz.*, A7S, A7SM and A7SC), both the increase in the amount of alloying elements in the alloy and the addition of Sr will affect the decrease in the eutectic solidification temperature so that the amount of the  $\alpha$ -Al phase will increase on passing from A7S to A7SM (356) to A7SC (319) alloys (in either unmodified or modified alloys). The enlarged sections of the cooling curves in Figure 6.7 compare the amount of undercooling observed in the 356 and 319 alloys in both unmodified and Sr-modified conditions.



(a)



(b)

**Figure 6.7** Enlarged sections of the cooling curves obtained for (a) 319 and (b) 356 alloys, comparing the undercooling observed in the unmodified and Sr-modified cases.

Primary dendrites for which a good number of secondary dendrites could be clearly observed were also measured for each structure. Table 6.5 lists the longest primary dendrite lengths that were observed in each case, and the corresponding number of secondary dendrites associated with each primary dendrite. From these values, the average thickness of the secondary dendrites could be calculated. The lengths of some 20-25 secondary dendrite arms were also measured from each alloy sample, to determine their average lengths. These are also listed in Table 6.5. From columns 3 and 4 of the table, it can be seen clearly that in the case of the Al-7%Si and Al-12%Si alloys, the primary dendrite lengths increase with the addition of Sr, as do the number of secondary dendrite arms per primary dendrite, and the secondary dendrite arm lengths as well. These observations more or less conform to those of Argo and Gruzleski.<sup>108</sup> In the case of the 356 alloy, it is seen that the primary dendrite length decreases in the modified alloy, which is in keeping with the equiaxed dendrite structure observed in Figure 6.5(b). The increase in thickness of the secondary dendrite arms is partly due to the increase in the  $\alpha$ -Al volume fraction, as well as their lateral expansion, as inferred from the reduction in the average length.

**Table 6.5** Primary and Secondary  $\alpha$ -Al Dendrite Measurements

Alloy	Alloy Code	Max. Primary Dendrite Length ( $\mu\text{m}$ )	No. of Secondary Dendrites	Av. Thickness of Secondary Dendrites ( $\mu\text{m}$ )	Av. Length of Secondary Dendrites ( $\mu\text{m}$ )
Al-7%Si	A7S	664	10	66.4	153.4
Al-7%Si+Sr	A7SS	1019	15	67.9	196.6
Al-12%Si	A12S	699	16	43.7	26.2
Al-12%Si+Sr	A12SS	1421	31	45.8	56.6
356	A7SM	1155	17	67.9	189.7
356+Sr	A7SMS	754	10	75.4	159.0
319	A7SC	790	15	52.7	133.1
319+Sr	A7SCS	866	14	61.9	133.8

From the data presented thus far, we have seen (a) how the primary dendrites in the modified 356 alloy possess an equiaxed structure and, thus, shorter lengths, and (b) how the increase in the mushy zone period ( $\alpha$ -Al precipitation) and, hence,  $\alpha$ -Al volume fraction, reduces the interdendritic eutectic region (*i.e.*, the Si volume fraction, Figure 6.6). It has also been reported that Sr improves fluidity by 15-30% (Hu and Pan;<sup>148</sup> Samuel *et al.*<sup>137</sup>). Apparently, in view of these observations, Sr addition should improve the feedability of the interdendritic regions (and hence decrease the porosity). Thus, some other factor should be sought to account for the increase in porosity with the addition of Sr.

The 319 alloy shows practically no change in the number of secondary dendrite arms (per primary dendrite) or their average length between the unmodified and modified conditions. With a greater number of alloying elements present in the alloy, there is competitive growth between the dendrites and the eutectic (and other phases), due to the rejection of a considerable amount of solute in front of them with the progress of solidification. According to Yang *et al.*,<sup>147</sup> both temperature and concentration must be considered for the start of the eutectic reaction in a multicomponent alloy such as 356 (which solidifies under non-equilibrium conditions), as the liquid concentration does not necessarily reach the eutectic concentration even if the temperature drops below the eutectic temperature. Thus, at any point in the casting, the eutectic reaction will start only if the two conditions

$$T_b < T_E \quad \text{and} \quad C_L^* \geq C_E$$

are satisfied, where  $T_b$  is the bulk temperature,  $T_E$  is the equilibrium temperature,  $C_L^*$  is the liquid concentration at the solid/liquid interface, and  $C_E$  is the initial composition of the

eutectic reaction. Applying similar considerations to the 319 alloys, it is easy to understand why the dendrites in the 319 alloy appear as they do in Figure 6.5(e), and also why the secondary dendrite arm lengths do not change from the unmodified to the modified alloy (Table 6.5).

In their study of the effect of phosphorus on the solidified structure of hypoeutectic Al-10% Si alloys (solidification rate 0.1 K/s), Kato *et al.*<sup>149</sup> have also reported that, with the addition of 50 ppm phosphorus, the  $\alpha$ -Al dendrite growth is blocked due to the rejection of phosphorus. The lengths of the  $\alpha$ -Al dendrites are also decreased, similarly.

## **CHAPTER 7**

### **INFLUENCE OF OXIDES ON POROSITY FORMATION IN**

### **SR-TREATED ALLOYS**

## CHAPTER 7

# INFLUENCE OF OXIDES ON POROSITY FORMATION IN SR-TREATED ALLOYS

### 7.1 INTRODUCTION

With respect to the modification of aluminum-silicon casting alloys, strontium has, by far, been employed most extensively. Although easier to handle than sodium, and more resistant to fade (*i.e.*, losing its modifying effect after a certain amount of time), Sr addition is also associated with porosity formation in these alloys.

A tremendous amount of work has been carried out to study Sr-related porosity, one of the earliest perhaps being that of Argo and Gruzleski<sup>108</sup> on porosity in Sr-modified A356 aluminum casting alloys, in which the authors distinguished between the fundamental differences in microshrinkage and microporosity formation in unmodified and Sr-modified hypoeutectic Al-Si alloys, using A356 alloy as an example. Lee and Sridhar<sup>106</sup> and Fuoco *et al.*<sup>150</sup> have commented that the effect of strontium on porosity formation is not well understood, even if the observations that a higher tendency for microporosity and an increase in percentage porosity in Sr-modified alloys are generally agreed upon in the literature.

McDonald *et al.*<sup>109</sup> have pointed out that despite all the research carried out on Sr-related porosity, only a few workers have investigated a range of Sr concentrations. What these studies do reveal, however, is that a vast difference in porosity characteristics is observed between Sr-free and Sr-containing castings. The Sr concentration is apparently not a critical factor in this regard, as such changes are observed even in alloys containing very low levels of Sr.

As the formation of gas porosity is directly related to the amount of dissolved hydrogen in the melt, the increase in porosity level with Sr addition was naturally assumed to be related to an increase in the hydrogen level of the melt. To this end, Denton and Spittle<sup>141</sup> reported that Sr-containing melts had a higher rate of gas absorption from their surroundings, and attributed to the possibility of a more permeable oxide layer. Other studies<sup>151</sup> showed that Sr additions do not normally introduce hydrogen into the melt, while yet others reported a decrease in the hydrogen content, *e.g.*, Shahini,<sup>107</sup> who related an increase in the density of reduced pressure test samples to a decrease in the hydrogen content.

These contradictions led researchers to focus on the problem of feedability in the mushy zone during solidification. As Sr results in depressing the eutectic Si temperature, the mushy zone ( $\alpha$ -Al dendrite solidification) region of the alloy is increased, and the increase in porosity levels observed with Sr addition is thus attributed to the latter. However, although this is true to a certain extent, the corresponding increase in freezing range does not satisfactorily explain the much higher increase in porosity levels observed in Sr-modified alloys.<sup>150</sup>

Further extending the feedability-related point of view, it has also been pointed out that one should look to the Al-Si eutectic part of solidification to explain the differences in porosity observed when Sr is added to Al-Si melts.<sup>140,21,142</sup> Given that the eutectic Si phase constitutes almost half the microstructure of Al-Si alloys (depending on the Si content), it would be expected that the Sr-modified Si phase would exert some sort of influence on porosity formation. In this connection, Dahle *et al.*,<sup>143</sup> who observed an orientation relationship between the  $\alpha$ -Al dendrites and eutectic Si in unmodified hypo-eutectic Al-Si alloys, and a lack of it in the (200 ppm) Sr-modified alloys (using electron microdiffraction techniques), have suggested that this represents a change in the mode of eutectic nucleation - from that occurring near the  $\alpha$ -Al dendrites in the Sr-free alloy, to that taking place within the eutectic liquid itself in the Sr-containing alloy. The mode in operation controls the distribution of the remaining liquid in the last stages of solidification when feeding becomes extremely difficult. This distribution, in turn, will define the connectivity of the feeding channels, and thus determine the resultant porosity profile in the solid casting.

In reviewing the literature, it is interesting to note that a number of small, but important, details in regard to Sr-related porosity are mentioned in passing, but the possibility of considering oxides as being responsible for these observations has not been taken too much into account, possibly due to the difficulties associated with the measurement of oxides, from both qualitative and quantitative points of view. In fact, Iwahori *et al.*<sup>152,120</sup> appear to be the earliest researchers to mention an oxide-related connection: they reported that the hydrogen level in Sr-modified melts is not lowered by vacuum degassing, and attributed this to the fact that hydrogen absorbed into the oxide in

the melt is more strongly fixed in the oxide by the addition of strontium to the melt (the oxides being considered as inclusions in the melt). According to them, in order to produce porosity-free castings, it is necessary to eliminate oxide inclusions from the melt before it is modified with Sr or degassed.

In this regard, Jacob *et al.*<sup>153</sup> observed that Sr additions to Al-Si alloys produced thicker but non-homogeneous surface oxide layers, which exhibited SrO regions up to 500  $\mu\text{m}$  long. Lee and Sridhar,<sup>106</sup> who carried out *in situ* observations of pore nucleation and growth in Sr-, and (Sr+TiB<sub>2</sub>)-treated Al-Si alloy melts using an X-ray temperature gradient stage (XTGS) technique, alluded to this point in their work, but could not, however, detect such oxides with their XTGS apparatus. In another context, Cao and Campbell<sup>154</sup> have also pointed out the influence of oxide films folded into the melt during pouring as being conducive to porosity formation.

It is the aim of the present chapter to show how the presence of oxides (Sr and Al) in the molten metal is the factor that mainly influences the porosity observed in Sr-containing Al-Si alloys. A series of experimental and industrial Al-Si casting alloys were selected for this part of our study, from simple experimental “binary” alloys such as Al-7%Si, Al-12%Si, to industrial 319 and 356 alloys, to cover a variety of alloy freezing ranges. It will be seen how the difference in porosity characteristics does not depend on the actual Sr level in the alloy, but on the presence of Sr and/or Al oxides in the molten metal and, consequently, in the solidified structure. The techniques of thermal analysis, optical microscopy, and SEM/EDX and EPMA analyses were employed to obtain the results that have been presented here.

It should be mentioned here, that the “binary” alloys referred to in this chapter are termed “binary” only in the sense that Al and Si are their main constituents, contrary to other alloying elements that are present, in addition, in the 356 and 319 alloys. As the chemical analyses listed in Table 7.1 show, these binary alloys also contain a certain amount of impurities, in spite of the fact that they were prepared from relatively pure (99.95%) Al and Si.

## 7.2 EXPERIMENTAL PROCEDURE

Table 7.1 lists the chemical compositions of the various alloys that were used and their respective alloy codes. Table 7.1 and Table 7.2 in the next section correspond to Tables 6.1 and 6.4 of Chapter 6, as the same alloy samples were also employed to obtain the results presented in this chapter. The tables have therefore been repeated here for convenience.

The alloys were cut into smaller pieces, cleaned, dried and melted in a 40 kg-capacity SiC crucible. The melting temperature was kept at  $725^{\circ} \pm 5^{\circ}\text{C}$ . The melts were degassed using pure dry argon for ~30 min, using a graphite rotary impeller (200 rpm; humidity of surroundings <15%). A 5-cm wide, 25-cm long plate made of refractory material, placed inside the crucible at an angle of ~35 degrees with the crucible wall, acted as a baffle during the melting and degassing process to avoid vortex formation. In those cases when the melts were modified with Sr, the required amount of Sr was added to the melt using Al-10% Sr master alloy, before the degassing was carried out.

In the case of the experimental alloys, the alloys were first prepared by melting pure aluminum (99.95%) at the same temperature, then adding silicon (99.95% pure) in the required amounts by means of a perforated graphite bell, to obtain the Al-7%Si, Al-12% alloys. The alloy melts were poured into ingot molds, and the solidified ingots were used as described above. Samplings for chemical analysis were also taken simultaneously for each pouring.

About 1 kg of the degassed melt was transferred by means of a ladle into a 1 kg-capacity SiC crucible (length/diameter ratio: 130 cm: 85 cm) that was preheated at 750°C in a small electric resistance furnace. The transfer procedure was carried out with extreme caution to minimize turbulence and took about 10 min. During the transfer, the SiC crucible was initially tilted at ~35 degrees, then raised slowly while the liquid metal was poured into it, till it was in an upright position at the end of the filling. When the melt temperature in the smaller crucible stabilized at 725°C, the melt was poured into a preheated (600°C) cylindrical graphite crucible (10 cm length, 6 cm diameter), as shown in Figure 3.2 (a) (see Chapter 3, Section 3.2.2). Again, for each pouring (into the graphite mold), a sample for chemical analysis was also done simultaneously (the spectrometric analyses were carried out at GMPT New Hampshire facilities).

For metallographic examination, samples (25 mm x 25 mm) were sectioned from the graphite mold castings (from the central part containing the thermocouple tip), mounted and polished. The microstructures were analyzed using (1) optical microscopy, (2) scanning electron microscopy (SEM), and (3) electron probe microanalysis (EPMA), as described in Chapter 3, Section 3.3.3.

**Table 7.1** Chemical Compositions (Wt%) of Alloys Used

Alloy	Code	Si	Fe	Cu	Mg	Mn	Cr	Ti	Sr	Al
<u>Experimental</u>										
Al-7%Si	A7S	6.74	0.1599	0.2825	0.0228	0.0316	0.0051	0.0246	0.0018	92.7
Al-7%Si+Sr	A7SS	6.71	0.1891	0.3656	0.0340	0.0331	0.0064	0.0274	0.0114	92.6
Al-12%Si	A12S	11.76	0.1451	0.1144	0.0119	0.0072	0.0012	0.0413	0.0010	87.9
Al-12%Si+Sr	A12SS	11.76	0.1451	0.1144	0.0119	0.0072	0.0012	0.0413	0.0245	87.8
Al-12%Si+high Sr	A12SS10	11.50	0.1811	0.0595	0.0213	0.0134	0.0065	0.0325	0.0927	88.0
<u>Industrial</u>										
319	A7SC	6.24	0.1084	3.683	0.0496	<0.0005	<0.0005	0.1332	0.0001	89.7
319+Sr	A7SCS	5.81	0.1145	3.584	0.0552	<0.0005	<0.0005	0.1466	0.0115	90.2
356	A7SM	6.50	0.1211	0.0470	0.3194	0.0008	0.0008	0.1110	0.0001	92.8
356+Sr	A7SMS	6.47	0.1332	0.0398	0.3283	0.0020	0.0020	0.1164	0.0070	92.8

### 7.3 INFLUENCE OF OXIDES ON POROSITY FORMATION

In this section, examples of the different types of pores observed in these alloys will be discussed. Based upon scanning electron microscopy (SEM), energy dispersive X-ray (EDX) spectroscopy, and electron probe microanalysis (EPMA) results, it will be shown how, in each case, these pores are associated with the presence of strontium oxide films or particles, within or in the vicinity of the pores. Table 7.2 shows that, compared to the porosity values obtained from well-degassed 319 alloy melt samples (hydrogen level  $\approx 0.1$  mL/100g Al, as measured by an AlScan apparatus), the porosity levels displayed by samples taken from 319 alloy melts that were deliberately gassed (hydrogen level  $\approx 0.25$  mL/100g Al) were comparatively much higher.

**Table 7.2** Percentage of Porosity Observed in Al-7%Si and 319 Alloys

Alloy	Hydrogen level (mL/100g)	Percentage Porosity (%)			
		Alloy Code <sup>a</sup>	No Sr	Alloy Code <sup>a</sup>	250 ppm Sr
Al-7%Si	0.1	A7S (351s)	0.36	A7SS	0.86
319	0.1	A7SC (517s)	2.2	A7SCS	2.3
	0.25*		2.86 <sup>b</sup>		3.4 <sup>b</sup>

<sup>a</sup> total solidification times (s) given in parentheses below the alloy codes

<sup>b</sup> gassed melt

It is well known that micropores can be rounded or irregular; the former are those mostly associated with hydrogen gas, while the latter, also classified as “interdendritic”, arise due to the effects of shrinkage.<sup>109</sup> In their studies of gas porosity and metal cleanliness in 356 and 319 casting alloys, Laslaz and Laty<sup>104</sup> remarked that gas porosity

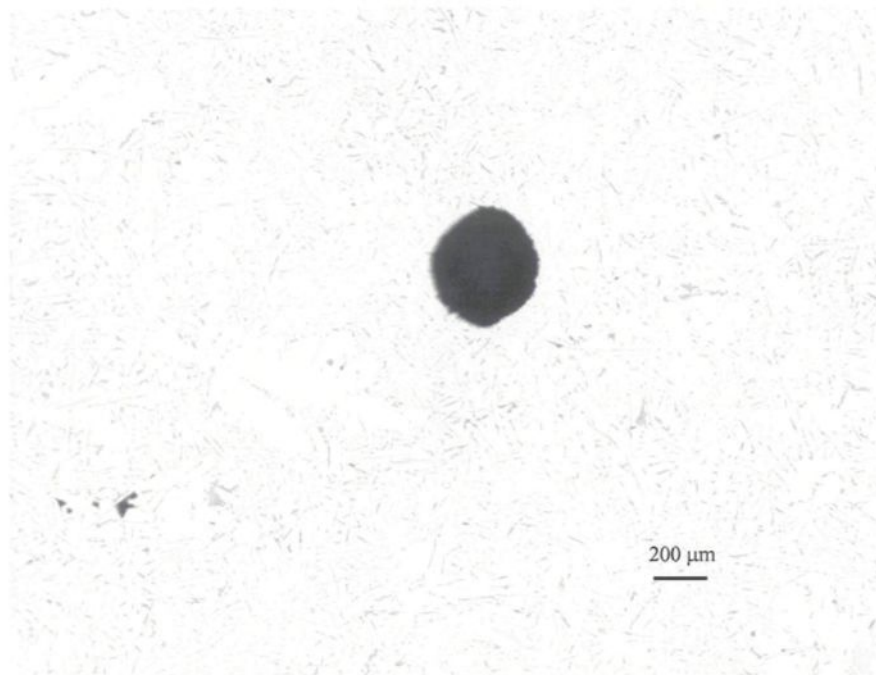
after solidification depends not only on the hydrogen content of the melt, but also on metal cleanliness – in terms of the oxides present in the melt. The oxides were incorporated into the melt either by stirring or by adding chips cut from the same ingots used for melting. Furthermore, they proposed that their observations of round pores being associated with a strongly oxidized melt, and elongated pores with a cleaner melt, supported the hypothesis that pores nucleate on oxide inclusions. They also suggested the possibility that Sr increases the ability of the oxides to nucleate pores.

### 7.3.1 Role of Strontium Oxide

Figure 7.1 shows an example of a rounded pore observed in the Al-12% Si alloy, surrounded mostly by eutectic Si regions. As can be noted, nothing is seen within or around the pore. As Fuoco *et al.*<sup>155</sup> have observed, pores will tend to have a rounded morphology if they are surrounded by eutectic Si cells/regions, as in the case of high silicon (>10%) alloys, rather than being impinged upon by dendrite arms that would alter their initial round shape. This is what is observed in Figure 7.1(a), in the unmodified alloy, *viz.*, even in the absence of Sr. Thus, it is not so much the fact that rounded pores are observed in modified alloys, as that they are observed surrounded by eutectic Si regions. Fang and Granger<sup>103</sup> are also of the opinion that the rounded pore morphology in the A356 alloy is due to the high eutectic volume fraction associated with the alloy.

The optical micrograph of Figure 7.1(b) also shows a rounded pore, this time in the modified Al-12% Si alloy (250 ppm Sr). Again, the pore is seen surrounded by the eutectic Si phase. However, in this case, the presence of fine particles can be noted inside the pore.

An SEM micrograph of such a pore, Figure 7.2(a), provided greater details of the contents of the pore: several white particles could be observed within its interior (note also the presence of  $\beta$ -Al<sub>5</sub>FeSi platelet fragments (grey)). Figure 7.2(b) shows the nature of these particles at a high magnification. These particles were identified as being Al-Sr-O, as confirmed by the composite EDX and oxygen scans shown in Figure 7.2(c). It should be noted that the K $\alpha$  line of Si and the L $\alpha$  line of Sr have closely similar energies, thus resulting in the thick peak observed in the EDX spectrum (see arrows in the inset). The exact stoichiometry of these particles could not be determined, however, due to the depth of the pore. Figure 7.2(d), taken at a much higher magnification, shows an example of the microporosity (arrowed) associated with the presence of these Al-Sr-O particles.



(a)



(b)

**Figure 7.1** Optical micrographs showing pore types observed in (a) unmodified, (b) Sr-modified Al-12% Si alloy.

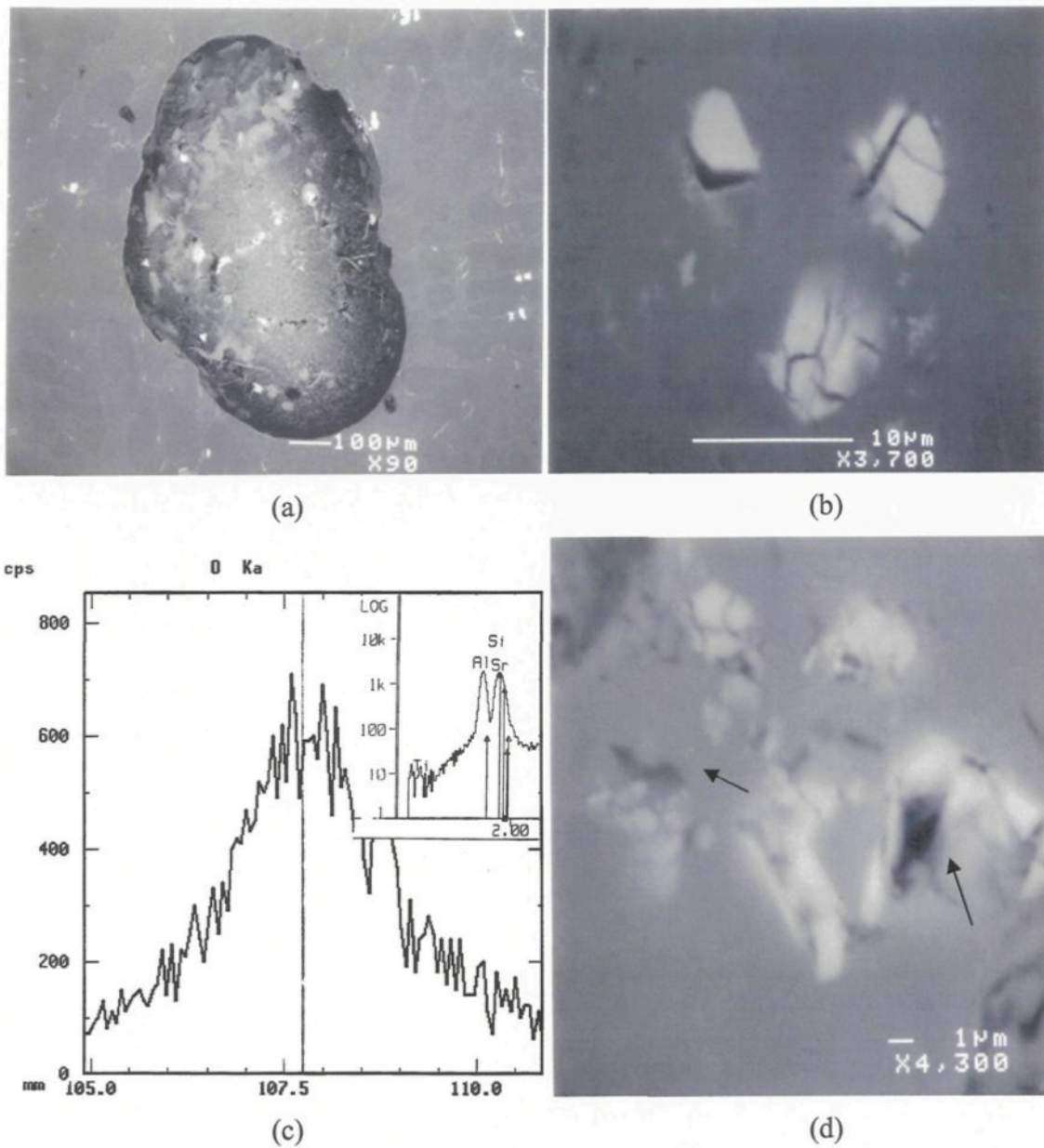
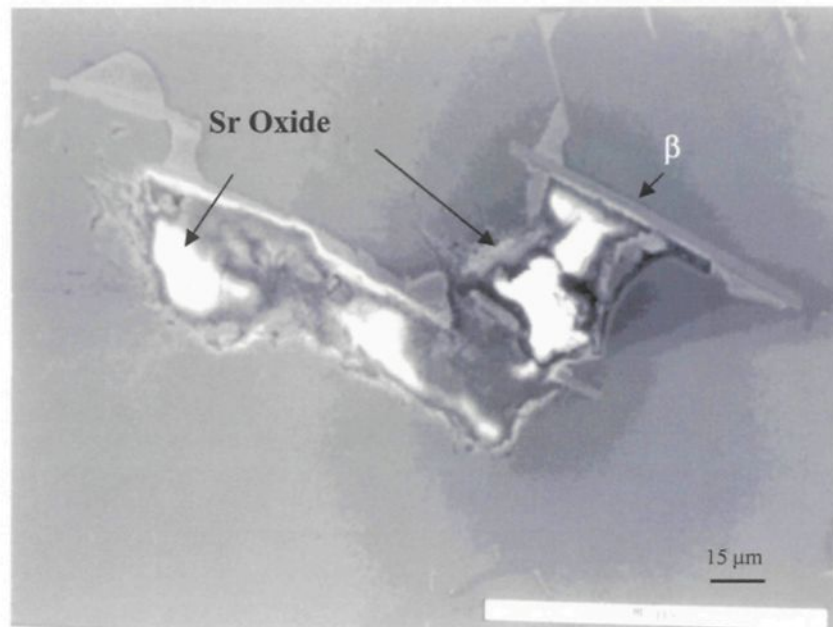


**Figure 7.2** (a) SEM micrograph showing white particles inside a pore in Sr-modified Al-12% Si alloy; (b) high magnification SEM showing Al-Sr-O particles; (c) composite of oxygen scan and EDX spectrum (inset) corresponding to Al-Sr-O particles, (d) high magnification SEM showing microporosity associated with Al-Sr-O particles (arrowed).

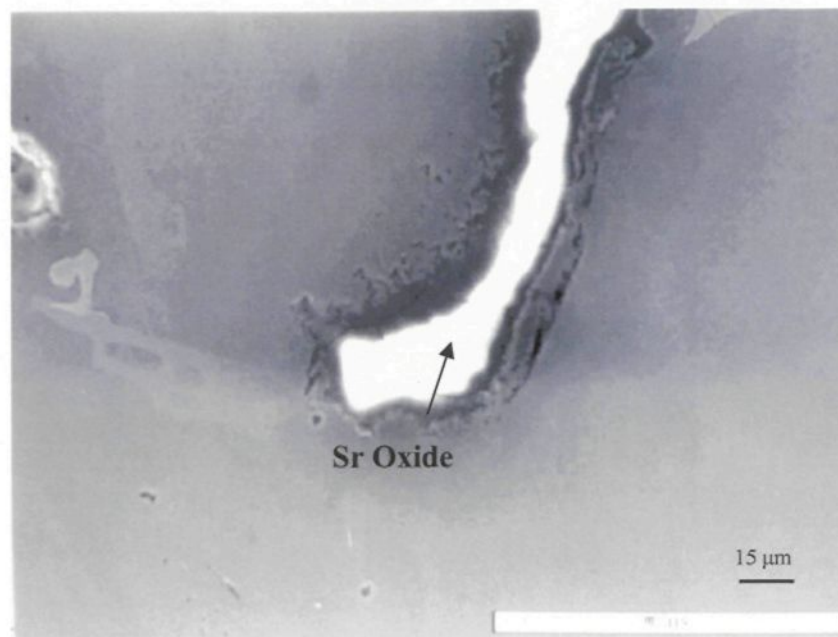
Figure 7.3(a) demonstrates a shrinkage-type pore, with an irregular morphology in the Sr-modified 319 alloy. Two features are noted: (a) the presence of  $\beta$ -Al<sub>5</sub>FeSi platelets along the edges of the pore, and (b) the presence of strontium oxide films and/or particles inside the pore. In a previous study (Samuel *et al.*<sup>156</sup>), it was shown that the  $\beta$ -Al<sub>5</sub>FeSi phase could be nucleated on Al<sub>2</sub>O<sub>3</sub> or MgO particles existing in the melt. From Figure 7.3(a), it would be reasonable to expect that the SrO films could also act as nucleation sites for the  $\beta$ -phase (arrowed). Another example of a thick strontium oxide film within a shrinkage cavity in the same alloy sample is shown in Figure 7.3(b). Cao and Campbell<sup>154</sup> have also reported that the wetted sides of double oxide films appear to act as nucleation sites for iron intermetallics.

In this connection, it ought to be mentioned that in a previous study,<sup>157</sup> which assessed the reliability of the Qualiflash filtration technique in the measurement of oxide films in A356 and A390 aluminum foundry alloys, it was also noted how the aluminum oxides were found associated with various microconstituents such as primary Si, MgO and TiB<sub>2</sub> particles.

In a recent study, Huang *et al.*<sup>158</sup> investigated the types of oxide films that can occur in pure Al, Al-Si and Al-Si-Mg alloys. They found that the polished specimens of these alloys exhibit “shining” spots that are in reality oxide films or particles, and suggested the use of an ultrasonic vibration technique that could assist (to a certain extent) in identifying these oxides. In the case of the Al-Si-Mg alloys, spinel was also observed to form. It is worth noting here that the strontium oxide regions in the pores displayed in Figure 7.3 are also extremely shiny in nature.



(a)



(b)

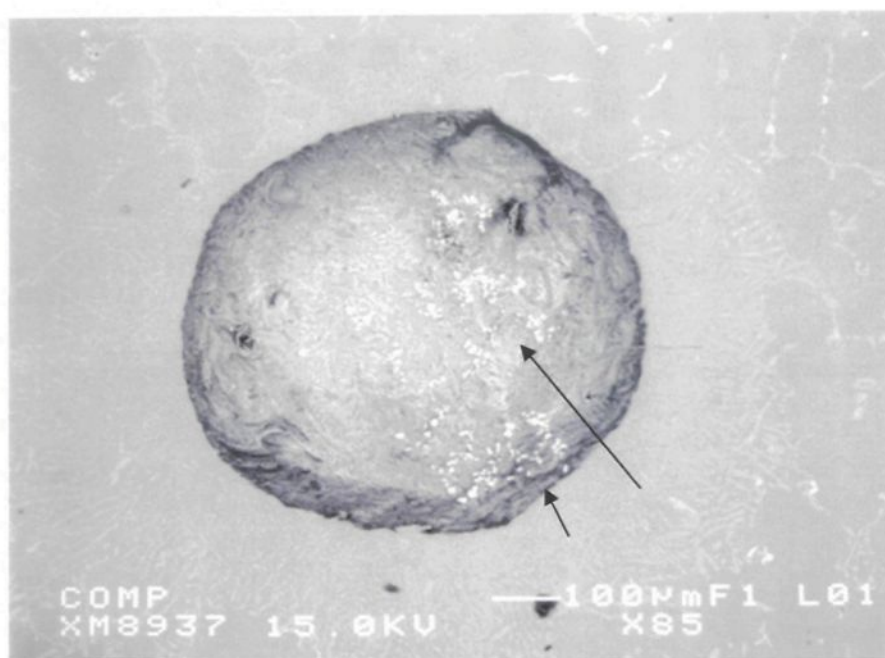
**Figure 7.3** SEM micrographs showing irregular shrinkage-type pores in Sr-modified 319 alloy. Note the presence of Sr oxides within, and  $\beta$ -Al<sub>5</sub>FeSi platelets along the edges of the pore.

To further confirm the relation of porosity with the presence of strontium oxide, some reduced pressure test (RPT) samples were also prepared. The samplings were taken from melts at 750 °C, taking care to avoid any turbulence. The RPT or vacuum gas test is a simple qualitative test used widely in foundries to assess the hydrogen level in the melt prior to casting.<sup>159</sup> It consists essentially of solidifying a sample of the melt under reduced pressure (usually in the 50 to 100 mm Hg range). This encourages pore formation, the pores expanding due to the lowered pressure and providing a much more porous sample than under atmospheric conditions of solidification.

The product, a cup-shaped specimen, permits the gas level to be assessed in three ways: a) viewing the top of the sample and judging a puffed up surface as corresponding to a heavy gas content in comparison to a smooth or concave surface representing a low level, (b) sectioning the sample, examining the roughly polished surface for porosity and comparing with a photographic standard, and (c) finer polishing of the sectioned half to better observe the porosity profile through the use of sophisticated techniques.<sup>159,160</sup> It has been shown that the results are influenced by the inclusions (including oxides) present in the melt,<sup>161</sup> as these act as nucleating agents that facilitate bubble formation during solidification of the sample under reduced pressure.

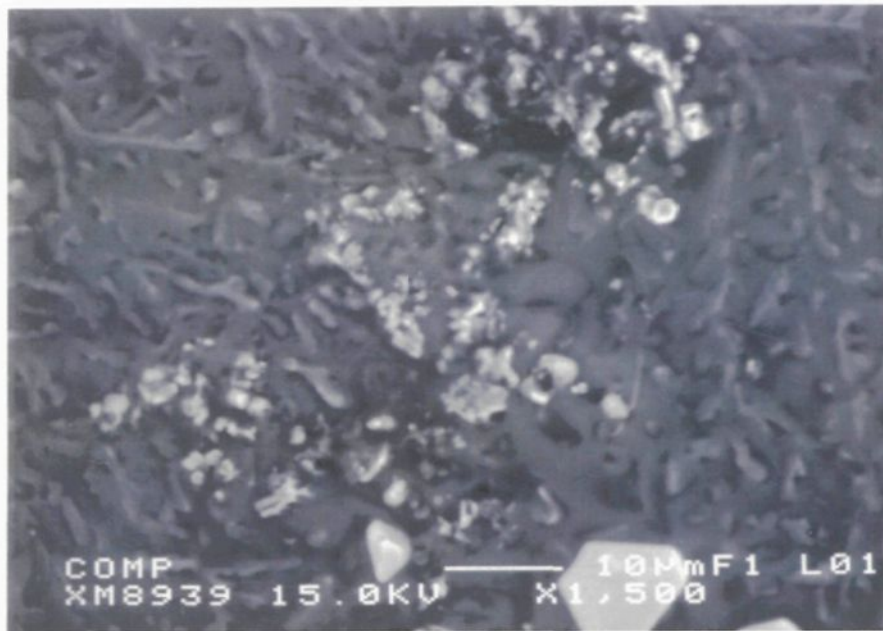
In the present study, the sole purpose of introducing RPT samples was to facilitate examining the insides of the (enlarged) pores in the Sr-modified alloys. Figure 7.4(a) displays a pore observed in Sr-modified 356 alloy, modified with 600 ppm Sr. A number of fine white particles are observed dotting the bottom of the pore (arrowed). The high magnification SEM micrograph of Figure 7.4(b) reveals the size and distribution of these

Al-Sr-O particles. The Sr image taken from Figure 7.4(a) is reproduced in Figure 7.4(c). The rounded morphology of the pore shown in Figure 7.4(a) matches well with the observations of Laslaz and Laty<sup>104</sup> who noted that their oxide-contaminated melt samples displayed large, round pores, and in large number. Correspondingly, the porosity levels would be high, as well. The percentage of porosity values in Table 7.2 for the Sr-modified alloys (containing Sr oxide inclusions) reflect this tendency.

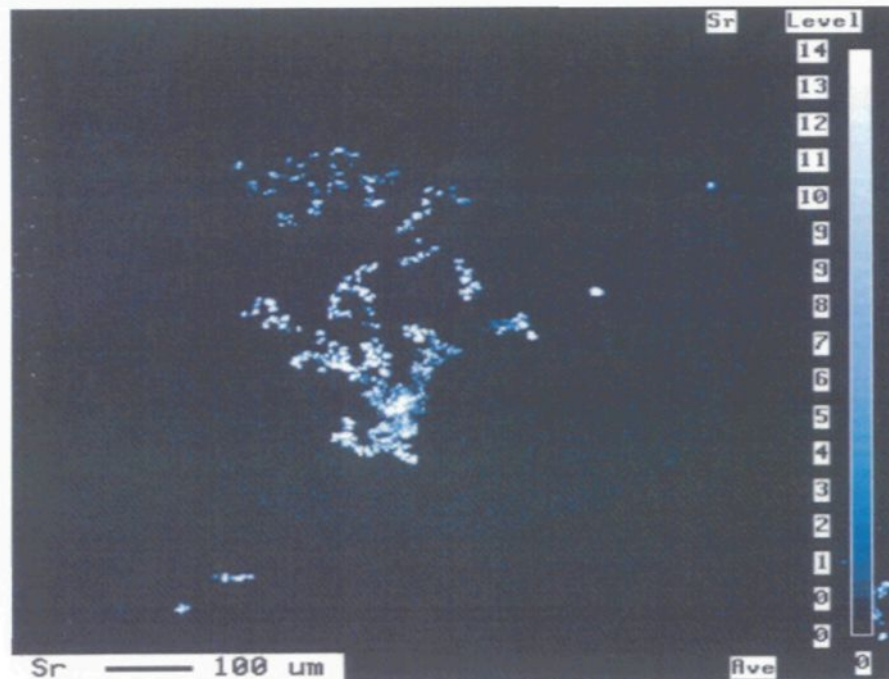


(a)

**Figure 7.4** SEM micrographs obtained from an RPT sample of the Sr-modified 356 alloy showing (a) a pore with fine white Al-Sr-O particles (arrowed), (b) size and distribution of Al-Sr-O particles, (c) Sr image of Al-Sr-O particles in (a).



(b)



(c)

**Figure 7.4** SEM micrographs obtained from an RPT sample of the Sr-modified 356 alloy showing (a) a pore with fine white Al-Sr-O particles (arrowed), (b) size and distribution of Al-Sr-O particles, (c) Sr image of Al-Sr-O particles in (a).

A sampling taken from the same Sr-modified 356 alloy melt was used to conduct a Prefil (pressure filtration technique) test. The Prefil apparatus is one of the more recent techniques used to determine melt cleanliness (see, *e.g.*, Simard *et al.* <sup>162</sup>). By passing ~2.5 kg of the molten metal through a filter under pressure (10 psi), the inclusions/films are concentrated in the region above the filter (pore sizes in the filter can vary from <1 to 123  $\mu\text{m}$ ). After the test, the solidified metal above the filter is sectioned, mounted and polished for metallographic examination. An example of the microstructure obtained from such a procedure is shown in Figure 7.5. The black arrows point to the formation of microporosity associated with the strontium oxide cluster. The wavelength dispersion spectroscopic (WDS) analysis confirmed the stoichiometric composition of this oxide to be  $\text{Al}_{2.3}\text{SrO}_{3.3}$  (close to  $\text{Al}_2\text{SrO}_3$ .)

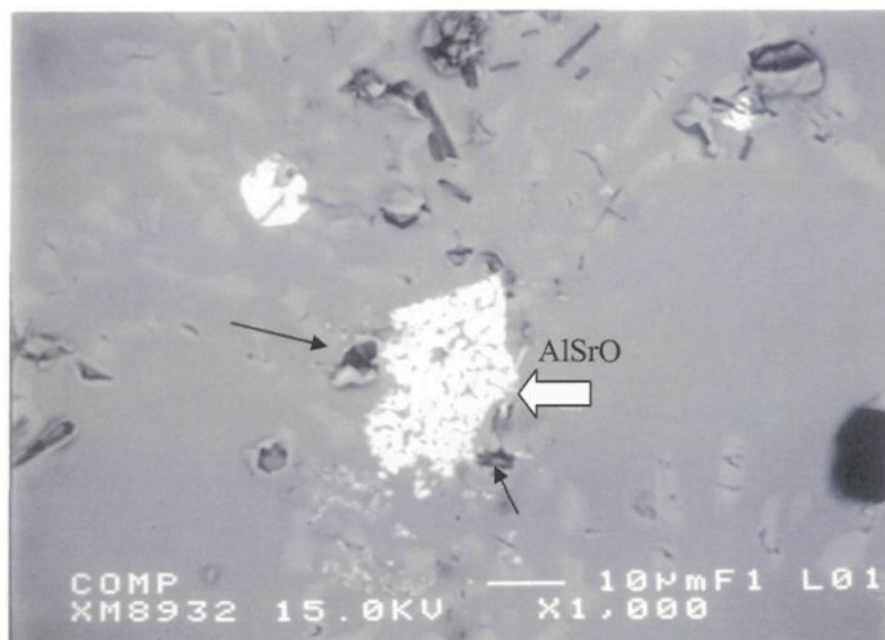


**Figure 7.5** SEM micrograph of a Prefil test sample obtained from the same Sr-modified 356 alloy melt (Figure 7.4), showing microporosity (black arrows) associated with the strontium oxide cluster (white arrow).

Electron probe microanalysis was carried out for the same sample. Figure 7.6 shows a series of micrographs depicting (a) the backscattered image, (b) the Al-, (c) the Sr-, and (d) the O images obtained from such Al-Sr-O films that were associated with microporosity (arrowed in Figure 7.6 (a)).

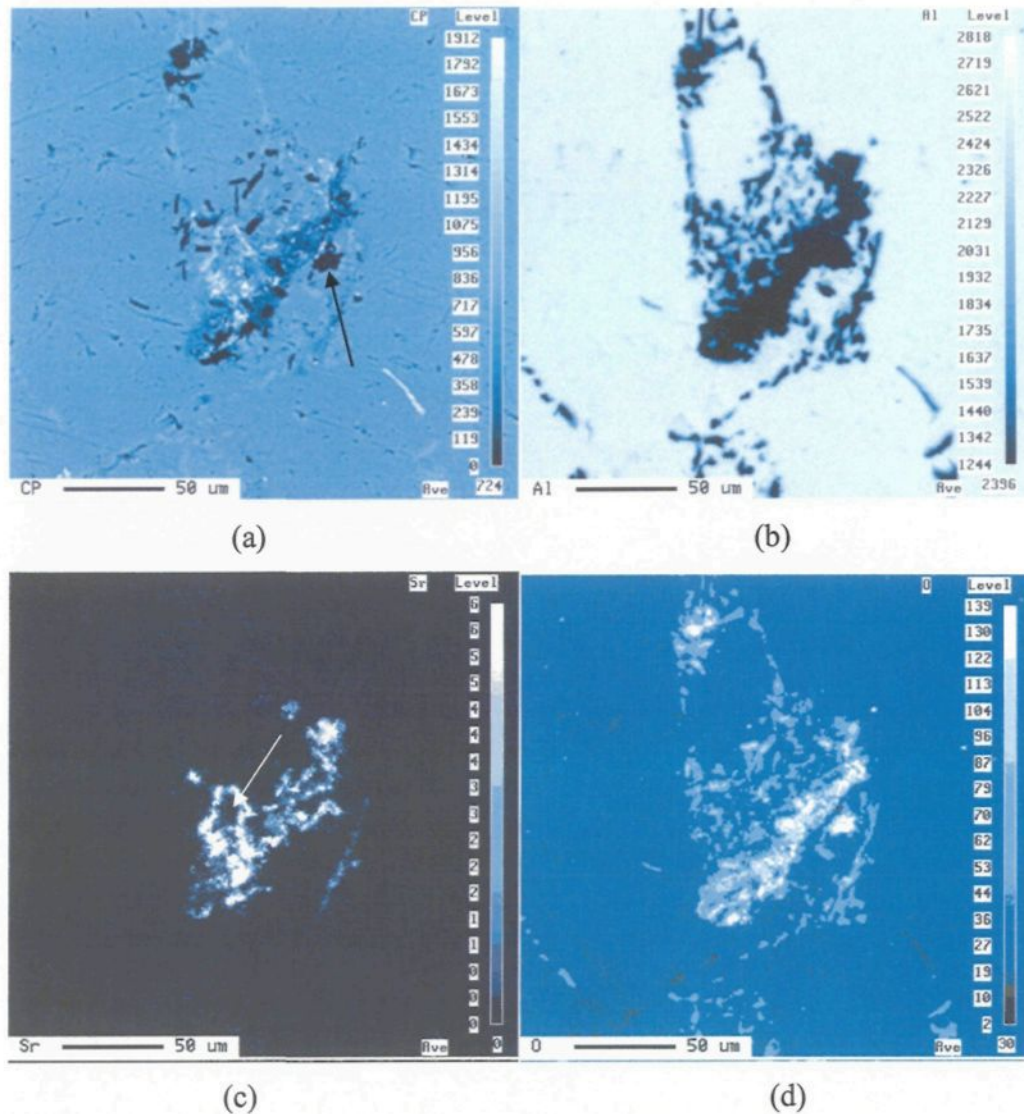


**Figure 7.6** EPMA analysis of the Prefil test sample of the Sr-modified 356 alloy showing (a) the backscattered image of Al-Sr-O films and associated microporosity, (b) the Al-, (c) the Sr-, and (d) the O images obtained from the Al-Sr-O films.

The apparent stability of these oxides (since they were observed in a number of cases, examples of which were shown in the preceding figures) can be understood based on thermodynamic considerations, in terms of the oxidation potential of the elements (Sr and Al) involved.<sup>163</sup>

Figure 7.7 shows the plot of free energy of formation versus temperature for aluminum-, strontium-, and magnesium oxides (calculated per mole of oxygen). As can be seen, strontium oxide has a much higher negative free energy than aluminum oxide, so its formation can take place very easily during the melt treatment process when the Sr addition is made (see also Table 2.4 in Chapter 2). The fact that the oxide was often observed in the solidified microstructure in spite of the degassing of the alloy melt (after the Sr addition and prior to casting), would suggest that the oxidation of the Sr in the melt took place during the 10 min-time interval when the melt was transferred from the larger to the 1-kg capacity crucible or was pre-existent in the Al-Sr master alloy.

To further confirm the observation of microporosity in association with strontium oxide, a limited number of experiments were carried out, where SrO powder was injected into a degassed melt of unmodified A356.2 alloy. The injection was carried out using a special powder injection technique fabricated in-house.<sup>164</sup> The melt containing the injected SrO particles was poured into a cylindrical metallic mold (19 mm in diameter with a cooling rate equivalent to a DAS of about 25  $\mu\text{m}$ ). Samples for metallographic examination were sectioned, mounted and polished. The samples were examined using an electron microprobe.

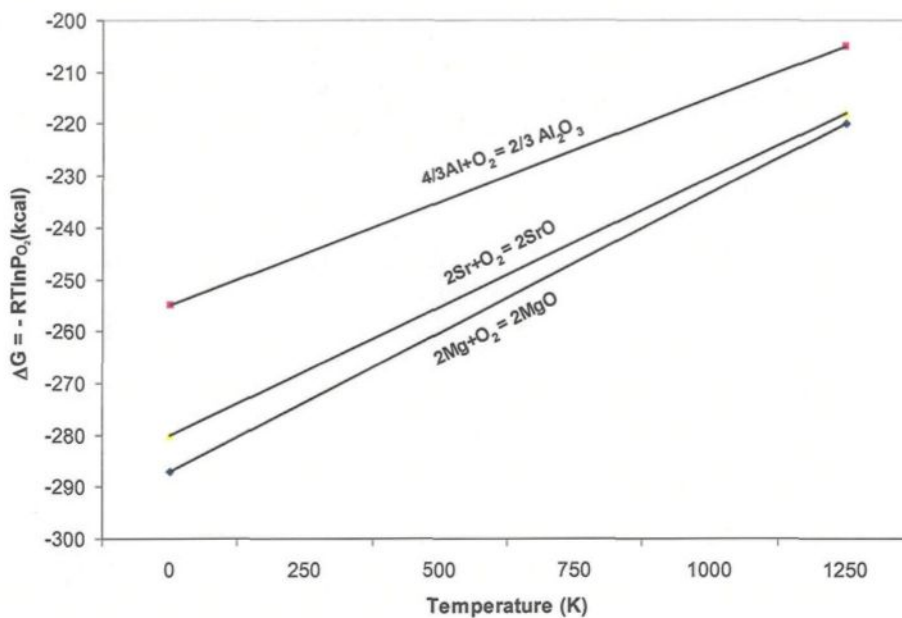


**Figure 7.7** Free energies of formation versus temperature for Al, Sr and Mg oxides.

A representative example of the results obtained is shown in Figure 7.8. The backscattered (BS) image in Figure 7.8(a), taken at 2000X magnification, clearly shows the presence of microporosity associated with the SrO particles, which are observed to be 2~3  $\mu\text{m}$  in size. The corresponding X-ray images for Fe, O and Sr, shown in Figures 7.8(b), (c) and (d), respectively, confirm that the microporosity is always associated with the presence of strontium oxide - be they particles or oxide films as observed in the earlier figures.

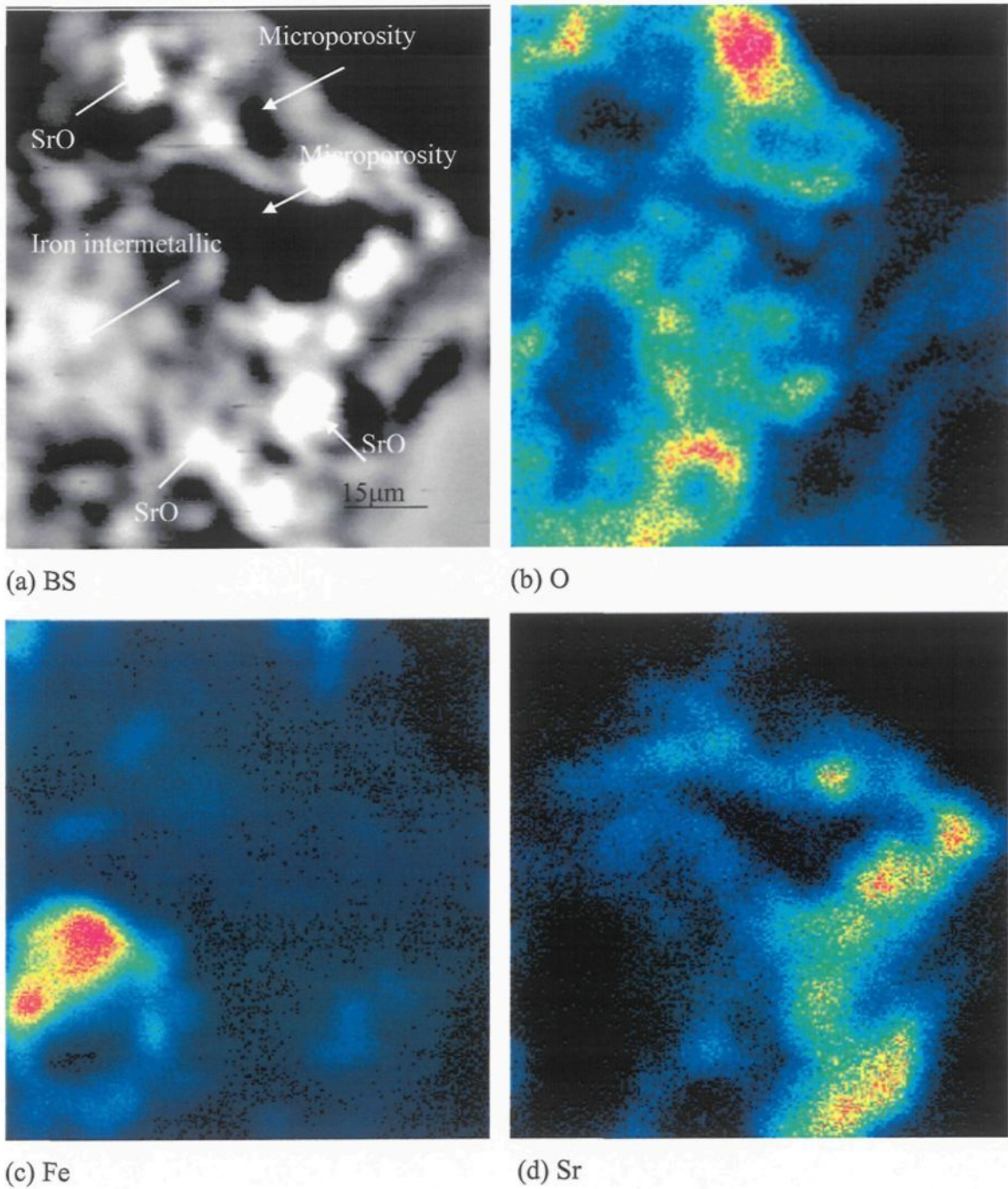


**Figure 7.8** Backscattered (a), and X ray images of (b) O, (c) Sr and (d) Fe obtained from an A356.2 alloy sample containing SrO particles, solidified in a cylindrical metallic mold (DAS ~25μm).

### 7.3.2 Role of Aluminum Oxide

To study the effect of aluminum oxides, in some cases, the melt was mechanically stirred to incorporate surface oxide films within the molten metal. The figures shown in this section were taken from samples that were obtained from such melt castings.

Figure 7.9 shows the optical micrograph obtained from the same Sr-modified Al-12%Si (A12SS) melt, but cast after stirring. The arrows point to the presence of solidified alloy material within the pores, giving an indication that the molten metal was entrapped within the oxide films. The open arrow shows how two pores are linked together by means of such oxide films. Compared to the pores related to strontium oxide, aluminum oxide films lead to the formation of coarser and deeper pores (*cf.* Figure 7.2 and Figure 7.9).

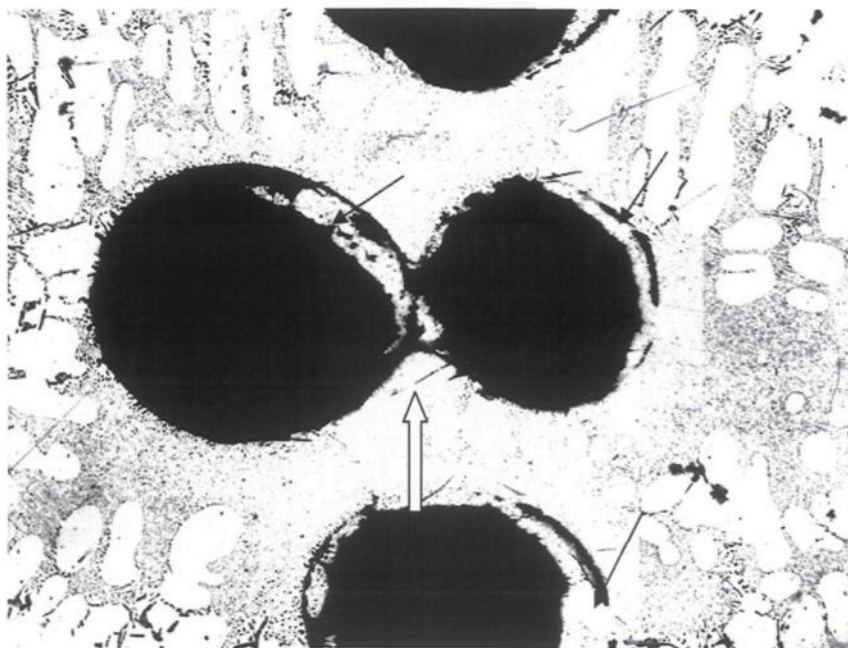
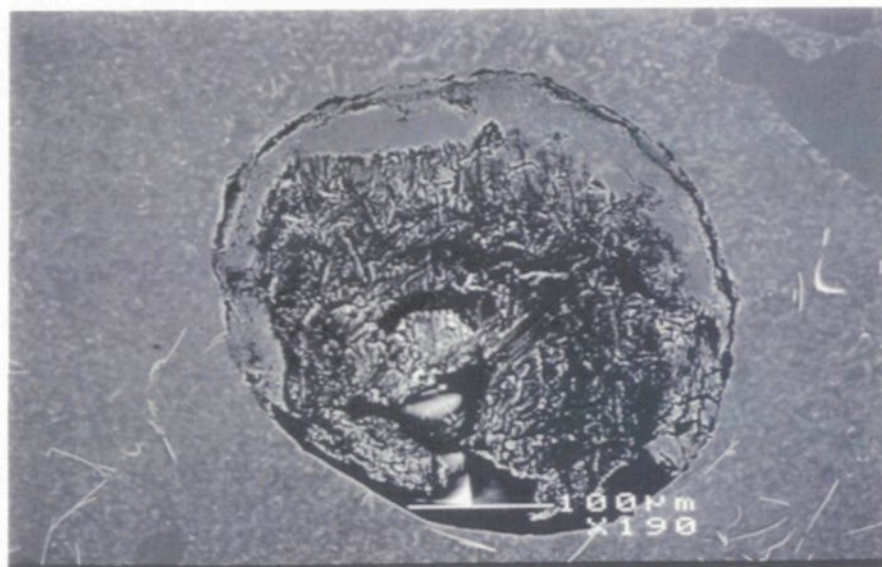


**Figure 7.9** Optical micrograph obtained from the Sr-modified Al-12%Si (A12SS) melt, cast after stirring, showing solidified alloy material entrapped within the oxide films, and how these oxide films can link two pores.

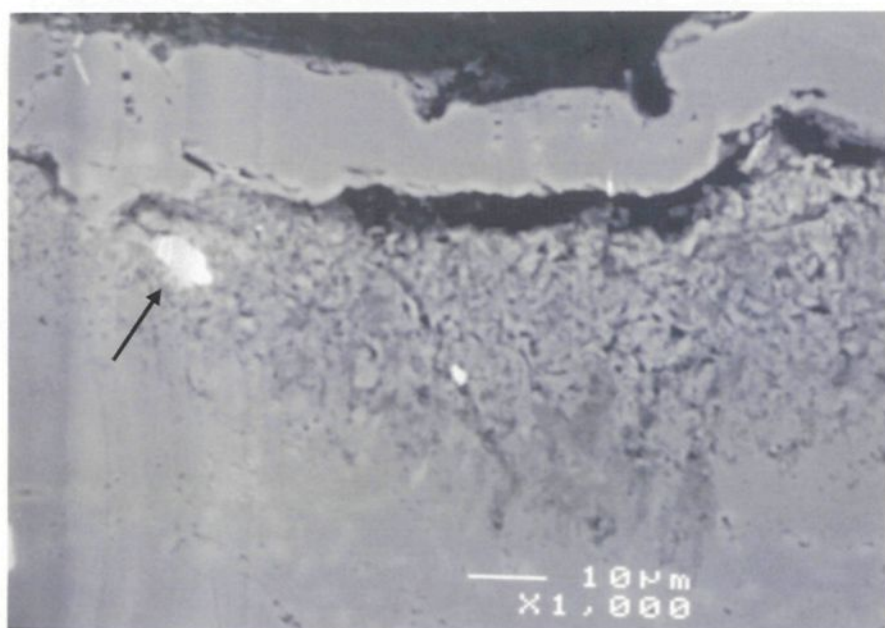
Figure 7.10(a) is an SEM micrograph taken from the same sample. Two features are noted : the large size of the pore, and the eutectic Al-Si phase surrounding the pore. A higher magnification SEM micrograph, Figure 7.10(b), clearly shows that the metal entrapped within the oxide film is separate from the edge of the pore. The “crumpled” region is probably part of the oxide film. The surrounding eutectic region is observed at the very bottom of the micrograph, and the white particle observed at the upper left corresponds to Al-Sr-O (arrowed).

The spherical form of these pores suggests the entrapment of gases within their interiors, which would increase the alloy hydrogen content. Given that, in the absence of inclusions, extremely high gas pressures are required to overcome the surface tension forces for the first hydrogen molecules to coalesce and form bubbles,<sup>161</sup> this should most likely be true. Iwahori *et al.*<sup>152</sup> have also reported that in oxide-containing melts, the hydrogen content is not decreased after vacuum degassing.

The SEM micrograph of Figure 7.11(a) shows the bottom of an aluminum oxide-associated pore. The crumpled nature of the aluminum oxide and the absence of the eutectic structure are evident. Figure 7.11(b) shows a composite of an EDX and oxygen scan taken from this region. It is to be mentioned here that due to the depth of the pore, the oxygen profile was difficult to obtain. The Si peak in the EDX inset was found to be thinner compared to that observed in the case of Figure 7.2(c) (taken from the strontium oxide-containing pore), where the Si and Sr peaks overlapped. In this context, Huang *et al.*<sup>158</sup> have also commented upon the difficulty of identifying the size and morphology of these oxide films.

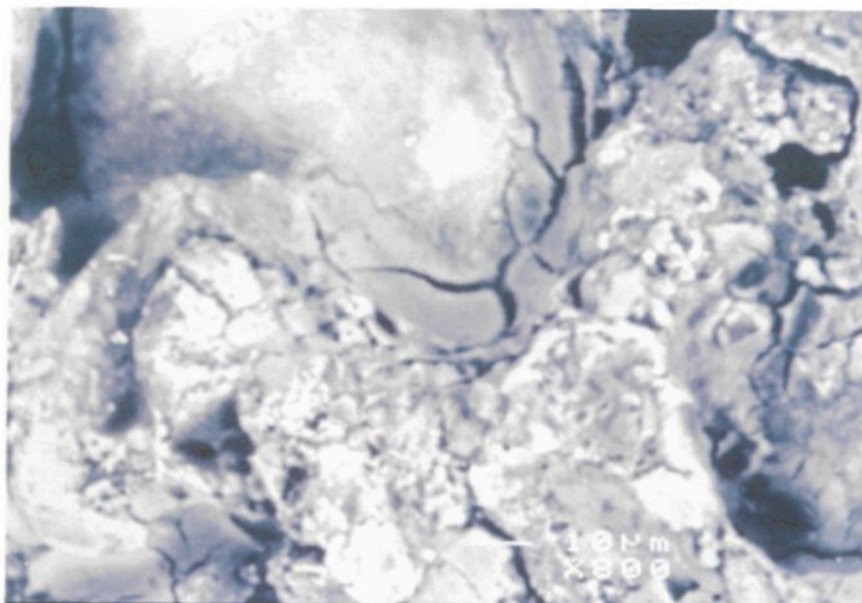


(a)

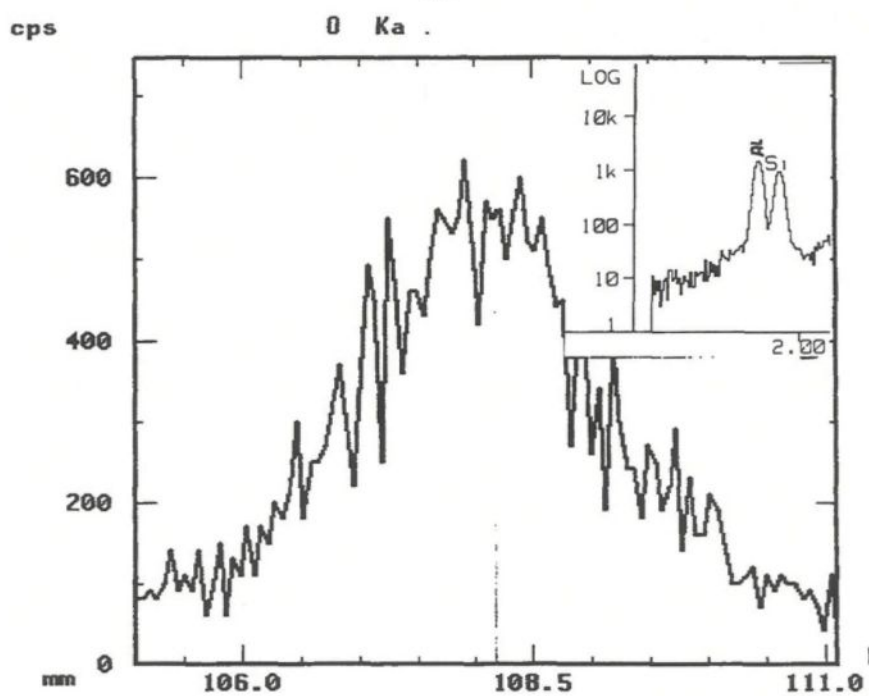


(b)

**Figure 7.10** (a) SEM micrograph taken from the A12SS sample of Figure 7.9, showing a large sized pore and the eutectic Al-Si region surrounding it, (b) high magnification micrograph of (a). Arrow in (b) points to an Al-Sr-O particle.



(a)



(b)

**Figure 7.11** (a) SEM micrograph showing the bottom of an aluminum oxide-associated pore, and (b) composite of oxygen scan and EDX spectrum (inset) taken from (a).

Figure 7.12 shows the backscattered image and the Al-, O-, and Sr images of such a pore. The absence of visible microstructural Al-Si eutectic details within the pore are noted in Figure 7.12(a). The Al and O images, Figure 7.12(b) and Figure 7.12(c), show clearly that the oxygen is concentrated within the pore, but is absent in the surrounding matrix, while the Al is concentrated in the matrix, but also to a reasonable extent within the pore, from which the presence of the aluminum oxide within the pore is confirmed. As for the Sr-image, Figure 7.12(d), the very tiny white spots (Al-Sr-O or Al-Si-Sr) observed, indicate the presence of some impurity traces of the element probably trapped within the oxide film.

From the above observations, it may be suggested that entrapped  $\text{Al}_2\text{O}_3$  oxide films are very effective in creating porosity. Degassing (using an inert gas such as pure, dry argon injected by means of a graphite rotary impeller running at high (200 rpm) speed) can be employed to remove the  $\text{Al}_2\text{O}_3$  films or particles. In the case of Sr-modified alloys, however, due to the high stability of the Al-Sr-O oxides, filtration using fine ceramic foam filters (20 ppi or 20 pores per inch) is recommended to prevent their passage into the final casting.

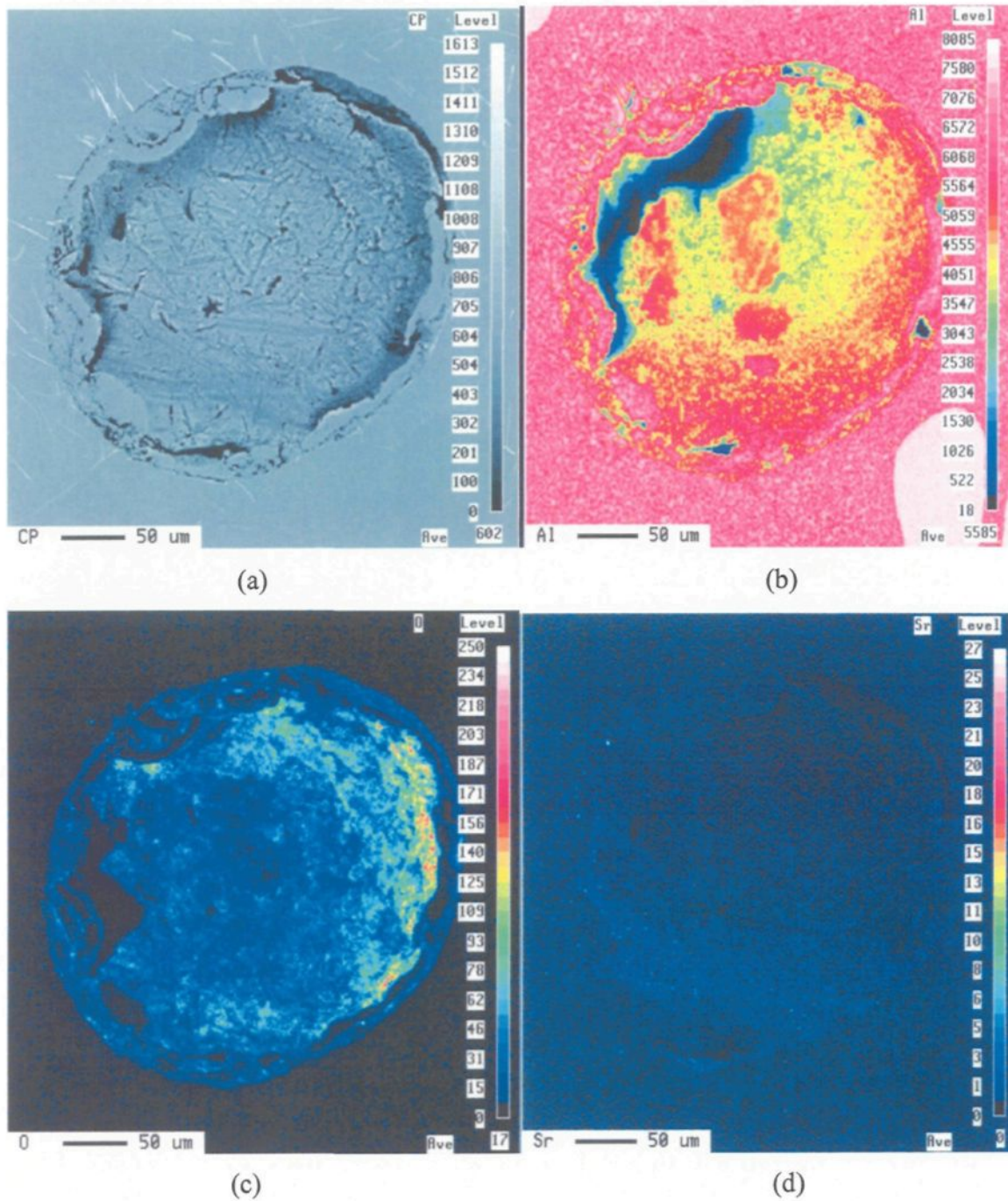
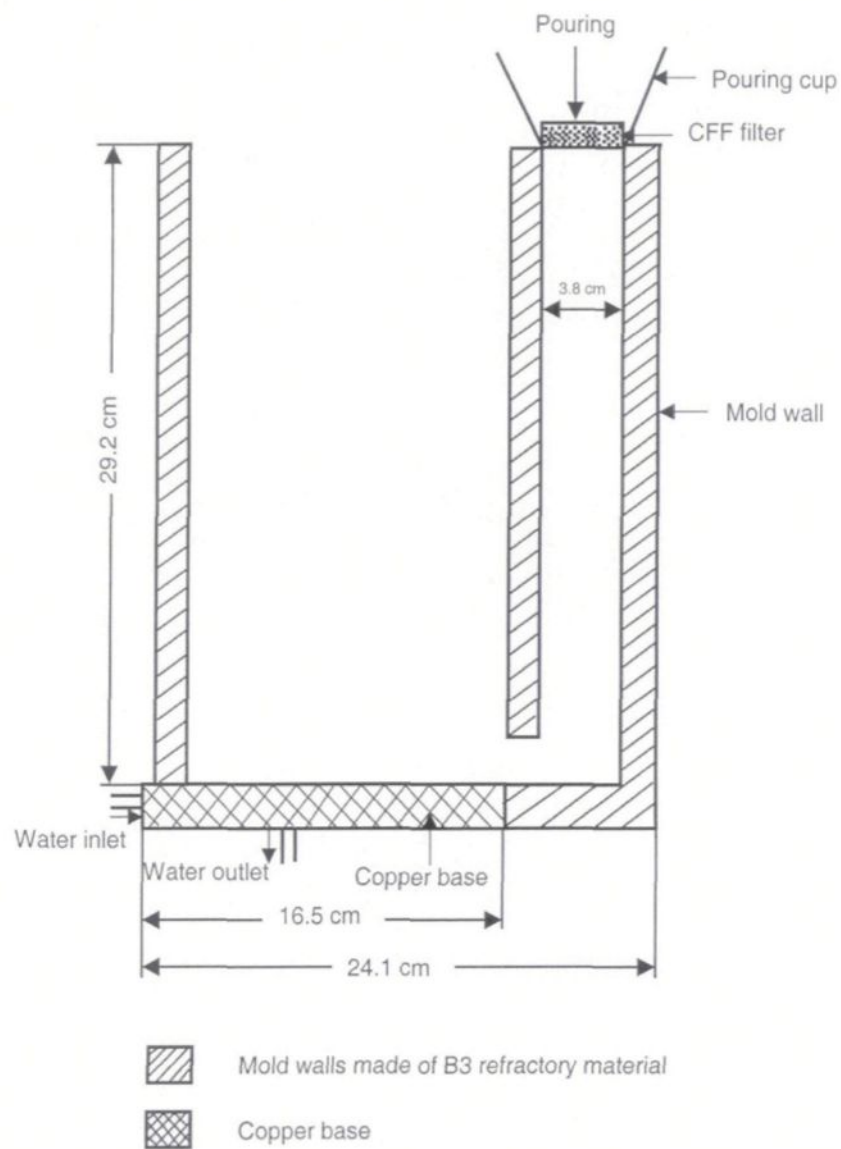


**Figure 7.12** a) Backscattered image, and (b) the Al-, (c) O-, and (d) Sr images of an aluminum oxide-associated pore of the type shown in Figure 7.9.

In keeping with these recommendations, a series of castings were prepared from the 319 alloy using an end-chill mold, which were used in an extensive investigation to study the effect of microstructure on the alloy performance.<sup>3,165</sup> A schematic diagram of the mold is shown in Figure 7.13(a). The inner surfaces of the mold were covered with 2 mm thick steel plates to prevent moisture from penetrating into the casting. The mold was dried by preheating at 120 °C for 3 hours, before the melt was poured through the pouring cup which had a ceramic foam filter (20 ppi) fitted to its bottom to remove oxides and other inclusions from entering the mold.

An example of the quality of castings obtained using these procedures is displayed in Figures 7.12(b) and 7.12(c), which show the radiographs of two end-chill mold castings that were obtained from well-degassed A319.2 alloy melts (hydrogen level ~0.1 mL/100g Al), the left one corresponding to a grain-refined melt (0.02 wt% Ti content), and the right one obtained from a 70 ppm Sr-modified melt.<sup>165</sup> Note the absence of clustered pores in either case. Both castings exhibited light porosity (rated 1-2 according to ASTM 155 testing standards), indicating the effectiveness of this technique in removing most of the Al<sub>2</sub>O<sub>3</sub> and AlSrO oxides, providing sound castings and, hence, acceptable performance in terms of mechanical properties.



(a)

**Figure 7.13** (a) Schematic diagram of end-chill mold and pouring arrangement for casting; (b,c) Radiographs of (b) H1T, and (c) H1S2 end-chill mold castings obtained from well-degassed melts of 319 alloy<sup>165</sup> (H1 : hydrogen level ~0.1 mL/100g Al; T : grain refined melt; S2 : 70 ppm Sr-modified melt).



(b)



(c)

**Figure 7.13** (a) Schematic diagram of end-chill mold and pouring arrangement for casting; (b,c) Radiographs of (b) H1T, and (c) H1S2 end-chill mold castings obtained from well-degassed melts of 319 alloy<sup>165</sup> (H1 : hydrogen level ~0.1 mL/100g Al; T : grain refined melt; S2 : 70 ppm Sr-modified melt).

**CHAPTER 8**  
**CONCLUSIONS**

## CHAPTER 8

### CONCLUSIONS

An extensive study was carried out to investigate the metallurgical parameters controlling the microstructural evolution of Al-Si-Cu and Al-Si-Mg alloys, where the microstructural characteristics of directionally solidified 319 and A356 type alloys were examined as a function of iron content, Sr addition and cooling rate. By analyzing the effects of these parameters on the precipitation of the  $\beta$ -Al<sub>5</sub>FeSi iron intermetallic phase, eutectic silicon modification and porosity formation, the following may be concluded.

1. The size of  $\beta$ -Al<sub>5</sub>FeSi platelets and their distribution are greatly affected by the amount of iron present, particularly at low cooling rates.
2. Addition of strontium leads to fragmentation of co-eutectic or post-eutectic  $\beta$ -Al<sub>5</sub>FeSi platelets. However, the effect of Sr diminishes with the increase in Fe concentration. Increasing the amount of Sr leads, instead, to precipitation of Al<sub>2</sub>Si<sub>2</sub>Sr phase particles.
3. At iron levels of ~ 0.4 wt pct in 319 alloys and ~ 0.4 (or 0.6) wt pct in 356 alloys the total percentage porosity is observed to be minimum due to improvements in the alloy fluidity. Further increase in the iron content and, hence, the size of the

$\beta$ -Al<sub>5</sub>FeSi platelets causes increase in porosity due to lack of feedability associated with larger sized  $\beta$ -platelets.

4. As both alloy fluidity and average maximum  $\beta$ -platelet size are found to increase with increasing Fe content, it is reasonable to suggest that the competition between these two factors determines the actual porosity observed at a given Fe level. Essentially, therefore, the amount of porosity formed is related to the permeability of, or the ease with which the molten liquid can flow through the interdendritic regions as solidification proceeds.
5. The 319 alloys exhibit larger pore sizes than the 356 alloys under the same conditions (of Fe content and cooling rate), owing to the larger solidification time of the former, caused by the precipitation of the CuAl<sub>2</sub> intermetallics in addition to that of Al-Si eutectic and  $\beta$ -Al<sub>5</sub>FeSi intermetallics.
6. Although branching of the  $\beta$ -Al<sub>5</sub>FeSi platelets leads to porosity formation, on the other hand, the platelets also limit pore growth.
7. In general, porosity parameters (percentage porosity, maximum pore area and maximum pore length) increase with increase in average maximum  $\beta$ -platelet lengths for both 319 and 356 alloys. Unmodified alloys show better correlations ( $R^2 = \sim 0.9 - 0.95$ ), however, than the Sr-modified alloys ( $R^2 = \sim 0.8$ ). This can be attributed to the formation of strontium oxides (particles or films) in the Sr-containing alloys which also provide nucleation sites for porosity formation (see conclusion 16).

8. In the context of the Si particle size, solidification time is as important as Sr addition in alloys containing a large number of alloying elements, for example as in the case of 319 vs. 356 alloy. Modification with Sr is more effective in 356 alloy than 319 alloy as a result of the difference in the total solidification time.
9. Iron assists in modifying the Si particles in the non-modified alloys, particularly at low cooling rates. The higher the Fe level, the finer the Si particles. In the Sr-modified alloys, the presence of Fe balances the increase in Si particle size with the increase in DAS, resulting in more or less uniform Si particle sizes, irrespective of the alloy composition. (*i.e.*, 356 or 319 alloy).
10. Silicon precipitates on  $\beta$ -Al<sub>5</sub>FeSi platelets no matter whether the alloy is modified or not, or whether the Fe level is low or high. The increase in the surface area of  $\beta$ -Al<sub>5</sub>FeSi platelets with increase in Fe content provides many more nucleation sites for the Si particles and, consequently, refinement of their size.
11. Overmodification of the Si particles takes place when the excess Sr precipitates in the form of Al<sub>2</sub>Si<sub>2</sub>Sr phase in co-eutectic and post-eutectic reactions. The Al<sub>2</sub>Si<sub>2</sub>Sr particles are polygonal in shape and incoherent with the matrix. The Al<sub>2</sub>Si<sub>2</sub>Sr phase can also precipitate directly from the melt when the Sr level is sufficiently high. In this case, the phase appears in the form of short, fine needles or rods.
12. The precipitation of co-eutectic Al<sub>2</sub>Si<sub>2</sub>Sr results in absorption of all Sr from the regions in which this phase occurs. These regions thus become depleted in Sr. Therefore, any Si particles in the surrounding area remain unmodified, *i.e.*, acicular in nature. The coarseness of the Si particles is a result of their remaining

unmodified rather than because of a reversion in morphology from fibrous to plate-like form.

13. The mechanism of the effect of Fe on Si modification in Sr-treated alloys is proposed to proceed as follows:

(a) In the under-modified condition, the  $\beta$ -Al<sub>5</sub>FeSi platelets precipitate in a bath of Al-Si-Sr liquid, where the Sr adheres to the surface of the platelets. The Si particles that nucleate on the  $\beta$ -platelets are thus very fine (average length  $\sim$ 1-2  $\mu$ m). Elsewhere in the matrix, however, the Si particles remain unmodified (average length  $\sim$ 9-12  $\mu$ m).

(b) In the well-modified condition, Al<sub>2</sub>Si<sub>2</sub>Sr particles precipitate at the edges or along the sides of the  $\beta$ -platelets in a co-eutectic reaction. As a result, the Si particles near the Al<sub>2</sub>Si<sub>2</sub>Sr particles are unmodified owing to the depletion of Sr in these areas, whereas those elsewhere in the matrix are well modified.

14 Depression in the eutectic Si solidification temperature in Al-7% Si alloys is caused by the addition of alloying elements such as Mg and Cu. Introduction of Sr to these alloys further depresses this temperature, with a corresponding increase in the volume fraction of the  $\alpha$ -Al phase. The primary dendrite solidification pattern changes from parallel rows to a branched form, producing an equiaxed type of structure and hence shorter primary dendrite lengths. This is expected to enhance the interdendritic feedability.

- 15 The lengths of the secondary dendrite arms are controlled by the rejection of solute atoms in front of the growing dendrites during solidification. The higher the alloying content of the alloy (*i.e.*, 319), the smaller the dendrite cell size. The longer solidification time in the 319 alloy also appears to have a considerable influence on the amount of porosity formed in the alloys, in addition to the effect of Sr.
- i. Pores observed in Sr-modified alloys are frequently associated with strontium oxides (films or particles). These particles/films are formed during melting, due to the high oxygen affinity of strontium, and are extremely difficult to be removed during degassing (using pure argon and a rotary impeller). This observation was conformed through injection of SrO powders into molten Al-Si alloys. The stoichiometric composition of these oxides is found to be  $\text{Al}_{2.3}\text{SrO}_{3.3}$  (or  $\text{Al}_2\text{SrO}_3$ ) from WDS analysis.
- 17 The morphology of the pores (round or irregular) is determined by the form of oxide, *i.e.*, fine, dispersed particles or thick films. The rounded pores are also observed surrounded by Al-Si eutectic regions.
- 18 Aluminum oxide films trapped in the molten metal can lead to the formation of coarser and deeper pores than those formed due to strontium oxide. These pores can also link with each other through the oxide films. Such pores are characterized by the presence of solidified metal trapped within the aluminum oxide films, close to the periphery, with no Al-Si eutectic features observed within the pore. The

form of these pores is controlled by the amount of gases entrapped within the pores during solidification. Correspondingly, the porosity level is also increased.

- 19 The aluminum and strontium oxides also act as favorable sites for the precipitation of other microstructural constituents, such as the  $\beta$ -Al<sub>5</sub>FeSi iron intermetallic phase.

## REFERENCES

- 
- 1 J.E. Gruzleski and B.M. Closset, *The Treatment of Liquid Aluminum-Silicon Alloys*, American Foundrymen's Society, Inc., Des Plaines, IL, U.S.A., 1990.
  - 2 L.A. Narayanan, F.H. Samuel and J.E., Gruzleski, "Crystallization Behavior of Iron-Containing Intermetallic Compounds in 319 Aluminum Alloy", *Metallurgical and Materials Transactions A*, Vol. 25A, Aug. 1994, pp. 1761-1773.
  - 3 Z. Ma, "Effect of Fe-Intermetallics and Porosity on Tensile and Impact Properties of Al-Si-Cu and Al-Si-Mg Cast Alloys", Ph.D. Thesis, Université du Québec à Chicoutimi, Canada, Nov., 2003.
  - 4 M. Lebyodkin, A. Deschamps and Y. Bréchet, "Influence of Second-Phase Morphology on Mechanical and Fracture Properties of Al-Si Alloys", *Materials Science and Engineering*, Vols A234-236, 1997, pp. 481-484.
  - 5 F. Paray and J.E. Gruzleski, "Factors to Consider in Modification", *AFS Transactions*, Vol. 92, 1994, pp. 833-842.
  - 6 L. Bäckerud, G. Chai and J. Tamminen, *Solidification Characteristics of Aluminum Alloys*, Vol. 2: Foundry Alloys, AFS/Skanaluminium, Des Plaines, IL, 1990, pp. 71-84.
  - 7 J.E. Hatch, *Aluminum: Properties and Physical Metallurgy*, American Society for Metals, Metals Park, Ohio, 1984, pp. 320-350.
  - 8 D.O. Northwood, X.C. Sun, G.E. Byczynski and J.H. Sokolowski, "A Metallurgical Study of the Heat Treatment of Aluminum Alloy 319 (Al-6Si-3.5Cu) Castings", *Proceedings of the International Symposium on Recent Metallurgical Advances in Light Metals Industries*, 34th Annual Conference of Metallurgists of CIM, Vancouver, British Columbia, August, 20-24, 1995, pp. 355-365.
  - 9 H. Baker, *Alloy Phase Diagrams*, ASM Handbook, Vol. 3, ASM International, Materials Park, Ohio, 1992, pp. 2-86.

- 
- 10 A.M. Samuel and F.H. Samuel, "Modification of Iron Intermetallics by Magnesium and Strontium in Al-Si Alloys", *International Journal of Cast Metals Research*, Vol. 10, 1997, pp. 147-157.
  - 11 K. Radhakrishna, S. Seshan and M.R. Seshadri, "Dendrite Arm Spacing in Aluminum Alloy Castings", *AFS Transactions*, Vol. 88, 1980, pp. 695-702.
  - 12 C. Mascré, "Influence du fer et du manganèse sur les alliages du type de l'A-S13 (Alpax)", *Fonderie*, Vol. 108, 1955, pp. 4330-4336.
  - 13 L. Grand, "Influence of Some Impurities on the Quality of Aluminum Foundry Alloys", *Fonderie*, Vol. 217, 1964, pp. 95-100.
  - 14 E.N. Pan, Y.C. Cherng, C.A. Lin and H.S. Chiou, "Roles of Sr and Sb on Silicon Modification of A356 Aluminum Alloys", *AFS Transactions*, Vol. 92, 1994, pp. 609-629.
  - 15 D. Apelian, G.K. Sigworth and K.R. Whaler, "Assessment of Grain Refining and Modification of Al-Si Foundry Alloys by Thermal Analysis", *AFS Transactions*, Vol. 92, 1984, pp. 297-307.
  - 16 Pacz, Aladar, United States Patent, 1,387,900, 1921.
  - 17 L.M. Hogan and M. Shamsuzzoha, "Crystallography of the Flake -Fibre Transition in the Al-Si Eutectic", *Materials Forum*, Vol. 10, 1987, pp. 270-277.
  - 18 S.Z. Lu and A. Hellawell, "The Mechanism of Silicon Modification in Aluminum-Silicon Alloys: Impurity Induced Twinning", *Metallurgical Transactions*, Vol. 18A, 1987, pp. 1721-1733.
  - 19 S.Z. Lu and A. Hellawell, "Modification and Refinement of Cast Al-Si Alloys", *Light Metals 1995*, J.E. Evans (Ed.), The Minerals, Metals and Material Society, Warrendale, PA, 1995, pp. 989-993.
  - 20 R. Sharan and N.P. Saksena, "Rare Earth Additions as Modifiers of Aluminum-Silicon Alloy", *AFS International Cast Metals Journal*, Vol. 2, No. 1, 1978, pp. 29-33.
  - 21 G.K. Sigworth, "Theoretical and Practical Aspects of the Modification of Al-Si Alloys", *AFS Transactions*, Vol. 91, 1983, pp. 7-16.

- 
- 22 B.J. Ye, C.R. Loper, Jr., D.Y. Lu and C.S. Kang, "An Assessment of the Role of Rare Earth in the Eutectic Modification of Cast Aluminum Silicon Alloys", *AFS Transactions*, Vol. 93, 1985, pp. 533-544.
  - 23 M. Garat and R. Scalliet, "A Review of Recent French Casting Alloy Development", *AFS Transactions*, Vol. 86, 1978, pp. 549-562.
  - 24 B. Closset and J.E. Gruzleski, "Structure and Properties of Hypoeutectic Al-Si-Mg Alloys Modified with Pure Strontium", *Metallurgical Transactions*, Vol. 13A, 1982, pp. 945-951.
  - 25 J.E. Gruzleski, "The Art and Science of Modification – Twenty Five Years of Progress", *AFS Transactions*, Vol. 100, 1992, pp. 673-683.
  - 26 L. Grand, "The Modification of Aluminum-Silicon Alloys" *Revue de l'Aluminium*, Vol. 29, 1952, pp. 5-15.
  - 27 M. Garat, G. Laslaz, S. Jacob, P. Meyer, P.H. Guerin and R. Adam, "The State of the Art of the Use of Antimony Sodium and Strontium Modified Aluminum Silicon Casting Alloys", *AFS Transactions*, Vol. 100, 1992, pp. 549-562.
  - 28 C.B. Kim and R.W. Heine, "Fundamentals of Modification in the Aluminum-Silicon System", *Journal of the Institute of Metals*, Vol. 92, 1964, pp. 367-376.
  - 29 J. Gobrecht, "The Influence of Alloying Elements on the Duration of Modification of Na and Sr in Al-Si Cast Alloys", *Giesserei*, Vol. 65, 1975, pp. 87-90.
  - 30 B. Closset, R.A.L. Drew and J.E. Gruzleski, "Eutectic Silicon Shape Control by In Situ Measurement of Resistivity", *AFS Transactions*, Vol. 94, 1986, pp. 9-16.
  - 31 P.D. Hess and E.V. Blackmun, "Strontium as a Modifying Agent for Hypoeutectic Aluminum Silicon Alloys", *AFS Transactions*, Vol. 83, 1975, pp. 87-90.
  - 32 G.C Chai and L. Bäckerud, "Factors Affecting Modification of Aluminum Silicon Alloys by Addition of Strontium-Containing Master Alloys", *AFS Transactions*, Vol. 100, 1992, pp. 847-854.
  - 33 W.D. Griffiths, M.R. Jolly, W. Kattlitz, R. Kendrick and A.M. Niblett, "The Effect of Simultaneous Additions of Sodium and Strontium on the Modification of Aluminum Silicon Alloy", *Light Metals 1991*, E. Rooy (Ed.), The Minerals, Metals and Material Society, Warrendale, PA, 1991, pp. 1047-1055.

- 
- 34 A. Flores V., J. Lopez , J.C. Escobedo B., A.H. Castillejos E. and F.A. Acosta G, "Effects of S and Sr Additions on the Microstructure and Mechanical Properties of the Al-Si 319 Alloy", *Canadian Metallurgical Quarterly*, Vol. 33, 1994, pp.133-138.
  - 35 N. Handiak, J.E. Gruzleski and D. Argo, "Sodium, Strontium and Antimony Interactions During Modification of AS7G03 (A356) Alloys", *AFS Transactions*, Vol. 95, 1987, pp. 31-38.
  - 36 R. Sharan and T.R. Anantharaman, "Modification of Aluminum–Silicon Alloys by Misch Metal Additions", *Current Science*, Vol. 36, No. 21, 1967, pp. 568-570.
  - 37 R. Sharan and T.R. Anantharaman, "Effect of Misch Metal Additions on the Properties of Aluminum and Its Alloys", *Transactions of the Indian Institute of Metals*, Vol. 17, 1964, pp. 89-93.
  - 38 I.S. Hirschhorn, "Recent Applications of the Rare Earth Metals in Nonferrous Metallurgy", *Journal of Metals*, Vol. 22, 1970, pp. 40-43.
  - 39 J. Chang, I. Moon and C. Choi, "Refinement of Cast Microstructure of Hypereutectic Al-Si Alloys through the Addition of Rare Earth Metals", *Journal of Materials Science*, Vol. 33, 1998, pp. 5015-5023.
  - 40 F.O. Traenkner, "Practical Techniques in Casting Aluminum", *Casting Engineering and Foundry World*, Fall, 1981, pp. 50-61.
  - 41 L. Luis-Martin and S. Ferreira-Rodriquez, "Permanent Modification of Al-Si Alloys at and Near to the Eutectic", *Fonderie*, Vol. 372, 1977, pp. 353-356.
  - 42 G. Medin, F. Jeglitsch, W. Meyer and G. Spiegel, "Casting Behavior and Mechanical Properties of Combination Refined Al-Si Alloys", *Proc. 45th International Foundry Congress*, 1978, Budapest.
  - 43 B. Gunther and H. Jurgens, "Influence of Minor Impurities on Mechanical Properties, Structure and Solidification Form of Eutectic and Near-Eutectic Al-Si Casting Alloys", *Giesserei*, Vol. 67, 1980, pp. 8-13.
  - 44 J.M. Lee and S.B. Kang, "A Study on the Change of Microstructures with P and/or Sr Treatment in A390 Alloy", *Journal of the Korean Institute of Metallurgy and Materials*, Vol. 33, No. 11, 1996, pp. 1406-1413.
  - 45 S. Shivkumar, C. Keller and D. Apelian, "Aging Behavior in Cast Al-Si-Mg Alloys", *AFS Transactions*, Vol. 98, 1990, pp. 905-911.

- 
- 46 B.M. Closset, "Modification and Quality of Low Pressure Aluminum Castings", *AFS Transactions*, Vol. 96, 1988, pp. 249-260.
  - 47 Mahmoud F. Hafiz and Toshiro Kobayashi, "Mechanical Properties of Modified and Nonmodified Eutectic Al-Si Alloys", *Journal of Japan Institute of Light Metals*, Vol. 44, No. 1, 1994, pp. 28-34.
  - 48 B. Closset and D. Fay, "Strontium Modification of Aluminum Investment Casting Alloys", *AFS Transactions*, Vol. 98, 1990, pp. 505-509.
  - 49 M.M. Haque, "Strontium Modification of Aluminum-Silicon Eutectic Alloy and the Factors Affecting It", *Metals Forum*, Vol. 6, No. 1, 1983, pp. 54-56.
  - 50 A. Couture, "Iron in Aluminum Casting Alloys - A Literature Survey", *AFS International Cast Metals Journal*, Vol. 6, No. 4, Dec. 1984, pp. 9-17.
  - 51 S. Nishi, T. Shinoda and E. Kato, "Effect of Iron Content, Beryllium Addition and Cooling Velocity on Mechanical Properties of Al-Si-Mg-Zn Cast Alloys", *Journal of Japan Institute of Light Metals*, Vol. 18, No. 12, 1968, pp. 627-635.
  - 52 W. Bonsack, "Discussion on the Effect of Minor Alloying Elements on Aluminum Casting Alloys", *ASTM Bulletin*, No. 117, August 1942, pp. 45-59; No. 124, Oct 1943, pp. 41-51.
  - 53 J.E., Eklund, "On the Effects of Impurities on the Solidification and Mechanical Behavior of Primary and Secondary Commercial Purity Aluminum and Aluminum Alloys", Ph.D Thesis, Helsinki University of Technology, 1991.
  - 54 S.G. Shabestari and J.E. Gruzleski, "The Effect of Solidification Conditions and Chemistry on the Formation and Morphology of Complex Intermetallic Compounds in Aluminum-Silicon Alloys", *Cast Metals*, Vol. 6, No. 4, 1994, pp. 217-224.
  - 55 S.G. Shabestari and J.E. Gruzleski, "The Kinetics of Formation and Growth of Complex Intermetallic Compounds in Aluminum-Silicon Alloys", *Cast Metals*, Vol. 6, No. 4, 1994, pp. 241-251.
  - 56 G. Gustafsson, T. Thorvaldsson and G.L. Dunlop, "The Influence of Fe and Cr on the Microstructure of Cast Al-Fe-Si Alloys", *Metallurgical Transactions A*, Vol. 17A, 1986, pp. 45-52.

- 
- 57 Y. Awano and Y. Shimizu, "Non-Equilibrium Crystallization of AlFeSi Compound in Melt-Superheated Al-Si Alloy Castings", *AFS Transactions*, Vol. 98, 1990, pp. 889-895.
- 58 A.M. Samuel, H.W. Doty and F.H. Samuel, "Influence of Melt Treatment and Solidification Parameters on the Quality of 319.2 Endchill Aluminum Castings", *Proe. 4th Int. Conf. on Molten Aluminum Processing*, Orlando, Florida, Nov. 12-14, 1995, pp. 261-294.
- 59 A.M. Samuel, F.H. Samuel and H.W. Doty, "Observations on the Formation of  $\beta$ -Al<sub>5</sub>FeSi Phase in 319 Type Al-Si Alloys", *Journal of Material Science*, Vol. 31, 1996, pp. 5529-5539.
- 60 L.A. Narayanan, F.H. Samuel and J.E. Grazleski, "Dissolution of Iron Intermetallics in Al-Si Alloys through Nonequilibrium Heat Treatment", *Metallurgical and Materials Transactions A*, Vol. 26A, 1995, pp. 2161-2174.
- 61 L.F. Mondolfo, "Manganese in Aluminum Alloys", The Manganese Center, Neuilly sur Seine, France, 1990, pp. 1-35.
- 62 C. Villeneuve and F.H. Samuel, "Fragmentation and Dissolution of  $\beta$ -Al<sub>5</sub>FeSi Phase during Solution Heat Treatment of Al-13%Si-Fe Alloys", *International Journal of Cast Metals Research*, Vol. 12, 1997, pp. 145-160.
- 63 P.N. Crepeau, "Effect of Iron in Al-Si Casting Alloys: A Critical Review", *AFS Transactions*, Vol. 103, 1995, pp. 361-366.
- 64 J. Gobrecht, "Ségrégations par gravité du fer, du manganèse et du chrome dans les alliages aluminium-silicium de fonderie", *Fonderie*, No. 376, mai, 1977, pp. 171-173.
- 65 J.L. Jorstad, "Understanding Sludge", *Die Casting Engineer*, Nov.-Dec. 1986, pp. 30-36.
- 66 A.N. Lakshmanan, S.G. Shabestari and J.E. Gruzleski, "Microstructure Control of Iron Intermetallics in Al-Si Casting Alloys", *Zeitschrift für Metallkunde*, Vol. 86, 1995, pp. 457-464.
- 67 C. Villeneuve, H.W. Doty and F.H. Samuel, "Effect of Trace Elements on  $\beta$ -Al<sub>5</sub>FeSi Characteristics, Porosity and Tensile Properties of Al-Si-Cu (319) Cast Alloys", *International Journal of Cast Metals Research*, Vol. 14, 2001, pp. 97-120.

- 
- 68 D.L. Colwell and R.J. Kissling, "Die and Permanent Mold Casting Aluminum Alloy Minor Elements", *AFS Transactions*, Vol. 69, 1961, pp. 610-515.
- 69 S. Murali, Ph.D Thesis, Indian Institute of Science, Bangalore, India, April, 1994.
- 70 S. Murali, S.K. Raman and K.S.S. Murthy, "Effect of Trace Additions on the Mechanical Properties and Fracture Toughness of Fe-Containing Al-7Si-0.3Mg Alloy", *Cast Metals*, Vol. 6, No. 4, 1994, pp. 189-198.
- 71 S. Murali, S.K. Raman and K.S.S. Murthy, "Al-7Si-0.3Mg Cast Alloy: Formation and Crystal Structure of  $\beta$ -FeSiAl<sub>5</sub> and (Be-Fe)-BeSiFe<sub>2</sub>Al<sub>8</sub> Phases", *Materials Science Forum*, Vols 217-222, 1996, pp. 201-212.
- 72 W.A. Bailey, "Beryllium Effect and Mechanical Properties of 356 Variet-T6 Aluminum Alloys", *Modern Casting*, August, 1964, pp. 443-454.
- 73 K.G. Wikle, "Improving Aluminum Castings with Beryllium", *AFS Transactions*, Vol. 86, 1978, pp. 513-518.
- 74 V. Zednik, "The Influence of Chemical Composition and Quality of Raw Materials on the Physical Properties of Silumin Gamma", *Metallurgie*, Feb. 1948, pp. 195-257.
- 75 F.H. Samuel, P. Ouellet, A.M. Samuel and H.W. Doty, "Effect of Mg and Sr Additions on the Formation of Intermetallics in Al-6 Wt Pct Si – 3.5 Wt Pct Cu- (0.45) to (0.8) Wt Pct Fe 319-Type Alloys", *Metallurgical and Materials Transactions A*, Vol. 29A, 1998, pp. 2871-2884.
- 76 A.M. Samuel, A. Pennors, C. Villeneuve, F.H. Samuel, H.W. Doty and S. Valtierra, "Effect of Cooling Rate and Sr-Modification on Porosity and Fe-Intermetallics Formation in Al-6.5%Si-3.5%Cu-Fe Alloys", *International Journal of Cast Metals Research*, Vol. 13, No.4, 2000, pp. 231-253.
- 77 L.R. Morris and F. B. Miners, "Aluminum Alloys", U.S. Patent No. 3926690, 1975.
- 78 G. Pucella, A.M. Samuel and F.H. Samuel, "Sludge Formation in Sr Modified Al-11.5 wt% Si Die Casting Alloys", *AFS Transactions*, Vol. 107, 1999, pp. 117-125.
- 79 S.G. Shabestari and J.E. Gruzleski, "Modification of Iron Intermetallics by Strontium in 413 Aluminum Alloys", *AFS Transactions*, Vol. 103, 1995, pp. 285-293.

- 
- 80 D.E. Talbot, "Effect of Hydrogen in Aluminum, Magnesium, Copper and Their Alloys", *International Metals Reviews*, Vol. 20, 1975, pp. 166-182.
- 81 W.R. Opie and N.J. Grant, "Hydrogen Solubility in Aluminum and Some Aluminum Alloys", *Transactions AIME, Journal of Metals*, Vol. 188, 1950, pp. 1237-1241.
- 82 D.E.J. Talbot and P.N. Anyalebechi, "Solubility of Hydrogen in Liquid Aluminum", *Materials Science and Technology*, Vol. 4, 1988, pp. 1-4.
- 83 C.E. Ransley and H. Neufeld, "The Solubility of Hydrogen in Liquid and Solid Aluminum", *Journal of the Institute of Metals*, Vol. 74, 1948, pp. 599-620.
- 84 R.Y. Lin and M. Hoch, "The Solubility of Hydrogen in Molten Aluminum Alloys", *Metallurgical Transactions A*, Vol. 20A, 1989, pp. 1785-1791.
- 85 X.Z. Li and X.F. Bian, "Behavior of Hydrogen in Superheated Aluminum and its Alloys Melt", *Materials Science Forum*, Vols 331-337, 2000, pp. 209-214.
- 86 H. Huang and J.T. Berry, "Evaluation of Criteria Functions to Minimize Microporosity Formation in Long-Freezing Range Alloys", *AFS Transactions*, Vol. 101, 1993, pp. 669-676.
- 87 J.A. Taylor, G.B. Schaffer and D.H. StJohn, "The Role of Iron in the Formation of Porosity in Al-Si-Cu-Based Casting Alloys: Part I. Initial Experimental", *Metallurgical and Materials Transactions A*, Vol. 30A, 1999, pp. 1643-1650.
- 88 N. Roy, A.M. Samuel and F.H. Samuel, "Porosity Formation in Al-9 Wt Pct Si-3 Wt Pct Cu Alloy Systems: Metallographic Observations", *Metallurgical and Materials Transactions A*, Vol. 26A, 1995, pp. 1-12.
- 89 J. Campbell, *The Solidification of Metals*, Iron and Steel Institute, Publication 110, London, 1967, 18 pp.
- 90 K. Kubo and R.D. Pehlke, "Mathematical Modeling of Porosity Formation in Solidification", *Metallurgical Transactions B*, Vol. 16B, 1985, pp. 359-366.
- 91 J. Zou, K. Tynelius, S. Shivkumar and D. Apelian, "Microporosity Formation in A356.2 Castings", *Production, Refining, Fabrication and Recycling of Light Metals*, Pergamon Press, New York, 1990, pp. 323-332
- 92 S. Shivkumar, D. Apelian and J. Zou, "Modeling of Microstructure Evolution and Microporosity Formation in Cast Aluminum Alloys", *AFS Transactions*, Vol. 98, 1990, pp. 897-904.

- 
- 93 J. Weigel and E. Fromm, "Determination of Hydrogen Absorption and Desorption Processes in Aluminum Melts by Continuous Hydrogen Activity Measurements", *Metallurgical Transactions B*, Vol. 21B, 1990, pp. 855-860.
  - 94 A. Nouruzi-Khorasani, "Gas Porosity in Aluminium Silicon Alloys", *Metal - Casting and Surface finishing*, September/October, 1996, pp. 34-38.
  - 95 E.L. Rooy, "Mechanisms of Porosity Formation in Aluminum", *Modern Casting*, 1992, pp. 34-36.
  - 96 P.M. Thomas, J.E., Gruzleski, "Threshold Hydrogen for Pore Formation During the Solidification of Aluminum Alloy", *Metallurgical Transactions B*, Vol. 9B, 1978, pp. 139-141.
  - 97 Q.T. Fang, P.N. Anyalebechi, and D.A. Granger, "Measurement of Hydrogen Porosity in Unidirectionally Solidified Aluminum Alloys" *Light Metals 1988*, L.G. Boxall (Ed.), The Minerals, Metals and Material Society, Warrendale, PA, 1988, pp. 477-486.
  - 98 S.-T. Kao, E. Chang and L.-C. Chan, "Effect of Hydrogen Content on Soundness of A356 Alloy Plate Castings", *AFS Transactions*, Vol. 103, 1995, pp. 531-536.
  - 99 N. Roy, L. Zhang, P.R. Louchez, F.H. Samuel, "Porosity Formation on Al-9 wt%Si-3wt%Cu-X Alloy Systems: Measurements of Porosity", *Journal of Materials Science*, Vol. 31, 1996, pp. 1243-1254.
  - 100 K.E. Tynelius, "A Parametric Study of the Evolution of Microporosity in Al-Si Foundry Alloys", Ph.D Thesis, Drexel University, Philadelphia, PA, 1992.
  - 101 X.G. Chen and J.E. Gruzleski, "Influence of Melt Cleanliness on Pore Formation in Aluminum-Silicon Alloys", *International Journal of Cast Metals Research*, Vol. 9, 1996, pp. 17-26.
  - 102 D. Emadi, J.E. Gruzleski and J.M. Toguri, "The Effect of Na and Sr Modification on Surface Tension and Volumetric Shrinkage of A356 Alloy and Their Influence on Porosity Formation", *Metallurgical Transactions B*, Vol. 24B, 1993, pp. 1055-1063.
  - 103 Q.T. Fang and D.A. Granger, "Porosity Formation in Modified and Unmodified A356 Alloy Castings", *AFS Transactions*, Vol. 97, 1989, pp. 989-1000.
  - 104 G. Laslaz and P. Laty, "Gas Porosity and Metal Cleanliness in Aluminum Casting Alloys", *AFS Transactions*, Vol. 99, 1991, pp. 83-90.

- 
- 105 X.F. Bian, Z.H. Zhang and X.F. Liu, "Effect of Strontium Modification on Hydrogen Content and Porosity Shape of Al-Si Alloys", *Materials Science Forum*, Vols 331-337, 2000, pp. 361-366.
  - 106 P.D. Lee and S. Sridhar, "Direct Observation of the Effect of Strontium on Porosity Formation During the Solidification of Aluminum-Silicon Alloys", *International Journal of Cast Metals Research*, Vol. 13, 2000, pp. 185-198.
  - 107 H. Shahani, "Effect of Hydrogen on the Shrinkage Porosity of Aluminum-Copper and Aluminum-Silicon Alloys", *Scandinavian Journal of Metallurgy*, Vol. 14, 1985, pp. 306-312.
  - 108 D. Argo, J.E. Gruzleski, "Porosity in Modified Aluminum Alloy Castings", *AFS Transactions*, Vol. 96, 1988, pp. 65-74.
  - 109 S.D. McDonald, K. Nogita, A.K. Dahle, J.A. Taylor and D.H. StJohn, "Eutectic Solidification and Porosity Formation in Al-Si Alloys: Role of Strontium", *AFS Transactions*, Vol. 108, 2000, pp. 463-470.
  - 110 J.A. Taylor, G.B. Schaffer and D.H. StJohn, "The Role of Iron in the Formation of Porosity in Al-Si-Cu-Based Casting Alloys: Part II. A Phase-Diagram Approach", *Metallurgical and Materials Transactions A*, Vol. 30A, 1999, pp. 1651-1655.
  - 111 J.A. Taylor, G.B. Schaffer and D.H. StJohn, "The Role of Iron in the Formation of Porosity in Al-Si-Cu-Based Casting Alloys: Part III. A Microstructural Model", *Metallurgical and Materials Transactions A*, Vol. 30A, 1999, pp. 1657-1662.
  - 112 R.C. Lemon and H.Y. Hunsiker, "New Aluminum Permanent Mold Castings C355 and A356", *AFS Transactions*, Vol. 64, 1956, pp. 255-260.
  - 113 M. Tsukuda, M. Harada, T. Suzuki and S. Koike, "The Effect of Si, Mg, Fe on the Mechanical Properties of Al-Si-Mg Alloys for Casting", *Journal of Japan Institute of Light Metals*, Vol. 28, no. 3, 1978, pp. 109-115.
  - 114 F.A. Badia, "Effect of Composition and Heat Treatment on the Tensile Properties of an Aluminum-11.5% Silicon-5% Nickel Casting Alloy", *Modern Casting*, Vol. 49, 1966, pp. 104-115.
  - 115 D.A. Granger, "Investigation of a Star-Like Intermetallic Phase Occuring in Alloy 339", *AFS Transactions*, Vol. 99, 1991, pp. 379-383.

- 
- 116 D. A. Granger, R.R. Sawtell and M. M. Kersker, "Effect of Beryllium on the Properties of A357.0 Castings", *AFS Transactions*, Vol. 92, 1984, pp. 579-586.
- 117 A. K. Gupta and B. K. Saxena, "Review: Pore Formation in Cast Metals and Alloys", *Journal of Materials Science*, Vol. 27, 1992, pp. 853-862.
- 118 F. Dimayuga: "Primary and Secondary Porosity in Sandcast Aluminum-Silicon Alloys", M. Eng. Thesis, McGill University, Montreal, Canada, 1981.
- 119 D.R. Irani and V. Kondic, "Casting and Mold Design Effects on Shrinkage Porosity of Light Alloys", *AFS Transactions*, Vol. 77, 1969, pp. 208-211.
- 120 H. Iwahori, K. Yonekura, Y. Yamamoto and M. Nakamura, "Occurring Behavior of Porosity and Feeding Capacities of Sodium- and Strontium- Modified Al-Si Alloys", *AFS Transactions*, Vol. 98, 1990, pp. 167-173.
- 121 J. Campbell, *Castings*, Butterworth-Heinemann, Oxford, U.K., 1991.
- 122 P.S. Mohanty, F.H. Samuel and J.E. Gruzleski, "Role of Inclusions on Pore Nucleation in Aluminum Casting Alloys", *Proc. Int. Sympos. on Light Metals Processing and Applications*, Quebec City, Quebec, Aug. 24 – Sep. 2, 1993, C. Bickert *et al.* (eds.), Canadian Institute of Mining, Metallurgy and Petroleum, Montreal, pp. 273-282.
- 123 N. Roy, A.M. Samuel and F.H. Samuel, "Porosity Formation in Al-9 Wt Pct Si-3 Wt Pct Cu Alloy Systems: Metallographic Observations", *Metallurgical and Materials Transactions A*, Vol. 27A, 1996, pp. 415-429.
- 124 H. Iwahori, H., Takamiya, K. Yonekura, Y. Yamamoto and M. Nakamura, "Influence of Iron and Manganese on Feedability of AC2B Aluminum Alloy", *Castings* (in Japanese), Vol. 60, No. 9, 1988, pp. 590-595.
- 125 G. Boudreault, A.M. Samuel and F.H. Samuel, "Microstructural Observations of Porosity in A319.2 Alloy: Effect of Mold Type/Cooling Rate", *AFS Transactions*, Vol. 107, 1999, Vol. 207-216.
- 126 M. Drouzy and M. Richard, "Effet des conditions de solidification sur la qualité des alliages de fonderie de A-U5 G T et A-S7 G, estimation des caractéristiques mécaniques", *Fonderie*, 1969, Vol. 285, pp. 500-504.
- 127 J.C. Jaquet and H.J. Huber, "Effect of the Solidification Conditions on Mechanical Properties and Microstructure of Hypoeutectic Aluminum-Silicon Alloys", *Geissereiforschung*, Vol. 38, No. 1, 1985, pp. 11-20.

- 
- 128 K.J. Oswalt and M.S. Misra, "Dendrite Arm Spacing (DAS): A Nondestructive Test to Evaluate Tensile Properties of Premium Quality Aluminum Alloy (Al-Si-Mg) Castings", *AFS Transactions*, Vol. 88, 1980, pp. 845-862.
- 129 G. Sigworth, "Determining Grain Size and Eutectic Modification in Aluminum Alloy Castings", *Modern Casting*, Vol. 77, No. 7, 1987, pp. 23-25.
- 130 M.H. Mulazimoglu, A. Zaluska, J.E. Gruzleski and F. Paray, "Electron Microscope Study of Al-Fe-Si Intermetallics in 6201 Aluminum Alloy", *Metallurgical and Materials Transactions A*, Vol. 27A, 1996, pp. 929-936.
- 131 A. Pennors, A. M. Samuel and F.H. Samuel, "Precipitation of  $\beta$ -Al<sub>5</sub>FeSi Iron Intermetallic in Al-6%Si-3.5%Cu (319) Type Alloys: Role of Sr and P", *AFS Transactions*, Vol. 106, 1998, pp. 251-270.
- 132 C. Villeneuve and F.H. Samuel, "Fragmentation and Dissolution of  $\beta$ -Al<sub>5</sub>FeSi Phase during Solution Heat Treatment of Al-13%Si-Fe Alloys", *International Journal of Cast Metals Research*, Vol. 12, 1999, pp. 145-160.
- 133 P.E. Crosely and L.F. Mondolfo, "The Modification of Aluminum-Silicon Alloys", *AFS Transactions*, Vol. 74, 1966, pp. 53-64.
- 134 G. Nagel and R. Portalier, "Structural Modification of Aluminum-Silicon Alloys by Antimony Treatment", *AFS International Cast Metals Journal*, Vol. 5, 1980, pp. 2-6.
- 135 Z. Poniewierski, "Effect of the Type of Modification on the Eutectic Microstructure of Aluminum-Silicon Alloys", *Revue Internationale des Hautes Températures et des Réfractaires*, Vol. 14, 1977, pp. 253-260.
- 136 S. Bercovici, "Control of Solidification Structures and Properties of Aluminum-Silicon Alloys", *Revue de l'Aluminium*, 1979, February, pp. 85-99.
- 137 A.M. Samuel, F.H. Samuel, C. Villeneuve, H.W. Doty and S. Valtierra, "Effect of Trace Elements on  $\beta$ -Al<sub>5</sub>FeSi Characteristics, Porosity and Tensile Properties of Al-Si-Cu (319) Alloys", *International Journal of Cast Metals Research*, Vol. 14, 2001, pp. 97-120.
- 138 R. DasGupta, C.G. Brown and S. Marek, "Analysis of Overmodified 356 Aluminum Alloy", *AFS Transactions*, Vol. 96, 1988, pp. 297-310.

- 
- 139 F.H. Samuel, A.M. Samuel, H.W. Doty and S. Valtierra, "Decomposition of Fe-Intermetallics in Sr-Modified Cast 6XXX Type Aluminum Alloys for Automotive Skin", *Metallurgical and Materials Transactions A*, Vol. 32A, 2001, pp. 2061-2075.
- 140 C. Lepage, "Effets des éléments alliés et des traitements thermiques sur la microstructure et les propriétés de tractions des alliages aluminium-silicium 413.0", M. Eng Thesis, Université du Québec à Chicoutimi, Canada, 2003.
- 141 R. Denton and J.A. Spittle, "Solidification and Susceptibility to Hydrogen Absorption of Al-Si Alloys Containing Strontium", *Materials Science and Technology*, Vol. 1, 1985, pp. 305-311.
- 142 J. M. Kim, H.W. Kwon, and C.R. Loper, Jr., "Feeding Behavior of Modified and Unmodified Al-Si Alloy", *AFS Transactions*, Vol. 104, 1996, pp. 743-749.
- 143 A.K. Dahle, J. Hjelen and L. Arnberg, "Formation of Eutectic in Hypoeutectic Al-Si Alloys", *Solidification Processing 1997, 4<sup>th</sup> Decennial International Conference on Solidification, 1997*, University of Sheffield, UK, pp. 527-530.
- 144 H. Fredricksson, M. Hillert, and N. Lange, "Modification of Aluminum-Silicon Alloys by Sodium", *Journal of the Institute of Metals*, Vol. 101, 1973, pp. 285-299.
- 145 S.C. Flood and J.D. Hunt, "Modification of Aluminum-Silicon Eutectic Alloys with Sodium", *Metal Science*, Vol. 16, 1981, pp. 287-294.
- 146 A.M. Samuel, J. Gauthier and F.H. Samuel, "Microstructural Aspects of the Dissolution and Melting of Al<sub>2</sub>Cu Phase in Al-Si Alloys During Solution Heat Treatment", *Metallurgical and Materials Transactions A*, Vol. 27A, 1996, pp. 1785-1798.
- 147 B.J. Yang, D.M. Stefanescu and J. Leon-Torres, "Modeling of Microstructural Evolution with Tracking of Equiaxed Grain Movement for Multicomponent Al-Si Alloy", *Metallurgical and Materials Transactions A*, Vol. 32A, 2001, pp. 3065-3076.
- 148 F. Hu and E.N. Pan, "A Study of the Fluidity of Al-Si and Al-Si-Cu Alloys", *Chukung (Journal of Chinese Foundrymen's Association)*, Vol. 23, No. 1, 1997, pp. 48-66.
- 149 E. Kato, H. Nomura, and N. Oshiro, "Effect of Phosphorus on Solidified Structure of Hypereutectic Al-Si Alloys", *Journal of Japan Institute of Light Metals*, Vol. 47, No. 12, 1997, pp. 667-671.

- 
- 150 R. Fuoco, E.R. Correa, and H. Goldenstein, "Effect of Modification Treatment on Microporosity Formation in 356 Alloy, Part I: Interdendritic Feeding Evaluation", *AFS Transactions*, Vol. 104, 1996, pp. 1151-1157.
- 151 B. Kolte, "Strontium Modification Gives Critical Melt Control", *Modern Casting*, 1985, May, pp. 33-35.
- 152 Iwahori, K. Yonekura, Y. Yamamoto, and M. Nakamura, "Dispersed Porosities and Feeding Ability of Strontium Modified Al-Si Alloys", *Imono (Journal of Japan Foundrymen's Society)*, Vol. 61, No. 1, 1989, pp. 31-36.
- 153 Jacob, M. Garat, G. Laslaz, P. Meyer, P. Guerin, and R. Adam, "État Actuel de l'Utilisation du Sodium, du Strontium et de l'Antimonie dans les Alliages Aluminium-Silicium Moulés", *Hommes et Fonderie*, No. 258, 1995, pp. 45-54.
- 154 X. Cao and J. Campbell, "Effect of Precipitation of Primary Intermetallic Compounds on Tensile Properties of Cast Al-11.5 Si-0.4 Mg Alloy", *AFS Transactions*, Vol. 108, 2000, pp. 391-400.
- 155 R. Fuoco, E.R. Correa and M. de Andrade Bastos, "Effect of Grain Refinement on Feeding Mechanism in A356 Aluminum Alloy", *AFS Transactions*, Vol. 106, 1998, pp. 463-470.
- 156 A.M. Samuel, F.H. Samuel, H.W. Doty, and S. Valtierra, "Effect of Superheat, Cooling Rate and Impurities on the Formation of Iron Intermetallics in Al-Si Die Casting Alloys", *AFS Transactions*, Vol. 109, 2001, pp. 679-696.
- 157 F.H. Samuel, P. Ouellet, and A. Simard, "Measurement of Oxide Films in Al-(6-17) wt% Si Foundry Alloys Using the Qualiflash Filtration Technique", *International Journal of Cast Metals Research*, Vol. 12, 1999, pp. 49-65.
- 158 L.W. Huang, W.J. Shu, and T.S. Shih, "Diagnosis and Analysis of Oxide Films in Al-Si-Mg Alloys", *AFS Transactions*, Vol. 108, 2000, pp. 547-560.
- 159 S.K. DeWeese, R. Atkinson, and W. Rasmussen, "RPT Measures Hydrogen Gas, Effect on Casting Quality", *Modern Casting*, April, 1992, pp. 29-31.
- 160 A.M. Samuel and F.H. Samuel, "The Reduced Pressure Test as a Measuring Tool in the Evaluation of Porosity Hydrogen Content in Al-7wt Pct Si – 10 Vol Pct SiC (P) Metal Matrix Composite", *Metallurgical Transactions A*, Vol. 24A, 1993, pp. 1857-1868.

- 
- 161 K.J. Brondyke and P.D. Hess, "Interpretation of Vacuum Gas Test Results for Aluminum Alloys", *Transactions AIME*, Vol. 230, 1964, pp. 1542-1546.
- 162 A. Simard, J. Proulx, D. Paquin, F.H. Samuel and N. Habibi, "On the Capability Study of the Improved Prefil-Footer to Predict Aluminum Melt Quality", in *Proc. 6th AFS International Conference on Molten Aluminum Processing*, Orlando, Florida, U.S.A., November 11-13, 2001.
- 163 W.M. Latimer, *The Oxidation States of the Elements and Their Potentials in Aqueous Solutions*, 2<sup>nd</sup> Edition, Prentice-Hall, Inc., Englewood Cliffs, N.J., 1952, pp. 280-283; pp. 315-323.
- 164 W. Khalifa, "Role of Inclusions in the Nucleation of  $\alpha$ -Aluminum and Iron Intermetallics in the Aluminum-Rich Corner of the Al-Si-Fe Ternary System", Ph.D , Université du Québec à Chicoutimi, Canada, 2003.
- 165 A.M. Samuel and F.H. Samuel, "Effect of Melt Treatment, Solidification Conditions and Porosity Level on the Tensile Properties of 319.2 Endchill Aluminum Castings", *Journal of Materials Science*, 1995, Vol. 30, pp. 4823-4833.